Please use block capitals.

Surname	ASHWORTH
First names (in full)	DAVID ALAN
Faculty board	PHYSICAL SCIENCES
Title of thesis	UNSTEADY AERODYNAMICS AND HEAT TRANSFER IN A TURBINE STAGE

N.B. The title stated here must be precisely the same as that stated on the title page of the thesis submitted.

A candidate wishing to amend the title previously approved by the faculty board must apply to the faculty board for permission to do so.

Declaration by the candidate as author of the thesis.

1. I understand that I am the owner of the copyright of this thesis and that the copyright rests with me unless I specifically transfer it to another person.
2. I understand that the University requires that if I am granted leave to supplicate I shall deposit one copy of my thesis in the Bodleian Library where it shall be available for consultation and that photocopies of it may be made available to those who wish to consult it elsewhere. I understand that the Library, before allowing the thesis to be consulted either in the original or in a photocopy, will require each person wishing to consult it to sign a declaration that he recognises that the copyright of the thesis belongs to me and that no quotation from it and no information derived from it may be published without my prior written consent.
3. I agree that my thesis shall be available for consultation in accordance with paragraph 2 above.

Signed ..... *Date* 19/5/87

Microfilmed
by BLLD
D 83740.

Notes

(a) If, for good reason, you do not wish your thesis or part of it to be made available for consultation or to be photocopied, you may apply to the relevant faculty board for dispensation from this requirement. Any such application should state, with full reasons, both the nature and the period of the dispensation requested, and should be sent with this form to the Graduate Studies Office. *If you are applying for dispensation, please tick this box:* ☐

(i) Dispensation for a limited period will always be granted in cases where confidentiality has been made a condition of access to material which is subsequently incorporated in a thesis.

(ii) Where confidential material forms only a small part of a thesis and the force of the thesis will not be seriously impaired by the removal of such material, the faculty board may grant permission for the confidential material to be deposited separately from the thesis, on the understanding that the thesis will be available for consultation or photocopying but access to the confidential material will be restricted.

(b) You may discover the names of persons who have consulted your thesis by writing to the Keeper of Western Manuscripts at the Bodleian Library requesting this information.

(c) You are requested to sign the declaration above even if you are applying for dispensation from the consultation requirement. If dispensation is granted, your thesis will *not* be made available for consultation or photocopying before the expiry of the dispensation period.

Do not forget to sign under Section 5 opposite.

UNSTEADY AERODYNAMICS AND HEAT TRANSFER IN A TRANSONIC TURBINE STAGE

D. A. Ashworth

St. John's College
University of Oxford

A thesis submitted in partial fulfillment of the
requirements of the degree of Doctor of Philosophy
at the University of Oxford, Trinity Term, 1987.

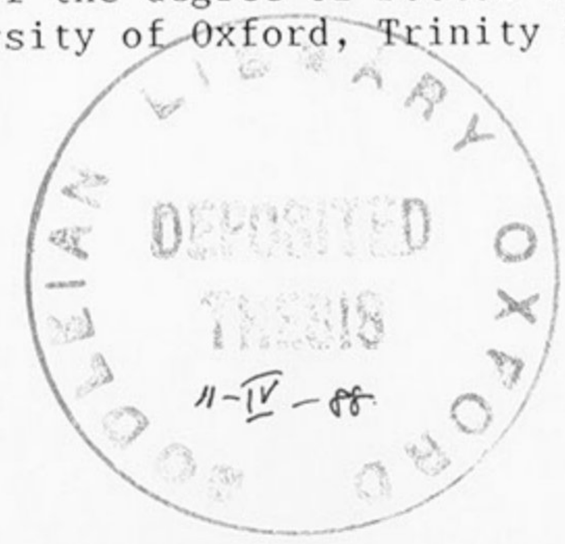

Department of Engineering Science,
Osney Laboratory,
Oxford.

To the memory of Don Schultz.

UNSTEADY AERODYNAMICS AND HEAT TRANSFER IN A TRANSONIC TURBINE STAGE

A Thesis Submitted for the Degree of Doctor of Philosophy by
D. A. Ashworth, St. John's College, University of Oxford

Trinity Term, 1987

ABSTRACT

In current design methods for gas turbines there are important features of the flow which are not yet within the scope of the available prediction methods for both the calculation of surface pressures and heat transfer rates. Such features include the prediction of three-dimensional viscous flowfields, the accurate location and strengths of the secondary flow regimes in a turbine passage, and allowance for time-dependent variations. It is the understanding of the time-varying phenomena which is the subject of this study. Such phenomena occur due to the periodic interaction between stages in a turbine, either that of a nozzle guide vane on a rotor downstream or vice-versa. In most contemporary designs of turbines the effects are due primarily to the wakes from the trailing-edge of the upstream airfoil, and to any associated shock structures resulting from transonic exit flow Mach numbers. The present investigation is concerned with furthering knowledge of these wake and shock interactions, using a method of simulation established in the Isentropic Light Piston Tunnel at Oxford. Measurements of heat transfer rates and pressures are presented, supported by flow visualisation methods such as surface oil-dots and schlieren photography, for two examples of high-pressure turbine rotor blades. The majority of analysis deals with the first of these (a highly-loaded transonic profile) whilst the second blade (designed for use in a large civil engine) is included for investigation of the effects of flow unsteadiness on the film cooling process.

The transition process is examined in detail by use of wide bandwidth heat transfer measurements, and a new method derived for modelling this process. It has been possible to observe the effect of the enhanced turbulence in the simulated nozzle guide vane wake and effects due to a shock-boundary layer interaction. The reaction of the blade boundary layers to these disturbances is identified, and trajectories of disturbed events tracked along the blade surfaces. The measurements which have been taken allow for some aspects of wake and shock interactions to be included in the design process for turbine blading. A better understanding has been obtained of how these types of transient flow regimes affect the boundary layers on the blade surfaces.

ACKNOWLEDGEMENTS

There are many people without whom this thesis would not have been possible. I am most indebted to the late Professor Don Schultz, who provided continual encouragement and inspiration as my supervisor for the majority of the time spent working on the thesis - Don will be sorely missed by all who knew him. Dr. Martin Oldfield kindly assumed the responsibility for my guidance through the latter stages of the thesis preparation, and I am most grateful for his support both before and after taking over my supervision. My thanks also go to Professor John LaGraff for his encouragement and extensive contributions to the experimental programmes. The tests could not have been carried out without the helpful assistance of Kevin Grindrod, and the contributions made by John Allen, Trevor Godfrey and all the other members of the Turbomachinery Group at the Osney Laboratory, too numerous to mention. I would particularly like to thank Dr. Denis Doorly for his work in developing the wake-passing equipment, and David Henshaw for helping make systems run so smoothly. I have appreciated the helpful discussions I have had with many people at Rolls-Royce plc, particularly those with Dr. Alan Forest, Dr. Adrian White and Mike Howard.

I am grateful to Rolls-Royce plc for providing financial support, both for myself and for the experimental programmes, together with the MoD (Procurement Executive), and to the AFOSR Grant No. 85-0295 for the support of some of the tests.

I have greatly appreciated all the help and support given by Jo in her painstaking preparation of the thesis.

I would finally like to thank my parents, family and friends who have made it all worthwhile.

CONTENTS

	Page
ABSTRACT	(i)
ACKNOWLEDGEMENTS	(ii)
CONTENTS	(iii)
NOMENCLATURE	(vii)
CHAPTER I - INTRODUCTION	
1.1 Objectives of the Thesis	1.1
1.2 Gas Turbine Performance	1.2
1.2.1 Overall Performance and the Influence of Unsteady Flows	1.2
1.2.2 Heat Transfer Rates to Turbine Blades	1.4
1.3 The Effects of Unsteady Flows	1.5
1.3.1 The Types of Unsteady Interactions in Turbines	1.5
1.3.2 The Effects of Unsteady Interactions on Turbine Blade Boundary Layers	1.7
1.4 The Context of the Current Study in the Design Process	1.9
1.5 Review of Contents	1.9
CHAPTER II - PREVIOUS WORK ON TRANSITION AND UNSTEADY PROCESSES	
2.1 The Nature of Transition	2.1
2.1.1 Boundary Layer Stability Theory	2.2
2.1.2 Competing Modes of Transition	2.4
2.1.3 Models of Turbulent Spot Growth	2.5
2.1.4 Turbulent Spot Production and Growth	2.6
2.2 The Influence of Embedded Wakes in the Freestream	2.7
2.2.1 Effects of Wakes on Simplified Geometries	2.8
2.2.2 Previously Used Wake Models	2.9
2.2.3 Examination of Wake Transport through Blade Rows	2.11
2.2.4 Effects of Shock Interactions with Boundary Layers	2.14
2.3 Other Tests on the ACE and B22 Blade Profiles	2.15
2.3.1 Measurements on the ACE Profile	2.16
2.3.2 Measurements on the B22 Profile	2.16

CHAPTER III - DETAILS OF THE EXPERIMENTS

3.1 Operation of the Isentropic Light Piston Tunnel 3.1

3.2 Unsteady Flow Generation in the ILPT 3.3

3.3 Reduction of Data and Methods of Analysis 3.4

3.3.1 Acquisition and Processing System 3.4
3.3.2 Pressure and Temperature Measurements 3.6
3.3.3 Heat Transfer Rate Measurements 3.8

3.4 Test Conditions 3.12

3.4.1 Operating Conditions 3.12
3.4.2 Inlet and Outlet Mach Number Distributions 3.13
3.4.3 Inlet Turbulence Level 3.13

3.5 Details of the Profiles Tested 3.14

3.5.1 Design Concepts for the ACE Blade 3.14
3.5.2 Comparison of the Two Profiles Investigated 3.15

CHAPTER IV - STEADY-STATE RESULTS

4.1 Flow Visualisation 4.1

4.1.1 Surface Flow Visualisation 4.1
4.1.2 Schlieren Photographs of the Steady Flowfield 4.2

4.2 Mach Number Distributions 4.3

4.2.1 Measured Surface Mach Number Distributions 4.4
4.2.2 Comparison with Prediction and Previous Measurements 4.5

4.3 Steady-State Heat Transfer Rate Measurements 4.7

4.3.1 Measured Heat Transfer Rates - An Overview 4.7
4.3.2 Analysis of Mean Heat Transfer Rates by a Correlation Approach 4.10
4.3.3 Comparison of Measured Heat Transfer Rates with Prediction 4.16
4.3.4 Time-Resolved Heat Transfer Rate Measurements from the Steady-State Tests 4.17

CHAPTER V - MEASUREMENT AND MODELLING OF THE NATURAL TRANSITION PROCESS

5.1 Measurements of Transition on the ACE Profile 5.1

5.1.1 Experimental Data 5.1
5.1.2 Analysis of Transition Data 5.3

5.2 Modelling the Natural Transition Process 5.4

5.2.1 Statistical Basis for Modelling Transition 5.5
5.2.2 Details of a Computer Simulation of Transition 5.9

CHAPTER VI - UNSTEADY RESULTS ON THE ACE PROFILE

6.1 Schlieren Photographs of the Unsteady Flowfield 6.1

6.2 Heat Transfer Rate Measurements 6.5

6.2.1 Heat Transfer Results for the 16 Bar Case 6.5
6.2.2 Heat Transfer Results for the 2 Bar Case 6.10

6.3 Unsteady Pressure Measurements 6.11

CHAPTER VII - PREDICTED WAKE AND SHOCK POSITIONS

7.1 Modelling of the Bar Wake 7.1

7.1.1 Method of Modelling the Wake 7.1
7.1.2 Details of the Computational Model 7.2

7.2 The Simplified Shock Model 7.4

7.2.1 Modelling the Bow Shock 7.5
7.2.2 Modelling the Recompression Shock 7.6
7.2.3 Details of the Computational Model 7.7

7.3 Results of the Predictions and Related Trajectory Analysis 7.8

CHAPTER VIII - WAKE-PASSING EXPERIMENTS ON A FILM COOLED PROFILE

8.1 Details of the B22 Experiments 8.1

8.2 Mean Heat Transfer Rate Measurements 8.3

8.2.1 Leading-Edge Film Cooling (Build 'A') 8.3
8.2.2 Suction Surface Film Cooling (Build 'B') 8.4
8.2.3 Pressure Surface Film Cooling (Build 'C') 8.5

8.3 Schlieren Results for the Film Cooled Profile 8.6

8.3.1 Leading-Edge Film Cooling (Build 'A') 8.7
8.3.2 Suction Surface Film Cooling (Build 'B') 8.8
8.3.3 Pressure Surface Film Cooling (Build 'C') 8.8

CHAPTER IX - CONCLUSIONS

9.1	Experimental Technique and Instrumentation	9.1
9.2	Mean Measurements of Heat Transfer and Pressure on the ACE Profile	9.2
9.3	Measurement and Analysis of Natural Transition on the ACE Suction Surface	9.3
9.4	Examination and Prediction of Wake and Shock Wave Effects	9.3
9.5	Effects of Wake-Passing on a Film Cooled Profile	9.4
9.6	Relevance to the Design Process	9.5
9.7	Recommendations for Future Work	9.6

REFERENCES
TABLES
FIGURES
PLATES
APPENDIX A - Transient Thermal Analysis
APPENDIX B - ACE Blade Co-ordinates

NOMENCLATURE

A^*	Throat area (m^2)
a	Speed of sound (m/s)
B	Blowing rate = $\rho_c u_c / \rho_\infty u_\infty$
b	Wake width
Bi	Biot number = $h\Delta x/k_s$
C	Blade chord (m)
c	Velocity (m/s)
c_p	Specific heat (kJ/kgK)
d	Bar diameter (m)
f	Propagation factor
Fo	Fourier number = $\alpha\Delta t/(\Delta x^2)$
Go	Goertler number defined by equation (4.10)
g(x)	Burst rate function ($/sm^2$)
H	Enthalpy (kJ/kg)
h	Heat transfer coefficient = $\dot{q}/\Delta T$ (W/m^2K)
i	$\sqrt{-1}$
K	Acceleration parameter = $\nu/U^2 dU/dx$
k	Thermal conductivity (W/mK)
l	Characteristic length (m)
M	Turbulence grid pitch (m)
M	Mach number = c/a
m	Pohlhausen parameter = $\theta^2/\nu\ dU/dx$
N	Rotational speed (rpm)
N_i	Scale factors for burst rate functions (i = 1,2,3)
n	Number (of blades)
n_b	Number of turbulent spots per 2 μs time-step ($/sm^2$)
Nu	Nusselt number = hC_{TN}/k_g
Nu_x	Local Nusselt number = hx/k_f
p,P	Pressure (Pa)
Pr	Prandtl number = $\mu c_p/k_g$
$\dot{q}$	Heat transfer rate (W/m^2)
R	Radius of curvature (mm)
r	Radius (m)
Re	Blade Reynolds number = $\rho_2 u_2 C_{TN} / \mu_2$
Re_x	Local Reynolds number based on surface length = $\rho_\infty u_\infty x / \mu_f$
Re^*	Integral Reynolds number = $\int \frac{u(x)}{\nu(x)}\, dx$
S	Entropy (J/K)
S1	Indicates bar bow shock
S2	Indicates bar re-compression shock
s	Surface (and length of)
s	Laplace transform variable
T	Temperature (K)
t	Time (s)
Tu	Turbulence level = u'/U_1
Tu_l	Local turbulence level = u'/U_∞
U,u	Velocity, normally in x-direction (m/s)
v	Velocity, normally in y-direction (m/s)
W	Pump tube volume (m^3)
x	Streamwise direction, unless otherwise defined (m)
y	Normal to surface, unless otherwise defined (m)
z	Pitchwise direction (m)

α	Lateral angle of spread for turbulent spot trailing-edges
α	Thermal diffusivity = $k/\rho c$
α	Oblique shock angle = arcsin (1/M)
α	Defined as $2\pi/\lambda$ for the Tollmien-Schlichting wavelength, λ
α_b	Relative velocity vector angle
β	Gas angle (measured from the axial direction)
β	Shock angle normal to U_{rel}, $\tan^{-1}\alpha$
β	Tollmien-Schlicting wave frequency
γ	Ratio of specific heats
γ	True intermittency factor
$\bar{\gamma}$	Intermittency factor as defined by Equation 5.1
ΔT	Temperature Difference
Δt	Time interval
δ	99% Boundary layer thickness
$\delta(x-x_o)$	Dirac delta function at $x = x_o$
δ_{max}	Maximum turning angle at a Mach number
$\bar{\delta}_n$	Complementary Kronecker delta of n variables
ϕ	Perturbation stream function
λ	Tollmien-Schlichting wavelength
μ	Dynamic viscosity (kg/ms)
ν	Kinematic viscosity (m^2/s)
ρ	Density (kg/m^3)
σ	Standard deviation
σ	Local oblique shock angle
σ_f	Propagation aspect ratio = $\tan\alpha(f_t^{-1} - f_l^{-1})$
η	Angle of the sonic line to the normal to U_{rel}
θ	Boundary layer momentum thickness (m)

Subscripts

amb	Ambient condition
ax	Axial direction
b	Bar (relative condition or datum for y_b)
b	Blade
blow	Coolant supply pressure
c	Coolant flow condition
c	Centroid streamline
c	Cold operating condition
crit	Critical Value
e	End point
f	Film temperature (Eckert definition)
g	Gas
h	Hot operating condition
h,m,t	Hub, mean and tip positions on the bar
i	Value at a given instant in time
i	Imaginary Component
i,init	Initial condition
l	Leading-edge
l	Local value
m	Parameter at the measuring instant
max	Maximum turning angle for a given approach Mach number
r	Reservoir
r	Recovery condition
r	Real component
rel	Relative bar condition
ref	Reference value

s	Substrate
s	Sonic line
s	Start point
sb	Point of intersection of the sonic line with the bar
tube	Value in the piston tube
TN	Tangential (or true) chord
t	Trailing-edge
t	Transition onset
w	Value at wall
o	Total (stagnation) condition
o	Start of turbulent spot activity
1	Inlet condition
2	Exit condition
∞	Freestream condition (static)

Superscripts

-	Time-averaged value
-	Tube condition
-	Laplace transformed variable
′	Fluctuating component(r.m.s.)
^,~	Turbulent quantities defined in Chapter I

CHAPTER I

INTRODUCTION

The subject of unsteady flow interactions within gas turbine engines is being pursued with increasing vigour as more confidence is gained not only by understanding the nature of these effects, but also how these affect conventional steady-state analysis. In this chapter the objectives of the present work are outlined. The general requirements for turbine performance are discussed, in terms of the operating environment and its effect on the blade boundary layers. The particular need to understand the unsteady effects in a turbine stage is covered, followed by a review of the contents of the thesis.

1.1 OBJECTIVES OF THE THESIS

The primary objectives of the current work are to improve our understanding of some unsteady flow processes in a simulation of a gas turbine environment. It is intended that such understanding can eventually be incorporated in the design process such that improvements may be obtained in efficiency and component life, thus making the business of gas turbine manufacture more cost-effective. The scope of this thesis covers the acquisition, analysis and prediction of these unsteady events as well as the basic steady flowfield on which these events are superimposed. The models developed could form the basis of additions to the conventional design methods, but their primary role is to enable better understanding of the processes involved. Such features as the interactions of freestream disturbances with the blade boundary

layers, the transitional behaviour of the developing boundary layers and the validity of the application of simplified models for such processes will be scrutinised. In addition to the predictions performed, attempts will be made to present data in a form which is easiest to interpret, since the interaction processes produce complex time-resolved results which may otherwise be difficult to interpret.

1.2 GAS TURBINE PERFORMANCE

1.2.1 Overall Performance and the Influence of Unsteady Flows

The requirement to reduce the specific fuel consumption (s.f.c.), defined as the ratio of the fuel flow rate to the thrust produced, is of critical importance to gas turbine designers. This is achieved to some extent by control of parameters such as the by-pass ratio, through careful choice of cycle parameters, particularly with regard to raising the overall thermal efficiency by increasing the turbine entry temperature (T.E.T.), and by improving the performance of the individual engine components. Examples of simplified cycles corresponding to typical engines developed over the last 30 years are given in Figure 1.1(a). The dramatic increase in pressure ratio from 5.75 in the Dart engine of 1955 to 28.40 in the RB211-524 engine of 1970 gives rise to higher efficiencies and specific work output, with an associated increase in T.E.T. The upward trend in T.E.T. with time is shown in Figure 1.1(b) from RUFFLES[1986]. An example of the benefit of increasing aero-engine T.E.T. is given in NICHOLSON[1981], where it was demonstrated that a 1.5% improvement in high-pressure turbine efficiency (defined as the ratio of the actual change in total temperature divided by the ideal change) leads to a 1% improvement in overall s.f.c. A plot of stage loading ($\Delta H/U^2$) against specific work function ($c_p \Delta T/T$), is a means by which a turbine operating point can be viewed in context with

other turbine designs, an example of which is given in Figure 1.2(a). The original operating point for the turbine profile which forms the major part of the current experimental work (the ACE or Advanced Core Engine turbine) shows that the design is at the upper end of the loading and specific work range. Constraints on the design of the blades such as temperature, creep life, fatigue stresses and rupture stresses can be superimposed on these charts and a method for optimising blade designs developed. These constraints limit the level of efficiency attainable, directly affecting the overall engine performance. Periodic temporal variation in turbine efficiency has an even greater effect due to the mis-matching of stages, even when the turbine is operating at its nominal design point. The types of unsteady flow present in gas turbines are discussed in Section 1.3.1. In general, any periodic variation due to the interaction of blade rows can result in the presence of more than one convected event in a passage at a given time. This can be demonstrated for a turbine by considering a typical design with 36 nozzle guide vanes (NGV's) and 61 rotor blades rotating at 9000 rpm, by considering the blade passing frequency (b.p.f.) defined by :

$$\text{b.p.f.} = \frac{N\ (\text{rpm})}{60}\ n_{NGV} \qquad \ldots (1.1)$$

Thus a blade passing frequency of 5 kHz is observed for the NGV signature as seen by the rotor, a typical transit time of 250 μs being equivalent to a frequency of 4 kHz. Distortions to the inlet flow to the rotor (such as highly turbulent patches, and periodic incidence changes) thus influence the performance of the rotor over a significant fraction of the NGV interaction time. Other structures (such as the possible trailing-edge shocks shed from the NGV) become more significant as the ratio of the number of NGV's to rotors increases, but attempts to reduce the numbers of NGV's by increasing

the space/chord ratio have had only limited success due to difficulties in maintaining the required amount of flow turning in the NGV's and the avoidance of suction surface flow separation.

1.2.2 Heat Transfer Rates to Turbine Blades

The primary limitation in the improvement of cycle efficiency by an increase in the T.E.T. is that of material limitations in the high pressure (HP) turbine stage, as the high temperatures, > 2400 K (corresponding to stoichiometric burning in the combustor) desirable from a performance point of view, are well above the melting point of suitable blade materials currently available. The rate of introduction of new materials is too slow to satisfy the requirements of efficiency improvement imposed by the current climate of rising fuel costs, and so a means must be found by which existing materials can be used. The increase in T.E.T. for civil engines in production from 1960 to 1986 is from 1300 K to 1500 K corresponding to a maximum metal temperature increase of only 50 K to 1263 K. The remainder of the increase in T.E.T. has only been possible due to two factors:

(i) The ability to understand, and hence improve, the prediction of the external heat transfer rate to turbine blades.

(ii) An improved capability for cooling the blades, both internally (using compressor outlet air pumped through cooling channels within the blade) and externally (by the use of films of the same cool air ejected onto the blade surface forming a barrier to the hot gases in the freestream).

In spite of these two factors, differences still exist between the performance of blades in the engine to those predicted or measured in simplified environments (such as 2-D cascade testing). The experiments reported here attempt to identify the nature of these differences by simulation of some of the unsteady effects present in

the engine whilst still enabling the kind of highly detailed measurements possible in a 2-D test. The significance of errors in the prediction of the surface heat transfer rate is not confined to the limits on T.E.T. attainable, but also to the blade life. As an example, an error in predicting the wall temperature by 65 K for a nickel alloy blade typically results in an order of magnitude of decrease in the life of the blade GRAHAM[1979]. In order to reduce the cost of operation of gas turbines whilst maintaining operating standards (i.e. not just s.f.c. but also lifeing requirements, limits on permissible noise levels, off-design performance and other legislated standards) blade designs have to become less conservative, and the effects of errors in design hence more significant. These exhibit themselves in failures through hot-spots and shroud curling, often due to secondary flows, and due to the cooling system not performing up to its expected level of effectiveness.

1.3 THE EFFECTS OF UNSTEADY FLOWS

1.3.1 The Types of Unsteady Interactions in Turbines

There are two distinguishable types of flow unsteadiness which affect the heat transfer rate to turbine blade surfaces:

(1) Freestream Turbulence

Characterised by small turbulent eddies rotating at high speeds, this type of unsteadiness is close to the classical definition of turbulence, and has velocity fluctuations u'/U typically of the order of a few percent. It occurs in the freestream far downstream of obstructions, such as a grid of cylindrical bars commonly used to generate isotropic turbulence in cascades, in order to simulate the high frequency flow disturbances emanating from a combustor. The length scales are such as to cause instabilities in surface boundary layers.

(2) Flow Disturbances

Covering a wide range of frequencies, these disturbances can be caused by local variations in freestream conditions. They may be due to unequal performance in components, e.g. uneven burning in the combustor. They also occur due to the interaction between blade rows in turbomachines in two ways. Firstly, the potential flowfields of successive blade rows interact, particularly if the axial spacing between rows is small. This type of unsteadiness tends to diminish exponentially with increases in spacing, and has little influence at the 25% axial chord spacing typical of current designs. The second interaction is due to the wakes and any associated shock structures from an upstream blade row being 'chopped' by the action of the rotor blades, causing events to occur at the b.p.f. in the downstream row. Although these are low frequency occurrences from the point of classical models of turbulence, each contain high frequency components which can intermittently disturb the downstream flow. These interactions are illustrated in Figure 1.2(b) from DOORLY[1983], with the effect of the velocity deficit in the wake causing an overall decrease in inlet angle, and an associated increase in turbulence level above that of the freestream.

The different types of fluctuation are shown in Figure 1.3(a) based on the nomenclature used in EVANS[1975], with three resulting definitions of 'turbulence' level, i.e.

(i)	(ii)	(iii)
Overall Disturbance Level	Freestream Tu level	Unsteadiness Level

$$Tu_D = \frac{\sqrt{V_D'^2}}{\bar{U}} \qquad \hat{Tu} = \frac{\sqrt{v'^2}}{\bar{U}} \qquad \tilde{Tu} = \frac{\sqrt{(u(t)-\bar{u}(t))^2}}{\bar{U}} \quad \ldots (1.2)$$

and $Tu_D^2 = \hat{Tu}^2 + \tilde{Tu}^2$. In this way an attempt is made to separate the overall disturbance level, Tu_D corresponding to types (1) and (2), into the two components, $\hat{Tu}$ and $\tilde{Tu}$. The problem at present is in understanding the nature of these fluctuations as they affect the blade boundary layers. Experimental evidence suggests that the intensity of turbulent fluctuations alone is not enough to define the reactions of surface boundary layers, as the length scales and phase relationships of the components of turbulent flows are also relevant to our understanding of boundary layer behaviour. By a full definition of unsteady flow and investigation of interactive boundary layer behaviour it is hoped that the division between turbulent types (1) and (2) above may be found, as these two types affect turbine blade boundary layers.

1.3.2 The Effects of Unsteady Interactions on Turbine Blade Boundary Layers

The heat transfer rate to turbine blade boundary layers depends on many factors, as described in NICHOLSON[1981], often considered to be steady-state in nature. The characteristics of a typical turbine blade boundary layer are drawn schematically in Figure 1.3(b). The heat transfer rate (for a given temperature difference) is assumed to be a function of the form:

$$\dot{q} = f(Re, \frac{dp}{dx}, R, Tu, K = \frac{\nu}{U^2}\frac{dU}{dx}) \qquad \ldots (1.3)$$

for the parameters of Reynolds number, streamwise pressure gradient, radius of curvature, turbulence level and acceleration parameter, K. Other parameters such as the surface roughness have effects which are generally second order, but can seriously affect the location and length of the region of transition from a laminar to a turbulent boundary layer state.

The convex curvature and high accelerations of the suction surface imply a stretching of turbulent eddies, so that an initially laminar portion is maintained longer than would be the case on an equivalent flat plate before transition to a turbulent boundary layer occurs. Increasing the level of freestream turbulence can enhance the heat transfer rate to a laminar boundary layer, and also promote the transition process. The higher heat transfer rate through the turbulent boundary layer results in an increase in mean level over the blade. The later part of the suction surface will be affected by the trailing-edge shock shed by the neighbouring blade if the exit Mach number is above sonic and this can lead to boundary layer separation causing high losses as the combined momentum deficit in the wake increases.

The pressure surface of the blade has concave curvature over much of its length which may lead to instabilities in the boundary layer if longitudinal (chordwise) Goertler vortices develop. Transition often occurs early on the pressure surface so that the heat transfer rates correspond to the turbulent levels, enhanced by curvature effects to even higher levels. If the acceleration parameter K reaches high enough levels ($> 2.5 \times 10^6$) then the boundary layer can change back to one similar to a laminar type, a phenomenon known as 're-laminarisation'.

Both surfaces are susceptible to other intermittent disturbances, and DOORLY and OLDFIELD[1985b] have shown that wakes shed through a turbine cascade cause an intermittent step change in boundary layer state from laminar to turbulent levels. There is also the possibility that unsteady shock-boundary layer interactions can occur, with the likelihood of associated separations of the boundary layers in transonic designs of turbines. Both wake and shock unsteadiness have greatest significance on the early portions of the

blade surfaces, with only convected effects of these disturbances on the later parts of the blade.

1.4 THE CONTEXT OF THE CURRENT STUDY IN THE DESIGN PROCESS

Figure 1.4 is an attempt to illustrate the role of the turbine research activity in the overall turbine design process. The areas touched on in this study are outlined in bold. The experiments performed here are driven by the need to develop better design methods which consequently require a more detailed understanding of the flow environment. The methods are examined with respect to the experimental data by comparison of predicted values of surface heat transfer rate, loss and pressure distributions, supported by methods for visualising the flowfield.

1.5 REVIEW OF CONTENTS

In Chapter II the background to the thesis subject is covered, with a review of related work in the literature.

The details of the experimental arrangement and methods of data acquisition and analysis are covered in Chapter III. The methods employed for the measurement of heat transfer rate in the unsteady environment are described and the test conditions are also specified. The choice and design of the blade profiles considered is discussed, and previous test results obtained on these profiles reviewed. The steady-state measurements made on the ACE profile are presented in Chapter IV enabling the effect of inlet incidence variation, exit Mach number, Reynolds number and isotropic freestream turbulence level to be identified as they affect surface Mach number distributions and heat transfer rates. Surface oil-dot flow visualisation and schlieren techniques have been used to allow a

fuller understanding of the flowfield. These steady-state results are then compared with predictions and previous test results.

In Chapter V the natural transition process is examined by use of the wide-bandwidth heat transfer results, such that the individual occurrence of turbulent bursts can be determined. A novel method for modelling these bursts and hence predicting transition is developed.

The overall effects of the unsteady interaction of the simulated NGV wakes and shock waves on surface heat transfer rates and pressures are presented in Chapter VI, together with schlieren results for the unsteady case.

The convection of the wake by the freestream and the movement of shock waves shed from the simulated NGV are compared with predictions in Chapter VII. The three-dimensional nature of the simulation is allowed for in the shock model. The trajectories of wake and shock-driven effects are compared with prediction and the changes in boundary layer state investigated.

Chapter VIII contains an examination of the interaction of the shed NGV wakes with a film cooled version of the B22 profile and includes a discussion of the magnitude of effects observed.

The conclusions drawn from this study and the recommendations for future work are given in Chapter IX.

CHAPTER II

PREVIOUS WORK ON TRANSITION AND UNSTEADY PROCESSES

Even in the apparently steady-state environment of a low freestream turbulence flow past a surface it is possible for unsteady disturbances to build-up in the surface boundary layer which cause a breakdown to a turbulent state. This laminar-turbulent transition process has been extensively studied, and much theoretical effort put into attempting prediction of the growth of disturbances within laminar boundary layers. Many aspects of this process are still not clear, particularly once the disturbances become non-linear, and these points will be discussed in detail in Chapter V.

The background material available for the subject of unsteady interactions is substantial, covering both the effects of NGV wake interactions with rotor blade boundary layers and previous data acquired on both of the profiles tested. This data includes pressure and heat transfer distributions around the profiles with the effects of film cooling on the blade surfaces as well as unsteady measurements on the uncooled version of the B22 blade.

2.1 THE NATURE OF TRANSITION

Osborne Reynolds first identified the phenomena associated with the breakdown of ordered laminar flows into ones containing eddies with enhanced mixing known as turbulent flows, using his now famous ink-jet experiment. He discovered that below a critical value of velocity of flow the flow remained laminar, a criterion now expressed as a critical Reynolds number, $Re_{crit} = ul/\nu$ for some characteristic

length, l. Disturbances from the freestream or due to surface roughness can either be amplified or damped out in the initially laminar boundary layer, depending on whether the boundary layer remains stable or becomes unstable to disturbances. The initial development of disturbances can be described by a linear stability theory outlined in Section 2.1.1. Alternative modes of transition are described in Section 2.1.2, and other experimental observations of the natural transition process detailed in Section 2.1.3.

2.1.1 Boundary Layer Stability Theory

This was investigated by use of a 'method of small disturbances' applied to the unsteady Navier-Stokes equations for a two-dimensional disturbance in a two-dimensional incompressible flowfield, as described in SCHLICHTING[1979]. A perturbation stream function for a single oscillation of the disturbance is assumed to be of the form:

$$\phi(x,y,t) = \phi(y)\, e^{i(\alpha x - \beta t)} \qquad \ldots (2.1)$$

where $\alpha = 2\pi/\lambda$ for a disturbance of wavelength λ,

ϕ = amplitude function (of the normal co-ordinate y alone),

$\beta = \beta_r + i\beta_i$, β_r a frequency of oscillation and β_i an amplification factor.

If the value of $\beta_i > 0$ then disturbances will be amplified (an unstable condition), otherwise they will be damped out (a stable condition). Substituting the stream function, equation (2.1), into the Navier-Stokes equations, keeping only the first-order terms in the disturbance velocity components, and applying the no-slip condition at the wall, results in an ordinary fourth-order differential equation for the amplitude function $\phi(y)$, as:

$$(U - \beta/\alpha)(\phi'' - \alpha^2\phi) - U''\phi = -\frac{i}{\alpha Re_\delta}(\phi'''' - 2\alpha^2\phi'' + \alpha^4\phi) \qquad \ldots (2.2)$$

known as the Orr-Sommerfeld equation (or the stability equation). Length scales are non-dimensionalised by the boundary layer

thickness, δ, velocities by the maximum velocity of the main flow, such that $Re_\delta = U\delta/\nu$, and the primes denote differentiation with respect to y/δ. The terms on the left-hand side of (2.2) correspond to inertial terms, whereas those on the right are viscous terms. Although only two-dimensional disturbances were allowed for in the derivation of this equation, theoretical studies have shown that periodic three-dimensional disturbances only induce instabilities at a higher Reynolds number than for the two-dimensional case, so that (2.2) describes the more critical disturbances to the flow providing that the amplification process remains linear. The solution to the Orr-Sommerfeld equation is most often presented in graphical form as a neutral stability diagram, which demonstrates that no amplification of disturbances takes place if:

(a) The Reynolds number is below a critical value.

(b) The disturbance wavelength is longer than a critical value, approximately equal to 6δ.

The inertial terms of equation (2.2) were analysed by Rayleigh who found that a necessary and sufficient condition for instability is that the velocity profile contains a point of inflexion. Viscous flows can become unstable even without a point of inflexion. This leads to the conclusion that from zero to more positive pressure gradients instabilities are likely, whereas the fuller velocity profiles associated with decreasing pressure will tend to be more stable.

Following the development of two-dimensional disturbances, three-dimensional effects start to appear and amplify in the unstable region, as shown schematically in Figure 2.1(a), over a region whose length is determined by the level of freestream turbulence and the streamwise pressure gradient. If the Reynolds number becomes high enough, at Re_t in Figure 2.1(a), the disturbances can break down into

patches of turbulent flow, intermittently occurring along the surface. The effect of freestream turbulence on this transition length is shown in Figure 2.1(b). This tends to move the point of transition closer to the point of neutral stability as Tu approaches 2 to 3%, the 'high' level of the present tests, causing an earlier transition for the same location of the neutral stability point. The turbulent structure builds up through intermittent patches of turbulence known as turbulent bursts or spots, and is discussed in Section 2.1.3.

2.1.2 Competing Modes of Transition

Alternative mechanisms for transition exist, including either the Goertler vortex instabilities, or those due to flow separations which may cause rapid transition to occur. The most likely modes of transition are given in Figure 2.2. These cover a frequency range from steady-state (for example, transition induced by a steady separation bubble) through lower frequency events (such as those due to blade-passing events) up to higher frequency (at the turbulent spot formation rate). Different types of transition may occur simultaneously and compete with each other in order to cause breakdown to fully turbulent flow. The fraction of time that the flow is turbulent at a given location is known as the intermittency of that point (as defined in SCHLICHTING[1979], for example). Typical intermittency paths along the surface are sketched in Figure 2.2 for each mode. If more than one mode exists a total intermittency can be calculated by summing the contributions as probabilities by adding the chance of any one occurring, then subtracting the chances of simultaneous occurrence. For two competing modes the total intermittency can be obtained from:

$$\gamma_{tot} = \gamma_1 + \gamma_2 - \gamma_1\gamma_2 \qquad \ldots (2.3)$$

and for N modes from:

$$\gamma_{tot} = \sum_{n=1}^{N} \left[\frac{(-1)^{n+1}}{n!} \sum_{\substack{i_1=1 \\ i_2=1 \\ \vdots \\ i_n=1}}^{N} \left\{ \prod_{j=1}^{n} \gamma_{i_j} \right\} \bar{\delta}_n \right] \quad \ldots \quad (2.4)$$

where $\bar{\delta}_n$ is a complementary Kronecker delta function of n variables such that $\bar{\delta}_n = 0$ if any subscripts repeat, $\bar{\delta}_n = 1$ otherwise, (e.g. $\gamma_1\gamma_2\gamma_3\bar{\delta}_3 = \gamma_1\gamma_2\gamma_3$, $\gamma_1\gamma_1\gamma_3\bar{\delta}_3 = 0$).

Numerous accounts exist of empirical allowances for transition, as will be mentioned below, which can model quite closely the mean levels of turbulence measured in the transitional boundary layer, all using two-dimensional methods, sometimes superimposed onto a finite difference solution such as that described by FOREST[1977]. In order to determine fully the amplification of disturbances through the Tollmien-Schlichting wave mechanisms to the development of three-dimensional turbulent bursts requires the solution of the non-linear unsteady Navier-Stokes equations in three-dimensions for the viscous region of the boundary layer. This is at present unlikely to form a practical method from the designers' point of view. Possible lines of development involve pursuing a two-dimensional non-linear solution so that more accurate extrapolation of the turbulent amplification rates may be possible, or the application of so-called two-equation k-ε models for turbulent energy dissipation.

2.1.3 Models of Turbulent Spot Growth

The first model for turbulent spot development was proposed by EMMONS[1951] based on observations of spots of turbulent flow in an otherwise laminar boundary layer of a water-flow experiment. Originally the spot was of an irregular shape, but grew into a 'kidney-shaped' disturbance as it was convected downstream. The

origins of the spots (known as the 'sources' of turbulence) were observed by Emmons to be distributed randomly along the surface. Emmons described the breakdown process as being similar to the way ocean waves break into white-caps:

> As the ocean waves approach the shore, their amplitudes (and frequency) change, so that at random points the wave tips break. Similarly, in the laminar boundary layer the amplitude and frequency of disturbances and the critical conditions change with distance from the leading edge. Every now and then at various points, the boundary-layer disturbances 'break' (whatever this may mean), and the flow becomes locally turbulent - a turbulent spot has been born. (EMMONS[1951])

Quite how far an ocean analogy may be pursued is not clear, but the nature of the origins of flow disturbances has been little investigated, and will be discussed below. Assuming that the process is entirely random, Emmons derived a theory for the resulting transition process. This was developed by Narasimha (summarised in NARASIMHA[1985]), McCORMICK[1968] and CHEN and THYSON[1971], and has been the basis for all the 'universal intermittency' models developed. These models, and a proposed new model for transition, will be discussed in more detail in Chapter V.

2.1.4 Turbulent Spot Production and Growth

The characteristic form of the turbulent spots observed by EMMONS[1951] was measured in detail by SCHUBAUER and KLEBANOFF[1955], and shown schematically in Figure 2.3(a). The spots of turbulent flow grow as they move in a downstream direction both in spanwise extent and due to the difference in velocities between the front (at $0.88U_\infty$) and the rear (at $0.50U_\infty$). Highly detailed measurements of these disturbances have been carried out more recently by WYGNANSKI et al.[1976] and CANTWELL et al.[1978], and a novel means of visualisation of the spots used in GAD-EL-HAK et al.[1981]. The work of WYGNANSKI and CANTWELL has determined the turbulent bursts to be

in the form of horse-shoe vortices, extending just above a boundary layer thickness into the flow. Examples of plan views of turbulent spots are given in Figure 2.3(b) and (c). They are often measured by the starting of a disturbance upstream by means of a spark or another brief disturbance, which appear to be similar in form to the naturally random pattern of disturbances. Sufficiently far downstream of the initiation points of disturbances in the unstable region they may coalesce to form a continuously turbulent boundary layer, thus completing the transition process.

Some references which are particularly relevant to the natural transition part of this thesis are listed, according to subject, in Figure 2.4. A large number of research programmes have investigated the nature of turbulent spots, as well as the structure of boundary layer turbulence and the development of three-dimensional disturbances. Details of the turbulence measurements are given in KLINE[1967], OWEN[1969], ARNAL and JUILLEN[1977,8] and HART[1978]. The development of three-dimensional disturbances is investigated in KLEBANOFF et al.[1962]. Theoretical studies have been traditionally based on linear theories for stability (as described above) and empirical models for the transition zone. Recently the advent of fast computers with high processing capabilities has encouraged the direct simulation of numerical disturbances by running time-accurate solutions of the Navier-Stokes equations for viscous flow. (See LEONARD[1981], KLEISER and SCHUMANN[1984] and KLEISER[1985] for examples of this technique.)

2.2 THE INFLUENCE OF EMBEDDED WAKES IN THE FREESTREAM

Studies of the effects of wake interactions fall into three main areas:

1. Simulation of wakes as they affect simplified geometries.

2. Modelling of airfoil wakes and comparison with measurements.

3. Examination of wake transport through a blade row.

2.2.1 Effects of Wakes on Simplified Geometries

Several studies have examined the interaction of a wake with some geometries simplified in comparison with an airfoil. The two cases considered are those of a flat plate (approximating to a blade surface) and a circular cylinder (as a leading-edge model). PFEIL and HERBST[1979] and PFEIL et al.[1983] investigated the transition on a flat plate boundary layer disturbed by wakes generated by a squirrel-cage of cylinders rotating upstream of the plate leading-edge. The laminar boundary layer became transitional in the perturbed flow, and a model for this process was developed in terms of distributions of turbulent spots in time and space. The conclusion from these experiments was that the first onset of transition was not affected by the periodic nature of the upstream flow, but the region of intermittency (until a fully turbulent boundary layer is established) is reduced in length along the plate, until at a critical wake-passing frequency the transition becomes instantaneous. Measurements of heat transfer rates to the instrumented blade of a turbine cascade were taken by BAYLEY and PRIDDY[1980], with a similar squirrel-cage spinning at variable distances upstream of the cascade inlet plane, to examine the effect of turbulence frequency and intensity. An attempt was made to correlate the data in terms of the ratio of perturbed to unperturbed Nusselt numbers plotted against a function of turbulence intensity and Strouhal number, improved upon by the inclusion of a Reynolds number term in the expression. A constant density tunnel was used for these tests, so that higher exit velocities and associated greater accelerations were necessary at higher Reynolds numbers,

affecting the nature of the transition process seen on the suction surface. ZHOU and SQUIRE[1985] considered the interaction between a wake shed from a stationary airfoil and a turbulent boundary layer, showing the process of re-distribution of velocity defect and turbulence levels. It was noted by ZHOU and SQUIRE that predictions of even this simplified situation became difficult under the influence of vortex-shedding from the trailing-edge. SIMONEAU et al.[1984] performed tests on a circular cylinder with wakes impinging from an upstream set of bars fixed to a rotating disc. The results showed periodic variations in velocity, with less periodicity as the bar-passing frequency increased. Since the effect of incidence angle alone has been shown to be small (in the order of 10% in MARZIALE and MAYLE[1984]) the increase demonstrated in overall Nusselt number must have been due to the increased turbulence in the wake region (quoted as up to 25%) causing the Nusselt number to be doubled. Future work by the same authors aims to examine the space-resolved effects of the wake-passing on the cylinder array.

2.2.2 Previously Used Wake Models

Early work in the field of modelling wakes was based on isolated airfoil data such as that obtained by SILVERSTEIN et al.[1939]. KEMP and SEARS[1953] derived velocity equations for the wake region, using a periodic flow condition in terms of a varying upwash component. An attempt to model the effects of wakes interacting with an airfoil in terms of velocity perturbations perpendicular and parallel to the airfoil chord was outlined in MEYER[1957]. He calculated the case for a thin airfoil cutting a 'negative jet' model for the wake; work later extended by LEFCORT[1965] for an airfoil of finite thickness. Both of these studies found significant variation in velocity as predicted by their models, and noted a distortion of the jet once cut

by the blade, with the magnitude of the pressure fluctuations predicted comparing well with measured data. SMITH[1966] reported some experimental data taken in a multi-stage compressor, describing a method for calculating the attenuation of a wake if the flow is considered to be inviscid, incompressible and two-dimensional, as under these conditions the vorticity of each wake element remains constant. Smith noted that the magnitude of the wake deficit would, therefore, be proportional to the wake width and could thus be related to the length of a transmitted wake segment through a passage.

Wake profiles in terms of velocity defects and turbulence levels have been measured downstream of several first stage rotor and stator rows in axial flow compressors. Results from cascade measurements (RAJ and LAKSHMINARAYANA[1973]) showed the asymmetry of the wake up to three-quarters of a chord downstream. Similarity in velocity profiles was obtained by the use of different length scales for the pressure and suction sides of the wake. The wake growth was considered in two parts, a 'near-wake' close to the trailing-edge up to 80% chord, and a 'far-wake' greater than one chord in the streamwise direction downstream of the trailing-edge. Measurements were made by LAKSHMINARAYANA and DAVINO[1979] of flow behind a compressor stator, and by RAVINDRANATH and LAKSHMINARAYANA[1979] behind a rotor. They measured high static pressure gradients across the wake near the trailing-edge, and noted high radial velocities characteristic of a trailing vortex system with the radial pressure gradient as the driving potential. Predictions of the decay of a wake downstream of a blade trailing-edge in terms of streamwise velocity profile parameters were presented by KOOL and HIRSCH[1982]. In this study the pressure gradient ensuing from the separation bubble at the trailing-edge was combined with an eddy viscosity

concept to predict the axial and tangential velocity profiles. More recent work has predicted the distortion of the wake in the blade-to-blade plane of axial flow turbines. HODSON[1984a], for example, assumed a wake velocity profile in creating a periodic boundary condition at inlet to an inviscid time-marching prediction for a turbine passage, dissipating the wake by use of an artificial viscosity. DOORLY[1983] calculated the distortion of a zero-strength linear disturbance as it progressed through a turbine cascade flowfield, predicted by the use of a time-marching method.

2.2.3 Examination of Wake Transport through Blade Rows

The influence of the wake on the flowfield as it passes through a turbine passage has been observed by several authors (JOSLYN et al.[1982], DRING et al.[1982], HODSON[1984b], BINDER et al.[1983,1984]) though in many cases these studies were carried out in low-speed facilities that are in many ways unrepresentative of the typical operating conditions of modern turbines, and which thus fail to exhibit all the correct physical processes. JOSLYN et al.[1982] noted the small effect of the potential flow interaction between stages in such a facility for inter-stage spacings greater than 15% of the axial chord. At exit from the inlet guide vane the velocity distributions showed periodic signals at blade-passing frequency and also fluctuations at 2600 Hz, explained in terms of vortex-shedding. DRING et al.[1982] measured vane and rotor velocity distributions on the same facility. The progression of events along the surface could be seen, together with analysis of the turbulent nature of the boundary layer from thin film measurements. They observed high turbulence regions in the wake regions of correspondingly low pressure, and low turbulence in the high pressure areas between wakes. Flow measurements by DRING et al.[1982] between

the stages of this low-speed facility identified minimum and maximum interaction times in the cycle, in terms of the degree of interaction between the stator wake and the rotor. The minimum interaction time corresponds to the time when the vane wakes pass 'virtually without interacting with the rotor airfoils' presenting a highly turbulent flow at rotor exit even in the normally unaffected core flow. The maximum interaction time occurs when the vane and airfoil wakes merge, causing the flow to be closer to that observed in low aspect ratio cascade tests.

Velocity measurements were made by HODSON[1983,1984a] in a low-speed facility of the rotor blade passage of an axial flow turbine. Both rotating frame hot-wire anemometry and surface static pressures were included in the test programme, as well as flow visualisation in a water turbine. Using a phase-locked averaging technique the surface velocity fluctuations were shown, and passage distributions of turbulence given. HODSON[1984b] also presented results of a prediction method, whereby an inviscid flowfield was subjected to a fluctuating boundary condition, simulating the velocity defect of the wake. By plotting out contours of high and low entropy, the chopping and distortion of the wake in the passage can be visualised. Before the wake is chopped by the blade, the different convection velocities in the freestream cause a bowing in the wake boundaries. Once the wake has been segmented by the airfoil leading-edges, Hodson identified further distortion as being due to the 'negative jet' effect (after MEYER[1957]), the shearing force due to the different convecting velocities on the pressure and suction surfaces and the effects of the high accelerations near the leading-edge.

DUNN[1984] has reported on tests of a full turbine stage, showing the effects of the presence of the rotor on the vane heat

transfer, and some data from the rotor itself has been published (DUNN[1986], DUNN et al.[1986]).

Laser velocimeter measurements within a cold air turbine stage have been performed by BINDER et al.[1983,1984] firstly for the stator alone, to examine the secondary flow effects and the wake mixing, and secondly for the interaction of these wakes with the rotor. Contours of unsteadiness (expressed as constant random velocity fluctuations at an instant) allow for a visualisation of the passage wakes. The wake-slip velocity (i.e. the vector difference between the rotor inlet and wake relative velocities) was seen to cause two counter-rotating circulation regions, resulting in under-turning outside of the wake boundary, and over-turning within the wake. High turbulence levels in the front part of the rotor were seen to be due to possible vortex breakdown in the stator wakes once cut by the rotor blades (BINDER[1985]). Instantaneous patterns of velocity fluctuations at cross-sections of constant axial chord allowed for some visualisation of the progress of the wakes through the passage in three dimensions. From these patterns it is possible to discern not only the two well-known vortices generated within the stator passage, but also two vortices due to the trailing-shed vorticity from the stator wakes.

DOORLY[1983] and DOORLY and OLDFIELD[1985a and b] have described the experimental arrangement for the current series of tests. The method of simulation is also described in ASHWORTH et al.[1985]. This simulation allows for realistic wake and shock structures to be investigated as they interact with a cascade of turbine blades at engine levels of Mach number, Reynolds number and gas-to-wall temperature ratios. Doorly compared the wake shed from a static test of a cylinder with that of an NGV, and found surprisingly little of the asymmetry one might have expected due to the thicker boundary

layers typical of blade suction surfaces. The same equipment was used for the current series of tests, modified to allow the investigation of the interaction between the wake and film-cooled regions of the B22 profile. The work presented by DOORLY examined the effects both in terms of the boundary layer interactions and the passage distortion of the wake, as observed by use of a schlieren technique. The fine time resolution of the data and its high signal-to-noise ratio allows for detailed analysis of the signals without having to resort to ensemble or phase-locked averaging systems that can tend to smooth out some of the important characteristics of the flow. DOORLY was able to identify the instantaneous effects on the boundary layers of the passing of the wakes along the surface, and found the existence of a transient separation bubble caused as the re-compression shock from the wake was cut by the blade leading-edge, from analysis of both unsteady heat transfer data and schlieren photographs. It is possible to identify effects on mean heat transfer levels, particularly those due to the forcing of transition at earlier locations along the blade than was found without wake interaction.

2.2.4 Effects of Shock Interactions with Boundary Layers

It is well known that the interaction of shock waves with surface boundary layers can cause significant effects due to the large pressure changes through the shock. The interaction with both laminar and turbulent boundary layers is discussed in SHAPIRO[1954]. If the shock wave is strong enough (a high enough adverse pressure ratio) the boundary layer separates under the shock. The shock-turbulent boundary layer interaction is characterised by a pair of reflected shocks, compared with a single reflected shock for non-separated interactions. The pressure rise required to cause

separation of the boundary layer has been correlated against local Reynolds number (Re_x) for laminar and turbulent boundary layer states but little information is available for the interaction with a transitional boundary layer. The interaction of a steady oblique shock wave with a turbulent boundary layer was investigated by HAYASHI et al.[1984] who made measurements of pressure and heat transfer rate (using a multi-layered thin film heat transfer gauge).

The subject of unsteady shock-boundary layer interaction has received far less attention due to the added complexity of the process. The majority of the available information on unsteady interactions involves shock waves whose interaction point moves only small distances along the surface, in an oscillatory fashion, as reported in GALLUS et al.[1986]. By the use of surface mounted strain gauges and high-speed schlieren photographs the unsteady processes were investigated. The movement of the shock resulted in a change in the separation point towards the rear of the profile. The other most relevant work which investigated the unsteady interaction was that due to DOORLY and OLDFIELD[1985a and b] using the same experimental equipment as the present tests (as mentioned above). An impinging shock wave was not strong enough to cause separation of the boundary layer on the blade suction surface but did cause a separation bubble once the shock passed the leading-edge, which then convected along the suction surface.

2.3 OTHER TESTS ON THE ACE AND B22 BLADE PROFILES

An important feature of the profiles chosen for the present series of tests is the considerable amount of data previously acquired, mainly steady-state measurements, as well as the unsteady

data available from the initial testing of the wake-passing simulation. A brief summary of the experimental data is given below.

2.3.1 Measurements on the ACE Profile

The ACE profile was initially tested by Rolls-Royce Aero Division at Bristol, with both surface pressures and heat transfer rates measured. An aerodynamic investigation was made into its performance with and without film cooling by HALLER[1980,1983]. Comparisons are also possible from experimental work at AVA-Goettingen. The same profile has been tested in the MIT Blowdown Facility as described by EPSTEIN et al.[1984] in a three-dimensional rotating facility, and comparison can be made between the highly instrumented 'Oxford' technique and the more realistic MIT method.

2.3.2 Measurements on the B22 Profile

Aerodynamic and heat transfer measurements were taken by NICHOLSON[1981], followed by large-scale aerodynamic tests using the Oxford University Engineering Laboratory (OUEL) Blowdown facility by KING[1986]. A study into secondary flows and losses was made by GREGORY-SMITH and GRAVES[1983] at Durham University. As well as the unsteady data from DOORLY[1983] and subsequent related papers, the B22 profile was used for an extensive investigation into its steady-state film cooling performance, for similar cooling configurations to those planned for the current test schedule, as described in HORTON[1985] and HORTON et al.[1985]. These results are referred to in Chapter VIII.

CHAPTER III

DETAILS OF THE EXPERIMENTS

The details of the acquisition and processing of the experimental data in the thesis are briefly reported, and the likely sources and magnitude of measurement errors are discussed. The operating conditions are detailed, and information relating to the blade profiles tested is given. The cascade inlet and outlet Mach numbers derived from sidewall static tappings are also presented. These establish, along with the Reynolds number, the cascade operating conditions.

3.1 OPERATION OF THE ISENTROPIC LIGHT PISTON TUNNEL

The operation of the Isentropic Light Piston Tunnel (ILPT) at Oxford has been described in detail in SCHULTZ et al.[1977], a general arrangement of the tunnel being shown in Figure 3.1. It suffices here to say that a single stroke of a free piston produces constant flow conditions for about 0.5 seconds at a gas-to-wall temperature ratio of 1.5, at engine levels of Mach number and Reynolds number. This intermittent form of operation has two major advantages over a continuous wind tunnel:

(i) The running costs are relatively low, especially important as the recent increases in fuel costs are inhibiting the use of some continuous facilities even in industry.

(ii) The step change in condition from zero velocity, ambient temperature to representative engine conditions during the test facilitates the measurement of heat transfer rate, a parameter which

is of great value in turbine design, yet one which is difficult to measure in continuously operating facilities.

The flow duration of the cascade can be most readily characterised by two functions. The first is the 'tube time', i.e. the flow duration which would occur if the gate valve (V_2) were opened at the start of the run and the test gas at pressure and temperature P_i and T_i was expelled steadily from the reservoir at P_r and T_r, known as 'cold' operation, mode 1.

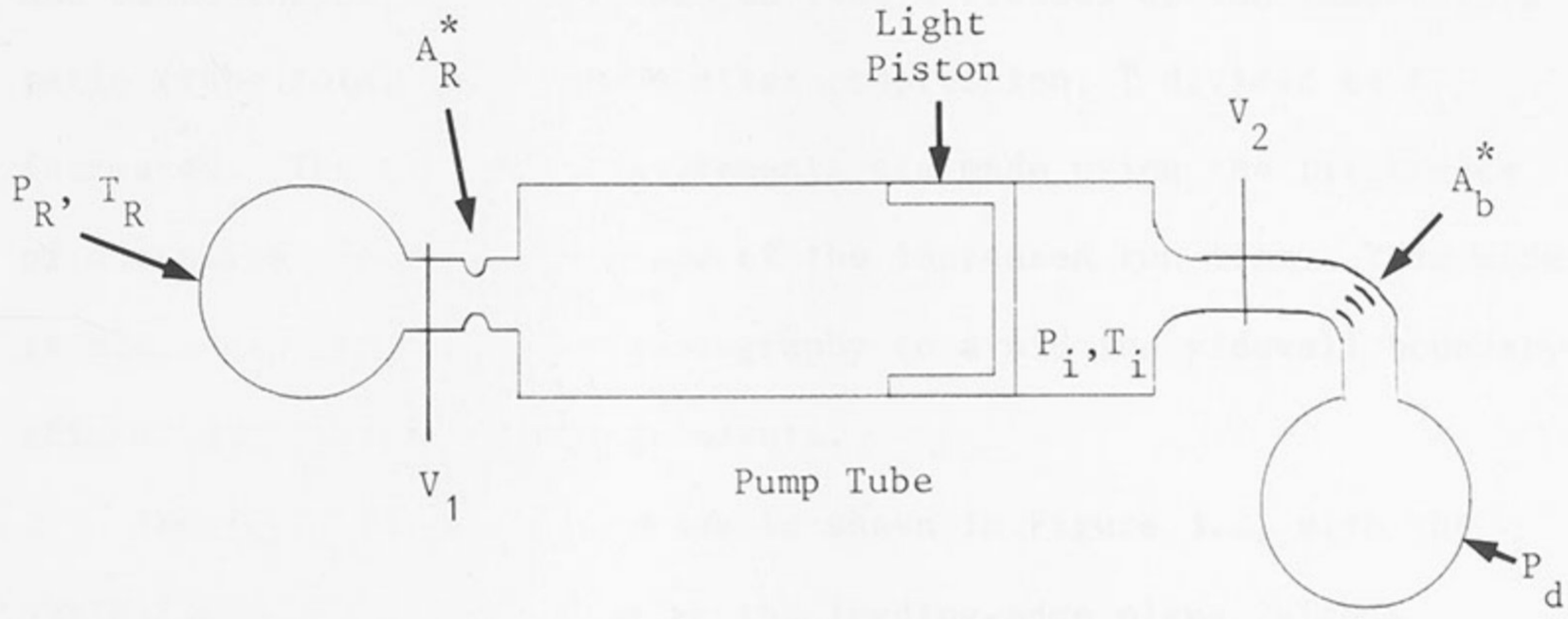

'Matching', i.e. maintenance of constant total pressure and temperature throughout the run is achieved by ensuring that the volumetric flow rate from P_r via A_r^* to the 'pump tube' is the same as that through the blade throat area, A_b^*.

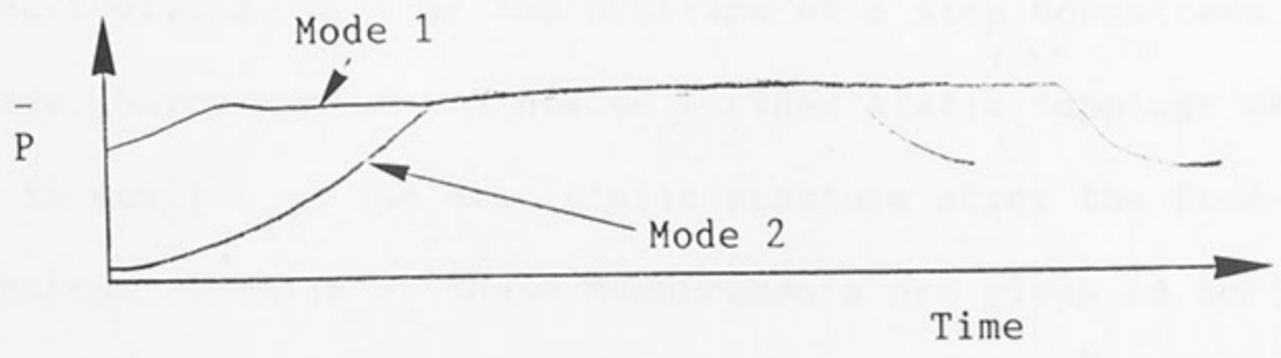

If, however, the gate valve is not opened at the same instant as the reservoir ball valves (V_1) the gas flowing from the reservoir drives the piston along the pump tube compressing the gas ahead of it and raising its temperature by purely isentropic compression, since the piston velocity is much less than that of the wave processes in

the tube. This is the normal mode of operation for heat transfer measurements (mode 2) with a gas-to-wall temperature ratio typically of 1.5:1.

Under these conditions, the running time of the ILPT is determined from:

$$\tau_{run} = \left[\frac{T_i}{\bar{T}}\right]^{\alpha} \frac{W}{\beta a_i A_b^*}, \quad \beta = \left[\frac{2}{\gamma+1}\right]^{\alpha}, \quad \alpha = \frac{\gamma+1}{2(\gamma-1)} \quad \ldots (3.1)$$

For fixed initial tube conditions and given pump tube volume (W) and blade throat area (A_b^*) the run time decreases as the temperature ratio (tube total temperature after compression, $\bar{T}$ divided by T_i) increases. The pressure measurements are made using the first mode of operation, to take advantage of the increased run time. This mode is also used for schlieren photography to avoid the sidewall boundary effects due to temperature gradients.

The geometry of the cascade is shown in Figure 3.2, with the variation in span from 50 mm at the leading-edge plane, with a uniform hade on one wall up to 56.095 mm at the trailing-edge (corresponding to a hade angle of 10°). Also shown in Figure 3.2 are the locations of the upstream and downstream sidewall static pressure tappings (13.61 and 14.06 mm from the the leading and trailing-edges respectively) as well as the position of a step downstream of the cascade, beyond which are placed further static tappings which were used in monitoring the exit static pressure after the free-jet expansion. Results of these measurements are given in Section 3.4.

3.2 UNSTEADY FLOW GENERATION IN THE ILPT

In order to allow simulation of the unsteady effects of the NGV wake and shock structures a system was developed as reported in DOORLY[1983,1985 a and b] whereby a disc is spun about an axis aligned in the axial flow direction with 'bars' formed out of

stranded steel cables attached to the rim of the disc such that they pass along a line parallel to the leading-edge plane some distance upstream of it. The centre-line of the disc rotation is sufficiently far away from the tunnel centre-line so that only the bars protrude through a slot in the sidewall, as shown in Figure 3.3 and in Plate 2. The spacing of the bars is determined by the design ratio of NGV to rotor pitches, given that a suitable cascade pitch is chosen to enable even spacing of the bars so that the disturbances will be uniform and the disc remains balanced. The stranded steel cable diameter is chosen to correspond as closely as possible to the trailing-edge thickness of the NGV (1.22 mm), in this case the nearest wire diameter available of 1.62 mm was used. In Figure 3.4(a) the relationship between an NGV and a rotor blade is shown, with the velocity triangles given for the 'engine' case and the simulated case. In testing rotor profiles in a cascade the conditions relative to the rotor are simulated, so that the rotor inlet relative velocity corresponds to the cascade inlet velocity. In order to achieve similarity between the rotor-stator interaction and the cascade simulation the bar velocity is set equal and opposite to the engine rotor velocity, and the NGV exit velocity is then correctly modelled by the relative bar velocity shown in Figure 3.4(b). The inter-row gap is set by the plane of location of the path of rotation of the bars, in this case 14.33 mm upstream of the leading-edge plane.

3.3 REDUCTION OF DATA AND METHODS OF ANALYSIS

3.3.1 Acquisition and Processing System

A scheme of the acquisition and processing system is shown in Figure 3.5 for the types of measurements most commonly applied, i.e.

pressure, heat transfer rate and flow visualisation techniques. The data was stored and processed in the following ways:

(i) Up to 64 A-D channels at sample rates typically around 400 Hz controlled by a PDP-11/34 mini-computer, also used for the mean data calculations, calibration and post-processing. The Tunnel OPerating SYstem (TOPSY) program suite described in BAINES[1983] allows for efficient storing, processing and output of the experimental data.

(ii) Up to 16 channels could be stored by the use of a Data Laboratories DL2800 series multi-channel transient recorder, which simultaneously stores 4096 points on each channel with a split time-base. This enables the starting transient and hence the baseline data for each channel to be captured at a slow sampling rate (typically 1 ms/sample or 1 kHz for 500 points) and the remaining points to be sampled at a fast rate, dependent on the bandwidth of the transducer used (typically 2 μs/sample or 500 kHz for the heat transfer measurements).

(iii) Some channels of data are recorded by the use of an S.E. Laboratories Ultra-Violet recorder type SE6008 which is used particularly for those tunnel parameters not stored by the computer (such as valve mechanisms) so that the careful tuning of the run to give steady conditions at the correct level during the test period can be maintained. This has also been used to cross-check with the data stored by other means, and is useful in checking for electrical interference effects.

(iv) Photographic techniques are employed for recording flow visualisation methods such as oil-dot surface shear measurements and schlieren methods.

(v) A Digital VAX 11/780 computer was used for subsequent data processing, and for the predictions made. Systems enabling the direct transfer of data from the tunnel computer to the VAX were

developed. A Hewlett-Packard 200 Series micro-computer was also used for thermal analysis of the blade (as described in Appendix A).

3.3.2 Pressure and Temperature Measurements

There were three types of pressure transducers used in the experiments:

(i) Conventional Semiconductor Transducers. National Semiconductor Corporation type LX-1620D transducers (now supplied by Sensym Ltd.) were used for the majority of the static pressure measurements, applied differentially with respect to a reference pressure normally held at a higher pressure. These transducers were connected to the blade and sidewall surface pressure tappings by the use of short lengths (of the order of 50 mm) of Scanivalve 1.58 mm bore plastic tubing, giving a bandwidth of approximately 2 kHz, more than enough to resolve the pressure accurately for the requirements of steady-state measurements within the run-time of the tunnel. These transducers have the advantage of being both cheap and easy to use, with the individual circuitry associated with each transducer resulting in a direct voltage signal proportional to the differential pressure across the two ports of the transducer. The transducer is connected to the correct tube connectors for the small bore tubing, and mounted in Araldite for robustness. These are calibrated prior to each series of tests by use of a reference gauge, using the same amplification and storage system as in the experiment to ensure the highest accuracy possible. As reported in NICHOLSON[1981] care is taken to take out common mode rejection due to spurious signals associated with a change in pressure level applied equally to both ports, and to cycle the calibration above and below a mean level so that a check on drift during the calibration can be made. These transducers were used for the sidewall static pressure measurements

shown in Figures 3.10 and 3.11, and for the blade static pressure measurements at the locations shown in Figure 3.6. The pressure instrumented blades are shown in Plate 1(b).

(ii) Kistler Type 7031 Quartz Pressure Transducers with Type 5001 Charge Amplifiers. These transducers are used for the important tunnel 'house-keeping' channels, i.e.:

P_o - inlet total pressure (measured by a sidewall mounted pitot tube at a quarter span)

P_{tube} (or $\bar{P}$) - pump tube total pressure (plenum measurement)

P_1, P_2 - inlet, exit sidewall static pressures

P_{ref} - reference tank pressure

P_{blow} - blowing pressure for injection systems (if used).

These are used in 'absolute' mode, referenced to a sealed chamber, with a separate charge amplifier associated with each transducer. They are more expensive than the semiconductor type, but are very reliable and linear in calibration, and require no common mode correction.

(iii) Kulite Pressure Transducers. Kulite type XCQ-062-50D transducers with a nominal bandwidth of 500 kHz were mounted flush with the blade surfaces at the three locations shown in Figure 3.6 to monitor the unsteady pressure changes due to the wake-passing simulation. They are used in a similar fashion to the Kistler transducers, but have small sensing elements suitable for insertion within the test blades without disturbing the freestream flow.

Examples of typical traces from a tunnel run are shown in Figure 3.7, all the traces measured with reference to the initial dump tank pressure except for $\bar{P}$, referenced to the initial tube pressure. The gas total temperature, T_o, is either measured by a probe inserted through the sidewall upstream of the cascade, or estimated by assuming an isentropic compression of the pump tube gas

from ambient temperature. The direct measurement of temperature was used in the later series of tests because of uncertainties about the bulk mean temperature of the gas in the pump tube prior to compression. The useful run time finishes as indicated due to the first signs of a 'cold vortex', which is established on the front face of the piston as it travels down the tube.

3.3.3 Heat Transfer Rate Measurements

The heat transfer rate to the blades is measured in the ILPT using a now well-established system described in SCHULTZ and JONES[1973] whereby the response of the blades to a step in heat transfer rate is assumed to follow that of a semi-infinite solution.

The governing heat diffusion equation:

$$\frac{\partial^2 T}{\partial x^2} = \frac{\rho c}{k} \frac{\partial T}{\partial t} \qquad \ldots (3.2)$$

may be solved for the heat transfer rate to the surface in terms of the surface temperature T_s to give:

$$\bar{\dot{q}} = \sqrt{\rho c k}\ \sqrt{s}\ \bar{T}_s \qquad \ldots (3.3)$$

where the bar signifies Laplace transformed variables. If the heat flux is constant ($\dot{q}_o$) the surface temperature rise is a parabolic function of time:

$$T = \frac{2}{\sqrt{\pi}\ \sqrt{\rho c k}}\ \dot{q}_o \sqrt{t} \qquad \ldots (3.4)$$

The semi-infinite assumption implies that the isotherms within the blade approximate to straight lines running parallel to the surface. The validity of this assumption has been checked by the use of a finite element model of the two-dimensional heat diffusion equation:

$$\frac{\partial^2 T}{\partial x^2} + \frac{\partial^2 T}{\partial y^2} = \frac{1}{\alpha} \frac{\partial T}{\partial t} \qquad \ldots (3.5)$$

with thermal diffusivity $\alpha = k/\rho c$, where all properties are those of the substrate. Surface boundary conditions are the measured temperature-time histories from a tunnel run, which have the form of the expected parabolic temperature rise from the start of the run. The method by which this modelling was carried out is detailed in Appendix A, and the results shown in Figure A.2. Clearly the isotherms at this instant in time corresponding to the time for which the mean data is typically presented closely follow the required values, save for some differences near to the trailing-edge and some effects of high curvature near to the leading-edge. The curvature effect has been examined by MAULARD[1968] in which a correction for the semi-infinite result for surface temperature rise is found to be:

$$T_s = \frac{2\dot{q}_o\sqrt{t}}{\sqrt{\pi\rho ck}} \left[1 - \frac{\sqrt{\pi}}{4}\frac{\sqrt{at}}{r} + \frac{1}{4}\frac{at}{r^2} \; .. \right] \quad \ldots (3.6)$$

for a constant step in heat flux, $\dot{q}_o$ at a time t. For the values relevant to the leading-edge of the ACE blade (i.e. a = 6.75E-7, t = 0.25 seconds, r = 1.8 mm) the correction terms are of the order -0.1 and +0.01 so that the surface temperature rise at the leading-edge could be up to 9% less than the semi-infinite assumption predicts. The correction is negligible over the rest of the instrumented surfaces.

The semi-infinite response has been shown to be analogous to an electrical transmission line response (SCHULTZ and JONES[1973]). In the technique used for these tests the temperature of a thin film gauge (TFG) mounted on an insulated substrate is monitored by means of its voltage change which is used as input to the analogue equivalent circuit. This results in an analogue circuit current directly proportional to the heat transfer rate, i.e.

$$i = \frac{V_o \alpha}{\sqrt{r/c}\ \sqrt{\rho c k}}\ \dot{q}\ , \qquad \sqrt{r/c} = \sqrt{\omega}\ |Z| \qquad \ldots (3.7)$$

where $|Z|$ is the value of the overall impedance of the transmission line and α is the temperature coefficient of resistance of the TFG. The analogues are calibrated by means of a purpose-built 'anti-analogue' unit which produces a pulse which the analogue circuit re-constructs into a square step function. The value $\sqrt{\omega}$/gain and the noise levels of the individual analogues can, therefore, be determined. Analogue circuitry was therefore used to convert temperature signals from platinum TFG's painted onto a Macor ceramic substrate directly into heat transfer rates. The positions of the thin film gauges used are shown in Figure 3.8, and photographs of the instrumented blades given in Plate 1.1(a) for 10 mm wide gauges, and 1.1(c) for a 4 mm gauge width. For the wide-bandwidth required in order to define the high-frequency events generated both by the wake-passing apparatus and the effects of turbulence on the heat transfer signals, the analogue circuitry was upgraded as described in OLDFIELD et al.[1984], to give a measured -3dB bandwidth of 86 kHz. This bandwidth corresponds to a rise-time of approximately 2 μs, with a nearly constant delay due to phase shifts of the order of 4 μs (as discussed in GEORGE et al.[1987]). The heat transfer signals are stored directly, and the surface temperature reconstructed by the processing software. As the blade heats up during the run, the driving temperature difference and hence the heat transfer rate decreases and a non-dimensional form of the heat transfer rate can be derived from this change, usually defined as:

$$\text{Nusselt Number, } Nu = \frac{\dot{q}_m}{(T_o - T_m)} \frac{C_{TN}}{k_g} \qquad \ldots (3.8)$$

as shown in Figure 3.7. It should be noted that this definition of Nusselt number is adopted due to the ease by which values such as $\dot{q}_m$

can be reconstructed if the measure point temperature is known, or to an isothermal wall temperature heat transfer coefficient using ambient temperature (or the initial blade temperature, if different). This is also helpful for comparison with data from other facilities by using a consistent form of data reduction. For the operation of the tunnel for the series of tests reported here, the non-dimensional form is particularly useful in reducing variation in levels between different runs of the tunnel due to slight changes in flow condition. It is also possible to interpret the Nusselt number as the ratio of convective to conductive heat transfer processes from the gas-side (N.B. the Biot number, referred to in Appendix A, relates the convective heat transfer to the conductivity of the substrate, and thus the temperature gradients near to the surface within the body.) Care needs to be taken if comparison is to be made with predictions (as will be given in Chapter IV) as the definitions of Nusselt and Stanton numbers generally refer to local conditions, and will be defined here as:

$$\text{Local Nusselt number, } Nu_x = \frac{q_m}{(T_r - T_m)} \frac{x}{\bar{k}_f} \qquad \ldots (3.9)$$

where the definitions of conductivity and Reynolds number are based on a film temperature (using the Eckert definition given in Chapter IV). The recovery temperature T_r is based on the local Mach number at the freestream edge of the boundary layer at the given x-location and a recovery factor, assumed to be the square root of the Prandtl number for laminar flow, and the cube root for turbulent flow. For an unknown state of the boundary layer a constant value of 0.87 is used for the recovery factor, based on experimental data, some way between the values of the laminar estimate ($\sqrt{Pr}$) and the turbulent value ($\sqrt[3]{Pr}$).

For the wake-passing experiments it is necessary to correct the temperature values due to the heating effect of the bars in the pre-run time, as the baseline for the processing software is taken at the start of the run. The correction (shown as ΔT_b in Figure 3.7) is fairly constant over all the gauges used, and is negligible when the tests are run with only two bars fitted to the disc. A system has been developed for monitoring and heating of the blades prior to the run for the purposes of variation of the gas-wall-coolant ratio for film-cooling tests, and this was used to monitor the bar-induced temperature rise in some of the later series of experiments. The data acquired by the transient recorder at fast sample rates was also scaled to Nu by use of the mean temperature rise for the same thin film gauge as constructed by the processing programs. This assumes that the variation in temperature over the maximum period of time for which the fast sample rate data is acquired (about 6 ms) is small in comparison with the driving temperature difference. This variation amounts to less than 0.5% for a typical run, so that this method of scaling the data is used.

The flow visualisation methods used are described with reference to the photographs given in Chapter IV.

3.4 TEST CONDITIONS

3.4.1 Operating Conditions

The operating conditions for the ACE tests are given in Figure 3.9 together with the actual values obtained for a run corresponding to each of the points in the test map. The conditions are determined by matching to a desired exit isentropic Mach number and Reynolds number defined by:

$$\text{Mach number,} \qquad M_2 = \sqrt{\{5((P_o/P_2)^{1/3.5} - 1)\}} \qquad \ldots (3.10)$$

and

Reynolds number, $Re = \frac{\rho U C_{TN}}{\mu}$ ... (3.11)

defined using inlet total and isentropic exit conditions. The temperature ratio T_g/T_w is then specified, at 1.5 for the heat transfer tests, but reduced to ≃1.05 for the pressure tests to increase the total run time and therefore to ensure greater accuracy in the measurements. The operating point for the B22 tests is given in Figure 8.1.

3.4.2 Inlet and Outlet Mach Number Distributions

Isentropic inlet and outlet Mach number distributions are given in Figures 3.10 and 3.11. (The tapping positions are shown in Figure 3.10.) The distributions show good pitchwise repeatability and are clearly influenced by the passage velocity gradients. In Figure 3.11 the exit Mach number distributions are given for the three nominal exit Mach number levels 0.85, 1.18 and 1.40. Also shown in Figure 3.11(a) are the arithmetic mean values and a pneumatic average value obtained by linking together tappings of an integral number of pitches. This single value was compared to the measurement downstream of the step and a comparative calibration performed. This showed that a more representative value of the exit condition, closer to the arithmetic mean of the exit sidewall pressures as shown in Figure 3.11(b), corresponded to the pneumatic average value and this was used subsequently as the basis for the exit Mach number.

3.4.3 Inlet Turbulence Level

A turbulence grid was fitted 208 mm upstream of the cascade leading-edge line at the tunnel centre-line in order to generate higher freestream turbulence than the normal background level of less than 0.8%. The original requirement for a 'high' turbulence level of about 3% was met by using a grid of 2 mm diameter cylindrical bars

spaced 15 mm apart. A comprehensive study of grid generated turbulence by ROACH[1987] correlated results from many facilities, resulting in a general correlation for the level of freestream turbulence of the form:

$$\frac{1}{Tu^2} = \frac{U}{u'^2} = \frac{A}{\Delta p/q}\left[\frac{x}{M} - \frac{x_o}{M}\right] \quad \text{for } x/M > 10 \qquad \ldots (3.12)$$

where x is the streamwise distance, M is the bar pitch, Δp the pressure drop across the grid and q the inlet dynamic head. The values of the constants A and x_o are found from correlation of experimental results, where A = 53 and x_o/M = 10 for parallel arrays of cylindrical bars. This correlation was applied to the ILPT for the required conditions of the test, giving a distribution of turbulence level with distance from the grid. For a $\Delta p/q$ of 0.2 the turbulence level 208 mm downstream of the grid is predicted to be 3.1%. The correlation by ROACH also predicts integral length scales for the turbulent flow, corresponding to a mean eddy size in the fluid in the streamwise (x) direction from:

$$\frac{\Delta x}{M} = \frac{6.2}{Re_M^{o.2}}\left[\frac{x/M - 10}{A \;/\; \Delta p/q}\right]^{0.3} \qquad \ldots (3.13)$$

resulting in a value of Δx = 2.1 mm and a characteristic frequency of 150 kHz at M_1 = 0.58.

3.5 DETAILS OF THE PROFILES TESTED

3.5.1 Design Concepts for the ACE Blade

The ACE turbine is designed for duty as a highly-loaded, high rpm transonic turbine designed for civil use as a single unshrouded high-pressure (HP) stage. The design on which the test was modelled was that of a cold-air turbine running at 9004 rpm with 36 NGV's and 61 rotors with an inlet total temperature of 457.4 K, as drawn in

Figure 3.12(a). The design intent was to produce an equivalent amount of work from this single un-shrouded turbine as for a less highly-loaded two-stage design, with an overall improvement in efficiency and reduction in weight. The blade co-ordinates are given in Appendix B.

3.5.2 Comparison of the Two Profiles Investigated

The two profiles investigated are mid-height sections of modern aero-engine high-pressure turbines, of single-stage unshrouded design. Whereas the ACE profile relates to a transonic highly-loaded profile suitable for military applications, the B22 profile would be used in large fan, high by-pass ratio civil engines. By comparing these profiles in Figure 3.12(b) and using information from Table 1 it is possible to distinguish some relevant characteristics of the unsteady flow regime. These are:

(1) The leading-edge configuration has commonality in nose radius but not in wedge-angle, with an angle of 62.32° for the ACE profile compared with 29.91° for the B22 profile. The ACE blade has an inlet angle of 58.06° to the B22 value of 42.75°. It has been found that the B22 profile is prone to separation on the suction surface side of the leading-edge, a phenomenon not observed on ACE.

(2) The work requirement is similar, with overall turning angles of 124.73° for ACE and 111.50° for the B22 profile.

(3) The aspect ratio based on true chord for the ACE tests is 1.21 compared with 0.74 for the B22 profile, implying higher overall levels of secondary flow in the B22 tests. There are five blades in the ACE cascade and four in the B22 cascade, although the periodicity still appears to be good (DOORLY[1983]).

(4) The design rotor relative inlet Mach number for the ACE cascade (0.58) is higher than for the B22 blade (at 0.32), and the shocks associated with the re-compression of the NGV wake for the ACE design

are much stronger (mid-span M_b = 1.165 for ACE compared with 0.9 for the B22 blade). The velocity diagrams at mid-height for both cascades are given in Figure 3.12(b).

CHAPTER IV

STEADY STATE RESULTS FOR THE ACE PROFILE

A comprehensive series of tests was performed in order to determine the characteristics of the ACE profile in terms of surface measurements of heat transfer rate and static pressure distributions, using the instrumentation described in Chapter III, supported by the use of schlieren photography and surface flow visualisation. The range of operating conditions under investigation was given in Figure 3.9, with the variation of inlet angle from the design value of 58.06° to 63.06° (i.e. 5° positive incidence, i = +5°) and 48.06° (i = -10°). These changes in incidence correspond to off-design running conditions in a corresponding engine, i = -10° being equivalent to an over-speed case with a reduced loading on the profile. The intention of the series of tests was twofold. The first reason was to identify the performance of this transonic profile and to allow comparison with prediction methods and other test data which were available. The second reason was to use this data and understanding of the blade performance as a basis on which to judge the unsteady interactions investigated.

4.1 FLOW VISUALISATION

4.1.1 Surface Flow Visualisation

Surface oil-dot flow visualisation photographs are given in Plates 3 and 4. Silicon oil mixed with titanium-dioxide powder is used to show the direction of surface shear as white streaks against the black painted background of the blades and the sidewalls. The

lengths of the streaks are roughly proportional to the magnitude of the surface shear, and hence it is possible to observe separation phenomena and surface secondary flow patterns. The technique is particularly well-suited to the pulse-like nature of the ILPT operation as the transient processes are short and do not smear the oil-dots. The alternative method of covering the surfaces with a complete film of oil to determine the dividing streamlines on the surface was not used, as much of this information can be extracted from the oil-dot technique, as well as the information for the shear vectors (as described in ATRAGHJI[1980]). The flow can be seen to be uniform along the blade surfaces, with a region of secondary flow developing on the suction surface so that by the trailing-edge plane about two-thirds of the span exhibits flow affected by the passage vortices. The increase in area due to the sidewall hade does not seem to have caused much asymmetry as far as these distributions are concerned. The sidewall oil-dots imply that the flow is quite uniform at inlet and exit, the only differences being due to the expected deviations due to potential flow effects at inlet, and wake effects at the outlet plane. In particular, the sidewall flow in the region of the opening for the wake generator disk is well-behaved (referring to Plate 2).

4.1.2 Schlieren Photographs of the Steady Flowfield

A reflected schlieren technique was used as described in HOLDER and NORTH[1949] and specifically by DOORLY[1983] for the present installation. This technique is particularly important in determining features of the unsteady flowfield, and will be studied further in Chapters VI, VII and VIII. As a baseline to this data, and as an overall view of the undisturbed flowfield, photographs are presented in Plate 5 for the design operating point (M_2 = 1.18,

Re_2 = 0.95 x 10^6, Tu ≃ 3%). The no-flow photograph allows the permanent areas of optical interference to be identified, and both horizontal and vertical knife-edge orientations are presented. The trailing-edge shock wave can be seen clearly as it impinges on the suction surface of the neighbouring blade, and the portions of high acceleration show up as darker tone around the leading edge. The photographs are cut-off in the axial direction by the limited window area dictated by the cascade hade angle. Plate 5(b) is at a low sensitivity, so that the trailing-edge shocks appear to be weak, compared to the higher sensitivity of Plate 5(c), at approximately the same operating point. In order to visualise better the unsteady features of the flow, the knife-edge was aligned with the image (vertical orientation) for the majority of the ACE tests.

4.2 MACH NUMBER DISTRIBUTIONS

The distributions of isentropic surface Mach number, derived from the local static pressure and inlet total pressure, are shown in Figures 4.1 and 4.2 for 'cold' conditions, i.e. T_o / T_{amb} = 1.05 but with Mach and Reynolds numbers maintained at correct values. The change to lower temperature ratio increases the run time of the tunnel (as described in Chapter III) to 1.5 seconds to enable better averaging of the measurements. The inlet and exit Mach number distributions were presented in Section 3.4. For the sake of completeness comparisons are presented with changes in incidence and exit Mach number as variables on separate graphs, and although this causes some repetitiveness it enables the independent effects to be determined.

4.2.1 Measured Surface Mach Number Distributions

Figure 4.1 shows three plots of isentropic surface Mach number against fractional surface length, the abscissa being chosen to correspond to comparisons with the heat transfer results presented later. At the design incidence (i = 0°) and exit Mach number (M_2= 1.18) the flow becomes sonic at 0.18 x/s on the suction surface, increasing steadily to a peak Mach number of 1.4 at 65% length. The pressure surface reaches a Mach number of just over 0.2 by 8% surface length with a steady increase to 0.7 by the last measurement point at 0.87 x/s. A trailing-edge base pressure tapping gives a Mach number value of 1.1. Variation in the exit Mach number has little effect on the pressure side distribution, and predominantly effects the later suction surface values, as the trailing-edge shock structure moves along the surface. At the low exit Mach number case, M^- (M_2 = 0.85) the suction surface levels are slightly lower over all but the first 8% x/s, but at the design point the levels agree up to 65% length with the M^+ case (M_2 = 1.4), at a Mach number of about 1.3. For the M^+ case the Mach number continues to increase to nearly 1.9 at 0.81 x/s. With a decrease in inlet incidence angle to i = -10° (corresponding to β_1 = 48.06°) the loading on the blade has been reduced, with a corresponding reduction in surface Mach number over the first 36% x/s. The effect of exit Mach number variation is similar to that of the design incidence case, as it is for the i = +5° case for which the loading is increased over the early suction surface, again up to 36% surface length. The effects of variation of incidence at each of the exit Mach numbers are given in Figure 4.2. The most significant differences between the results occur on the first 36% of the suction surface, with the values at different incidences coinciding after this point. A clear reduction in loading on the early suction surface is evident from Figures 4.1

and 4.2. As will be discussed later the changes in pressure gradient considerably effect the boundary layer development along the suction surface, particularly relevant to the wake-passing simulation as the state of the boundary layer has a direct bearing on the nature of the boundary layer interactions.

4.2.2 Comparison with Prediction and Previous Measurements

Comparisons of the measured Mach number distribution at the design point exit Mach number of 1.18 were performed using several methods, some of the results of which are given as Figures 4.3 to 4.5. The variation of incidence and the high suction surface Mach numbers presents a good test case for prediction methods even for this relatively simple geometry. The two types of predictions used were:

(i) Streamline Curvature Methods. These perform a calculation in the blade-to-blade plane and iterate for solutions to the conservation equations of mass flow, continuity and the state equations along a set of streamlines and a quasi-orthogonal grid. Allowance can be made for a 'stream-tube height' variation through the passage, so that endwall boundary layer development and hade angle can be accounted for in a 'quasi-3-D' fashion in the otherwise two-dimensional solution. Due to such modifications and the ease of use of these methods they are commonly used as the fundamental turbine blade aerodynamic design tool in industry, for both prediction and inverse methods.

(ii) Finite Element Methods. These vary in detail, but effectively solve the same equations as above on a fixed grid, the distribution of which ideally uses elements whose dimensions are inversely proportional to the rates of change of parameters across them.

Results from fully three-dimensional and two-dimensional time-marching methods are compared with measurements at mid-span for the design incidence. The 2-D method was run at Oxford using a code supplied by Dr. J. D. Denton (as described in DENTON[1983]) and is used subsequently for overall flowfield velocity predictions in Chapter VII.

The results of a finite element prediction in comparison with ILPT data and those acquired by other cascade tests are given in Figure 4.3, plotted against fractional axial chord at the design incidence of $\beta_1 = 58.06°$. The ILPT data is compared with:

(i) Experimental data from Rolls-Royce derived from surface static pressure tappings in a similar fashion to the ILPT measurements, but in a continuously operating tunnel. The same facility was used to measure heat transfer rates, and comparative operating conditions are given in Figure 4.9, the main difference being in sidewall hading, as the Rolls-Royce test facility was designed with equal hade on both sidewalls.

(ii) A finite element prediction including a viscosity model, allowing for boundary layer growth, shock and wake effects.

Good agreement is evident for all three on the pressure surface, and the early suction surface, but the last 25% of the suction surface length still shows significant differences between the test data and the prediction, in the region of the passage shock. The viscosity model appears to have smeared out the shock effect, but attempts to reduce the viscosity result in instabilities in the solution. A comparison of the inviscid DENTON 2-D time-marching prediction with data from the ILPT and a streamline curvature calculation is given in Figure 4.4. These predictions perform badly over the late suction surface, but otherwise are in reasonable

agreement, particularly since these are 2-D predictions which make no allowance for sidewall hade angle.

Comparison of the measured surface Mach numbers with the original design streamline curvature predictions are given in Figure 4.5 for the three incidences tested. The trends indicated by the test data are followed by the prediction, but the level only agrees well in the i = -10° case. The later suction surface results are less in agreement due to difficulties for this method in coping with Mach numbers above about 1.2.

4.3 STEADY-STATE HEAT TRANSFER RATE MEASUREMENTS

Using the experimental technique described in Section 3.3.3 the heat transfer rates in the 'steady-state' flow condition, i.e. without the wake passing apparatus in use, are presented in terms of surface distributions for conditions of low and high freestream turbulence level and for the variation in operating conditions given in Figure 3.9. The heat transfer rates at the design point are compared with measurements taken by Rolls-Royce using an entirely different experimental technique (described below). The nature of the boundary layer (laminar, transitional or turbulent) is examined by comparison of data acquired at high sampling rates, and with correlations for heat transfer rates through boundary layers and with finite difference prediction methods.

4.3.1 Measured Heat Transfer Rates - An Overview

Results are presented in Figures 4.6 to 4.9 for surface Nusselt number against fractional surface perimeter, so that comparison can be made for the effects of variation in operating condition on the steady-state heat transfer rates. This data is presented in the form of the non-dimensional Nusselt number, Nu, defined by equation (3.8),

plotted against fractional surface perimeter from the nominal leading-edge point, gauge number 1 in Figure 3.8. The corresponding gauge positions are marked on Figure 4.6(a), together with error bands shown as dashed lines above and below the data for Run 4540 as calculated automatically by the operating system. The method of deriving the errors, expressed as 95% confidence limits, is given in BAINES[1986]. The uncertainty in the measurement of Nu is typically of the same order as the run-to-run repeatability of the ILPT, deviations greater than this order are open to physical interpretation. For the 'low' freestream turbulence case (of < 0.8% u'/U) the boundary layers are initially laminar following the enhanced level due to impingement effects early on the surface, near to the stagnation point, as shown in Figure 4.6(a). The Nusselt number drops from a level of about 2500 near the leading-edge to about 500 on both surfaces. By about 30% x/s on the pressure surface an increase in heat transfer rate to a level of approximately 1100 by 50% x/s corresponds to transitional behaviour, with the level indicating a turbulent boundary layer for the remainder of the surface. The suction surface also undergoes a transition starting at about 50% x/s, but it is difficult to determine the extent of completion from this form of data presentation. With higher freestream turbulence level (Tu ≃ 3%) the leading-edge heat transfer rate increases to a Nusselt number of 3100, and transition is brought forward to about 20% x/s on the suction surface and apparently as early as the instrumentation could measure on the pressure surface, at 7% x/s. The influence of freestream turbulence will be discussed in more detail in Chapter V. The effect of changes in the steady-state value of inlet incidence (angle β_1) is to alter the suction side transitional behaviour, and does not significantly affect the pressure surface values, as shown in Figure 4.6(b). The reason for

the change in transition on the suction surface is due to the significant differences in acceleration up to an x/s of 0.40 over the range of 15° of incidence change from i = -10° through i = 0° to i = +5° (and will be discussed in Section 4.3.2 below).

For the design incidence case (β_1 = 58.06°) the effects of variation in exit Mach and Reynolds number are shown in Figure 4.7. The low Reynolds number (0.44×10^6) results are at a generally lower level than the design case, with steady levels maintained along the surface except for a slight increase towards the suction surface trailing-edge. The high Reynolds number (1.4×10^6) also reflects the Reynolds number scaling effect (although the heat transfer data is not reduced to a common value by simple division by a power of Reynolds number, such as $Re^{0.5}$ as is sometimes used). The variation of exit Mach number from 0.85 to 1.4 has little effect on the pressure surface heat transfer rates. The most significant variations in level occur late on the suction surface, close to the impingement point of the trailing-edge shock from the neighbouring blade, at 70% x/s for the design exit Mach number of 1.18. Similar effects of Mach and Reynolds number variation are found at i = -10° and i = +5° as shown in Figures 4.8(a) and (b). The unloaded negative incidence case delays transition on the suction surface, whilst leaving the pressure surface largely unchanged. The i=+5° tests indicate an earlier suction surface transition, corresponding to the sharp change in pressure gradient forcing transition to occur over the region from 0.18 to 0.31 x/s.

A comparison is possible between measurements in the ILPT (by use of the semi-infinite heat transfer assumption and analogue circuitry to give heat transfer rates) and some previous tests using a technique known as MITFA which derived heat transfer coefficients for the same profile under similar nominal conditions of Mach and

Reynolds numbers. The MITFA technique is described in BARRY et al.[1982] and BEACOCK et al.[1982]. It consists of measuring the phase lag and amplitude variation between thermocouples either side of a thin walled model, with a temperature difference across the wall modulated by varying the internal fluid temperature. For the MITFA tests the external gas temperature was 900 K and the internal coolant temperature fluctuated about 500 K. Details of the tests and results are given in Figure 4.9. The dashed lines correspond to ILPT data for the high and low Reynolds number tests, and also shown are the results for i = +5°, closer to the incidence at which the MITFA tests were reported to have been performed. There is a noticeably higher level to the MITFA data in comparison with the design case data from the ILPT, but the results compare reasonably well in character.

4.3.2 Analysis of Mean Heat Transfer Results by a Correlation Approach

A common form of presentation of flat plate heat transfer data is in the form of $\log(Nu_x)$ against $\log(Re_x)$ plots, so that comparison can be made with simple correlations of the form :

$$Nu_x = C \ Pr^m \ Re_x^n \ , \quad \text{for constants } C \ , \ m \text{ and } n. \qquad \ldots (4.1)$$

Since the Prandtl number, Pr, typically does not vary considerably for the range of conditions encountered, this type of relationship is linear on the log-log plot. Modifications to the simple form of correlations are possible to allow for such effects as freestream turbulence and pressure gradient, for either laminar or turbulent boundary layers. The transition region between the two regimes could also be allowed for by the inclusion of some intermittency model, reflecting the amount of time that the boundary layer is in a turbulent state. (There is still much uncertainty concerning the form of such an intermittency model, as will be discussed in

Chapter V.) It was decided to investigate this form of data presentation for the airfoil results in order to determine the likely boundary layer states and transition regions, and to see how much effect surface curvature has on the levels of heat transfer rate.

The definitions of Nu_x and Re_x used are:

$$Nu_x = \frac{q_m}{\overline{T}_r - \overline{T}_m} \frac{x}{\overline{k}_f} \quad \ldots (4.2) \qquad \text{and} \qquad Re_x = \frac{\rho_\infty u_\infty x}{\mu_f} \quad \ldots (4.3)$$

where: q_m, T_m = measure point values

x = length from nominal stagnation point

T_r = recovery temperature (based on recovery factors $r_l = Pr^{.5}$, $r_t = Pr^{1/3}$)

k_f, μ_f = conductivity, viscosity at T_f

ρ_∞, u_∞ = density, velocity at static conditions

Pr = Prandtl number $\mu_f c_p / k_f$ for c_p = 1005 kJ/kgK

T_f = Eckert temperature

$= T_\infty + 0.5(T_o - T_\infty) + 0.22(T_r - T_\infty)$.

Nu_x is derived (where necessary) from :

$$Nu_x = St\ \rho_\infty u_\infty c_p \frac{x}{k_f} \quad \ldots (4.4)$$

for a Stanton number:

$$St = \frac{q_m}{\rho_\infty u_\infty c_p (T_r - T_m)} = \frac{h_m}{\rho_\infty u_\infty c_p} \quad \ldots (4.5)$$

i.e. $Nu = Re\ St\ Pr.$

The results are compared with the following four correlations, derived by integral methods as detailed in KAYS and CRAWFORD[1980] unless otherwise stated.

Case (1): Laminar Boundary Layer $Nu_x = Nu_x(Re, Pr)$

The simplest form for a laminar boundary layer on a flat plate with constant freestream conditions:

$$Nu = 0.332\ Re_x^{0.5}\ Pr^{1/3} \qquad \ldots (4.6)$$

Case (2): Laminar Boundary Layer $Nu_x = Nu_x(Re, Pr, Tu)$

An attempt to model the enhancing effect of freestream turbulence on the laminar heat transfer level was made by BROWN and MARTIN[1982] of the form:

$$Nu = 0.332\ Re_x^{0.5}\ Pr^{1/3}\ (1 + f(Re_c, Tu_l)) \qquad \ldots (4.7)$$

for $f(Re_c, Tu_l) = 0.028\ Re_c^{0.532}\ Tu_l$,

where Re_c = Reynolds number based on true chord and isentropic exit static conditions

and Tu_l = local turbulence intensity $Tu_{in}\ \dfrac{u_{in}}{u_\infty}$

Case (3): Turbulent Boundary Layer $Nu_x = Nu_x(Re, Pr)$

The integral method together with experimental data gives the relationship:

$$Nu = 0.0296\ Re_x^{0.8}\ Pr^{0.4} \qquad \ldots (4.8)$$

Case (4): Turbulent Boundary Layer $Nu_x = Nu_x(Re^*, Pr, R)$

By the use of an integral Reynolds number $Re^* = \int \dfrac{u(x)}{\nu(x)}\,dx$ an attempt is made to allow for pressure gradient effects in the streamwise direction. The wall-to-gas temperature ratio T_m/T_∞ and radius of curvature (assumed to be equal both along and normal to the streamwise direction) are also allowed for, in the relationship:

$$St = 0.0287\ Pr^{-0.4}\ \frac{R^{0.25}(T_r - T_\infty)^{0.25}\mu^{0.2}\ T_m/T_\infty}{\left[\int_o^x R^{1.25}(T_r - T_\infty)^{1.25}\rho_\infty u_\infty dx\right]^{0.2}} \qquad \ldots (4.9)$$

These are compared with the design case suction surface data for $Tu \simeq 3\%$ in Figure 4.10. The simple correlations (4.6) and (4.8) act

as outer bounds to the data, with cases (4.7) and (4.9) being much closer to the measured values. The data clearly starts at a value close to the laminar level, and rises over a portion of the surface from 18% to 53% x/s to the turbulent level. Also evident from this form of presentation is the apparent effect of the shock/boundary layer interaction at gauges 18 and 19, due to a local thickening of the boundary layer, resulting in a lowering of the Nusselt number, prior to the region of interaction. The passage shock does not appear to have caused a large scale separation, indicating that the shock pressure ratio is below a critical value for separation. Calculation of this value is dependent on the nature of the boundary layer, values given for laminar and turbulent shock/boundary layer interactions in SHAPIRO[1954], but there is uncertainty about the critical values for a transitional boundary layer. The heat transfer returns to the turbulent level for gauges 20 and 21. Also for the suction surface the effects of incidence change are shown in Figures 4.11(a) and (b). At the i = -10° condition, it is clear that transition has been moved to later on the surface, over the range 46% to 90% x/s. The kink in the data at gauges 18 and 19 corresponds to the shock/boundary layer interaction point. At i = +5° the aforementioned abrupt reversal of the normally favourable pressure gradient on the suction surface results in transition observable from this form of presentation as occurring between gauges 11 and 13. Following this reversal in pressure gradient, the suction surface reverts to a favourable gradient again, and the data no longer follows the turbulent level. This could be due to a re-laminarisation of the boundary layer, the turbulent eddies reducing in amplitude along the blade due to the stabilising effect of the favourable pressure gradient. Changes in Reynolds number have been shown to affect the heat transfer in a consistent fashion, but not to

follow a simple scaling factor of a function of Reynolds number. The reason for this is made clear by examination of the suction surface data presented in Figure 4.12. The low Reynolds number case (Run 4517) lies close to the laminar level on the early part of the suction surface, undergoing transition only towards the rear part, from 75% x/s onwards. The high Reynolds number case (Run 4515) closely follows the turbulent level along practically all the surface. The effect of Reynolds number on the transition process is discussed in Chapter V, and clearly demonstrated by this form of data presentation. A summary plot showing the predictions for changes in incidence and freestream turbulence level is given in Figure 4.13, using equations 4.7 and 4.9 for the laminar and turbulent predicted levels respectively. As well as the suction surface predictions, an estimate of the leading-edge heat transfer rate is shown, assuming that the ratio $Nu/\sqrt{Re}$ (based on leading-edge diameter) is approximately equal to unity (LOWERY and VACHON[1975]). Also shown are the measured values for the pressure surface, which are greater than those predicted over nearly all of the surface.

The pressure surface results are shown in Figure 4.14(a) and (b), plotted with the standard flat plate correlations (4.6) and (4.8). For the low turbulence case in Figure 4.14(a) comparison can be made with correlation (4.7) assuming a freestream turbulence level of 0.8%, although the actual level is not known. The data for both turbulence levels is similar from gauge 5 (48% x/s) onwards, at values slightly above that of correlation (4.7). The early surface values for the higher turbulence case also exceeds the correlation. The effect of Reynolds number on the heat transfer rate is shown in Figure 4.14(b), in which the values can be seen to follow the trend of the turbulent correlation, and are coincident up to a $\log(Re_x)$ of 5.1 (i.e. $Re_x = 125,900$). After this point the low Reynolds number

case drops to a lower value of Nu_x, with the higher cases staying coincident until $\log_{10}(Re_x) = 5.3$ ($Re_x = 200,000$) after which the design Reynolds number case tails off to a lower value than the $1.5 \times Re_d$ condition. For all test conditions apart from the low turbulence test the data indicates that the pressure surface undergoes an early transition, possibly as a result of a small separation bubble near to the leading-edge, or more likely due to the action of so-called Taylor-Goertler vortices on the surface. These longitudinal vortices (as shown schematically in Figure 4.15(a)) can build up on concave surfaces as the radial pressure gradient and viscous forces present are not great enough to damp out small disturbances in the flow in the presence of large centrifugal forces. A stability theory concerning the development of Goertler vortices on concave surfaces was developed by TAYLOR[1923] and GOERTLER[1954]. This was investigated further by SMITH[1955], who showed that it was possible to identify a line of neutral stability for amplification of such disturbances, enclosing a region for which amplification will take place, showing a similarity to the Tollmien-Schlichting analysis for flat plate boundary layer stability. Work by McCORMACK et al.[1970] and BROWN and MARTIN[1982] has examined the influence of Taylor-Goertler vortices on measured heat transfer rates. They cause an enhancement in level for at least the laminar portion of concave surfaces, and can affect the location of transition. This trend has been confirmed by other experimental work, such as reported in CRANE et al.[1987]. Goertler vortex activity is often characterised by a Goertler number, Go, defined as:

$$Go = Re_\theta \sqrt{\{\theta/R\}} \qquad \ldots (4.10)$$

(or sometimes the square of this quantity), where θ is the boundary layer momentum thickness. FOREST[1977] estimated a value for a critical Go of 4.5 above which Goertler vortex activity becomes

important. This threshold is often applied, using a predicted laminar value for θ, in determining the onset of Goertler vortex-induced transition. For the ACE tests, Go exceeds 4.5 prior to the first measurement point, but an interesting result follows by plotting the Goertler number based on a predicted turbulent momentum thickness. The Goertler number is plotted for the three test Reynolds numbers in Figure 4.15(b), and can be seen to follow similar trends to the heat transfer data in terms of the diminishing effect of Goertler vortex activity likely towards the trailing-edge. The high Goertler numbers early on the surface could cause the early transition, with the later surface trends indicating increased damping of turbulent eddies accompanying a reduction in Goertler numbers. However, there is insufficient evidence from these results to confirm that this explanation is correct.

4.3.3 Comparison of Measured Heat Transfer Rates With Prediction

A finite difference prediction technique as developed by SPALDING and PATANKAR[1970] and developed by FOREST[1977] was used to examine our capability to predict heat transfer rates from the measured Mach number distributions. The program was run for the three incidences tested ($i = 0°$, $i = -10°$ and $i = +5°$) at the design operating point, the results of which are shown in Figures 4.16, 4.17 and 4.18 respectively. Also shown in these figures is the Mach number distribution used as input to the program, and the derived value of the acceleration parameter, K. The pressure surface values at all three incidences are in reasonable agreement, all predicting an early transition for this 3% turbulence level. The program also predicts the suction surface laminar values well, and the start of transition is in reasonable agreement for each case. The length of the transition and subsequent turbulent boundary layer development on

the suction surface are less well predicted for the design and negative incidence tests. The sudden deceleration in the positive incidence case causes transition to occur by 30% surface length, as indicated by both the data and the prediction. This could be due to a separation following the change in sign of the velocity gradient.

4.3.4 Time-Resolved Heat Transfer Rate Measurements from the Steady-State Tests

The nature of the boundary layer state can often be identified by examination of data taken at high sample rates (at 2 μs per sample) using the acquisition system described in Chapter III. Examples of such results are given in Figures 4.19 to 4.22 for the design incidence tests with low and high freestream turbulence level. The heat transfer rate has been scaled to the Nusselt number Nu as defined by equation (3.8). A total of 3.2 ms of data is given in each plot, 0.4 ms between each vertical division. With low freestream turbulence the suction surface undergoes a gradual transition, as discussed in Section 4.3.2, over the range 0.3 to 0.65 fractional surface length. In Figure 4.19 the gauges show signals characteristic of laminar boundary layers until gauge 14, in which small upward peaks in heat transfer rate can be observed. This activity is more noticeable in gauge 16, but by gauge 18 a less coherent turbulent signal is present. These results are consistent with previous observations of a natural transition, the spikes corresponding to spots of turbulence (as discussed in Chapter II, and observed by DOORLY[1983]). The spots are not clearly defined due to the effect of spanwise averaging over the 10 mm gauge width. This process will be examined in more detail in Chapter V. At the higher freestream turbulence level all of the early gauges (from 10 to 16 as shown in Figure 4.20) have characteristically turbulent signals. It

is thought that this is due both to the penetration of turbulence into the laminar layer early on the surface, followed by the shorter transition region identified in Section 4.3.2. The signals from the pressure surface with the low level of freestream turbulence (Tu < 0.8%) have low fluctuation levels, normally associated with laminar flow (Figure 4.21). This contradicts the evidence both from Figure 4.6(a) and from the correlation analysis in Section 4.3.2 that the boundary layer is turbulent by gauge 5 (0.48 x/s). If a natural transition process occurred in the apparent transition region of 0.24 to 0.48 x/s, one would expect the same spikes of turbulent flow to be evident. This is more supporting evidence to suggest that another transition process is occurring, that due to a Goertler-induced transition. The longitudinal vortex structure associated with this type of instability would have an un-determined effect on the spanwise gauges used for these tests. At the higher freestream turbulence level (Tu ≃ 3%) the signals are characteristic of turbulent flow, as seen in Figure 4.22. The leading-edge (gauge 1) has much higher fluctuation levels than observed elsewhere on the blade (and is at the higher level associated with the stagnation point flow, plotted here on a scale of 2000 to 4000 in Nusselt number to preserve the scale factor on the ordinate).

CHAPTER V

MEASUREMENT AND MODELLING OF THE NATURAL TRANSITION PROCESS

The natural transition process observed in Chapter IV on the suction surface of the ACE profile is analysed in this chapter in terms of turbulent spot growth. The background to the turbulent spot production and propagation processes has been given in Chapter II. In the present chapter transitional heat transfer data taken from the ACE suction surface is described. The turbulent activity is analysed in terms of mean values of intermittency and convection rates. Statistically-based methods of modelling the transition process from laminar to turbulent flow are examined and compared with a new model which is proposed. A time-marching calculation for the unsteady characteristics exhibited in the transitional heat transfer results is developed.

5.1 MEASUREMENTS OF TRANSITION ON THE ACE PROFILE

Measurements of transitional heat transfer rate signals are presented in this section, together with an analysis of the signals which determined the natûre of the transition process observed in this experiment.

5.1.1 Experimental Data

The $\log(Nu_x)$ versus $\log(Re_x)$ form of presentation of mean heat transfer data gives an indication of the transition lengths for some of the different test conditions under investigation. A more detailed look at the nature of the transition process is possible by

use of the high time-resolution of the heat transfer rate measurement system described in Chapter III. Following the early tests on the ACE profile a series of tests on the suction surface was developed by Professor J. E. LaGraff and analysed by the author, as presented in SCHULTZ et al.[1986] and ASHWORTH et al.[1987]. For these tests narrower thin film gauges covering 4 mm of the span were used so that less spanwise averaging of three-dimensional disturbances occurred. The cascade was tested at the i = -10° condition for which a long transition length exists on the ACE suction surface.

The results of tests with both low and high levels of freestream turbulence are given in Figure 5.1 for gauges at eight locations along the suction surface. Each vertical division corresponds to 500 μs of data sampled at 2 μs intervals, and the vertical range for each trace covers 0 to 2000 in Nusselt number, Nu. All the gauges show quiet laminar signals for the low turbulence case up to the 65% x/s value given. The high turbulence case shows an early enhancement for the first few gauges, with the first signs of convected disturbances appearing on the gauge at x/s = 0.28. From this gauge onwards enhanced heat transfer levels corresponding to turbulent spots can be followed from one gauge to the next, building up the amount of time that each gauge spends at a turbulent level as the spots move downstream. The apparent increase in magnitude of the turbulent level corresponds to the same level of Nusselt number covering only a portion of even these shorter gauges.

An alternative presentation of this data is to plot the heat transfer rates as a surface, with the height representing heat transfer rate, and the surface co-ordinates being time and surface length, as shown in Figure 5.2. By this means it is possible to see the growth and merger of the turbulent bursts, demonstrating the coherent nature of the spots as they convect downstream. The orderly

nature of this convection process is clearly visible with the time-scales expanded, as is also shown in Figure 5.3. The experimental data is plotted with adjacent gauges closely-spaced so that tracking is possible of turbulent activity from one gauge to the next. Two disturbances which occur between an x/s of 0.15 and 0.19 can be tracked along the surface until they merge by x/s = 0.65. This is characteristic of natural transitional behaviour, and it would be expected that the nature of the spot growth and merger would entirely define the transition process once the disturbances have developed out of the laminar flow region. It should be noted that the apparent increase in peak Nusselt number observed as the spots grow (as shown in Figures 5.1 to 5.3) is not due to an increase in turbulent level but to the effect of spanwise-averaging that occurs even for these narrower gauges, since the spots originate as point events and may still be small relative to the gauges.

5.1.2 Analysis of Transition Data

A means was derived for calculating an intermittency factor $\bar{\gamma}$ defined (e.g. in SCHLICHTING[1979]) as the amount of time that the heat transfer rate is above a threshold level divided by the total time, as shown in Figure 5.4(a), which also indicates the paths by which the bursts convect between gauges. The lower trace indicates the method used, whereby an intermittency threshold is chosen so that it is above a laminar level, and the amount of time spent above this level numerically summed to give the intermittency factor

$$\bar{\gamma} = \frac{\sum_{i=1}^{n} \Delta t_i}{t_2 - t_1} \qquad \ldots (5.1)$$

The results of such a calculation are compared against predicted values using the method of FOREST[1977] for the design and 1.5 times

design values of Reynolds number in Figure 5.4(b). The level of agreement for the start of the transition process for this critical part of current heat transfer models is good, although the results indicate significantly slower transition above an intermittency factor of 0.5.

The convection rate indicated in Figure 5.4(a) was also investigated by means of a signal analysis program developed by Dr. D. J. Doorly and described in DOORLY[1983]. By use of cross-correlations between adjacent thin film gauges it is possible to determine the mean convection rate of events from one gauge to the next, as indicated in the cross-correlation peak of Figure 5.5(a). It was not possible to determine the leading-edge and trailing-edge of the turbulent structures individually, as each burst only lasted for an average of 25 μs. These convection rates can then be compared against those due to the local freestream velocity, as presented in Figure 5.5(b) for events starting at the earliest gauge from which disturbances appeared to convect. Various fractions of the freestream velocity are shown, with the disturbances following rates between 0.6 to 0.8 times the freestream velocity.

5.2 MODELLING THE NATURAL TRANSITION PROCESS

A model for the natural transition process has been developed which allows for the effects of varying freestream velocity (or pressure gradient). The model is based on a statistical analysis of the turbulent spot development from sources of turbulence due to the breakdown of Tollmien-Schlichting waves as described in Chapter II. The model developed is analysed first by straightforward numerical integration, and then in a 'time-marching' mode to enable comparison with the time-resolved data acquired from the ILPT.

5.2.1 Statistical Basis for Modelling Transition

The Emmons' model for transition will be detailed in this section, together with models derived from the theory presented in EMMONS[1951]. Emmons considered flow in the (x,z,t) space shown in Figure 5.6(a) and (b), where x is the streamwise direction, z the spanwise direction and t is time. In this view, the spot sweeps out a volume with a shape dependent on the convection and growth of the spot. The spot clearly does not propagate ahead of its source, otherwise the 'spot would be self-sustaining and the body would be permanently covered by turbulence' (EMMONS[1951]). This volume is known as the propagation cone for a source at $P_o(x_o, z_o, t_o)$. The surface elements ('propagation rays') may or may not be straight. In order to determine whether a given point P(x,y,t) is turbulent it is necessary to find the region upstream of the point P for which all the points P_o could influence the state of the point P (known as the 'dependence volume' R for P, shown in Figure 5.6(b)). Emmons has shown that the intermittency factor at a given point in the flow for some source rate density g(x,z,t) is given by

$$\gamma(x) = 1 - \exp \{ - \int_R g(x,z,t)\, dV \} \qquad \ldots (5.2)$$

The source rate density function g(x,z,t) is still largely unknown at present (as CHEN and THYSON[1971] state there are very few measurements of the frequency of spot production, even on a flat plate). Attempts can be made to estimate the rate assuming that the dependence on x,z,t is known. Since the process is random, it seems that a constant rate with time is most likely (or that at least a time-averaged assumption for g(x,z,t) will be accurate). The breakdown process causing the generation of bursts described in Chapter II would imply spanwise preferred origins for the turbulent spots if the 3-D process were stable in time. This has been observed

experimentally if small disturbances are used to induce the three-dimensional instabilities leading to breakdown (KLEBANOFF et al.[1962]) but no evidence suggests that preferred locations exist in randomly perturbed flow. If no time-dependence or spanwise-dependence occurs, then the rate is a function of streamwise length alone and (5.2) becomes

$$\gamma = 1 - \exp\{-\int_R g(x)\, dV\} \qquad \ldots (5.3)$$

In deriving this expression no assumptions have been made as to the nature of spot propagation and growth, but only that the likelihood of a point being turbulent is due to the most upstream spot generated within the dependence cone, i.e. that this spot would over-run any subsequent spots, so that spots are not counted more than once leading to artificially high intermittency. If the spots observed previously are believed to be representative of all spots, then it is possible to determine the dependence cone in terms of surface length and freestream velocities. Assuming that the leading and trailing-edges of the spots convect at fractions of the freestream velocity f_l and f_t respectively, the locus of points generated is given by:

$$\Delta t_l = \int \frac{dx}{f_l U_\infty(x)} \qquad \ldots (5.4a)$$

$$\Delta t_t = \int \frac{dx}{f_t U_\infty(x)} \qquad \ldots (5.4b)$$

and

$$\Delta z_t = \int \tan(\alpha(x))\, dx \qquad \ldots (5.4c)$$

where z refers to the spanwise direction and $\alpha(x)$ the angle of spread of the spot trailing-edge points. Integration over the path length from the spot origin implies an area of cone cross-section:

$$A(x) = \left[\int \tan(\alpha(x))dx\right]\left[\int (f_t^{-1} - f_l^{-1})\frac{dx}{U_\infty(x)}\right] \qquad \cdots (5.5)$$

Then the intermittency function is represented by:

$$\gamma = 1 - \exp\left\{-\int_{x_o}^{x} g(x') \left[\int_{x'}^{x} \tan(\alpha(x))dx\right] \left[\int_{x'}^{x} (f_t^{-1} - f_l^{-1})\frac{dx}{U_\infty(x)}\right] dx'\right\} \quad \ldots (5.6)$$

where x′ is a dummy variable for the outer integral. This equation can be numerically integrated for known values of $U_\infty(x)$, $\alpha(x)$ and even f_l and f_t as functions of x. Experimental data suggests that the propagation rates are constant and experimental results suggest that α is constant, at least for a flat plate (after a short development period for each burst). Defining a shape parameter σ_f as:

$$\sigma_f = \tan\alpha(f_t^{-1} - f_l^{-1}) \quad \ldots (5.7)$$

for uniform velocity (5.6) becomes:

$$\gamma = 1 - \exp\left\{-\frac{\sigma}{U_\infty}\int_{x_o}^{x} g(x')(x-x')^2 dx'\right\} \quad \ldots (5.8)$$

This equation has been used as the basis for 'universal' intermittency distributions. Three models for the burst rate function g(x) will be discussed here, as shown in Figure 5.6(c).

Model I

The first, used by Emmons, relied on the source rate function g(x) being constant, say $g(x) = N_1$. This leads to the intermittency distribution:

$$\gamma = 1 - \exp\left\{-\frac{N_1\sigma}{U_\infty}(x - x_o)^3\right\} \quad \ldots (5.9)$$

This was proposed by Emmons, and used later as the form for a correlation of transition data in ABU-GHANNAM and SHAW[1980]. Defining a fraction of transition length (from γ of 1% to 99%) as η, they fitted their experimental data to a curve defined by:

$$\gamma = 1 - \exp(-5\eta^3) \quad \ldots (5.10)$$

Model II

The second model was proposed in NARASIMHA[1957] based on examination of the form of the intermittency factor. Narasimha showed that if the source rate function is defined as a Dirac delta function, say $g(x) = N_2 \delta(x - x_o)$, then the intermittency distribution will be of the form:

$$\gamma = 1 - \exp\{ - \frac{N_2 \sigma}{U_\infty} (x - x_o)^2 \} \qquad \ldots (5.11)$$

or the equivalent form:

$$\gamma = 1 - \exp(- 0.0365 \eta^2) \qquad \ldots (5.12)$$

Much of Narasimha's work has relied on the validity of this expression. Experimental data for flat plate tests supports the general form of this intermittency path model, a good comparison given in PARK and SIMON(1987).

Model III

A more general form of (5.6) is to allow a preferred streamwise location for spot production, whilst allowing a lower probability of spot formation with distance away from this mean. One possible distribution is to assume a normal (Gaussian) distribution for g(x) of variance s about a mean μ, such that:

$$g(x) = \frac{N_3}{\sqrt{2\pi s}} \exp (- \frac{(x - \mu)^2}{2 s}) . \qquad \ldots (5.13)$$

This can be substituted in (5.6) with σ constant to give:

$$\gamma = 1 - \exp \{ - \frac{N_3 \sigma}{\sqrt{2\pi s}} \int_{x_o}^{x} \exp (- \frac{(x'-\mu)^2}{2s}) (x - x') \int_{x'}^{x} \frac{dx}{U_\infty(x)} dx' \} .$$

$$\ldots (5.14)$$

This equation approaches the first two models as s approaches infinity and zero respectively. A comparison of the three models is given in Figure 5.7 for a flat plate test example using data acquired by GOSTELOW[1987]. The same numerical integrator was used for all

three predictions, with the appropriate g(x) substituted for each case. It is clear that all the models approach the correct path (given that the onset location x_t and transition end x_e were matched with the measured data). However, it is also clear that attempting to derive a likely g(x) from the intermittency function will be difficult due to the low sensitivity of γ on the form of g(x), irrespective of the problems of signal noise in performing the differentiation. In NARASIMHA[1957] a method was proposed to enable better normalisation of the transition length due to the problems of measuring intermittencies of < 0.05 with other noise present. He proposed plotting the function $\sqrt{-\ln(1-\gamma)}$ against x, which would be linear if (5.11) held true. This gave some encouragement to the 'preferred streamwise location' model, but such interpretation should be treated carefully, as experimental data satisfying (5.14) would not deviate that significantly from (5.11) given the inevitable scatter on the data.

5.2.2 Details of a Computer Simulation of Transition

The experimental data described in Section 5.2 would act as a good test case for transition models since simultaneous time-resolved signals for a number of streamwise locations has been acquired. The models proposed in Section 5.2.1 should provide a means of estimating the mean intermittency along the surface, provided that a means be found to estimate the starting position for transition, and the scaling factor (N_i) required to force transition to progress at the correct rate. To calculate the instantaneous values seen by sensing elements in the transition zone an attempt must be made to go back to the original principles of Emmons' 1951 paper. It should be possible to feed in assumptions of spot generation and growth into a time-marching model for the surface intermittent region, given the

random nature of the generation process. Such a model has been developed, requiring input data for:

(i) Velocity at given streamwise locations, $U_\infty(x)$

(ii) The scaling parameter, mean and variance of the source rate function (values for N_3, μ and s in (5.14))

(iii) Propagation parameters for the spots (values for α, f_l and f_t in (5.7))

(iv) Geometry of the surface (spanwise extent z_1 and streamwise length x_1) and the sensor length

(v) The time-step Δt for the marching calculation and the time-period for which a solution is required, ΔT.

Each turbulent spot is defined by four points, as shown in Figure 5.8, such that the self-similar shape of the spot approximates to that observed experimentally. This differs slightly from the assumptions of triangular spots implied by the statistical models presented previously. The prediction process is as follows:

(1) Generate a random number of spots (point sources) over the surface, with randomly chosen z values in $(0, z_1)$ and x-values in $(0, x_1)$ corresponding to the probability distribution implied by (5.13). The average number of spots generated for each time-step is given by:

$$\Delta N = N_3 x_1 z_1 \Delta t$$

(2) Increment the spot corners according to (5.4) using the local freestream velocity interpolated from $U_\infty(x)$ and the appropriate convection rates. No allowance is made for over-lapping spots, and they are convected until they are swept off the end of the region under investigation. Calculate for each sensing element the proportion covered by turbulence (irrespective of the number of spots covering the gauge) and store this data in an output file.

(3) Return to step (1) until elapsed time equals ΔT.

(4) Calculate the average intermittency for each gauge and output the average ΔN values and distribution of spots together with estimates of the laminar and turbulent Nusselt numbers (predicted by the method given in Chapter IV) and the transitional value defined by:

$$Nu = (1-\gamma)\, Nu_l + \gamma\, Nu_t \qquad \ldots (5.15)$$

A typical view of the coverage of turbulent spots frozen at an instant in time is shown in Figure 5.8, together with the mean value of intermittency factor and the burst rate function used as input. Clearly, if the estimate of spot size is accurate, the rise and fall times observed on the time-resolved data (Figures 5.1 to 5.4) can be attributed to each spot gradually covering a larger fraction of the measuring gauges, also shown in Figure 5.8. The measured intermittencies derived by a simple thresholding of the unsteady signal will be higher than those predicted, requiring a higher bursting rate than is actually present. Figure 5.9 shows a comparison between predicted mean intermittency factors and measured data by taking both a simple threshold definition for $\bar{\gamma}$ (as shown in Figure 5.4(a)) and by using an area-weighted technique, dividing the area above the threshold by the area if the signal were at a fully-turbulent (predicted) level. Predicted instantaneous heat transfer rates are compared in Figure 5.10 with experimental data at the design operating point, using the match to the mean values shown in Figure 5.9 to determine the parameters μ, σ, and n_b (the number of bursts per 2 μs time-step). The main differences are due to the turbulent fluctuations from the freestream, not included in the prediction model. The growth rate and origin for the intermittency path model were chosen to match the experimental data, and the angle of spread (α) fixed at 8°. This α value is slightly less than the

10° observed in flat plate tests, and was chosen to agree qualitatively with data in accelerating flows. Particular reference was made to NARASIMHA et al.[1984] in which angles of spread for varying freestream accelerations were presented. No attempt was made in the paper to correlate the spread angle with acceleration, but an approximate correlation of the data available in the paper with acceleration parameter, K is of the form:

$$\alpha = \alpha_o \left(1 - K / K_o \right) \qquad \ldots (5.16)$$

with α_o = 10.3° (consistent with flat plate tests where K = 0) and K_o = 1.5E-6. For the typical ACE suction surface acceleration parameter during the transition start region of K ≃ 0.3E-6 this results in the predicted value of $\alpha \simeq 8°$. The effect of variation in sensing element width is shown in Figure 5.11. The widths chosen correspond to:

(a) 1.25 mm : narrow sensors typical of hot-wire anenometry systems

(b) 4 mm : used for the present i = -10° tests

(c) 10 mm : previously used in the ILPT, and for the i = 0° tests.

Clearly, as the gauge width increases the definition of individual turbulent spots diminishes and a reading more closely approximating the mean intermittent value is approached. The difference in characteristic signals with a change in gauge width can be seen by comparison of Figure 4.19 (i = 0°, Tu ≃ 3%) and Figure 5.10 (i = -10°, Tu ≃ 3%).

It was most encouraging that the time-marching model was able to both match the mean values of intermittency whilst capturing the essential features of the unsteady heat transfer signals. As well as providing a means by which transition may be modelled once the burst rate distribution and spreading angle are known, such a model has enabled a more detailed analysis of the unsteady character of the natural transition process. Further research into the performance of

such a model will be carried out in parallel with a forthcoming series of tests using a highly-instrumented test section on a flat plate with varying streamwise pressure gradient. In these tests a pair of narrower (≃ 2 mm wide) gauges at each streamwise location will be used, in order to allow determination of the spot origins and angle of growth.

CHAPTER VI

UNSTEADY RESULTS ON THE ACE PROFILE

The steady-state behaviour of the ACE profile has been examined in Chapter IV, and the randomly unsteady transition processes investigated in Chapter V. In this chapter the effects of periodic perturbations to the flowfield due to simulated NGV wakes are examined, by the use of schlieren photographs and through measurements of surface heat transfer rates and static pressures. The method of simulation has been described in Chapter III. The nature of the wake and shock structures shed from the bar will be discussed with reference to schlieren photographs of the unsteady flowfield. The time-resolved heat transfer rate measurements (referred to as 'instantaneous') will then be examined, together with the unsteady pressure measurements and the effects on the mean rates of heat transfer and the mean pressure distribution.

6.1 SCHLIEREN PHOTOGRAPHS OF THE UNSTEADY FLOWFIELD

Plates 6 to 15 are examples of schlieren photographs (using the technique described in Chapter III) showing four passages of the ACE cascade at various instants in the bar-passing cycle, with the instrumented blade in the centre of the photograph. The general character of the unsteady effects can be seen in Plates 6 and 7, with variation in exit Mach number, bar speed and the number of bars, at a freestream turbulence level of $\simeq$ 3%. Varying the exit Mach number of the cascade (as shown in Plate 6) only has a marked effect towards the late suction side of the flowfield, and the bar-passing effects

are unchanged. Weak normal shocks are present on the late suction surface in Plate 6(a), as would be expected at M_2 = 0.85. With increasing exit Mach number oblique shocks develop on the suction surface, originating from the adjacent pressure surface trailing-edge. (The schlieren sensitivity is lower in the design Mach number case, Plate 6(b) with the knife-edge horizontal, which results in the passage shock showing less clearly in these early tests.) Plate 6(a) shows the view when the bar is about level with the lower edge of this picture. The position of the bar is estimated by measuring the position of the opposite bar on the wake generator, by use of a photodiode. At this position in the cycle a small amount of mottled tone (corresponding to higher turbulence levels) is visible encroaching into the passage below the instrumented blade, with evidence of higher turbulent activity in the passages above the instrumented blade. This feature was identified by DOORLY and OLDFIELD[1985b] to be due to the wake shed from the bar, being convected into the passage by the freestream velocity. In the lowest passage a thin line is visible entering the field of view approximately in the axial direction, curling to meet the blade pressure surface at about 50% axial chord. Such lines on the schlieren correspond to shock waves (as shown by the steady passage shocks). DOORLY and OLDFIELD[1985a] noticed similar shock wave activity even at the lower relative bar Mach number of 0.93 used in the original tests. At the relative bar Mach number of 1.17 for the ACE design, much stronger shock waves are present, as indicated in Plate 6(c) in which the shock wave has caused a severe disruption to the boundary layer near to the crown of the suction surface. At a lower bar Mach number (M_b = 0.82 at mid-span) there is little shock activity visible (Plate 7(a)). With 16 bars fitted to the wake generator, the flow appears to be highly disturbed, with increased

shock activity and background turbulence (Plates 7(b) and (c)). In Plate 7(c) oil-dots were painted on the cascade side of the schlieren window, enabling the direction of the mean surface shear to be identified.

The remaining ACE schlieren photographs presented here (Plates 8 to 15) were taken with low freestream turbulence level (Tu < 0.8%) in order to distinguish better the wake fluid from the background turbulence level. The plates are twice the actual scale of the cascade, and are at successive points in the bar-passing cycle, varying from 0.23% cycle in Plate 8 to 19.35% cycle in Plate 15. The instrumented blade is marked on a drawing of the blades next to the photographs, as well as the indicated bar position and a prediction for the approximate location of the wake and shock structures generated by the bar, using methods to be described in Chapter VII. (The predicted bow shock wave is labelled 'S1' and re-compression shock wave 'S2'. Only the part of the shock which is generated towards the cascade is shown.) By following through the series of Plates 8 to 15 it is possible to identify the movement of the unsteady flow features, the bar wake and shock waves, as the bar moves in a downwards direction (in this view of the schlieren plane).

The wake appears in the uppermost passage in Plate 8 (at Δt_c = 5 μs) and is just entering the passage above the instrumented blade. At successive time intervals, the wake can be seen to convect through the passages, distorted from its original shape due to the variation of freestream velocity. The wake has entered the passage below the instrumented blade by Δt_c = 160 μs (Plate 11), and the next passage down by Δt_c = 370 μs (Plate 14). Due to the high accelerations through the passage, the extent of the wake region is unclear once the wake has been convected a significant amount into

the passage. This is thought to be due to the reduction in local freestream turbulence level as the wake width increases.

At the values of $M_b \simeq 1.2$ there are two shock waves caused by the bar, due to the fact that the flow approaching the bar cannot turn past the bar (and the expanding wake) at an angle greater than δ_{max}, the maximum turning angle for a given Mach number. As a result of this, a bow shock establishes itself upstream of the bar, and a recompression shock downstream of the bar, symmetrically disposed about the relative velocity line, U_{rel}. These shock waves extend away from the bar symmetry line, weakening with distance, becoming asymptotic to Mach lines far from the bar. However, in the NGV-rotor interaction process simulated in these tests, the part of the shock generated towards the cascade interacts with the blade surfaces in a complex fashion, dictated by the geometrical arrangement of the cascade. The shocks are reflected from the blade suction surfaces (and re-reflected from the pressure surfaces) until the shocks reach the leading-edge. They are then 'chopped' by the leading-edge, appearing to generate a diffracted shock front in the subsequent passage. At $\Delta t_c = 5$ μs (Plate 8) the bow shock can be seen to be reflecting from the suction surface of the blade below the instrumented one. By $\Delta t_c = 50$ μs (Plate 9) the diffracted front of the bow shock is entering the next passage down, and by $\Delta t_c = 95$ μs this has reached the suction surface of the next blade. It appears that this shock wave may have caused a small separation bubble as it passes the blade leading-edge, which convects along the pressure surface, shown as a small dark region on the schlieren photographs. A weak reflection of the bow shock is visible at $\Delta t_c = 160$ μs (Plate 11). The recompression shock can be seen to follow a similar path at a later time, but shows as a multiple number of lines, both before and after being reflected from the surface.

This is thought to be due to the three-dimensionality of the recompression shock, but is not fully understood. The reflected elements of the shocks follow trajectories which are not always amenable to simple analysis. This is hardly surprising given the nature of this flow environment, with three-dimensional unsteady shock interactions occurring in this varying velocity flowfield.

6.2 HEAT TRANSFER RATE MEASUREMENTS

The effects on the blade heat transfer rate will be examined in terms of measurements of both instantaneous and ensemble-averaged heat transfer rate at the design "16 bars" condition and some suction surface results from the second series of tests with 2 bars fitted to the wake generator (and narrower gauges covering 4 mm of the span).

6.2.1 Heat Transfer Results for the 16 Bar Case

The instantaneous values of heat transfer rate to both surfaces of the ACE profile are shown in Figures 6.1 to 6.4 with low ($Tu < 0.8\%$) and high ($Tu \simeq 3\%$) levels of freestream turbulence. The 16 bar case corresponds to the design pitch ratio between the NGV and rotor. This was modelled by fixing the mid-span bar pitch at 57.33 mm (compared with the cascade pitch equal to 34.03 mm) giving a pitch ratio of 1.685. In Figure 6.1 data is plotted from the suction surface gauges 10 to 15 (as defined in Figure 3.8) from gauge 10 at 0.08 fractional surface length (x/s) to gauge 15 at 0.46 x/s. A sample of 2 milli-seconds of data acquired at a sample rate of 2 μs (or 500 kHz) has been selected out of a total of 7 milli-seconds of data taken at this high sample rate. Approximately 8 bar cycles are shown, as indicated by the timing signal shown at the top of the figure, with a cycle time of 224 μs (b.p.f = 4.46 kHz) which corresponds to a rotational speed of 16724 rpm and a relative bar

Mach number (M_b) of 1.176. The bar indicator spike indicates the time when a bar is approximately normal to the cascade, on the cascade turntable centre-line indicated in Figure 3.2. (The values of these bar parameters for this and other experimental tests which are referred to in this thesis are given in Table 4.) Also included on the figure for each gauge position are the mean values of heat transfer rate for four cases:

(i) Experimental data with no wakes, Tu < 0.8% (no grid, N)

(ii) Experimental data with no wakes, Tu ≃ 3.0% (grid-in, G)

(iii) Predicted laminar level (as described in Chapter IV, L)

(iv) Predicted turbulent level (as described in Chapter IV, T).

The heat transfer rates from the first four gauges show strong periodic variation at the bar passing frequency. Each cycle from gauge 10 is characterised by a sharp rise to the order of 3 times the original value in ≃ 10 μs. The level then drops back in about 60 μs to a level close to that before the disturbance occurred, until a second rise occurs to a level ≃ 1.4 times the base level. This gradually decreases again towards the base level and then the cycle repeats. The sharp 'spike' occurs on average about 25 μs before the nearest bar indicator mark and the smaller enhancement region starts at about 100 μs after the bar indicator. Apart from the spike region, the heat transfer varies approximately between the undisturbed value (N) and the predicted turbulent level (T). The next gauge along the surface (gauge 11 at 6.4 mm further downstream) shows an even larger spike occurring at an earlier time in the cycle (50 μs before the bar indicator) and an apparently reduced size secondary event at a slightly earlier time than on gauge 10. In addition to the positive changes noticeable on gauge 10, gauge 11 exhibits a dip in heat transfer prior to the main spike. As will be discussed in Chapter VII, the rapid excursions in heat transfer on

the early suction surface gauges are associated with the interaction of shock waves shed from the bar at this higher relative bar Mach number, M_b = 1.165. In the earlier series of tests performed by Doorly the shock waves were weaker (at M_b = 0.93) and only caused a significant effect once past the blade leading-edge, where the shock wave caused a separation bubble which convected along the suction surface, as described in Chapter II. The rapid excursions in heat transfer rate in the ACE tests can be seen to occur first on gauges close to the crown of the suction surface (defined as the maximum pitchwise location of the blade, at $x/s \simeq 0.3$), then on gauges successively closer to the leading-edge with increasing time. This will be investigated later, as the results suggest that the shock waves are having a direct effect on the boundary layer. (The upwards spike on gauge 12 of Figure 6.1 has been clipped due to saturation of the measuring system, and would otherwise be similar to that observed on Run 4543 in Figure 6.2.)

The smaller periodic disturbance is similar to that observed by DOORLY[1983] and identified as being due to the increased turbulence level in the wake shed from the bar. This locally high level of turbulence can trip the boundary layer to a turbulent state, returning to the undisturbed state following the wake interaction. It would be expected that the wake effect would be convected along the surface by the freestream and thus show on downstream gauges. However, with this pitch ratio between the bars and the cascade the shock effect from the next cycle appears to dominate. Downstream of the suction surface crown (gauges 14 and 15 on Figure 6.1) the signals are more randomly turbulent in nature, fluctuating between levels close to laminar and turbulent predictions. The signals are similar at the higher freestream turbulence case (shown in Figure 6.2), suggesting that the unsteady processes are dominating

the naturally transitional boundary layer characteristic (as shown in Figure 4.19).

The pressure surface results for the 16 bar case are shown in Figures 6.3 and 6.4 with low and high levels of freestream turbulence, compared with predicted levels as defined for Figures 6.1 and 6.2. The results show a highly-coherent periodic structure at the b.p.f., almost appearing to be a sinusoidal variation about the undisturbed level. There are no sharp excursions in heat transfer as present on the suction surface. This is attributed to the geometry of the interaction of the bar shock waves and the blade, as only weak shock activity would be expected on the pressure surface. The peak-to-peak fluctuation level shown in Figure 6.3 (at Tu < 0.8%) increases with increasing surface length, from $\Delta Nu \simeq 250$ at gauge 4 to $\Delta Nu \simeq 1500$ at gauge 9 (the last pressure surface gauge). A similar effect occurs at the higher freestream turbulence level (Figure 6.4) but with slightly higher random perturbations evident on the signals. No satisfactory explanation has yet been found for this behaviour, which will be discussed later. It is possible that the unsteady wake effects are interacting with structures present in the undisturbed boundary layer, possibly causing an initial heat transfer enhancement in the presence of the wakes, followed by a period of unsteady development as the boundary layer returns to the undisturbed levels. Such a hypothesis would need to be confirmed by further experimental work, not within the scope of this thesis. An alternative explanation is that the unsteady pressure field caused by the wake affects the boundary layer, but this too has yet to be confirmed.

The amount of periodicity in the signals can be determined by ensemble-averaging the unsteady signals in the manner described by DOORLY[1983] and others. The bar indicator signal is used to

determine the origin and length for a cycle, then the experimental result averaged over a number of cycles. The process of averaging n cycles in this fashion is to reduce the random fluctuation level by √(n-1), whilst ideally leaving the periodic signal unchanged. Small differences between cycles will, however, reduce the periodic signals to some extent. Ensemble-averaged heat transfer results from selected gauges of both surfaces are shown in Figures 6.5 (at Tu < 0.8%) and 6.6 (at Tu ≃ 3%). The trends identified in the earlier results are confirmed by examination of these figures. The pressure surface results, gauges 1 to 6, shown in Figure 6.6 show that the periodic events seen on one gauge occur in a similar way on downstream gauges. An alternative way of examining the coherence of events between gauges is by viewing the surface formed by plotting the heat transfer rate against surface length for a number of successive time intervals, as shown in Figures 6.7 for the suction surface, and 6.8 for the pressure surface. In these plots, a number of interpolated values are constructed between adjacent gauge positions such that the spacing between the gauges on the surface is maintained (as described in Chapter V). The actual (or interpolated) results are joined together by lines which are almost at constant time. By allowing a slight time shift in connecting the traces together it is possible to visualise the trajectory of events from one gauge to another. A constant time-shift of -8 μs was used in Figure 6.7, which closely follows the trajectory of the shock-driven heat transfer spike. In Figure 6.8 a positive time-shift of 6 μs was used, which allows a clear visualisation of the coherence of structures on the pressure surface. (It should be emphasised that this form of data presentation is primarily intended to give a qualitative feel for the gauge-to-gauge coherence of events, and not as a quantitative tool.)

Figure 6.9 demonstrates the lack of periodicity in signals from later positions on the suction surface (over a range of 0.46 to 0.90 x/s). Gauge 19 exhibits random sudden shifts in level, which correspond to the movements of the passage shock interaction point on the suction surface. The effect does not appear to be driven by the periodic bar-passing events.

The mean effects of the wakes and shocks on the measured heat transfer rate are summarised in Figure 6.10 for the low and high freestream turbulence tests. In both cases the mean levels are increased over the early part of both surfaces, with a greater enhancement in the grid-out case. Once the boundary layer on either surface is fully turbulent, the levels with and without bars are similar.

6.2.2 Heat Transfer Results for the 2 Bar Case

As part of the program of experimental work arranged by Professor J. E. LaGraff, using narrower (4 mm wide) thin film gauges on a suction surface instrumented ACE blade at i = -10° (as discussed in Chapter V), time-resolved data was taken with 2 bars fitted to the wake generator, some of which is presented in Figure 6.11 (from ASHWORTH et al.[1987]). At the higher freestream turbulence level (Tu ≃ 3%) the transitional boundary layer is disturbed by a strong shock-driven disturbance for the high relative bar Mach number, M_b = 1.17, Figure 6.11(a) and (c). Similarly to the 16 bar tests, the events occur first close to the crown of the suction surface, moving towards the leading-edge as time increases. This trajectory can be clearly identified in Figure 6.12, which shows a plot of early suction surface Nusselt number (for Tu < 0.8%) against surface length for a number of time-intervals (as described above), with a time-shift of -6 μs between traces. These constant trajectory lines

closely follow the shock events, the trajectories of which will be discussed in Chapter VII. In contrast to the 16 bar results, another spike occurs in each cycle, preceding the larger spike by ≃ 75 μs, which corresponds to the bow shock preceding the bar. This effect was not noticeable in the 16 bar case due to the interaction of the wake from the next bar.

In Figure 6.11(b) the bar was run at a low relative bar Mach number (M_b = 0.83), and a clear superposition of the turbulent wake region is visible on the naturally transitional boundary layer. Ensemble-averaged results of the test with the bars running at this subsonic relative bar Mach number are shown in Figure 6.13. Because of the long cycle time with the lower rotational speed of the bars, it was only possible to average over three cycles, and some of the random elements of the transition process can still be seen (as opposed to periodic events at the b.p.f.). The wake is clearly defined, and its trajectory will be examined in Chapter VII. Another significant periodic effect precedes the bar and appears to be a weak shock effect, even at the low bar Mach number, as it follows the expected trajectory of the shocks observed earlier (as opposed to the convected events which move downstream with increasing time).

6.3 UNSTEADY PRESSURE MEASUREMENTS

A brief series of tests was carried out in order to examine the instantaneous (and mean) pressure response to the bar-passing phenomena. Kulite pressure transducers were mounted directly into the instrumented blade (as discussed in Chapter III) at the three locations shown in Figure 3.6.

The results from the transducer set into the leading-edge are shown in Figure 6.14 with variation in bar speed for the 2 bar case, and with no bars fitted. At the high relative bar Mach number,

M_b = 1.165, the pressure rises corresponding to the bow shock (S1) and the recompression shock (S2) can be clearly seen. With the reduced level of M_b = 0.8 no shock wave effects are visible, but a dip in level corresponding to the bar wake is evident. The case with no bars fitted shows the datum signal, with the background level of turbulence at 3%.

The results from all three transducers at the two bar Mach number levels are shown in Figures 6.15 and 6.16, and the peak-to-peak variation in levels are compared with the steady-state pressure distribution at the design incidence in Figure 6.17. All of the traces show effects at the bar-passing frequency, with strong shock activity at the higher relative bar Mach number. These large pressure fluctuations are thought to cause (at least in part) the rapid observed variations in heat transfer rate, and are the subject of further investigation (as reported in JOHNSON et al.[1988]).

The mean effect of the bar wakes and shock waves on the measured static pressure distribution around the blade is shown in Figure 6.18. This is compared with the pressure distribution at the i = -10° incidence case, to investigate whether the bars induced a mean negative incidence due to the velocity deficit in the wake. The total pressure in the wake-passing tests was only measured upstream of the rotating bars, so that a correction has to be made in order to compare with the undisturbed Mach number distribution. This correction was calculated by assuming that the early pressure surface points are little affected by incidence change (as is shown in Figure 4.2). Matching the Mach number levels at the pressure surface point indicated in Figure 6.18, it can be seen that the Mach number distributions are similar, supporting the idea that a net negative incidence change is induced by the bars.

CHAPTER VII

PREDICTED WAKE AND SHOCK POSITIONS

The significant effects of wake and shock interaction with the turbine blade under investigation have been demonstrated in previous chapters. In order to quantify these effects, and to develop a means by which our understanding of these unsteady phenomena may be brought within the scope of current design techniques, simplified models of the wake and shock structures generated by the bar-passing apparatus were developed. In this chapter the basis for the models will be given. These predictions will be compared with experimental data and analysis performed of the event trajectories.

7.1 MODELLING OF THE BAR WAKE

The wake itself is almost 2-dimensional in form, varying in height across the span due to the 3-dimensional bar geometry. Figure 7.1(a) is a representation of an idealised wake as would be shed from a bar cutting through a uniform velocity flowfield, generating a helical structure. In the schlieren plane (the x,y plane as marked in Figure 7.1(a)) the edges of the wake are barely visible. It was therefore decided that only a 2-dimensional calculation is necessary.

7.1.1 Method of Modelling the Wake

The procedure follows that described in DOORLY[1983], differing in the following respects:

(a) The hand-calculation procedure has been replaced by a computational model allowing for different profiles and flowfield

predictions to be used, and enabling parametric studies to be performed (e.g. variation of the un-distorted wake model parameters).

(b) An allowance is made for the spreading of the wake either side of the relative velocity line. The leading and trailing-edges of the wake are separated by a width proportional to the square-root of the distance from the bar along the line of the relative bar velocity U_{rel} with the constant of proportionality derived from a database of wake measurements, confirmed by a correlation of measurements reported in SCHLICHTING[1979]. The correlation is of the form:

$$b = 0.5692 \sqrt{l\ C_D\ d} \qquad \ldots (7.1)$$

where l is the distance from the bar. For the Mach number range 1.0 to 1.2 the drag coefficient is approximately equal to 2.0, so that for the ACE blade (7.1) can be expressed as:

$$b = 0.033 \sqrt{(x(i) - x_o)/\sin \alpha_b} \qquad \ldots (7.2)$$

using the nomenclature of Figure 7.1(b). The angle α_b corresponds to the inclination of U_{rel} to the pitchwise line (the y-axis), obtained from the velocity triangle in Figure 3.12(b) as:

$$\sin \alpha_b = \frac{U_{in}}{U_{rel}} \cos \beta_1 \qquad \ldots (7.3)$$

and $x(i)$, x_o refer to the x co-ordinates at a section i and the origin of co-ordinates (at the bar) respectively.

7.1.2 Details of the Computational Model

The prediction procedure is shown in Figure 7.2 and described below.

(i) A prediction of the flowfield velocity is made, in this case using the Denton scheme (as described in DENTON[1983]) and stored by the program.

(ii) The relative velocity U_{rel} is calculated (assumed constant across the span), the centre-line of the undistorted wake is

calculated from the specified bar position and the width, b/2, added.

(iii) The wake is shifted back in time so that the bar will return to its specified position following the marching process of the prediction routine.

(iv) From this initial position elements of the wake are convected by time steps (typically of the order of 1 μs) using the local velocity interpolated from the prediction until the bar reaches the specified location. The differential velocities in the flowfield cause distortion of the wake along its length and across its width as it is accelerated through the passage. The change in shape of the wake as the routine marches is shown in Figures 7.3 and 7.4 for the ACE and B22 blades respectively.

(v) Care needs to be taken about the so-called 'chopping' of the wakes by the blade leading-edge, and its subsequent convection through the passage such that the discretisation of the model does not force the wake lines into or away from the solid boundaries. The tendency for points to move away from the suction surface due to its convex curvature is countered by automatically moving points, which would otherwise gather on the concave pressure surface, onto the suction surface of the same blade. The ends of the wake in each passage are monitored so that it is possible to derive the amount of time that the edge of the boundary layer is subject to the wake flow.

This simple scheme, which could be incorporated in the blade design process, agrees well with the shapes of the wake on the schlieren photographs (as compared in Plates 8 to 15 for the ACE

blade and 19 to 22 for the B22 blade), so that the fraction of time that the heat transfer rate to the surface is affected by the wake could be calculated and included in the intermittency term of a prediction. It also demonstrates that, to the level of our measuring ability, second-order effects such as the 'negative jet' effect do not significantly affect the wake position, confirming the results of DOORLY[1983], and that the assumption that this flow unsteadiness may be superimposed on the steady flowfield is valid.

7.2 THE SIMPLIFIED SHOCK MODEL

As mentioned previously, there will be two shock waves generated by the bar:

(i) The bow shock (S1) preceding the bar - a detached shock whose shape and separation distance are a function of M_b for a given bar diameter, rotational speed and radius.

(ii) The re-compression shock (S2) - a shock with a virtual origin at the confluence point downstream of the bar, asymptotic to the Mach angle, $\alpha = \arcsin M_b^{-1}$.

The bow shock position is determined by a model developed by Moeckel as described in SHAPIRO[1954]. The position of the recompression shock is less well determined, and only an approximation to its position may be established. The shock prediction is based on the assumption that for a small element of the bar the flow is two-dimensional with respect to the plane containing U_{rel} and normal to the bar axis, i.e. a quasi three-dimensional approach. Details of the method of predicting both shocks are given below, followed by a description of the computational model.

7.2.1 Modelling the Bow Shock

There are several assumptions made in this prediction of the two-dimensional location of the bow shock, which enable its position to be fixed as a function of the inlet Mach number and the cylinder diameter. These are that:

(i) The sonic line (marked as 's' to 'sb' in Figure 7.5) is a straight line, emanating from the point on the body where its contour is inclined at the maximum wedge angle at the given M_b.

(ii) Since the detached shock asymptotes to the Mach angle, α, at large distances from the bar axis and is normal to this axis, it is assumed that its shape is that of a hyperbola defined by the equation $\beta y = \sqrt{\{x^2 - x_o^2\}}$, using the notation of Figure 7.5.

(iii) Continuity is applied for fluid crossing the sonic line, with conditions defined by those corresponding to the mass centroid streamline for this flow.

(iv) The inclination of the sonic line, η , is taken as the mean of the turning angle θ_s for which the downstream flow is exactly sonic, and δ_{max}, the maximum possible turning angle for a given M_b.

The procedure for calculating the shock location was programmed in the following steps:

(a) Knowing the bar radius and rotational speed the local bar velocity is found. This is combined vectorially with the inlet velocity vector to determine the relative velocity, and hence M_b.

(b) Values for β, θ_s, δ_{max}, σ_s (the shock angle at the sonic line intersection point) and the ratio A^*/A for isentropic flow are all determined from M_b.

(c) The distances x_{sb} and y_{sb} are calculated from the cylinder geometry and δ_{max}.

(d) From curve fits to the oblique shock tables, the total pressure ratio p_{o_c}/p_{o_∞} (where p_{o_c} refers to the isentropic stagnation pressure

on the centroid streamline downstream of the shock) is determined for the shock angle corresponding to the centroid streamline, σ_c obtained from the continuity assumption and the equation of the hyperbola from:

$$\tan^2\sigma_c = \frac{4}{\cot^2\sigma_s} - \frac{3}{\bar{\beta}^2} \qquad \ldots (7.4)$$

(e) The assumption that the sonic line is straight and normal to the flow direction allows the continuity equation for plane flow to be put in the form:

$$\frac{y_s}{y_{sb}} = \left[1 - \frac{p_{o_\infty}}{p_{o_c}} (A^*/A)\cos\eta \right]^{-1} \qquad \ldots (7.5)$$

(f) Finally, the separation distance L/y_{sb} is found from the geometry and equation of the hyperbola, as:

$$\frac{L}{y_{sb}} = \frac{y_s}{y_{sb}} (\beta^2\tan\sigma_s - \beta\sqrt{\beta^2\tan^2\sigma_s - 1} + \tan\eta) - \tan\eta \qquad \ldots (7.6)$$

and the equation of the hyperbola is determined. As the angle of the shock to the incoming flow is known, the shock strength can also be calculated and used for subsequent calculations in determining the nature of the reflection process.

7.2.2 Modelling the Recompression Shock

The method used, as mentioned above, is to assume that the shock is straight and originates at the Mach angle from the line of U_{rel} at a virtual origin downstream of the bar. This distance was determined primarily from experimental observations, and supported by the method described in MARTELLI and BORETTI[1985]. The resulting position of the shock S2 at mid-span is shown in Figure 7.5(b), weakening with distance away from the relative velocity line as in reality it asymptotes towards the Mach angle.

7.2.3 Details of the Computational Model

As U_{rel} varies in both magnitude and direction so does the associated shock structure and unlike the wake this variation needs to be accounted for in order to visualise the shock structure. The relative bar Mach number, M_b, varies for the ACE tests from about unity at the hub to a maximum of 1.25 at the tip, the actual value determined from:

$$M_b^2 = \frac{U_{rel}^2}{\gamma RT_1} = \frac{U_b^2 + U_1^2 - 2U_bU_1\cos(\frac{\pi}{2} + \beta_1)}{\gamma RT_1} \qquad \ldots (7.7)$$

where $U_b = \omega r_b = \frac{2\pi N}{30} r_b$, and N is the rotational speed in rpm.

The method of prediction was computerised as follows:

(i) For assumed constant inlet conditions and a specified position of the bar M_b is calculated and its direction determined.

(ii) The equation of the bow shock in the two-dimensional plane described above is derived from M_b using the method described in Section 7.2.1, shock properties and turning angles obtained by curve-fit equations where necessary over a range of Mach numbers from 1.0 to 1.5.

(iii) The recompression shock is assumed to be straight and inclined at the Mach angle α ($= \sin^{-1} 1/M_b$) to the direction of the relative velocity line, described in Section 7.2.2.

(iv) The portions of the shocks downstream of the the axial leading-edge point are 'chopped', and diffracted from an origin at the axial leading-edge. Allowance is made for the convection of the shock by the freestream as it moves away from this point, by allowing a propagation of the un-distorted bow shock along the line of the shock, at a rate approximately equal to the local tangential velocity. The ends of the shocks are lined up with the pressure surface, and assumed to terminate there, with no reflections taken into account from

this surface. Inspection of the schlieren photographs implies that the shock is weaker towards this surface and that neglecting this reflection is not important.

(v) Finally, the points of intersection with the blade suction surface are calculated, and the shocks are simply reflected from an origin mid-way between the two intersection points. Once the shock position in the leading-edge plane passes the blade leading-edge point, the shock automatically resumes to a simply diffracted shock again, as the motion of the shock in the later part of the passage is not considered important enough to justify the additional complexity of maintaining the 'free' end of the chopped shock.

7.3 RESULTS OF THE PREDICTIONS AND RELATED TRAJECTORY ANALYSIS

The results of the wake predictions for the ACE and B22 blades are given in Figures 7.3 and 7.4. Views of the shock structures for both profiles are given in Figures 7.7 and 7.8. These may be compared with the experimental schlieren results in Plates 8 to 15 and Plates 19 to 22.

The intersection of both shocks with the blade suction surface can be determined with respect to the position of the bar, and compared with observed positions deduced from schlieren photographs, and also from the measured rapid variations in heat transfer rate. High accuracy is necessary when comparing quantitatively with measured data, due to the intrinsicly high errors associated with this positional information. These errors are:

(i) The possible error in measuring the true bar position (of the order of 5mm);

(ii) Uncertainty as to the amount of deflection of the bar;

(iii) The approximation in shock location due to the simplifying assumptions made (particularly in assuming the freestream velocity to be constant).

The schlieren taken of the ACE cascade (Plates 8 to 15) indicate that there are time-shifts between the measured position of the bar and that corresponding to the wake and shock predictions. A program calculating the probable bar deflection due to the counteracting centrifugal and drag forces (Program AP2BRS as described in DOORLY[1983]) predicts that the mid-span bar deflection would be between 2 to 5 mm approximately along the line of the relative velocity vector, U_{rel}. This correction has not been applied in the ACE predictions, but has been used for the B22 tests as is discussed in Chapter VIII. Despite some uncertainty about the exact bar position, the information obtained from such a prediction helps in our understanding of this type of unsteady interaction in a qualitative sense, and leads the way for further calculations and comparisons with other methods of obtaining this kind of information. These include the type of unsteady calculation applied to a full flowfield solution at present under development (e.g. that of GILES[1987]), which employ periodic variation of the boundary conditions for a flowfield prediction, allowing for simulation of the wake and shock perturbations to a steady-state solution.

In Figure 7.9 measurements are presented for the trajectories of the events observed in Chapter VI based on the definitions shown for the threshold levels. The turbulent patch due to the wake is defined in extent by the leading-edge and trailing-edge values at 50% of the change between the undisturbed and disturbed levels. Within the wake-affected region three peaks can also be tracked, shown as W1, W2 and W3. The trajectories of these events support the hypothesis given in Chapter VI that it is possible to observe embedded

structures within the wake, possibly due to vortex activity. All the wake related events (taken from Run 5696 data shown in 6.11) convect at similar rates to those observed for turbulent spots, as described in Chapter V. These values can be compared with the predicted trajectories of events in the freestream from the 'striped-air' model, and with propagation rates calculated as fractions of the freestream velocity, in Figure 7.10. The leading-edge data follows closely to the high propagation rates (0.88 to $1.0U_\infty$) whereas the trailing-edge rates are closer to $0.5U_\infty$. These results suggest that the processes involved in the transfer through the boundary layer to the wall of events at the boundary layer edge can be similar, whether the events are naturally occurring or forced, as indicated in Figure 7.10. The striped-air calculated values for the time that the boundary layer is tripped to a turbulent level are used (together with the appropriate convection rates) in Figure 7.11 to predict the instantaneous fluctuations in the heat transfer signals through the transition region with a wake superimposed. The transition prediction is at the same conditions as given in Figure 5.10.

The measured trajectory rates for the effects of the bar shock waves can also be compared with expected values, by plotting a series of lines which follow the time history of a bar passing by the blade in the pitchwise direction, first impinging on the surface near the suction surface crown, as shown in Figure 7.12(a) and (b) at the two incidences tested. Due to the lower inlet velocity at $i = -10°$ the bar is run at a higher speed to maintain the correct relative bar Mach number, reflected in the shallower gradient of the time against length curves.

CHAPTER VIII

WAKE-PASSING EXPERIMENTS ON A FILM COOLED PROFILE

The objective of the experiments described in this chapter was to examine the performance of a film cooled profile subject to the effects of wakes and shock waves. Previous testing on this profile has been discussed in Chapter II. These tests combined for the first time the film cooling and wake-passing experiments, and were intended to give an overall understanding of the interaction processes. The investigation was in two parts:

(i) Measurement of the mean heat transfer rate to the profile with variation in blowing rate for each of three film cooled configurations. The tests were carried out with and without the wake-passing apparatus, and with low and high levels of freestream turbulence (< 0.8% and 2.5% at inlet).

(ii) Analysis of schlieren photographs of the unsteady flowfield in order to investigate whether films showed noticeable transient effects of the wake and shock-wave events.

8.1 DETAILS OF THE B22 EXPERIMENTS

The film-configurations tested are defined in Table 5, and the cascade configuration shown in Figure 8.1. The leading-edge and suction surface builds (referred to as builds 'A' and 'B') were the same as described in HORTON et al.[1985]. The pressure surface build ('C') was a similar configuration to that tested previously, but positioned further downstream (at 75% axial chord, 66% surface length, compared with 50% x/C_{ax} for Horton's build 'C'). This was

changed since the earlier tests revealed a poor performance (low cooling effect) for the film at 50% x/C_{ax} compared with a film row positioned at 85% x/C_{ax} The poor performance of the 50% x/C_{ax} film row was explained as being due to high negative surface curvature (-0.03 1/mm) at this location causing the lower momentum cooling-air to be driven by the radial pressure gradient away from the surface. By 75% x/C_{ax} the surface curvature is very low (< -0.005 1/mm) and it was therefore predicted that this later position would improve on the 50% x/C_{ax} film whilst cooling more of the surface than the 85% x/C_{ax} film row. The tests reported here were at a fixed value of non-dimensional temperature ratio, θ, approximately equal to unity, where θ is defined as:

$$\theta = \frac{T_g - T_c}{T_g - T_w} \qquad \ldots (8.1)$$

where T is temperature, and subscripts g,c,w refer to the gas and coolant total conditions and the wall temperature respectively. The blowing rate was chosen as the variational parameter defining the injection process, defined by:

$$B = \frac{\rho_c u_c}{\rho_\infty u_\infty} \qquad \ldots (8.2)$$

where ∞ corresponds to the static freestream condition. The blowing rate is typically varied over the range (0, 1.5). In other respects the tests were matched to those described in DOORLY and OLDFIELD[1985a], with the relative bar Mach number M_b = 0.93 at mid-span, as detailed in Table 5. For the heat transfer tests the ratio Tg/Tw was set to a nominal value of 1.5 (based on the pre-run wall temperature) for the heat transfer tests, with Tg $\simeq$ 450 K and Tw $\simeq$ 300 K. The schlieren tests were set to a 'cool' temperature ratio Tg/Tw $\simeq$ 1.2 for reasons of optical quality described in Section 8.3.

8.2 MEAN HEAT TRANSFER RATE MEASUREMENTS

Each of the three film configurations tested will be considered separately in this section. The tests were carried out using the same experimental equipment as described in HORTON et al.[1985] and shown in Figure 8.1. A new blade was manufactured for the pressure surface film configuration and modifications were necessary for all the blades tested in order to avoid interference with the wake-passing apparatus. These modifications were only minor in nature, involving re-routing of the thin film gauge leads and altering the coolant supply system to feed from one side of the cascade, as opposed to the dual feed used by Horton. A correction for pre-run heating of the wall during the spin-up of the bars was made as described in Chapter III.

8.2.1 Leading-Edge Film Cooling (Build 'A')

The two rows of 15 holes (as described in Table 5) were positioned close to the leading-edge on both surfaces, and fed from a common supply. The assumption is made that the external conditions will be similar to engine experience of leading-edge configurations even if the flow rates are different for each row. These are assumed to trip the boundary layer to a turbulent state despite the high accelerations near to the leading-edge, due to the highly turbulent nature of the film-cooling jets. The heat transfer results from the leading-edge build are shown in Figures 8.2(a) and (b) for 2.5% freestream turbulence level. The steady-state results with no bars fitted, Figure 8.2(a), are given for a range of blowing rate from zero to 1.8. The suction surface heat transfer levels are reduced at all blowing rates compared with the baseline condition, with a slight decrease in heat transfer rate as the blowing rate increases. The pressure surface heat transfer rate is little affected by the

leading-edge film, apart from a small reduction at the 0.18 x/s position. In fact, the pressure surface traces only serve to confirm the good run-to-run repeatability of the cascade for the range of conditions tested. HORTON et al.[1985] observed that the suction surface side film appeared to be intermittent at blowing rates around the 0.5 level, with some ingestion of mainstream flow occurring.

The results with 8 bars fitted to the wake generator are shown in Figure 8.2(b). There is a slight increase in heat transfer rate with zero blowing rate compared with the no-bars case, consistent with that observed in DOORLY[1983] on the same profile with no film cooling. A reduction in suction surface heat transfer rate with increasing blowing rate is observed, but with slight differences from the no-bars case. The reduction in suction surface heat transfer rate at blowing rates of 0.5 and 1.0 is approximately the same as that in the no-bars case, but a further reduction to levels close to those observed without bars occurs at the higher blowing rates. This tends to suggest that the increased average mixing due to the wakes may not penetrate through the higher blowing rate films. The presence of the bars has little effect on the pressure surface heat transfer rate but the higher blowing rate cases (B = 1.5 and 1.8) indicate a small reduction in heat transfer late on the surface. No such reduction was evident in the no-bars case.

8.2.2 Suction Surface Film Cooling (Build 'B')

The row of film-cooling holes on the suction surface at 25% x/s (as described in Table 5) caused no significant effect on the blade heat transfer with zero cooling flow. The no-bars results were presented by HORTON[1985] and demonstrated a similar cooling effect to that presented in Figures 8.3(a) and (b) for the 8 bar case. The levels of blowing rate were chosen to correspond to those used in the

earlier series of tests. Figures 8.3(a) and (b) show the cooling effect of the suction surface film at gas-to-wall temperature ratios of 1.5:1 and 1.3:1. The film effectiveness (shown as a reduction in heat transfer rate) increases with blowing rate up to B = 0.92, but at B = 1.5 there is a reduction in effectiveness close to the film. This is most clearly visible on the T_g/T_w = 1.3:1 test results shown in Figure 8.3(b) as the overall level of the results for B = 1.5 in Figure 8.3(a) is reduced due to a slight change in operating condition. This reduced effectiveness at high blowing rates is commonly attributed to 'lift-off' of the film as the momentum of the film fluid becomes sufficiently strong to cause a significant separation region downstream of the film cooling row. The film gradually diffuses back to the surface and the heat transfer rate returns to values close to those at B = 0.92.

8.2.3 Pressure Surface Film Cooling (Build 'C')

Examples of the effect of the film cooling row at 65% surface length on the pressure surface at low freestream turbulence level are shown in Figures 8.4(a) and (b), with and without 8 bars upstream of the cascade. The no-bar case shown in Figure 8.4(a) performs in a similar fashion to the later surface film tested by Horton, showing best cooling effect at the lowest blowing rate (B = 0.5) with a reduced effectiveness as the blowing rate increases. This could be due to increased turbulent mixing at the higher blowing rates combined with an increased migration of the film away from the surface as the film momentum increases.

In the 8 bar case, Figure 3.4(b), a similar performance is observed but the zero blow heat transfer rate is slightly higher. As a result of this, a more significant cooling effect is noticeable with increasing blowing rate than in the no-bars case, suggesting

that the film is acting so as to reduce the penetrating effect of the higher bar-induced freestream turbulence.

8.3 SCHLIEREN RESULTS FOR THE FILM COOLED PROFILE

The same reflected schlieren system described in Chapter III was used for the B22 tests, but it was necessary to operate at a higher gas-to-wall temperature ratio ($T_g/T_w \simeq 1.2$) in order to allow better visualisation of the coolant flows. This results from increasing the temperature ratio (and the density gradient) between the mainstream and the coolant flows, hence increasing the effect shown in the schlieren technique. However, this also increases the background level of noise in the photographs due to the increased temperature gradients in the sidewall boundary layers, which can make the differentiation of the wake less clear than at temperature ratios closer to unity. It was decided that clear visualisation of the films was a higher priority, as the visualisation of the wakes without film cooling has been already presented in DOORLY and OLDFIELD[1985a and b]. The alternative of running close to unity temperature ratio and reducing the coolant temperature was considered to add too much complexity to the experiment. The horizontal knife-edge orientation was chosen in an attempt to enhance the effects of variation in density gradient across the coolant films.

The schlieren photographs presented in Plates 16 to 22 were all taken at the design operating condition of $M_2 = 0.96$ and $Re_2 = 2.02E6$, with 2 bars fitted to the wake generator and a relative bar Mach number of 0.93. As described in DOORLY and OLDFIELD[1985a], and discussed in Chapter VII, as well as the wake shed from the bar, weak bow and re-compression shocks are also visible. The steady flow

weak shocks are also visible along the later part of the suction surface, as would be expected at an exit Mach number 0.96.

8.3.1 Leading-Edge Film Cooling (Build 'A')

Schlieren photographs of the leading-edge configuration are shown in Plate 16 for four blowing rates at a similar time in the bar-passing cycle, at about 5.0% of the cycle. The two upper blades in this picture are cooled, as indicated by the supply pipes which show on the photographs as dark lines. This time in the cycle was chosen to see if the stronger re-compression shock wave caused any affect on this configuration, by comparison of the two film cooled blades. No effects of the shock waves are apparent upon examination of these photographs, and this is thought to be due to the weak nature of the shocks at the B22 operating condition as discussed in Chapter VII. The wake is just encroaching into the upper passage, showing as a mottled region due to its higher turbulence level. A small disturbance to the suction surface film can be observed at the location of the Build 'B' row (at 25% x/s), even though an attempt was made to smooth the surface when blocking this film row prior to the Build 'A' tests.

Also visible on the photographs are thin wavy lines which emanate from close to the blade leading-edge on the pressure side, in the direction of the adjacent blade. These were observed to some extent on all the configurations and cycle fractions, and are believed to be due to the horse-shoe vortex near to at least one of the sidewalls (as observed by GAUGLER and RUSSELL[1982], for example). There was insufficient time to investigate whether these effects could be predicted by models of the passage secondary flows, but they occur close to the expected positions.

The suction surface film is barely visible at B = 0.5, Plate 16(a), but thickens with increasing blowing rate. A more significant amount of cooling flow is visible on the blade pressure side, again increasing in thickness with increased blowing rate. Since only very slight differences were observed on the pressure surface heat transfer rate with the leading-edge films, it must be assumed that either the films are being driven away locally to the surface, or that the increased turbulent mixing due to the films is off-setting the coolant effect. It was of some surprise that the schlieren and heat transfer rate measurements indicated such different performances of the pressure-side films, and this issue has still to be resolved. Examples of the leading-edge configuration at other times in the cycle are shown in Plates 20 to 22, again showing little effect due to the wakes or shocks.

8.3.2 Suction Surface Film Cooling (Build 'B')

The suction surface film row at 25% x/s is shown in Plate 17 with variation in blowing rate about 1% of the bar cycle. The re-compression shock waves from the bar had just passed the film row at this cycle time, but no effect of this is noticeable on the photographs. The film becomes increasingly thicker as the blowing rate increases, and the high values of acceleration prior to the film can be seen as a dark patch (indicating high changes in density gradient). Plate 19 shows a comparison between the predicted positions of the wakes and shock waves shed from the bar for configuration 'B' at the low blowing rate of 0.5.

8.3.3 Pressure Surface Film Cooling (Build 'C')

Schlieren photographs of Build 'C' (65% surface length) are shown in Plate 18 at about 40% to 50% of the bar cycle with variation in blowing rate from 1.0 to 2.8. The film thickness increases with

blowing rate, until at the higher rates there is evidence of complete lifting-off of the film, even in spite of the uneven film ejection which could obscure this in the schlieren photographs.

CHAPTER IX

CONCLUSIONS

The conclusions to be drawn from the testing and analysis described in this thesis will be presented in separate sections, each corresponding to the following major areas of interest:

1. The experimental technique and instrumentation;
2. Mean measurements of heat transfer and pressure on the ACE profile;
3. Measurement and analysis of natural transition on the ACE suction surface;
4. Examination and prediction of wake and shock wave effects;
5. Effects of wake-passing on a film cooled profile;
6. Relevance to the turbine design process;
7. Recommendations for future work.

9.1 EXPERIMENTAL TECHNIQUE AND INSTRUMENTATION

(i) The ILPT provided a reliable means of establishing engine representative flow conditions for a range of operating conditions. The ability to vary independently such parameters as Mach and Reynolds numbers, freestream turbulence level, inlet angle and wake and shock wave passing has given a clear understanding of the boundary layer behaviour.

(ii) Without a turbulence generating grid fitted the tunnel operates with low enough levels of background freestream turbulence level (< 0.8%) so that laminar boundary layers can be developed on blade surfaces. The inlet boundary layers on the sidewall are

sufficiently thin (≃ 1-2 mm) so that the centre-line flow is approximately two-dimensional, in spite of the low aspect ratio of the cascade which increases the relative importance of secondary flows.

(iii) The wide-bandwidth heat transfer and pressure instrumentation combined with simultaneous data acquisition for a number of channels enables many unsteady features of boundary layer behaviour to be examined in sufficient detail to support theoretical analysis. These measurements were usefully supported by flow visualisation techniques (schlieren photography and surface oil-dots).

(iv) The importance of simplified models for the complex interaction processes has been demonstrated (such as the use of striped-air models).

9.2 MEAN MEASUREMENTS OF HEAT TRANSFER AND PRESSURE ON THE ACE PROFILE

(i) Inlet and outlet pressure surveys indicate that the cascade established pitchwise periodic flow. The blade pressure distributions show the expected effects of incidence and exit Mach number variations.

(ii) Variation of freestream turbulence level, Reynolds number and inlet angle all affected the transitional behaviour of the blade surface boundary layers at mid-height. The suction surface results indicated a natural transition, driven by disturbances in the freestream, caused by breakdown of Tollmien-Schlichting waves into turbulent spots eventually merging together to form a turbulent boundary layer state. The pressure surface transition was earlier than would be predicted for natural transition, and was likely to be due to Goertler vortex activity driven by the combination of freestream disturbances and concave curvature.

(iii) Analysis of blade heat transfer data was helped by comparison of measured levels with those for laminar and turbulent boundary layers as predicted by integral methods. Presentation of data in terms of local conditions allows clear identification of laminar, transitional and turbulent regions.

9.3 MEASUREMENT AND ANALYSIS OF NATURAL TRANSITION ON THE ACE SUCTION SURFACE

(i) The suction surface natural transition process was examined in detail, and the nature of the turbulent spot formation and propagation defined. The convection rate and growth of turbulent spots in this transonic boundary layer has been quantified.

(ii) A stochastic model for turbulent spot production has been formulated based on a statistical analysis of the transition process. This compares well with measurements taken from the ACE profile, both in terms of instantaneous and time-averaged values.

9.4 EXAMINATION AND PREDICTION OF WAKE AND SHOCK WAVE EFFECTS

(i) Simulated NGV wakes caused significant periodic fluctuations to the measured surface heat transfer rate. The ACE suction surface showed a marked increase in level in the laminar and transitional regions due to the increased turbulence in the wake fluid raising the heat transfer to turbulent levels. The ACE pressure surface interaction was complicated by an apparent interaction between the steady coherent turbulent structures due to Goertler vortex activity and the wake fluid, resulting in fluctuations above and below the undisturbed level. These results were consistent with those observed in previous wake-passing experiments.

(ii) There were few significant long-term effects of the unsteady interaction. The wake-induced turbulent patch has been shown to

convect at rates similar to those observed for isolated turbulent spots, after which the boundary layer soon returns to its undisturbed state. Similarly, the shock interaction has most effect only close to the time of the interaction event, or the convected turbulent patch downstream. In the strongly affected early suction surface region effects of reflected shock wave activity have also been identified. These can cause effects on the heat transfer rate which persist throughout the cycle.

(iii) It was possible to predict the unsteady nature of the wake interaction with the transitional blade boundary layer by a combination of a prediction of the wake position in the freestream with the time required for freestream events to affect the surface. A fundamental similarity between the periodic wake interactions and the random turbulent spot effects has been shown.

(iv) The strong shock waves present in the ACE tests caused direct effects on the measured heat transfer and pressures, due to the large pressure changes across the shock. There is evidence of separation of the boundary layer due to this interaction over at least some of the surface, with an induced turbulent patch convecting downstream of the interaction point. This earlier work on a weaker shock interaction on the B22 blade indicated a similar effect, but only once the shock had passed the blade leading-edge.

(v) The essential features of the shock wave generation process by the bar have been modelled, although no attempt was made to try and develop an unsteady three-dimensional model for the bar shock waves.

9.5 EFFECTS OF WAKE-PASSING ON A FILM COOLED PROFILE

(i) The wakes and associated shock-wave structures generated in the tests on the film cooled B22 profile caused a systematic increase in the overall heat transfer rate to the profile, but largely

unaffected the film cooling performance for the conditions tested. This was due in part to the shock waves only being significantly strong near to the tip of the bar. It was surprising that the wakes increased the levels of heat transfer in a systematic fashion even in the presence of film cooling. It was expected that either little effect would be seen or that the film performance would deteriorate.

(ii) Schlieren flow visualisation and subsequent analysis confirmed the wake and shock structures previously measured (reported in DOORLY and OLDFIELD[1985a]). The film rows were clearly visualised by using the schlieren technique, and were similar in appearance to those observed in steady flow (HORTON[1985]).

(iii) In some instances it appears that the presence of an effective coolant film on the blade surface can form a barrier to the enhanced turbulence due to the wakes.

9.6 RELEVANCE TO THE TURBINE DESIGN PROCESS

(i) The effects of wake-passing are, in general, to increase the heat loading to the turbine blade, which needs to be allowed for in the design process.

(ii) The wakes produce a mean negative change in incidence which leads to a reduction in blade loading and hence work output.

(iii) The unsteady separation and transition processes cause changes to the boundary layer state which are likely to increase the blade loss.

(iv) The unsteady thermal loading to the surface, resulting from the high fluctuations in heat transfer rate, could result in detrimental effects on blade life, particularly with regard to ceramic or thermal barrier coated blades.

(v) It has become clear in the course of this study that an understanding of the unsteady aerodynamic and heat transfer processes

is essential to the turbine design process, even if this results in methods which are applied steady-state methods.

9.7 RECOMMENDATIONS FOR FUTURE WORK

(i) The nature of the natural transition process has been clearly identified by examination of the heat transfer traces and comparison with simulated values. It was not possible to determine the turbulent spot origins due to the limitation of only having one gauge at a given streamwise location. It is proposed that this limitation will be overcome in part by using two narrow gauges at each streamwise point. Analysis of the signals from such gauges should allow for better determination of the angle of spread of turbulent spots and hence the spot origins. By such techniques it may be possible to determine the rate of spot generation along the surface and thus confirm a model for the formation rate in a realistic gas turbine environment.

(ii) The shock-wave and wake interaction effects have been examined in some detail in order to determine the nature of the unsteady interaction on the ACE profile. More analysis of this data should reveal the fundamental physical processes which lie at the heart of these significant unsteady effects. The effects of wake interactions on the ACE pressure surface are still not understood, requiring a detailed analysis to reveal whether the wakes interact with established vortex structures or affect the surface due to local pressure and velocity changes.

(iii) The pressure surface behaviour of both profiles tested has yet to be understood, both in terms of the possibilities of leading-edge separation and the presence of structured longitudinal vorticity.

(iv) The interaction between the bar-generated wakes and shock-waves and film cooled profiles needs to be investigated in more

detail so that the effects of variation in shock strengths and film positions can be determined.

REFERENCES

ABU-GHANNAM, B. J. and SHAW, R., 'Natural Transition of Boundary Layers - The Effects of Turbulence, Pressure Gradient, and Flow History', J. Mech. Eng. Sci., Vol. 22, No. 5, pp. 213-228, 1980.

ADACHI, T. and YOSHINORI, M., 'Three-Dimensional Velocity Distribution Between Stator Blades and Unsteady Force on a Blade due to Passing Wakes', JSME, Vol. 22, No. 170, pp. 1074-1082, 1979.

ADAMS, E. W. and JOHNSTON, J. P., 'A Mixing Length Model for the Prediction of Convex Curvature Effects on Turbulent Boundary Layers', ASME J. Eng. for Power, Vol. 106, pp. 143-148, 1984.

ARNAL, D. and JUILLEN, J.-C., 'Etude Experimentale et Theorique de la Transition de la Couche Limite', Rech. Aerosp., No. 2, pp. 75-88, 1977.

ARNAL, D. and JUILLEN, J.-C., 'Etude de l'intermittence dans une Region de Transition de la Couche Limite', Rech. Aerosp., No. 3, pp. 147-166, 1977.

ARNAL, D., JUILLEN, J.-C. and MICHEL, R., 'Analyse Experimentale de la Transition de la Couche Limite avec Gradient de Pression Nul ou Positif', 21st Annual Conference on Aviation and Astronautics, Israel, 1979.

ARNAL, D., HABIBALLAH, M. and COUSTOLS, E., 'Theorie de l'Instabilite Laminaire de Criteres de Transition en Ecoulement bi et Tridimensionnel', Rech. Aerosp., No. 2, pp. 125-143, 1984.

ASHWORTH, D. A., LaGRAFF, J. E., SCHULTZ, D. L. and GRINDROD, K. J., 'Unsteady Aerodynamic and Heat Transfer Processes in a Transonic Turbine Stage', ASME J. Eng. for Power, Vol. 107, pp. 1022-1030, 1985.

ASHWORTH, D. A., LaGRAFF, J. E. and SCHULTZ, D. L., 'Unsteady Interaction Effects on a Transitional Turbine Blade Boundary Layer', Proc. 2nd Joint JSME/ASME Thermal Engineering Conference, Hawaii, March, 1987.

ATRAGHJI, E., 'More Than Meets the Eye: The Oil Dot Technique', Flow Visualisation II, Hemisphere Press, 1980.

BAINES, N. C., 'A Guide to TOPSY', O.U.E.L. Report No. 1462/83, April, 1983.

BAINES, N. C., 'Measurement of Uncertainty in Aerodynamic Cascade Testing', Internal Report, Dept. Mech. Eng., Imperial College, London, 1986.

BARRY, B., FOREST, A. E. and WHITE, A. J., 'Measurements of Heat Transfer Coefficients on Gas Turbine Components - Part I: Description, Analysis and Experimental Verification of a Technique for Use in Hostile Environments', ASME Paper No. 82-GT-174, 1982.

BAYLEY, F. J. and PRIDDY, W. J., 'Effects of Free-Stream Turbulence Intensity and Frequency on Heat Transfer to Turbine Blading', ASME Paper No. 80-GT-79, 1980.

BEACOCK, R. J., HORTON, F. G., KIRKER, T. J. and WHITE, A. J., 'Measurements of Heat Transfer Coefficients on Gas Turbine Components - Part II: Applications of the Technique Described in Part I and Comparisons with Results from a Conventional Measuring Technique and Predictions', ASME Paper No. 82-GT-175, 1982.

BEARMAN, P. W., 'On Vortex Shedding from a Circular Cylinder in the Critical Reynolds Number Regime', J. Fluid Mech., Vol. 37, Part 3, pp. 577-585, 1969.

BINDER, A. and ROMEY, R., 'Secondary Flow Effects and Mixing of the Wake Behind a Turbine Stator', ASME J. Eng. for Power, Vol. 105, pp. 40-46, 1983.

BINDER, A., FOERSTER, W., KRUSE, H. and ROGGE, H., 'An Experimental Investigation into the Effect of Wakes on the Unsteady Turbine Rotor Flow', ASME J. Eng. for Power, 84-GT-178, 1984.

BINDER, A., 'Turbulence Production Due to Secondary Vortex Cutting in a Turbine Rotor', ASME J. Eng. for Power 85-GT-193, 1985.

BINDER, A., FOERSTER, W., MACH, K. and ROGGE, H., 'Unsteady Flow Interaction Caused by Stator Secondary Vortices in a Turbine Rotor', ASME Paper No. 86-GT-302, 1986.

BLAIR, M. F., 'Influence of Free-Stream Turbulence on Boundary Layer Transition in Favorable Pressure Gradients', ASME J. Eng. for Power 82-GT-4, Vol. 104, pp. 743-750, 1982.

BROWN, A. and MARTIN, B. W., 'Heat Transfer to Turbine Blades with Special Reference to the Effects of Mainstream Turbulence', ASME Paper No. 79-GT-26, 1979.

BROWN, A. and MARTIN, B. W., 'Flow Transition Phenomena and Heat Transfer Over the Pressure Surfaces of Gas Turbine Blades', ASME J. Eng. for Power 81-GT-107, Vol. 104, pp. 360-367, 1982.

CAMUS, J. J. and BRYANSTON-CROSS, P. J., '1 MHż Bandwidth, Real-Time Schlieren Techniques in a Linear Transonic Cascade', Proc. Symp. Measuring Techniques in Transonic and Supersonic Cascades and Turbomachines, Lyon, October, 1981.

CAMUS, J. J., DENTON, J. D., SOULIS, J. V. and SCRIVENER, C. T. J., 'An Experimental and Computational Study of Transonic Three-Dimensional Flow in a Turbine Stage', ASME J. Eng. for Power 83-GT-12, Vol. 106, pp. 414-420, 1984.

CANTWELL, B., COLES, D. and DIMOTAKIS, P., 'Structure and Entrainment in the Plane of Symmetry of a Turbulent Spot', J. Fluid Mech., Vol. 87, No. 4, pp. 641-672, 1978.

CHAMBERS, F. W. and THOMAS, A. S. W., 'Turbulent Spots, Wave Packets and Growth', Phys. Fluids 26(5), pp. 1160-1162, 1983.

CHEN, K. K. and THYSON, N. A., 'Extension of Emmons' Spot Theory to Flows on Blunt Bodies', AIAA Journal, Vol. 9, No. 5, pp. 821-825, 1971.

CONSIGNY, H., RICHARDS, B. E. and VILLE, J. P., 'Short Duration Measurements of Heating to Cooled Gas Turbine Surfaces', ASME Paper No. 78-GT-22, 1978.

CONSIGNY, H. and RICHARDS, B. E., 'Short Duration Measurements of Heat-Transfer Rate to a Gas Turbine Rotor Blade', ASME, J. Eng. for Power, Vol. 104, pp. 542-551, 1982.

CRANE, R. I., LEOUTSAKOS, G. and SABZVARI, J., 'Transition in Pressure-Surface Boundary Layers', ASME J. Turbomachinery, Vol. 109, pp. 296-302, 1987.

DENTON, J. D., 'An Improved Time-Marching Method for Turbomachinery Flow Calculation', ASME J. Eng. for Power, Vol. 105, pp. 514-520, 1983.

DOORLY, D. J., 'A Study of the Effect of Wake Passing on Turbine Blades', D.Phil. Thesis, University of Oxford, 1983.

DOORLY, D. J. and OLDFIELD, M. L. G., 'Simulation of the Effects of Shock Wave Passing on a Turbine Rotor Blade', ASME Paper No. 85-GT-112, J. Eng. for Gas Turbines and Power, Vol. 107, pp. 998-1006, 1985a.

DOORLY, D. J. and OLDFIELD, M. L. G., 'Simulation of Wake Passing in a Stationary Turbine Rotor Cascade', J. Prop. and Power, Vol. 1, No. 4, pp. 316-318, 1985b.

DOORLY, D. J., OLDFIELD, M. L. G. and SCRIVENER, C. T. J., 'Wake-Passing in a Turbine Rotor Cascade', AGARD Symposium on Heat Transfer and Cooling in Gas Turbines, 1985.

DRING, R. P., JOSLYN, H. D., HARDIN, L. W. and WAGNER, J. H., 'Turbine Rotor-Stator Interaction', ASME J. Eng. for Power, Vol. 104, pp. 729-742, 1982.

DUNHAM, J., 'Predictions of Boundary Layer Transition on Turbomachinery Blades', AGARD-AG-164, pp. 55-71, 1972.

DUNN, M. G., 'Turbine Heat Flux Measurements: Influence of Slot Injection on Vane Trailing Edge Heat Transfer and Influence of Rotor on Vane Heat Transfer', ASME J. Eng. for Gas Turbines and Power, Vol. 107, No. 1, pp. 76-83, 1984.

DUNN, M. G., 'Heat-Flux Measurements for the Rotor of a Full-Stage Turbine: Part 1 - Time-Averaged Results', ASME Paper No. 86-GT-77, 1986.

DUNN, M. G., GEORGE, W. K., RAE, W. J., WOODWARD, S. H., MOLLER, J. C. and SEYMOUR, P. J., 'Heat-Flux Measurements for the Rotor of a Full-Stage Turbine: Part 2 - Description of Analysis Technique and Typical Time-Resolved Measurements', ASME Paper No. 86-GT-78, 1986.

EMMONS, H. W., 'The Laminar-Turbulent Transition in a Boundary Layer - Part I', J. Aero. Sci., Vol. 18, No. 7, July, 1951.

EPSTEIN, A. H., GUENETTE, G. R. and NORTON, R. J. G., 'The MIT Blowdown Turbine Facility', ASME Paper No. 84-GT-116, 1984.

EVANS, R. L., 'Turbulence and Unsteadiness Measurements Downstream of a Moving Blade Row', ASME J. Eng. for Power, Vol. 97, No. 1, pp. 131-139, 1975.

FOREST, A. E., 'Engineering Predictions of Transitional Boundary Layers', AGARD CP No. 224 on Laminar-Turbulent Transition, Paper No. 22, Amsterdam, 1977.

FRASER, C. J. and MILNE, J. S., 'Integral Calculations of Transitional Boundary Layers', Proc. Inst. Mech. Eng., Vol. 200, No. C3, pp. 179-187, 1986.

GAD-EL-HAK, M., BLACKWELDER, R. F. and RILEY, J. J., 'On the Growth of Turbulent Regions in Laminar Boundary Layers', J. Fluid Mech., Vol. 110, pp. 73-95, 1981.

GAD-EL-HAK, M., BLACKWELDER, R. F. and RILEY, J. J., 'Visualisation Techniques for Studying Transitional and Turbulent Flows', Flow Visualisation II, Ed. W. Merzkirch, Hemisphere Press, ISBN No. 0-89116-2342-1, 1982.

GALLUS, H. E., BROICHHAUSEN, K.-D. and HENNE, J. M., 'Experimental Unsteady Shock-Boundary Layer Interaction at Single Blades and in Linear Cascades', ASME Paper No. 86-GT-218, 1986.

GAUGLER, R. E. and RUSSELL, L. M., 'Flow Visualisation Study of the Horseshoe Vortex in a Turbine Stator Cascade', NASA TP 1884, 1982.

GAUGLER, R. E. and RUSSELL, L. M., 'Comparison of Visualised Turbine Endwall Secondary Flows and Measured Heat Transfer Patterns', ASME J. Eng. for Gas Turbines and Power, Vol. 106, pp. 168-172, 1984. (Also NASA RM 830160.)

GILES, M. B., 'Calculation of Unsteady Wake/Rotor Interactions', AIAA-87-0006, 1987.

GEORGE, W. K., RAE, W. J., SEYMOUR, P. J. and SONNENMEIER, J. R., 'An Evaluation of Analog and Numerical Techniques for Unsteady Heat Transfer Measurement with Thin Film Gauges in Transient Facilities', Proc. 2nd Joint JSME/ASME Thermal Engineering Conference, Hawaii, March, 1987.

GOERTLER, H., 'On the Three-Dimensional Instability of Laminar Boundary Layers on Concave Walls', NACA T.M. No. 1375, 1954.

GOSTELOW, J. P., private communication, 1987.

GRAHAM, R. W., 'Fundamental Mechanisims that Influence the Estimate of Heat Transfer Rate to Gas Turbine Blades', NASA T. M. 79128, 1979.

GREGORY-SMITH, D. G. and GRAVES, C. P., 'Secondary Flows and Losses in a Turbine Cascade', AGARD CP-351, 1983.

GUEST, P. G., 'Numerical Methods of Curve Fitting', Cambridge University Press, 1961.

HALLER, B. R., 'The Effects of Film Cooling on the Aerodynamic Performance of Transonic Turbine Blades', Ph.D. Thesis, University of Cambridge, September, 1980.

HALLER, B. R. and CAMUS, J. J., 'Aerodynamic Loss Penalty Produced by Film Cooling Transonic Turbine Blades', ASME J. Eng. for Power 83-GT-77, 1983.

HAN, L. S. and COX, W. R., 'A Visual Study of Turbine Blade Pressure-Side Boundary Layers', ASME J. Eng. for Power, Vol. 105, pp. 47-52, 1983.

HART, M., Ph.D. Thesis, Cambridge University, 1978.

HAYASHI, M., SAKURAI, A. and ASO, S., 'Measurement of Heat Transfer Coefficients in Shock Wave-Turbulent Boundary Layer Interaction Regions with a Multi-Layered Thin Film Heat Transfer Gauge', Kyushu University Technology Reports, Vol. 57, pp. 455-462, 1984.

HODSON, H. P., 'Boundary Layer and Loss Measurements on the Rotor of an Axial-Flow Turbine', ASME J. Eng. for Power 83-GT-4, 1983.

HODSON, H. P., 'An Inviscid Blade-to-Blade Prediction of a Wake-Generated Unsteady Flow', ASME J. Eng. for Power 84-GT-43, 1984a.

HODSON, H. P., 'Boundary-Layer Transition and Separation near the Leading Edge of a High-Speed Turbine Blade', ASME J. Eng. for Power 84-GT-179, 1984b.

HODSON, H. P., 'Measurements of Wake-Generated Unsteadiness in the Rotor Passages of Axial Flow Turbines', ASME J. Eng. for Power 84-GT-189, 1984c.

HOLDER, D. W. and NORTH, R. J., 'The 9 x 3 Induced Flow High-Speed Wind Tunnel at the National Physical Laboratory', ARC R & M No. 2781, June, 1949.

HORTON, F. G., 'Aerodynamics and Heat Transfer of Turbine Blading', D.Phil. Thesis, University of Oxford, 1985.

HORTON, F. G., SCHULTZ, D. L. and FOREST, A. E., 'Heat Transfer Measurements with Film Cooling on a Turbine Blade Profile in Cascade', ASME Paper No. 85-GT-117, 1985.

JAMES, C. S., 'Observations of Turbulent-Burst Geometry and Growth in Supersonic Flow', NACA T. N. 4235, 1958.

JOHNSON, A. B., RIGBY, M. J., OLDFIELD, M. L. G., AINSWORTH, R. W. and OLIVER, M. J., 'Surface Heat Transfer Fluctuations on a Turbine Rotor Blade Due to Upstream Shock Wave Passing', paper to be presented ASME, 1988.

JONES, T. V., SCHULTZ, D. L. and HENDLEY, A. D., 'On the Flow in an Isentropic Light Piston Tunnel', ARC R & M No. 3731, January, 1973.

JONES, T. V., SCHULTZ, D. L., OLDFIELD, M. L. G. and DANIELS, L. C., 'A New Transient Facility for the Measurement of Heat Transfer Rates', AGARD CP-229, High Temperature Problems in Gas Turbine Engines, Paper No. 39, Ankara, 1979.

JOSLYN, H. D., DRING, R. P. and SHARMA, O. P., 'Unsteady Three-Dimensional Turbine Aerodynamics', ASME Paper No. 82-GT-161, 1982.

JOSLYN, H. D., CASPAR, J. R. and DRING, R. P., 'Inviscid Modeling of Turbomachinery Wake Transport', AIAA Paper No. AIAA-85-1132 presented at the AIAA/SAE/ASME/ASEE 21st Joint Propulsion Conference, 1985.

KAYS, W. M. and CRAWFORD, M. E., 'Convective Heat and Mass Transfer', 2nd Edition, McGraw-Hill, 1980.

KEMP, N. H. and SEARS, W. R., 'Aerodynamic Interference between Moving Blade Rows', J. Aero. Sci., Vol. 20, No. 9, pp. 585-597, 1953.

KING, P. I., 'Aerodynamics of High Performance Turbine Blading', D.Phil. Thesis, University of Oxford, 1986.

KIOCK, R., 'Turbulence Downstream of Stationary and Rotating Cascades', ASME Paper No. 73-GT-80, 1973.

KLEBANOFF, P. S., TIDSTROM, K. D. and SARGENT, L. M., 'The Three-Dimensional Nature of Boundary Layer Instability', J. Fluid Mech., Vol. 12, 1962.

KLEISER, L. and SCHUMANN, U., 'Spectral Simulations of the Laminar-Turbulent Transition Process in Plane Poiseuille Flow', Special Methods for Partial Differential Equations, Ed. R. G. Voigt et al., Society for Industrial and Applied Mathematics, pp. 141-163, 1984.

KLEISER, L., 'Three-Dimensional Processes in Laminar-Turbulent Transition', Non-Linear Dynamics of Transcritical Flows, Springer-Verlag, pp.123-154, 1985.

KLINE, S. J., REYNOLDS, W. C., SCHRAUB, F. A. and RUNSTADLER, P. W., 'The Structure of Turbulent Boundary Layers', J. Fluid Mech., Vol. 30, Part 4, pp. 741-773, 1967.

KOOL, P. and HIRSCH, Ch., 'A Prediction Scheme for the Decay of a Turbomachine Blade Wake', ASME Paper No. 82-GT-273, 1982.

LAKSHMINARAYANA, B. and DAVINO, R., 'Mean Velocity and Decay Characteristics of the Guidevane and Stator Blade Wake of an Axial Flow Compressor', ASME J. Eng. for Power 79-GT-9, 1979.

LEFCORT, M. D., 'An Investigation into Unsteady Blade Forces in Turbomachines', ASME J. Eng. for Power, pp. 345-354, 1965.

LEONARD, A., 'Turbulent Structures in Wall-Bonded Shear Flows Observed via Three-Dimensional Numerical Simulations', IUTAM Conference on Transitional Flows, Madrid, 1981.

LINDBERG. P.-A., FAHLGREN, E. M., ALFREDSSON, P. H. and JOHANSSON, A. V., 'An Experimental Study of the Structure and Spreading of Turbulent Spots', 2nd IUTAM Symposium on Laminar-Turbulent Transition, Novisibirsk, pp. 617-624, 1984.

LOWERY, G. W. and VACHON, R. I., 'The Effect of Turbulence on Heat Transfer from Heated Cylinders', Int. J. Heat and Mass Transfer, Vol. 18, pp. 1229-1242, 1975.

MARTELLI, F. and BORETTI, A., 'A Simple Procedure to Compute Losses in Transonic Turbine Cascades', ASME Paper No. 85-GT-21, 1985.

MARTIN, B. W. and BROWN, A., 'Factors Influencing Heat Transfer to the Pressure Surfaces of Gas Turbine Blades', Int. J. Heat and Fluid Flow, Vol. 1, No. 3, pp. 107-114, 1979.

MARZIALE, M. L. and MAYLE, R. E., 'Effect of an Oscillating Flow Direction on Leading Edge Heat Transfer', ASME J. Eng. for Power, Vol. 106, pp. 222-228, 1984.

MAULARD, J., 'Surface Temperature Thermal Fluxmeters for Shock Tubes', Rech. Aerosp., No. 126, 1968.

McCORMACK, P. D., WELKER, H. and KELLEHER, M., 'Taylor-Goertler Vortices and Their Effect on Heat Transfer', ASME J. Heat Transfer, Vol. 92, pp. 101-112, 1970.

McCORMICK, M. E., 'An Analysis of the Formation of Turbulent Patches in the Transition Boundary Layer', J. Appl. Mech., pp. 216-219, June, 1968.

McDONALD, H. and FISH, R. W., 'Practical Calculations of Transitional Boundary Layers', AGARD-AG-164, pp. 29-54, 1972

MEYER, R. F., 'A Heat Flux Meter for Use with Thin Film Surface Thermometers', N.R.C. Canada Aero Report LR-279, 1960.

MEYER, R. X., 'The Effects of Wakes on the Transient Pressure and Velocity Distributions in Turbomachines', ASME Paper No. A-83, August, 1957.

MICHEL, R., ARNAL, D. and COUSTOLS, E., 'Stability Calculations and Transition Criteria on Two- or Three-Dimensional Flows', 2nd IUTAM Symposium on Laminar-Turbulent Transition, Novisibirsk, pp. 553-562, 1984.

NARASIMHA, R., 'On the Distribution of Intermittency in the Transition Region of a Boundary Layer', J. Aero. Sci., Vol. 24, pp. 711-712, 1957.

NARASIMHA, R., 'Some Properties of Boundary Layer Flow During the Transition from Laminar to Turbulent Motion', J. Fluid Mech., Vol. 3, 1958.

NARASIMHA, R., 'A Note on Certain Turbulent Spot and Burst Frequencies', Indian Inst. of Science, Dept. of Aeronautical Eng., Paper No. 78-FM-10, 1978.

NARASIMHA, R., 'Subtransitions in the Transition Zone', 2nd IUTAM Symposium on Laminar-Turbulent Transition, Novisibirsk, pp. 141-152, 1984.

NARASIMHA, R., 'The Laminar-Turbulent Transition Zone in the Boundary Layer', Prog. Aerospace Sci., Vol. 22, pp. 29-80, 1985.

NICHOLSON, J. H., 'Experimental and Theoretical Studies of the Aerodynamic and Thermal Performance of Modern Gas Turbine Blades', D.Phil. Thesis, University of Oxford, O.U.E.L. Report No. 1362/81, 1981.

NICHOLSON, J. H., FOREST, A. E., OLDFIELD, M. L. G. and SCHULTZ, D. L., 'Heat Transfer Optimised Turbine Rotor Blades - An Experimental Study Using Transient Techniques', ASME J. Eng. for Power, Vol. 106, pp. 173-182, 1984.

O'BRIEN, J. E., SIMONEAU, R. J., LaGRAFF, J. E. and MOREHOUSE, K., 'Unsteady Heat Transfer and Direct Comparison to Steady-State Measurements in a Rotor Wake Experiment', Proc. 8th Int. Heat Transfer Conference, San Fransisco, Paper No. JW-16, Hemisphere Publ. Corp., N.Y., 1986.

OLDFIELD, M. L. G., JONES, T. V. and SCHULTZ, D. L., 'On-line Computer for Transient Turbine Cascade Instrumentation', IEEE Trans. Aero. Elect. Sys., Vol. AES-14 No. 5, pp. 738-748, 1978.

OLDFIELD, M. L. G., BURD, H. J. and DOE, N. G., 'Design of Wide-Bandwidth Analogue Circuits for Heat Transfer Instrumentation in Transient Tunnels', Proc. 16th ICHMT Symposium on Heat and Mass Transfer in Rotating Machinery, Dubrovnik, Hemisphere Publ. Corp., N.Y., pp. 233-258, 1984.

OWEN, F. K., 'Transition Experiments on a Flat Plate at Subsonic and Supersonic Speeds', AIAA Journal, Vol. 8, No. 3, pp. 518-523, 1970.

PAL, S. and RAJ, R., 'Wake Behaviour in the Presence of Free Stream Turbulence', ASME J. Eng. for Power, Vol. 103, pp. 490-498, 1981.

PARK, W. C. and SIMON, T., 'A Test of the MLH Models for Prediction of Convex-Curved Transitional Boundary Layer Heat Transfer Behaviour', Proc. 2nd Joint JSME/ASME Thermal Engineering Conference, Hawaii, March, 1987.

PARKER, R. and WATSON, J. F, 'Interaction Effects between Blade Rows in Turbomachines', Proc. I.Mech.E., Vol. 186, No. 21, 1972.

PETRIE, A. M. and SIMPSON, H. C., 'An Experimental Study of the Sensitivity to Freestream Turbulence of Heat Transfer in Wakes of Cylinders in Crossflow', Int. J. Heat and Mass Transfer, Vol. 15, pp. 1497-1513, 1972.

PFEIL, H. and HERBST, R., 'Transition Procedure of Instationary Boundary Layers', ASME Paper No.79-GT-128, 1979.

PFEIL, H., HERBST, R. and SCHROEDER, T., 'Investigation of the Laminar-Turbulent Transition of Boundary Layers Disturbed by Wakes', ASME J. Eng. for Power, Vol. 105, pp. 130-137, 1983.

PRIDDY, W.J. and BAYLEY, F. J., 'Effects of Freestream Turbulence on the Distribution of Heat Transfer Around Turbine Blade Sections', Int. J. Heat and Fluid Flow, Vol. 6, No. 3, 1985.

RAJ, R. and LAKSHMINARAYANA, B., 'Characteristics of the Wake Behind a Cascade of Airfoils', J. Fluid Mech., Vol. 1, Part 4, pp. 707-730, 1973.

RAVINDRANATH, A. and LAKSHMINARAYANA, B., 'Mean Velocity and Decay Characteristics of the Near- and Far-Wake of a Compressor Rotor Blade of Moderate Loading', ASME Paper No. 79-GT-202, 1979.

ROACH, P. E., 'The Generation of Nearly Isotropic Turbulence by Means of Grids', Heat and Fluid Flow, Vol. 8, No. 2, 1987.

ROLLS-ROYCE INC., 'ROLLS-ROYCE LIMITED - TURBINE COOLING RESEARCH', Report submitted by Rolls-Royce Inc., Atlanta ATLR 0254, December, 1983.

RUED, K. and WITTIG, S., 'Free-Stream Turbulence and Pressure Gradient Effects on Heat Transfer and Boundary Layer Development on Highly Cooled Surfaces', ASME J. Eng. for Gas Turbines and Power, Vol. 107, pp. 54-59, 1984.

RUED, K. and WITTIG, S., 'Laminar and Transitional Boundary Layer Structures in Accelerating Flow with Heat Transfer', ASME Paper No. 86-GT-97, 1986.

RUFFLES, P. C., 'Reducing the Cost of Aero Engine Research and Development', Rolls-Royce Report, 1986.

SCHLICHTING, H., 'Boundary Layer Theory', McGraw-Hill, 7th Edition., 1979.

SCHUBAUER, G. B. and KLEBANOFF, P. S., 'Contributions on the Mechanics of Boundary Layer Transition', NPL Proc. Symp. Boundary Layer Effects in Aerodynamics, 1955.

SCHULTZ, D. L. and JONES, T. V., 'Heat Transfer Measurements in Short Duration Hypersonic Facilities', AGARDOGRAPH NO. 165, 1973.

SCHULTZ, D. L., JONES, T. V., OLDFIELD, M. L. G. and DANIELS, L. C., 'A New Transient Facility for the Measurement of Heat Transfer Rates', AGARD Symposium on High Temperature Problems in Gas Turbines, 1977.

SCHULTZ, D. L., ASHWORTH, D. A., LaGRAFF, J. E., JOHNSON, A. B. and RIGBY, M. J., 'Wake and Shock Interactions on a Transonic Turbine Stage', AGARD PEP 68th(B) Specialists' Meeting on Transonic and Supersonic Phenomena in Turbomachines, Neubiberg, 1986.

SEYB, N. J., 'The Role of Boundary Layers in Axial Flow Turbomachines and the Prediction of Their Effects', AGARD-AG-165, 1972.

SHAPIRO, A. S., 'The Dynamics and Thermodynamics of Compressible Fluid Flow', Ronald Press, Vol. 2, pp. 884-886, 1954.

SHARMA, O. P. and GRAZIANI, R. A., 'Influence of Endwall Flow on Airfoil Suction Surface Midheight Boundary Layer Development in a Turbine Cascade', ASME J. Eng. for Power, Vol. 105, pp. 147-155, 1983.

SILVERSTEIN, A., KATZOFF, S. and BULLIVANT, W.K., 'Downwash and Wake Behind Plain and Flapped Airfoils', NACA Report No. 651, 1939.

SIMONEAU, R. J., MOREHOUSE, K. A. and VAN FOSSEN, G. J., 'Effect of a Rotor Wake on Heat Transfer from a Circular Cylinder', ASME J. Heat Transfer 84-HT-25, 1984.

SMITH, A. M. O., 'On the Growth of Taylor-Goertler Vortices Along Highly Concave Walls', Quart. Applied Maths., Vol 13., No. 3, 1955.

SMITH, L. H., 'Wake Dispersion in Turbomachines', ASME J. Basic Eng., pp. 688-690, 1966.

SPALDING, D. B. and PATANKAR, S. V., 'Heat and Mass Transfer in Boundary Layers', 2nd Edition, Intertext Books, London, 1970.

SYKES, D. M., 'The Supersonic and Low-Speed Flows Past Circular Cylinders of Finite Length Supported at One End', J. Fluid Mech. Vol. 12, pp. 367-387, 1962.

TAYLOR, G. I., 'Stability of a Viscous Liquid Contained Between Two Rotating Cylinders', Phil. Trans. Roy. Soc., Vol. 223, 1923.

VAN ATTA, C. W. and MAUTNER, T. S., 'The Wall Shear Stress Signature of a Turbulent Spot: Direct Measurements and Momentum Integral Calculations', 2nd IUTAM Symposium on Laminar-Turbulent Transition, Novisibirsk, pp. 607-616, 1984.

VAN DYKE, M., 'An Album of Fluid Flow', 1982.

WALKER, G. J., 'Transitional Flow on Axial Turbomachine Blading', AIAA 25th Aerospace Sciences Meeting, AIAA-87-0010, 1987.

WEST, G. S. and HAN, L. S., 'Flow Transition in Gas Turbine Airfoil Boundary Layers: Fundamentals and Empiricisms', AFWAL-TR-85-2055, 1985.

WHITFIELD, C. E., KELLY, J. C. and BARRY, B., 'A Three-Dimensional Analysis of Rotor Wakes', Aero. Q., Vol. 23, pp. 285-299, 1972.

WITTIG, S., DULLENKOPF, K., SCHILZ, A. and HESTERMANN, R., 'Laser-Doppler Studies of the Wake-Effected Flow Field in a Turbine Cascade', ASME Paper No. 86-GT-160, 1986.

WYGNANSKI, I., SOKOLOV, M. and FRIEDMAN, D., 'On a Turbulent 'Spot' in a Laminar Boundary Layer', J. Fluid Mech., Vol. 78, No. 4., pp. 785-819, 1976.

WYGNANSKI, I., HARITONIDIS, J. H. and KAPLAN, R. E., 'On a Tollmien-Schlichting Wave Produced by a Turbulent Spot', J. Fluid Mech., Vol. 92, pp. 505-528, 1979.

WYGNANSKI, I., 'The Effects of Reynolds Number and Pressure Gradient on the Transitional Spot in a Laminar Boundary Layer', IUTAM Conference on Transitional Flows, Madrid, 1981.

YORK, R. E., HYLTON, L. D. and MIHELC, M. S., 'An Experimental Investigation of Endwall Heat Transfer and Aerodynamics in a Linear Vane Cascade', ASME, J. Eng. for Gas Turbines and Power, Vol. 106, pp. 159-167, 1984.

ZHOU, Ming De and SQUIRE, L. C., 'The Interaction of a Wake with a Turbulent Boundary Layer', Aeronautical Journal, 1985.

COMPARISON OF THE ACE AND B22 TESTS IN THE ILPT

		ACE	B22
Cascade Details			
Pitch	(mm)	34.30	56.70
Number of Blades in Cascade		5	4
Aspect Ratio, (Span/Axial Chord)		1.44	0.96
Aspect Ratio, (Span/True Chord)		1.21	0.74
Inlet Span	(mm)	50.00	50.00
Hade Angle	(°)	10.00	0.00
Turbulence Grid:			
Bar Diameter (15 mm Pitch)	(mm)	2.00	2.00
Distance Upstream of Cascade	(mm)	208.00	394.00
Profile Details			
Scale Factor on Proconsel File		1.32	1.32
Axial Chord	(mm)	34.82	51.92
True (or Tangential) Chord	(mm)	41.18	67.48
Stagger Angle	(°)	30.79	39.27
Turning Angle	(°)	124.73	111.50
Inlet Plane:			
Inlet Angle	(°)	58.06	42.75
Leading Edge Circle Radius	(mm)	1.79	1.82
Inlet Wedge Angle	(°)	62.32	29.91
Exit Plane:			
Outlet Angle	(°)	-66.67	-68.75
Trailing Edge Circle Radius	(mm)	0.48	0.69
Outlet Wedge Angle	(°)	8.27	5.04
Wake-Generation Details			
Bar Diameter	(mm)	1.50	0.93
Distance Upstream of Cascade	(mm)	14.33	24.00
Design Relative Bar Mach Number (at Mid-Span Radius of 0.149 mm)		1.17	0.90
Design Number of Bars		16	8
Bar-Passing Frequency	(kHz)	5.00	2.50
Design Test Conditions			
Inlet Mach Number		0.58	0.32
Exit Mach Number		1.18	0.96
Exit Reynolds Number	($\times 10^6$)	0.95	2.02

Table 1 : Comparison of the ACE and B22 Tests in the ILPT. The ACE Tests form the Major Part of the Thesis. The B22 Profile is used for some film cooling studies (as referred to in Chapter VIII) and was the Profile Used in the First Series of Wake-Passing Tests (DOORLY[1983]).

TOPSY VERSION 1.0 PROCESSED RESULTS 05-OCT-86 18:55:15 PREFIX : C RUN 4540

PBAR kPa	(+/-)	psia	P0 kPa	(+/-)	psia	TBAR K	(degC)	T0 K	(degC)	TAMB K	(degC)	TBLD K	(degC)	TDRIVE	TRATIO
279.45	0.80	40.53	262.61	1.15	38.09	467.9	194.9	467.9	194.9	298.5	25.5	298.5	25.5	169.5	1.568

	P(kPa)	P(psia)	P/P0	(+/-)	Mach No.	(+/-)	Re	(+/-)
Exit	97.44	14.13	0.3711	0.0054	1.280	0.011	9.1267E+05	1.1190E+04

CH	MP	Xposn	Qmeas kW/m2	Tmeas degK	Q0m kW/m2	HTCm kW/m2K	Num	Numi	Q0x kW/m2	HTCx kW/m2K	Nux	Nuxi	comment
9	9	0.960	158.41	336.74	204.64	1.208	1327.8	1327.8	184.01	1.086	1194.0	1194.0	PS TFG 9
8	8	0.840	150.17	335.66	192.40	1.135	1248.4	1248.4	214.70	1.267	1393.1	1393.1	PS TFG 8
7	7	0.710	140.77	333.22	177.10	1.045	1149.2	1149.2	193.20	1.140	1253.6	1253.6	PS TFG 7
6	6	0.590	133.78	331.32	165.97	0.979	1076.9	1076.9	140.24	0.828	910.0	910.0	PS TFG 6
5	5	0.480	132.67	331.16	164.38	0.970	1066.6	1066.6	170.12	1.004	1103.9	1103.9	PS TFG 5
4	4	0.360	131.08	330.77	161.95	0.956	1050.9	1050.9	181.16	1.069	1175.5	1175.5	PS TFG 4
3	3	0.240	128.58	330.52	158.59	0.936	1029.0	1029.0	170.14	1.004	1104.0	1104.0	PS TFG 3
2	2	0.120	132.32	330.95	163.71	0.966	1062.3	1062.3	158.96	0.938	1031.5	1031.5	PS TFG 2
1	1	0.000	291.44	370.65	507.71	2.996	3294.4	3294.4	445.49	2.629	2890.7	2890.7	PS TFG 1
10	10	-0.080	149.51	334.73	190.22	1.122	1234.3	1234.3	199.95	1.180	1297.4	1297.4	SS TFG 10
11	11	-0.180	103.67	323.25	121.43	0.717	787.9	787.9	135.79	0.801	881.1	881.1	SS TFG 11
12	12	-0.240	98.22	323.08	114.92	0.678	745.7	745.7	145.56	0.859	944.5	944.5	SS TFG 12
13	13	-0.310	110.13	326.35	131.83	0.778	855.4	855.4	168.13	0.992	1090.9	1090.9	SS TFG 13
14	14	-0.380	120.99	328.94	147.52	0.871	957.2	957.2	184.20	1.087	1195.2	1195.2	SS TFG 14
16	16	-0.530	128.94	331.21	159.84	0.943	1037.1	1037.1	209.81	1.238	1361.4	1361.4	SS TFG 16
17	17	-0.610	120.51	328.23	146.19	0.863	948.6	948.6	191.03	1.127	1239.5	1239.5	SS TFG 17
18	18	-0.680	101.91	323.65	119.70	0.706	776.7	776.7	127.97	0.755	830.4	830.4	SS FTG 18
19	19	-0.760	99.39	320.36	114.14	0.674	740.6	740.6	47.57	0.281	308.7	308.7	SS TFG 19
20	20	-0.830	122.42	326.74	146.95	0.867	953.5	953.5	149.32	0.881	968.9	968.9	SS TFG 20
21	21	-0.900	123.46	326.40	147.84	0.872	959.3	959.3	176.56	1.042	1145.6	1145.6	SS TFG 21

Table 2 Typical Processed Data Listing for One Heat Transfer Build Run of the ILPT. Conditions are for the Design Case ($i = 0°$, $M_2 = 1.28$, $Re_2 = 0.91E6$, $T_g/T_w = 1.568$).

TOPSY VERSION 1.0 PROCESSED RESULTS 05-OCT-86 18:56:53 PREFIX : C RUN 4650

PBAR kPa	(+/-)	psia	P0 kPa	(+/-)	psia	TBAR K	(degC)	T0 K	(degC)	TAMB K	(degC)	TBLD K	(degC)	TDRIVE	TRATIO
153.16	0.41	22.22	147.22	0.90	21.35	297.0	24.0	297.0	24.0	288.3	15.3	288.3	15.3	8.8	1.030

	P(kPa)	P(psia)	P/P0	(+/-)	Mach No.	(+/-)	Re	(+/-)
Exit	62.98	9.13	0.4278	0.0073	1.172	0.013	9.1659E+05	1.2424E+04

CH	MP	Xposn	P(kPa)	P(psia)	P/P0	(+/-)	Mach No.	(+/-)	Re	(+/-)	comment
20	21	0.870	108.49	15.74	0.7369	0.0041	0.675	0.006	7.4285E+05	9.9237E+03	P/S PT. 21
21	23	0.700	123.94	17.98	0.8419	0.0032	0.502	0.006	6.0098E+05	8.0902E+03	P/S PT. 23
22	25	0.510	134.98	19.58	0.9169	0.0028	0.354	0.006	4.4784E+05	6.2989E+03	P/S PT. 25
23	26	0.410	137.95	20.01	0.9371	0.0027	0.306	0.007	3.9232E+05	5.7406E+03	P/S PT. 26
24	27	0.330	139.73	20.27	0.9491	0.0027	0.274	0.008	3.5422E+05	5.4779E+03	P/S PT. 27
25	28	0.230	140.56	20.39	0.9548	0.0028	0.258	0.008	3.3458E+05	5.4685E+03	P/S PT. 28
26	29	0.140	140.98	20.45	0.9576	0.0026	0.249	0.008	3.2415E+05	5.2291E+03	P/S PT. 29
27	30	0.070	141.39	20.51	0.9604	0.0026	0.241	0.008	3.1366E+05	5.2127E+03	P/S PT. 30
1	1	0.000	146.02	21.18	0.9918	0.0029	0.108	0.020	1.4382E+05	8.2310E+03	S/S PT. 1
2	2	0.030	110.54	16.03	0.7509	0.0040	0.653	0.006	7.2724E+05	9.7170E+03	S/S PT. 2
3	3	0.080	96.24	13.96	0.6537	0.0048	0.804	0.007	8.1985E+05	1.0956E+04	S/S PT. 3
4	4	0.130	86.03	12.48	0.5844	0.0053	0.911	0.008	8.6594E+05	1.1588E+04	S/S PT. 4
5	5	0.180	77.11	11.18	0.5238	0.0038	1.007	0.006	8.9420E+05	1.1875E+04	S/S PT. 5
6	6	0.240	75.11	10.89	0.5102	0.0039	1.030	0.006	8.9904E+05	1.1946E+04	S/S PT. 6
7	7	0.300	66.35	9.62	0.4507	0.0065	1.131	0.011	9.1378E+05	1.2314E+04	S/S PT. 7
8	8	0.360	67.71	9.82	0.4600	0.0043	1.115	0.007	9.1218E+05	1.2158E+04	S/S PT. 8
9	9	0.410	62.24	9.03	0.4228	0.0046	1.181	0.008	9.1698E+05	1.2255E+04	S/S PT. 9
10	10	0.480	63.78	9.25	0.4332	0.0044	1.162	0.008	9.1607E+05	1.2227E+04	S/S PT. 10
11	11	0.530	57.61	8.36	0.3914	0.0045	1.240	0.009	9.1761E+05	1.2278E+04	S/S PT. 11
12	12	0.590	55.23	8.01	0.3751	0.0048	1.271	0.010	9.1665E+05	1.2289E+04	S/S PT. 12
13	13	0.650	44.87	6.51	0.3048	0.0052	1.422	0.012	9.0140E+05	1.2163E+04	S/S PT. 13
14	14	0.700	49.67	7.20	0.3374	0.0051	1.349	0.011	9.1082E+05	1.2254E+04	S/S PT. 14
15	15	0.760	56.17	8.15	0.3816	0.0046	1.259	0.009	9.1714E+05	1.2282E+04	S/S PT. 15
16	16	0.810	53.41	7.75	0.3628	0.0048	1.296	0.010	9.1531E+05	1.2278E+04	S/S PT. 16
17	17	0.870	51.52	7.47	0.3500	0.0049	1.323	0.010	9.1334E+05	1.2266E+04	S/S PT. 17
18	18	0.930	56.08	8.13	0.3809	0.0075	1.260	0.015	9.1710E+05	1.2462E+04	S/S PT. 18
19	19	1.000	69.90	10.14	0.4748	0.0043	1.089	0.007	9.0909E+05	1.2112E+04	S/S PT. 19

Table 3 Typical Processed Data Listing for One Pressure Build Run of the ILPT. Design Conditions at Negative Incidence ($i = -10°$, $M_2 = 1.172$, $Re_2 = 0.92E5$, $T_g/T_w = 1.03$).

Run	M_2	Re_2/1E6	Tu (%)	Bars	M_b	Speed (rpm)
i = 0°						
4543	1.28	0.92	3	16	1.17	16676.
4544	1.28	0.91	3	16	1.15	16343.
4546	1.28	0.91	3	16	1.18	16962.
4555	1.28	0.96	0.8	16	1.18	16724.
4556	1.28	0.95	0.8	16	1.17	16650.
i = -10°						
5696	1.20	0.91	3	2	0.83	13257.
5698	1.19	0.92	3	2	1.15	22288.
5721	1.19	0.93	0.8	2	1.15	22222.

Table 4 : Summary of Test Conditions for Some Heat Transfer Runs for the ACE Build

DETAILS OF THE THE B22 FILM COOLING TESTS

Configuration	A	B	C
Description	Leading-Edge	Suction Surface	Pressure Surface
x/cax	L/E	25%	75%
x/s	L/E	23%	66%
Hole Diameter (mm)	0.64	0.64	0.37
No. of Holes	22 x 2	21	14
Pitch/diameter	2.90	3.0	4.55
Length/diameter	7.0	7.4	8.0
Angle to Surface (°)	-	40	30
Radial Inclination (°)	30	0	0
Surface Curvature (1/mm)	-	0.083	-0.005
Mach Number (design)	0.15	0.80	0.40
Accln. Par. K (E-6)	-	1.00	2.00

Inlet Mach Number $M_1 = 0.32$, Inlet Angle $\beta_1 = 42.75^{\circ}$.

Outlet Mach Number $M_2 = 0.96$, Outlet Angle $\beta_2 = -68.50^{\circ}$.

Relative Bar Mach Number $M_b = 0.93$.

Table 5 B22 Film Cooling Test Details. Descriptions of the performance of these film rows, and for some other configurations, are given in HORTON[1985].

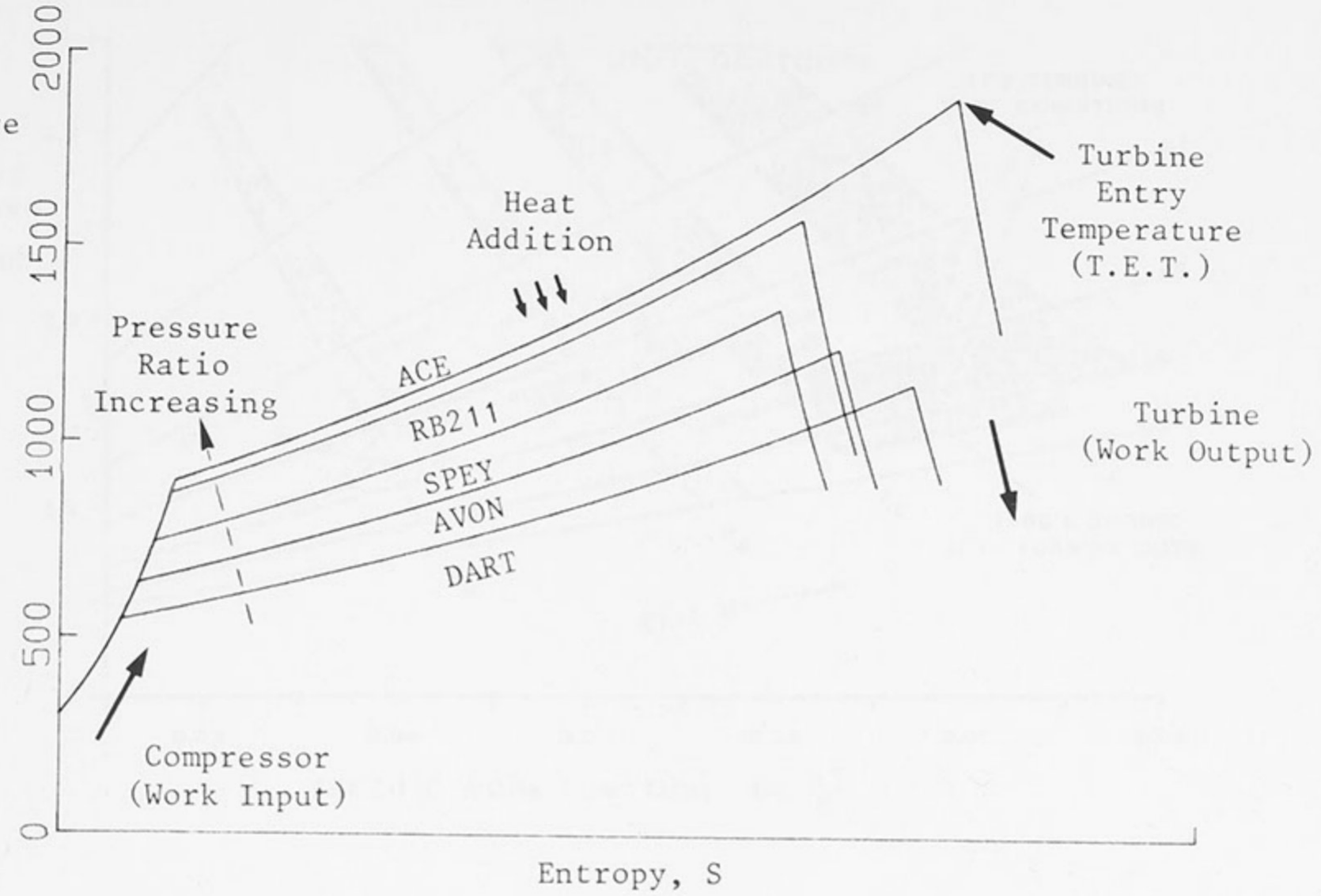

Fig. 1.1(a) Simplified Cycle Diagrams for some Rolls-Royce Engine Designs. Pressure Ratios have Steadily Increased with Time from ∿ 6 for the Dart up to ∿ 30 for the RB211 and the ACE Designs.

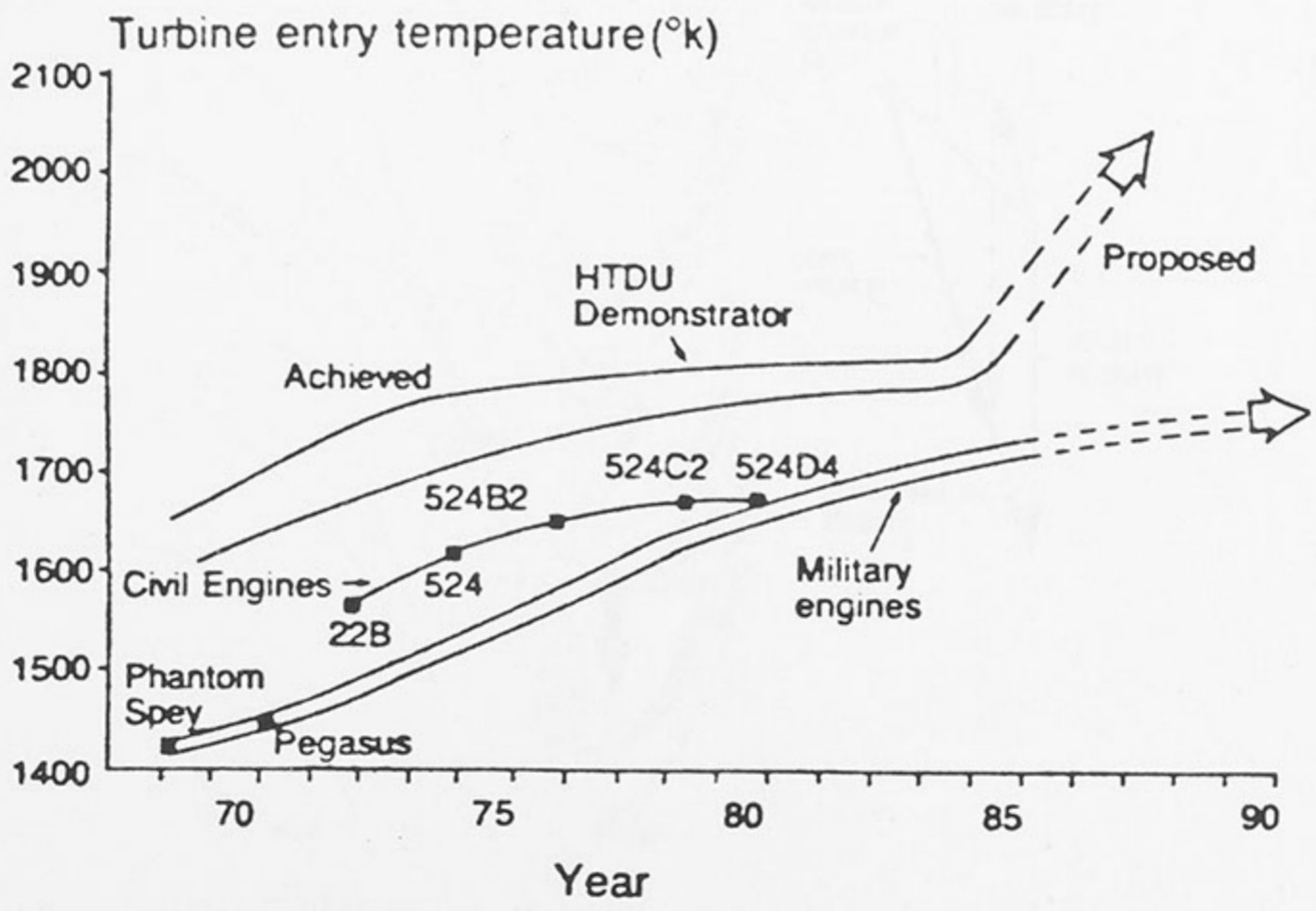

Fig. 1.1(b) Diagram Showing the Increase in Turbine Entry Temperature with Time for Typical Aero-Engines. (Ruffles[1986])

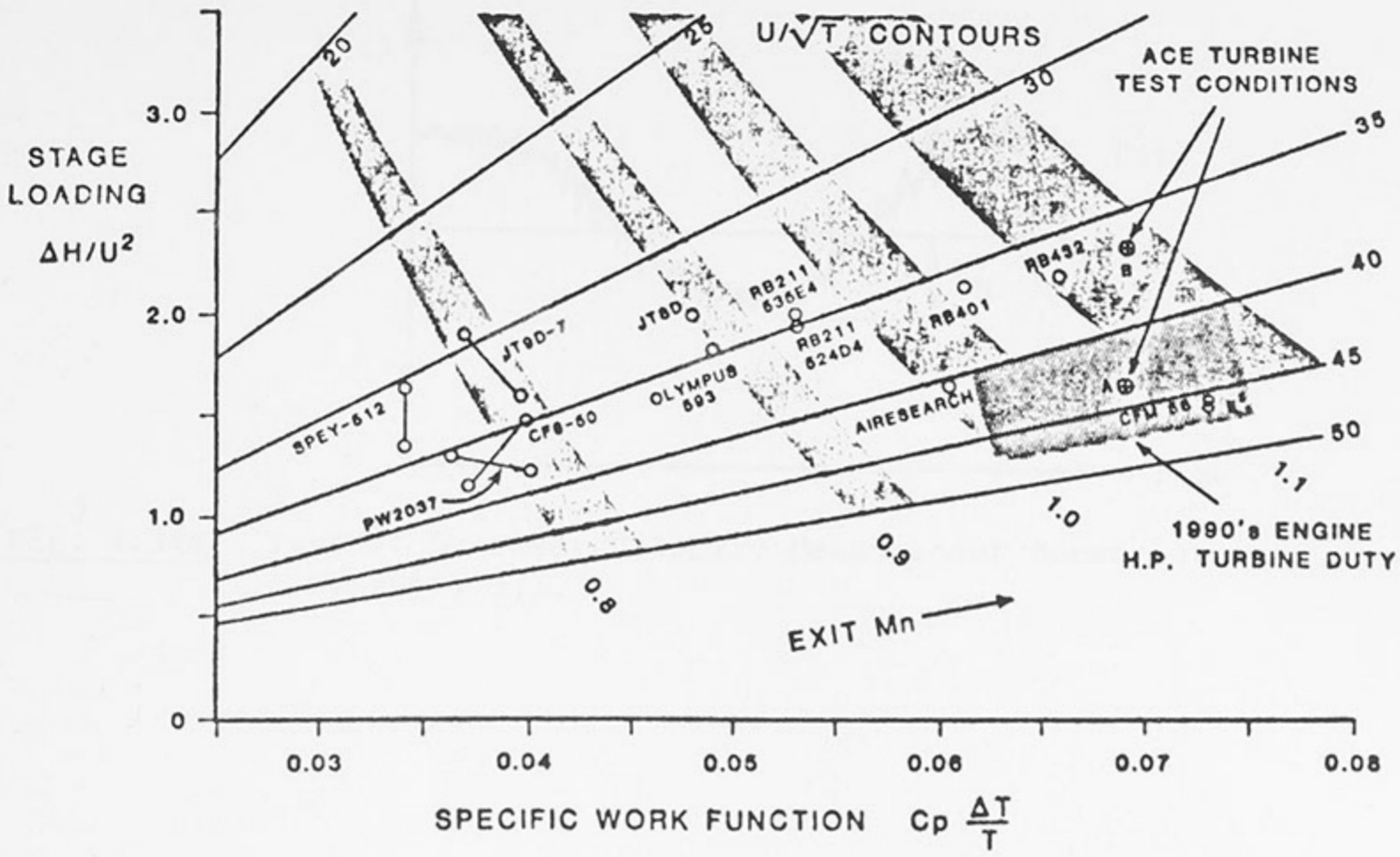

Fig. 1.2(a) A Plot of Stage Loading Against Specific Work Function for Various Turbine Designs. ROLLS-ROYCE INC.[1983].

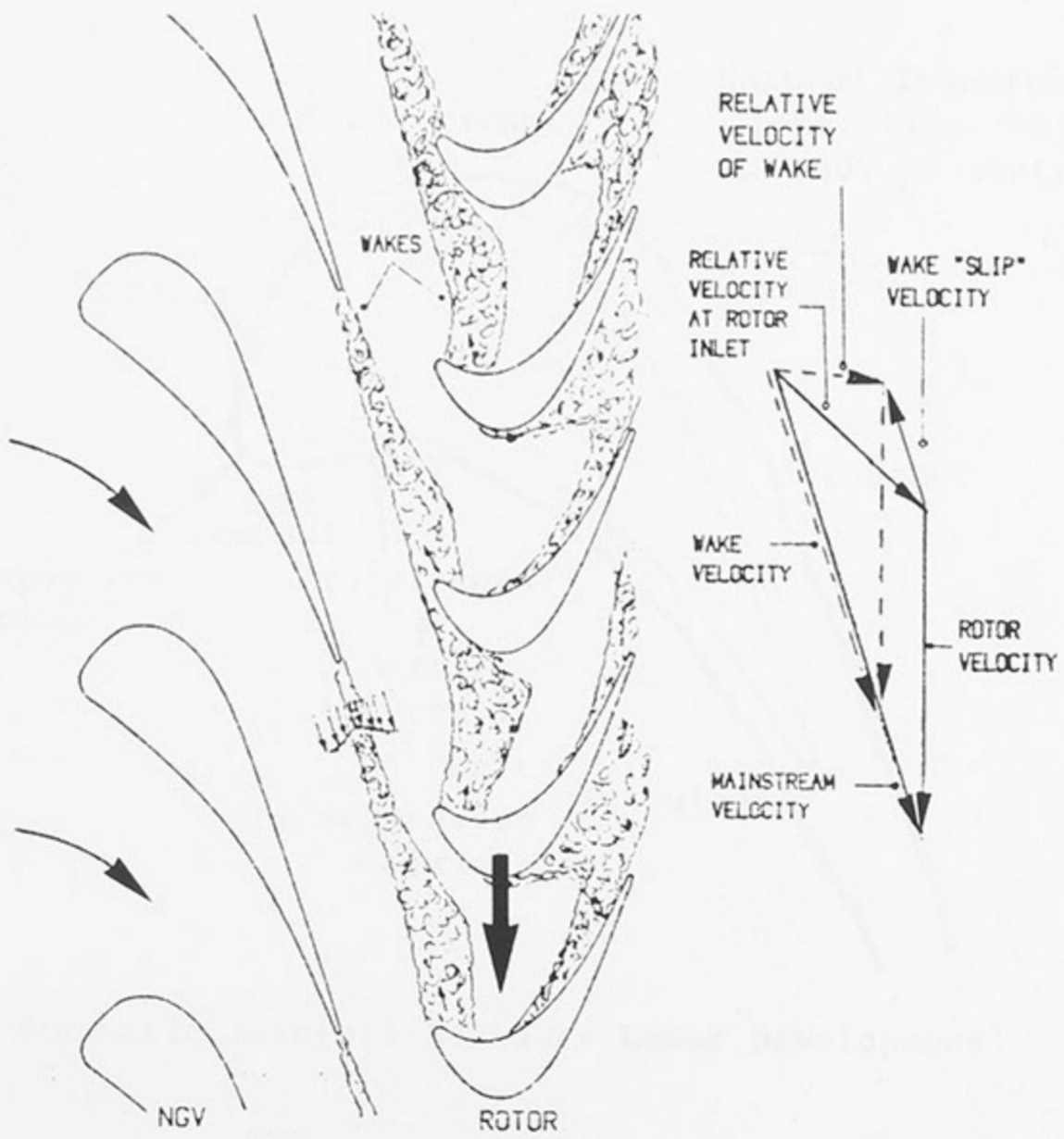

Fig. 1.2(b) Typical NGV-Rotor Relationship for a First Stage Turbine with the Velocity Triangle (after DOORLY [1983]).

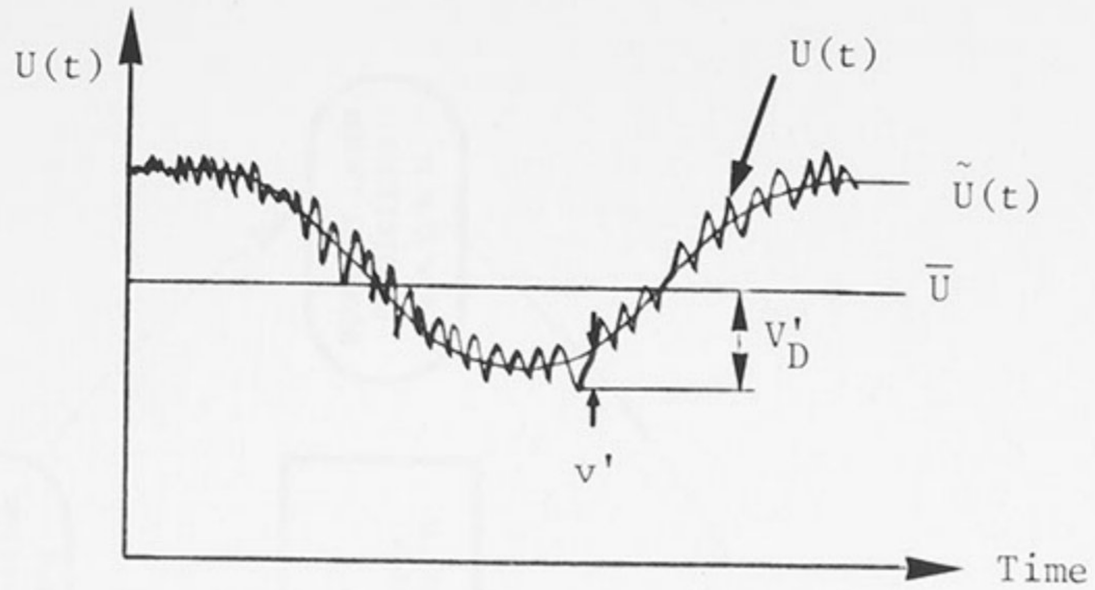

Fig. 1.3(a) Typical Unsteady Velocity Measurement Nomenclature (after EVANS[1975]).

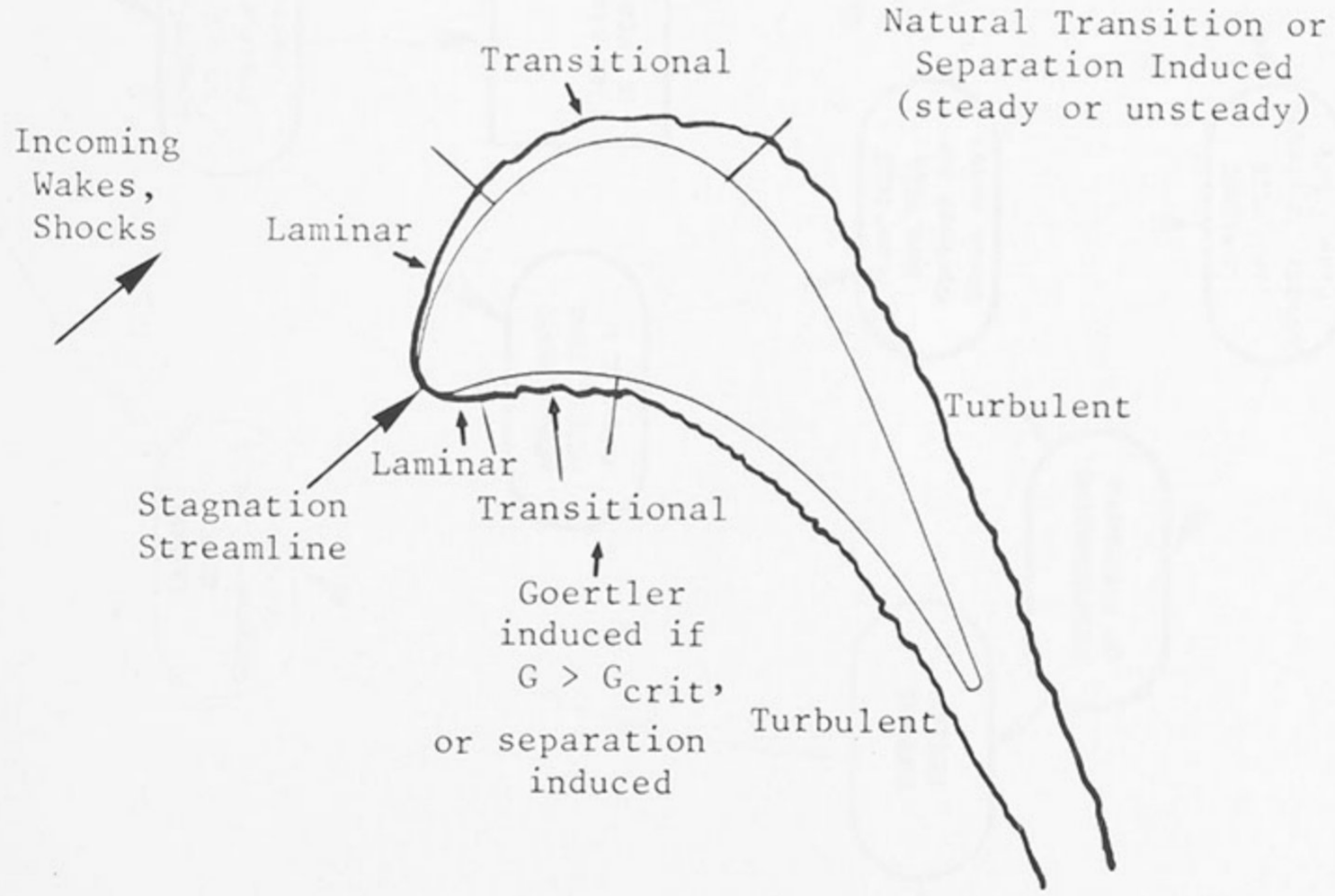

Fig. 1.3(b) Schematic Aerofoil Boundary Layer Development.

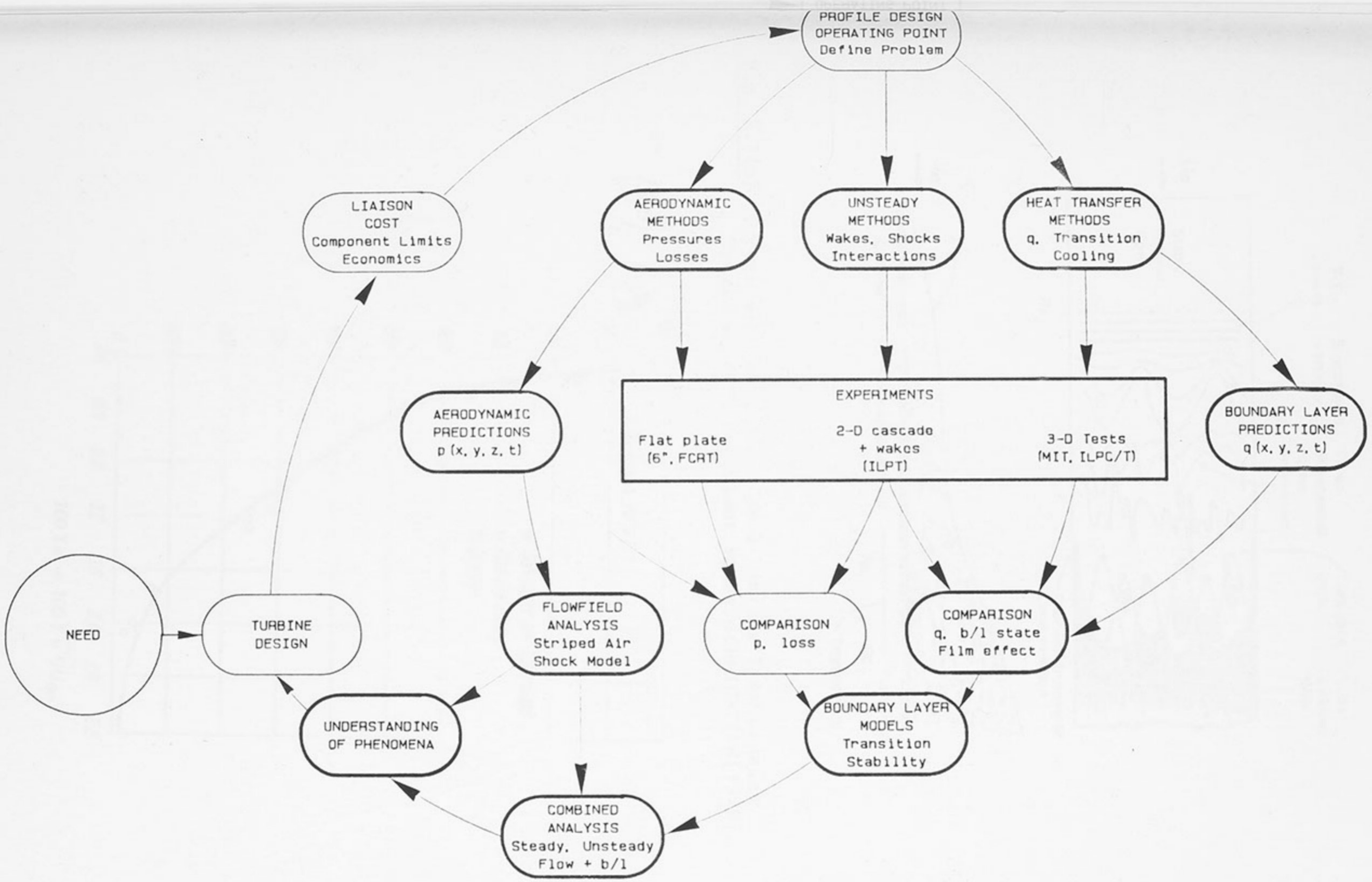

Fig. 1.4 Diagram Showing the Context of Turbine Research Activity in the Overall Design Process. (Areas outlined in bold are investigated in the present study.)

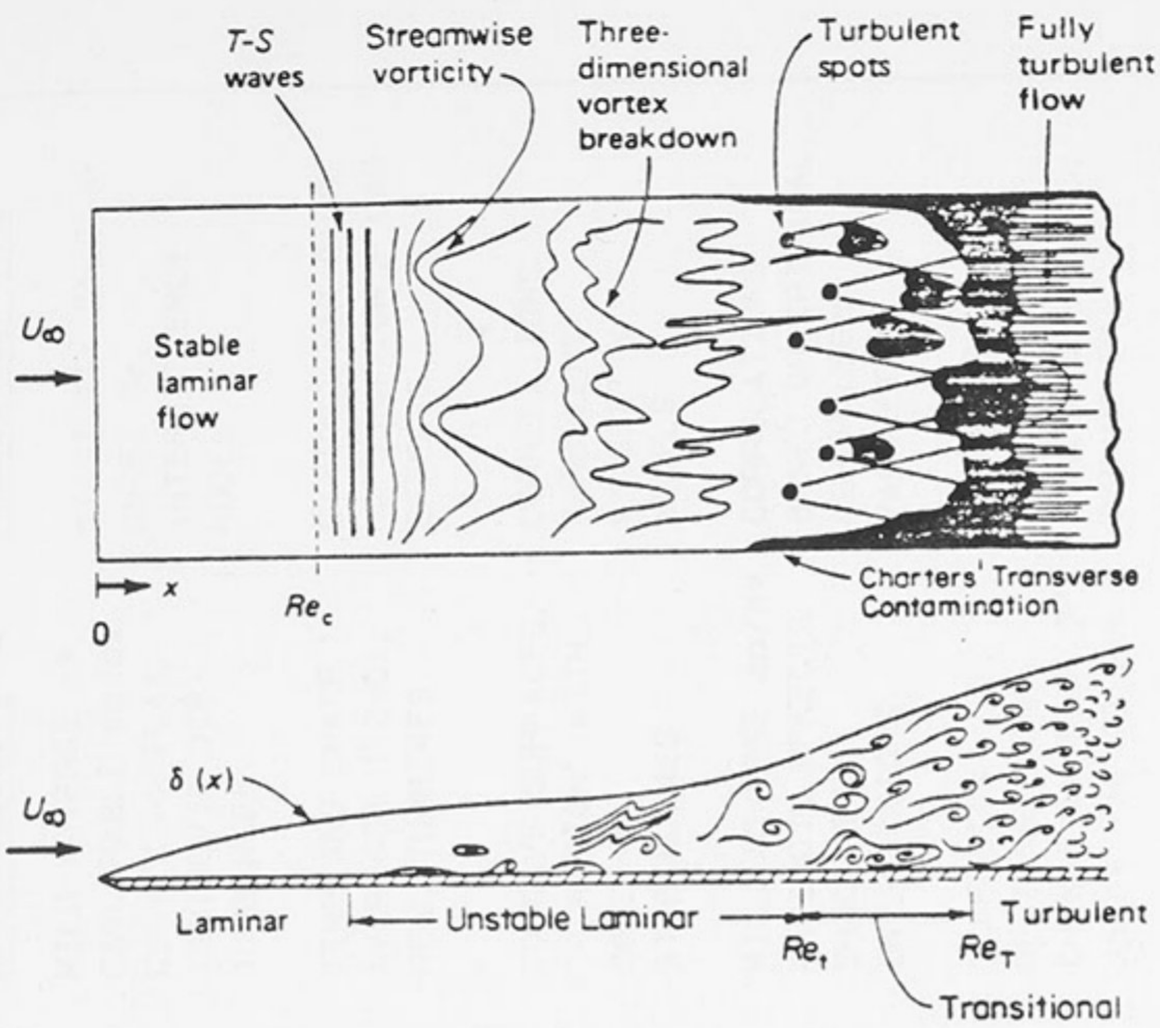

Fig. 2.1(a) Growth of Disturbances in a Laminar Flow Causing Breakdown to a Turbulent State. SCHLICHTING[1979].

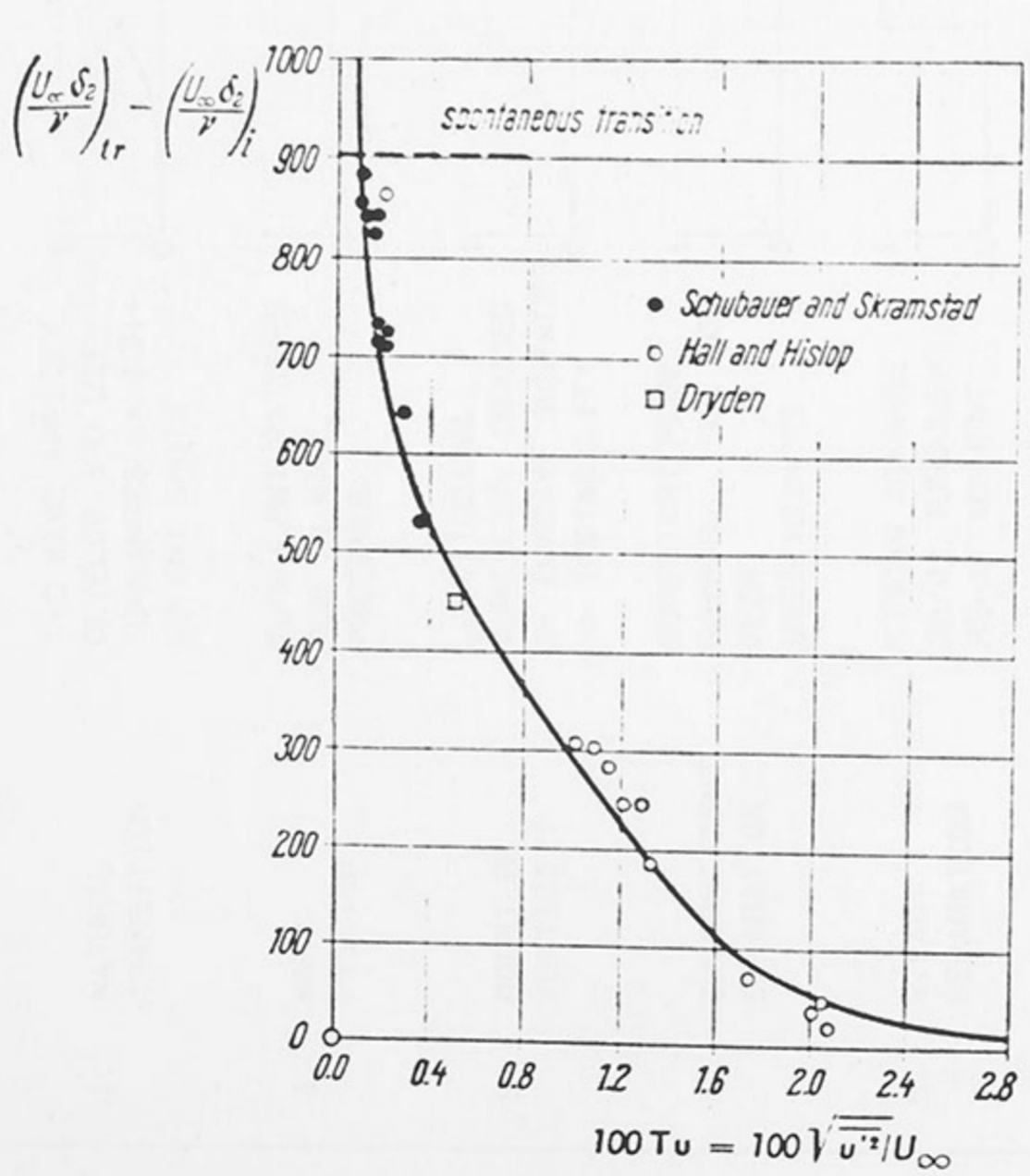

Fig. 2.1(b) Effect of Variation in Freestream Turbulence Level on the Change in Momentum Thickness Reynolds Number from the Neutral Stability Point (i) to the Start of Transition (tr). SCHLICHTING[1979].

	MODE	DESCRIPTION	TYPICAL γ	APPLICABILITY	PREDICTION TYPE
1.	NATURAL TRANSITION	T-S WAVE AMPLIFY, DEVELOP 3-D DISTURBANCES -> TURBULENT SPOTS	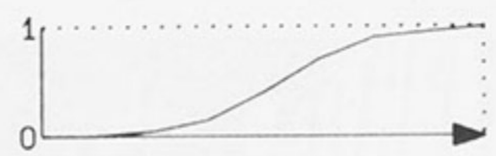	MILD ADVERSE -> FAVOURABLE dp/dx, CONVEX -> FLAT, ISOTROPIC DISTURBANCES	STABILITY CALC.-> ONSET Re, INTERMITTENCY MODEL
2.	WAKE PASSING	TURBULENT PATCHES DUE TO WAKE PRESENCE	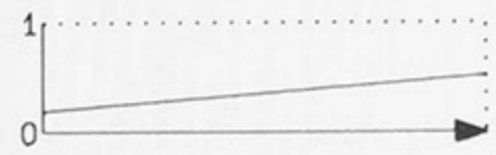	TIME AND SPACE AVERAGED (~2-D), REAL TURBINES	STRIPED-AIR CALC. -> DURATION + LAG EFFECTS
3.	GOERTLER VORTICITY	LONGITUDINAL VORTICITY INDUCED BY CONCAVE SURFACES -> INSTABILITY	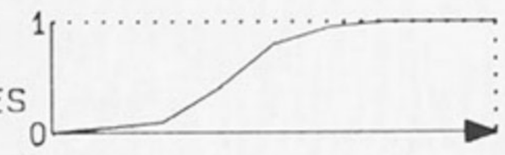	CONCAVE SURFACES, OR REGIONS WITH CONCAVE STREAMLINES	CORRELATIONS, TURBULENT VISCOSITY MODELS
4.	INTERMITTENT SEPARATION	MOMENTARY FLOW REVERSAL, DUE TO FLOW UNSTEADINESS	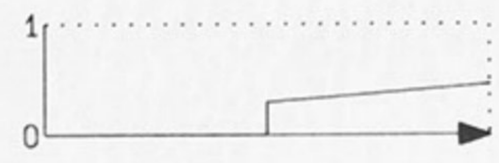	MILD ADVERSE dp/dx, PERIODIC EFFECTS, SHOCK/B.L. INTERACTIONS	CORRELATIONS BASED ON CRITICAL POHLHAUSEN PARAMETER
5.	STEADY SEPARATION	STRONG ADVERSE dp/dx, TURBULENT RE-ATTACHMENT	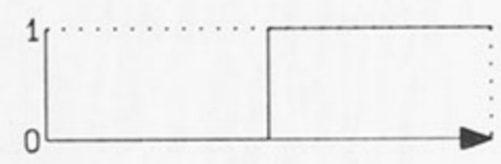	DIFFUSION REGIONS, NEAR CHANGE IN SIGN OF dp/dx -ve TO +ve	CORRELATION FOR CRITICAL POHLHAUSEN PARAMETER

SURFACE LENGTH

Fig.2.2 Description of Some of the Competing Modes of Transition from Laminar to Turbulent Flow. All Predictions of Transition are Still Under Development. ("striped-air" refers to a wake prediction method outlined in DOORLY[1983] and described in Chapter VII.)

(a)

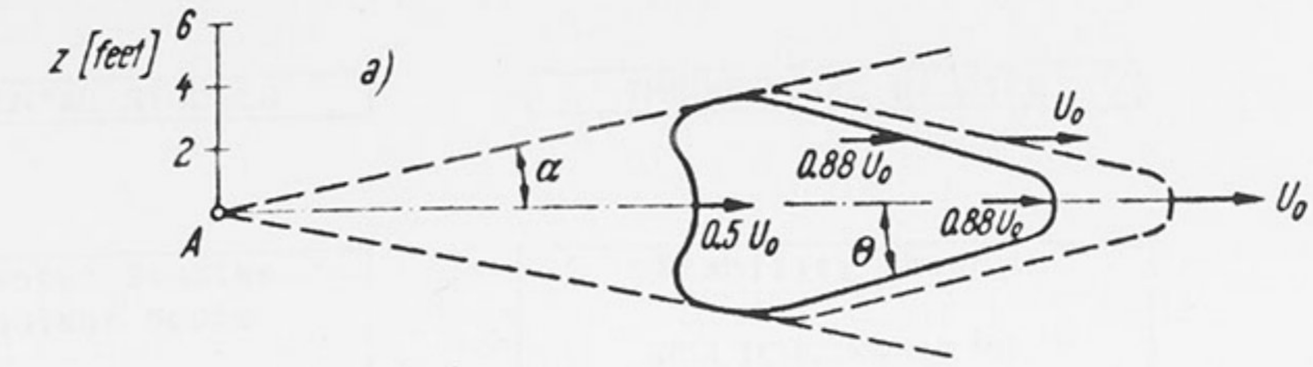

(b)

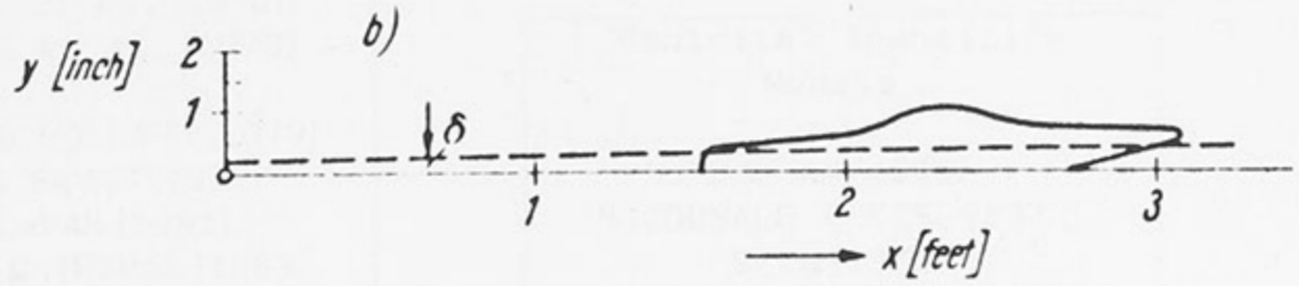

(b)
Re = 0.2E6

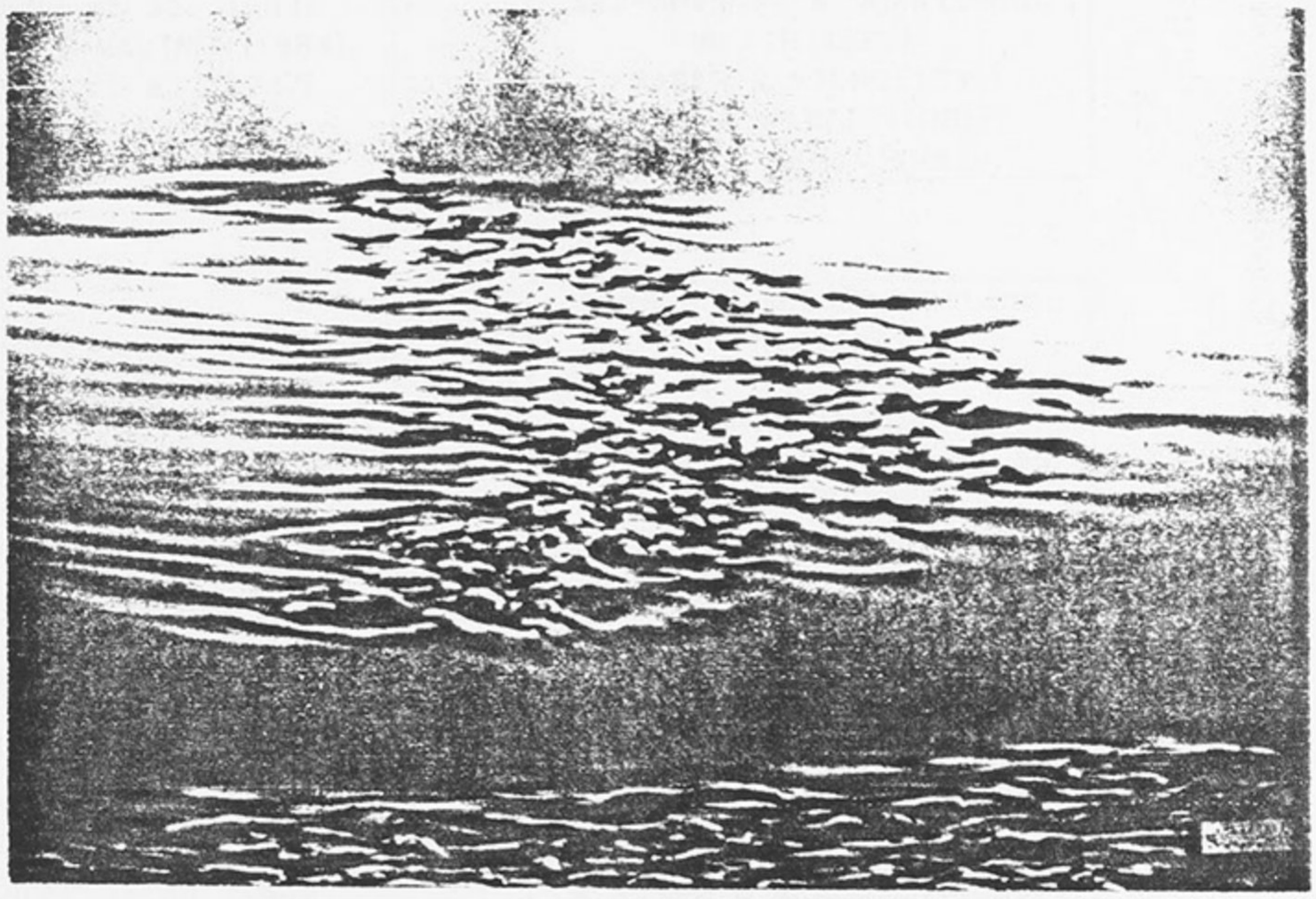

(c)
Re = 0.4E6

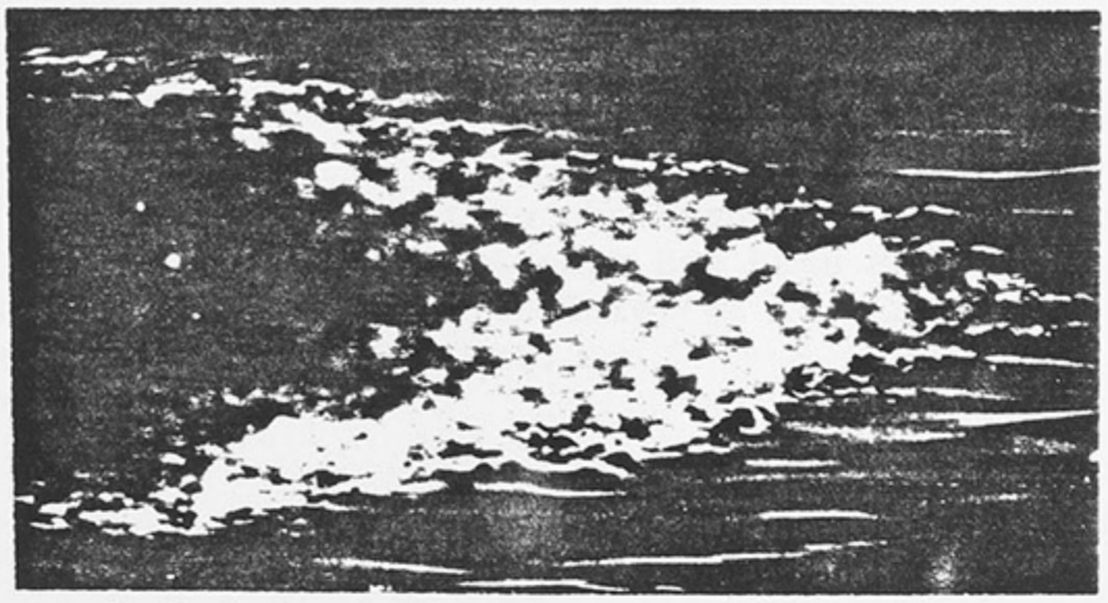

Fig. 2.3 Measurements of Turbulent Spots from other Experimental Studies:

(a) Detailed Hot-Wire Measurements Defining the Extent of the Spot Normal to the Wall and in the Spanwise Direction. (SCHUBAUER & KLEBANOFF[1955])

(b) Plan View Visualised by use of Aluminium Flakes Suspended in Water. (CANTWELL et al.[1978])

(c) Plan View using Smoke in Air from van DYKE[1982].

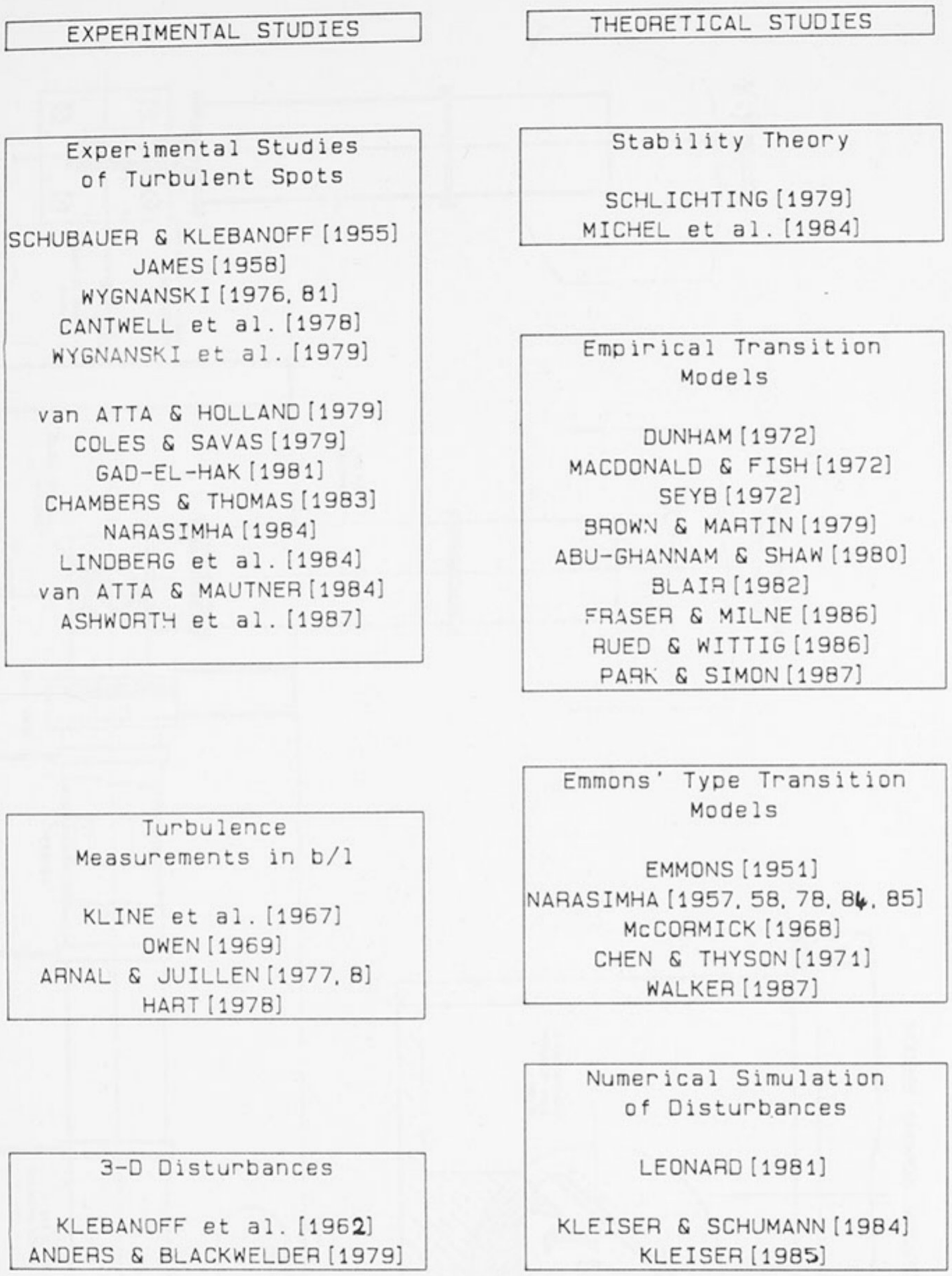

Fig. 2.4 Survey of References Relevant to the Transition Work Covered in the Thesis. An Attempt has been Made to Separate the Specific Areas of Interest for Each Reference According to Subject.

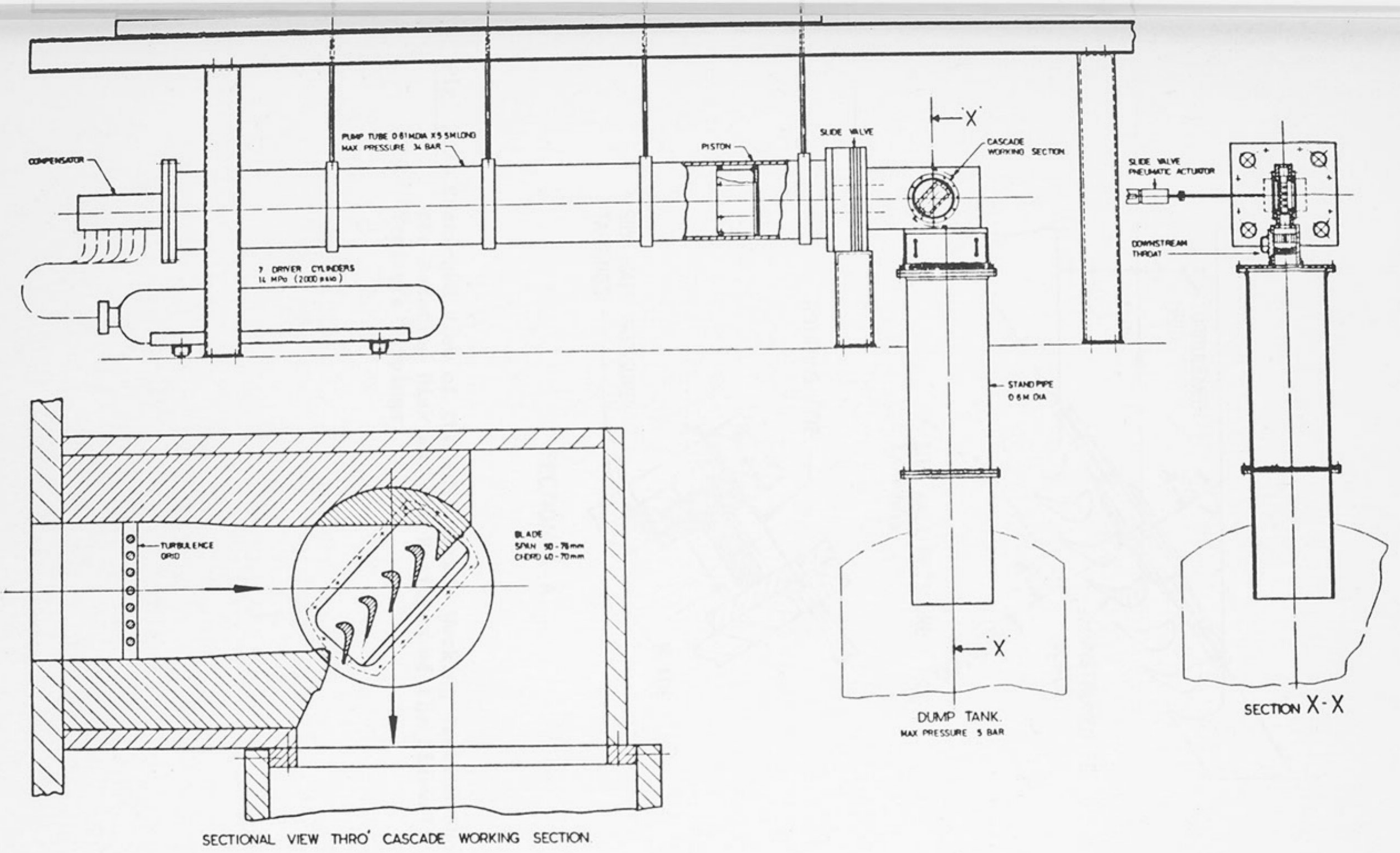

Fig. 3.1 General Arrangement of the ILPT.

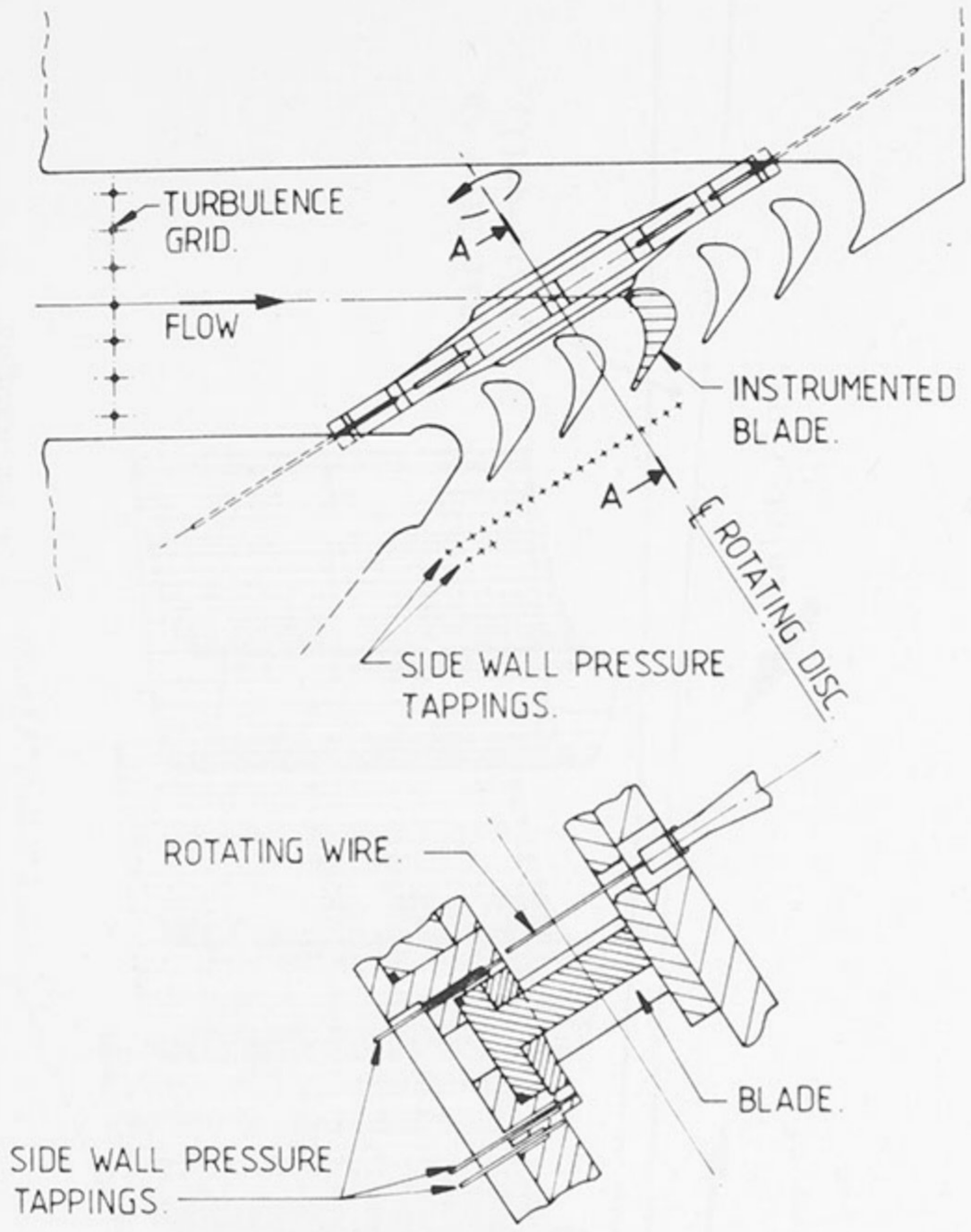

Fig. 3.2 Sectioned View of the ACE Cascade Working Section Showing the Rotating Disk and the Position of the Sidewall Pressure Tappings.

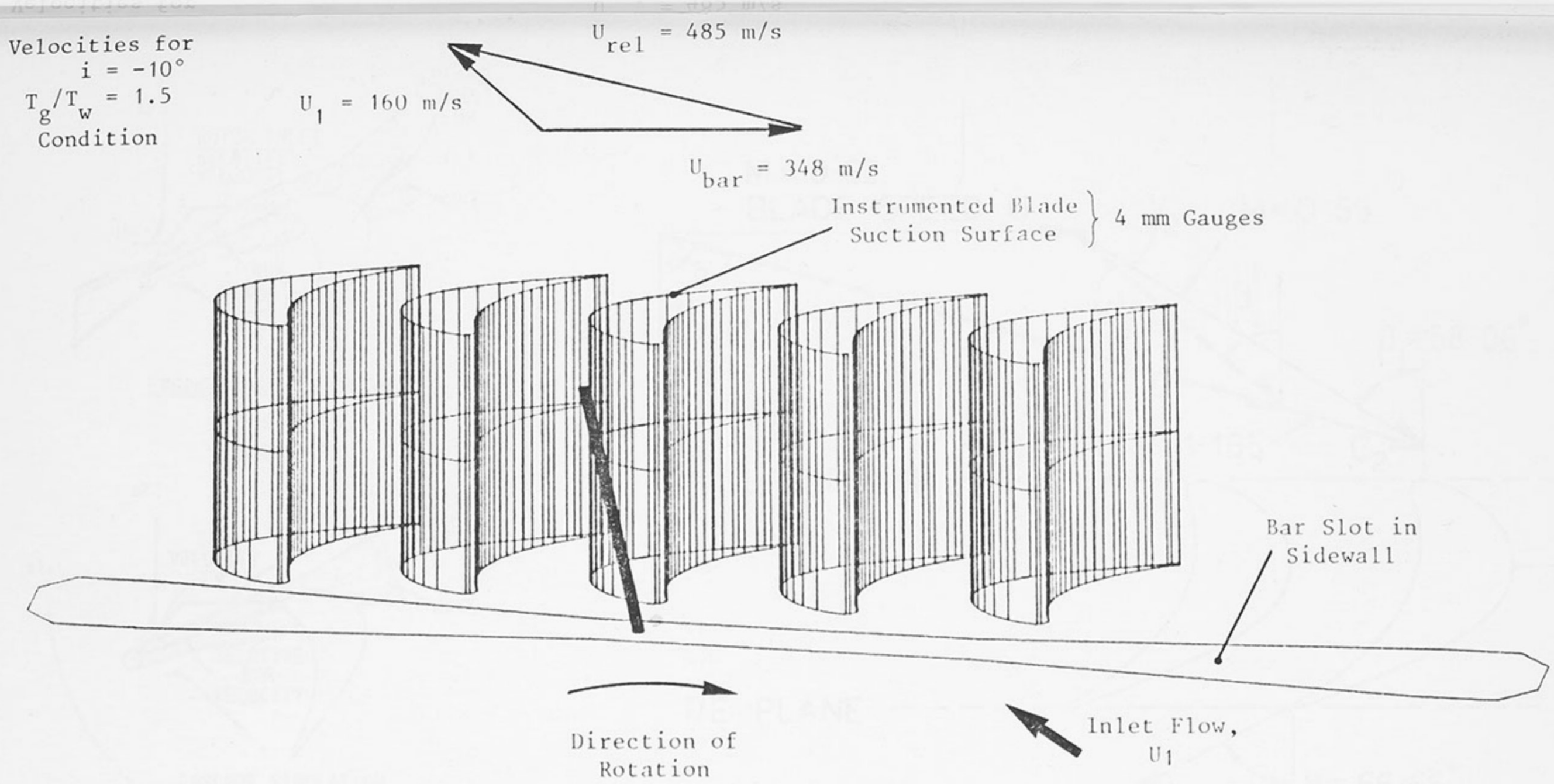

Fig. 3.3 View of the ACE Cascade Showing the Bar Rotating through the Slot in the Sidewall.

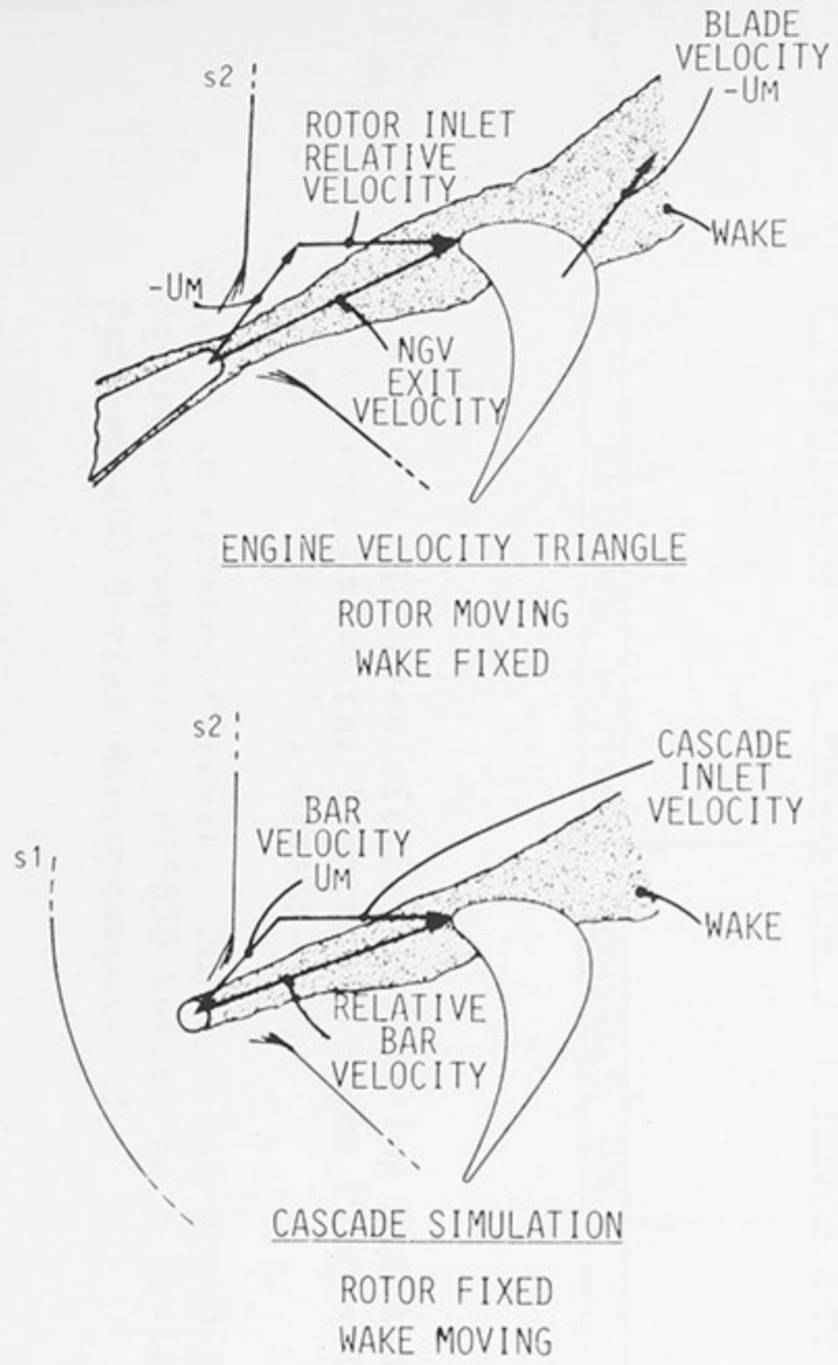

Fig. 3.4(a) Means by Which the Engine NGV-Rotor Interaction is Simulated in the Cascade.

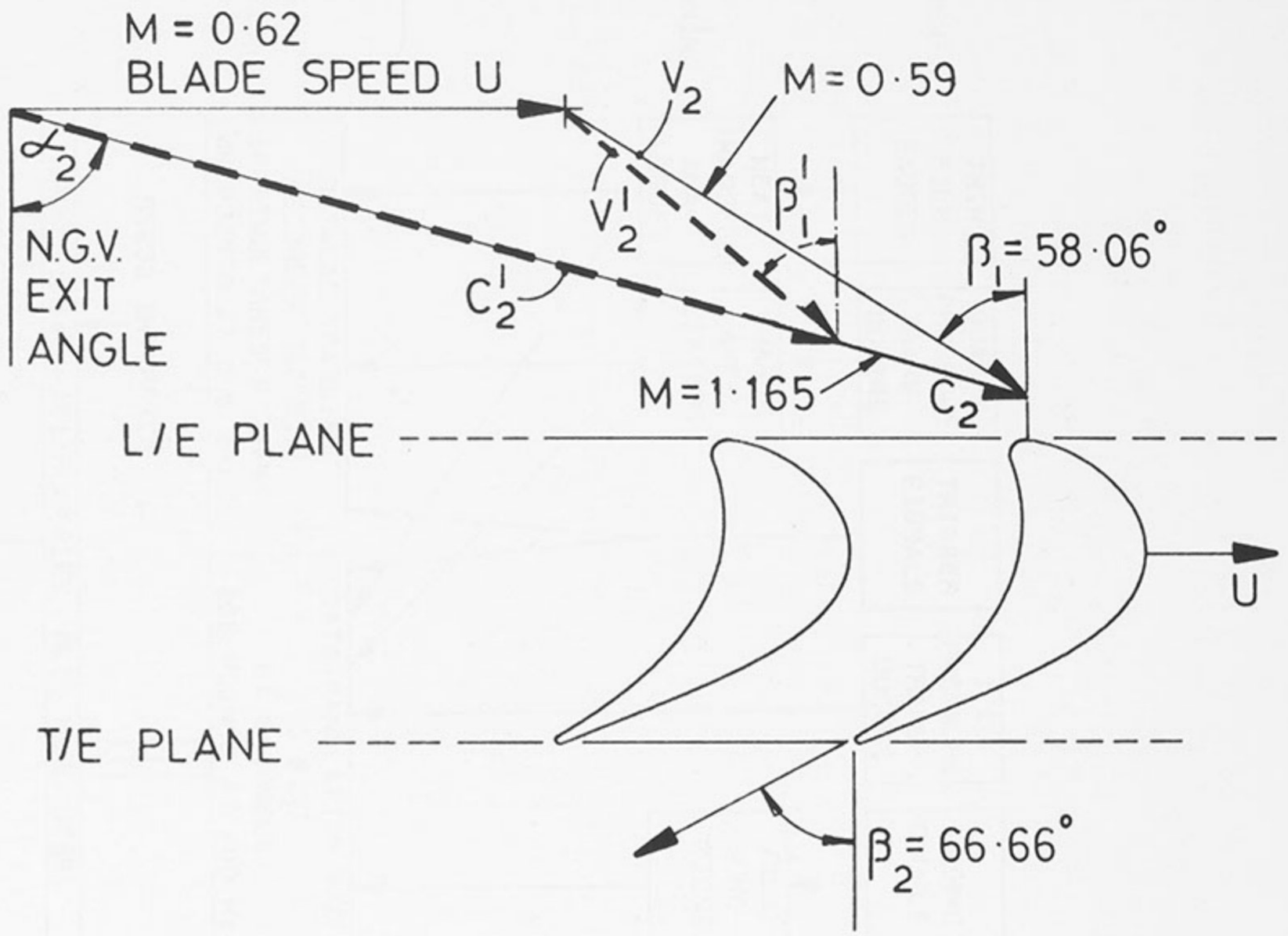

Fig. 3.4(b) Velocity Triangles at i = 0° Showing Reduced Incidence Caused by the Deficit in the Wake.

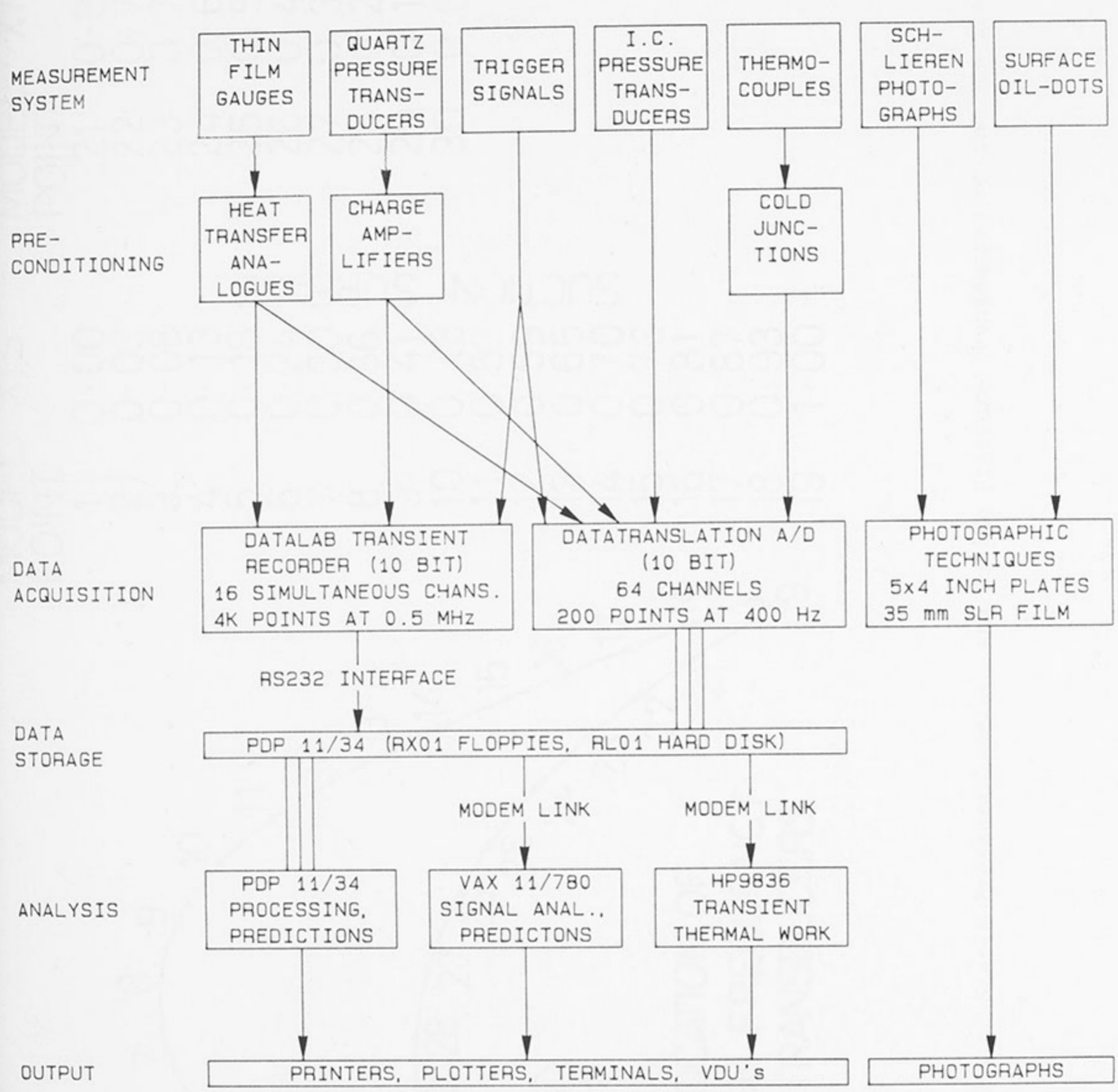

Fig. 3.5 Flowpath for the Acquisition, Processing and Analysis of Data Taken using the Isentropic Light Piston Tunnel (ILPT) at Oxford University.

(I.C. = Integrated Circuit. PDP and VAX are Digital Equipment Computers. HP9836 Refers to a Hewlett-Packard 200 Series Micro-computer.)

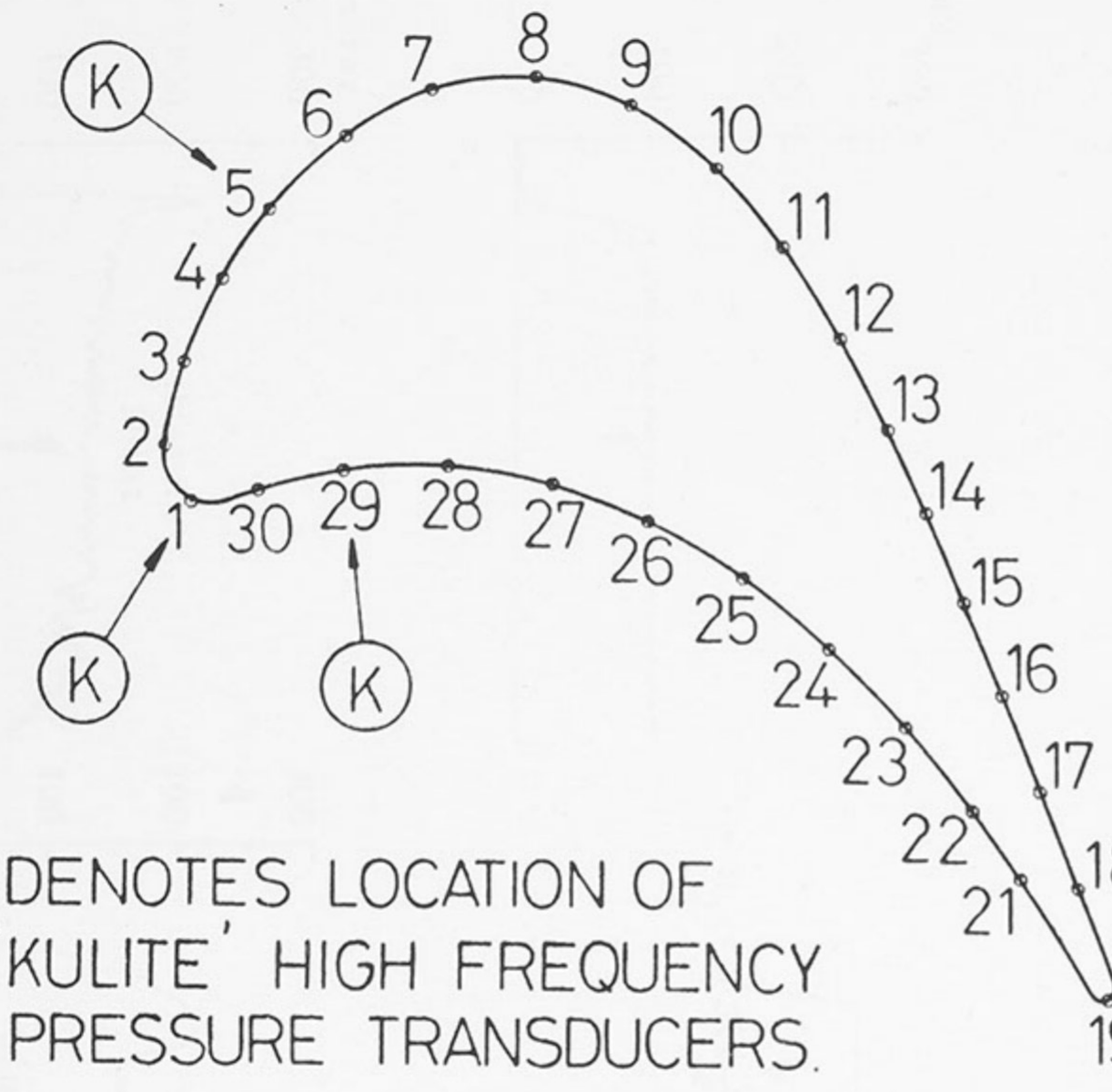

(K) DENOTES LOCATION OF 'KULITE' HIGH FREQUENCY PRESSURE TRANSDUCERS.

MODEL POINT.	X/S	
1	0·00	
2	0·03	
3	0·08	
4	0·13	
5	0·18	
6	0·24	
7	0·30	
8	0·36	
9	0·41	SUCTION SURFACE.
10	0·48	
11	0·53	
12	0·59	
13	0·65	
14	0·70	
15	0·76	
16	0·81	
17	0·87	
18	0·93	
19	1·00	

MODEL POINT.	X/S	
21	0·87	
22	0·79	
23	0·70	
24	0·61	
25	0·51	
26	0·41	
27	0·33	
28	0·23	
29	0·14	
30	0·07	PRESSURE SURFACE.

Fig. 3.6 Positions of Static Pressure Tappings and Kulite Pressure Transducers on the ACE Blade.

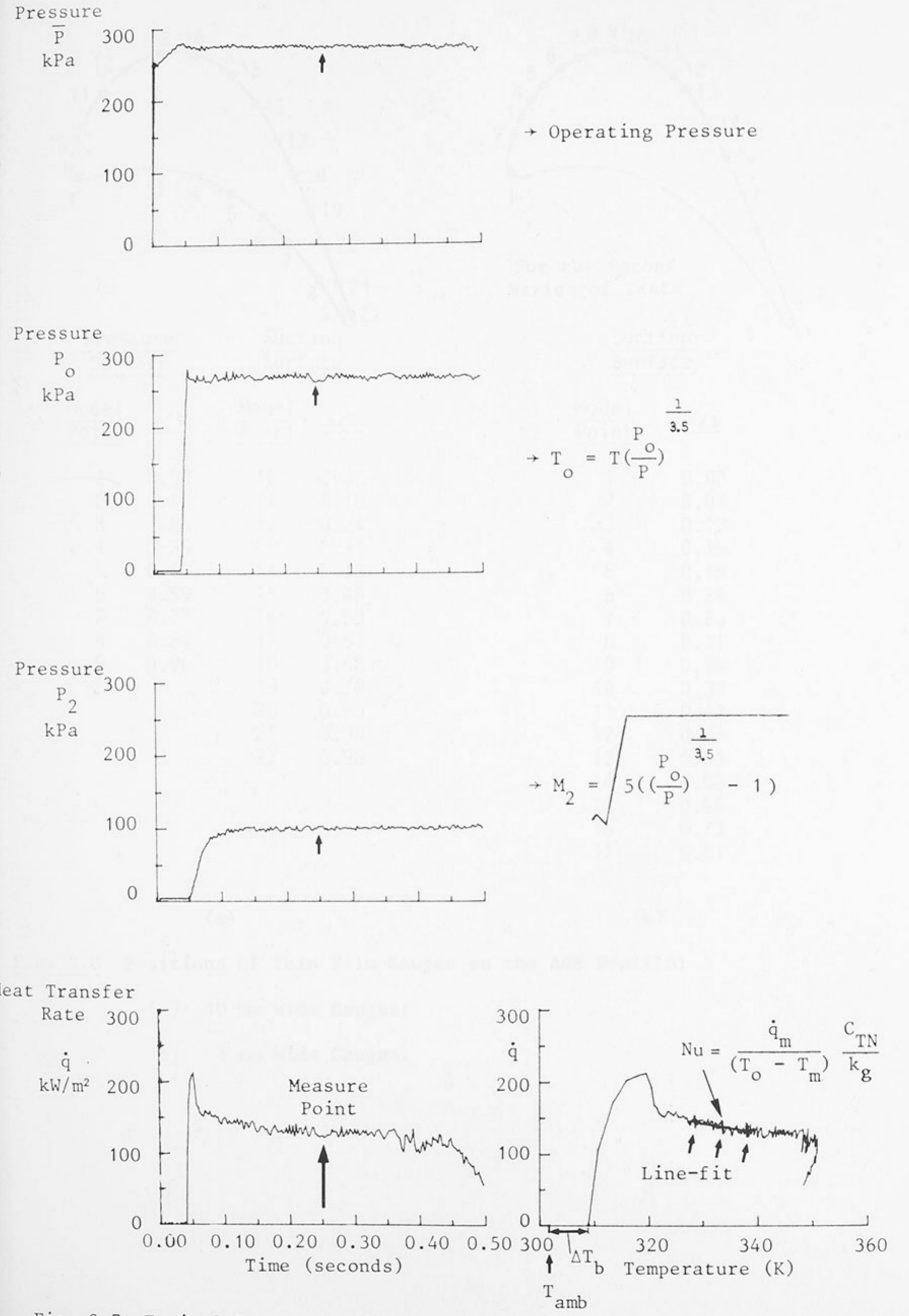

Fig. 3.7 Typical Pressure and Heat Transfer Channels from an ILPT Run.

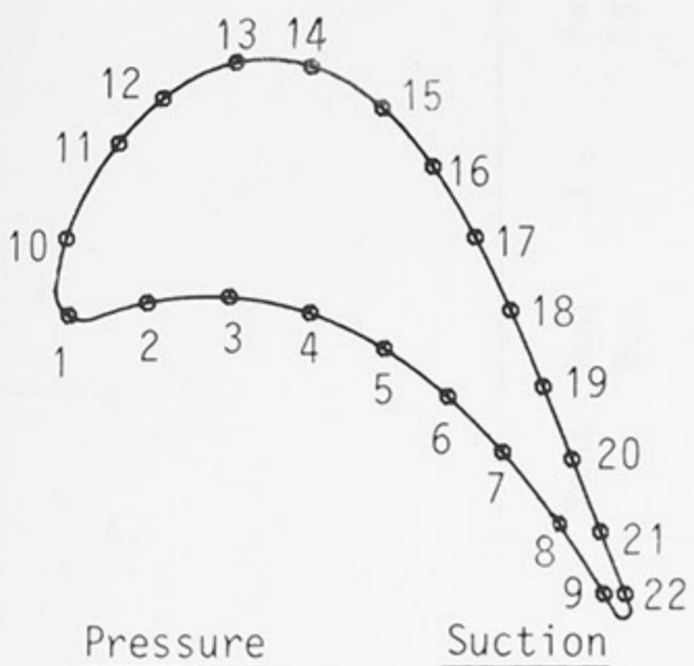

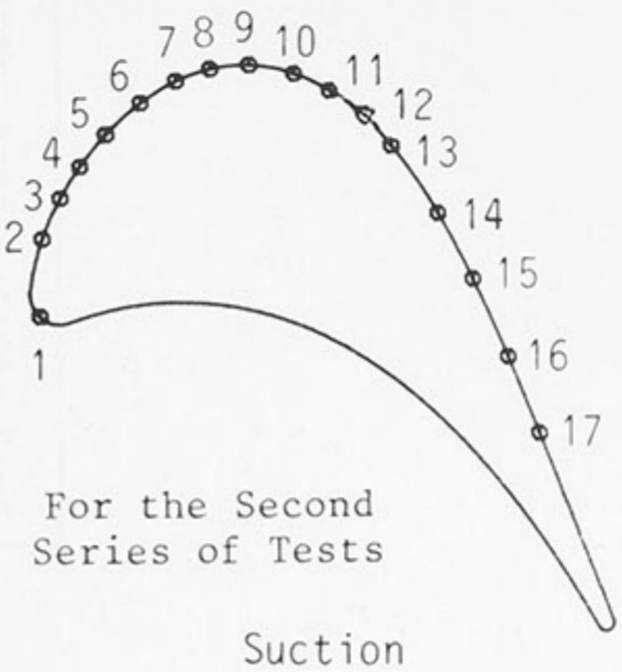

For the Second Series of Tests

Pressure Surface		Suction Surface	
Model Point	x/s	Model Point	x/s
1	0.00	10	0.08
2	0.12	11	0.18
3	0.24	12	0.24
4	0.36	13	0.31
5	0.48	14	0.38
6	0.59	15	0.46
7	0.71	16	0.53
8	0.84	17	0.61
9	0.96	18	0.68
		19	0.76
		20	0.83
		21	0.90
		22	0.96

(a)

Suction Surface	
Model Point	x/s
1	0.00
2	0.08
3	0.12
4	0.15
5	0.19
6	0.24
7	0.28
8	0.31
9	0.35
10	0.39
11	0.43
12	0.47
13	0.51
14	0.58
15	0.65
16	0.73
17	0.81

(b)

Fig. 3.8 Positions of Thin Film Gauges on the ACE Profile:

(a) 10 mm Wide Gauges;

(b) 4 mm Wide Gauges.

Test	Run No.	M	Re E5	T/To	Po psia
M+	TARGET	1.40	9.19	1.5	35.31
i=0	4511	1.426	8.789	1.552	37.38
i=-10	4594	1.418	8.738	1.511	35.20
i=+5	4569	1.427	8.699	1.498	35.12

Test	Run No.	M	Re E5	T/To	Po psia
Re-	TARGET	1.18	4.60	1.5	17.32
i=0	4520	1.282	4.344	1.554	18.45
i=-10	4580	1.194	4.497	1.521	17.82
i=+5	4578	1.183	4.401	1.537	17.81

Test	Run No.	M	Re E5	T/To	Po psia
DES	TARGET	1.18	9.19	1.5	34.61
i=0	4540	1.280	9.127	1.568	40.53
i=-10	4583	1.196	9.153	1.494	35.88
i=+5	4565	1.158	8.811	1.502	34.90

Test	Run No.	M	Re E5	T/To	Po psia
Re+	TARGET	1.18	13.8	1.5	51.96
i=0	4516	1.173	13.26	1.555	55.14
i=-10	4598	1.201	13.59	1.529	54.18
i=+5	4575	1.215	12.80	1.538	52.66

Test	Run No.	M	Re E5	T/To	Po psia
M-	TARGET	0.85	9.19	1.5	37.39
i=0	4507	0.858	8.870	1.540	38.62
i=-10	4586	0.845	8.912	1.466	36.17
i=+5	4572	0.860	8.569	1.499	36.40

Fig. 3.9 Operating Conditions for the ILPT ACE Heat Transfer Tests.

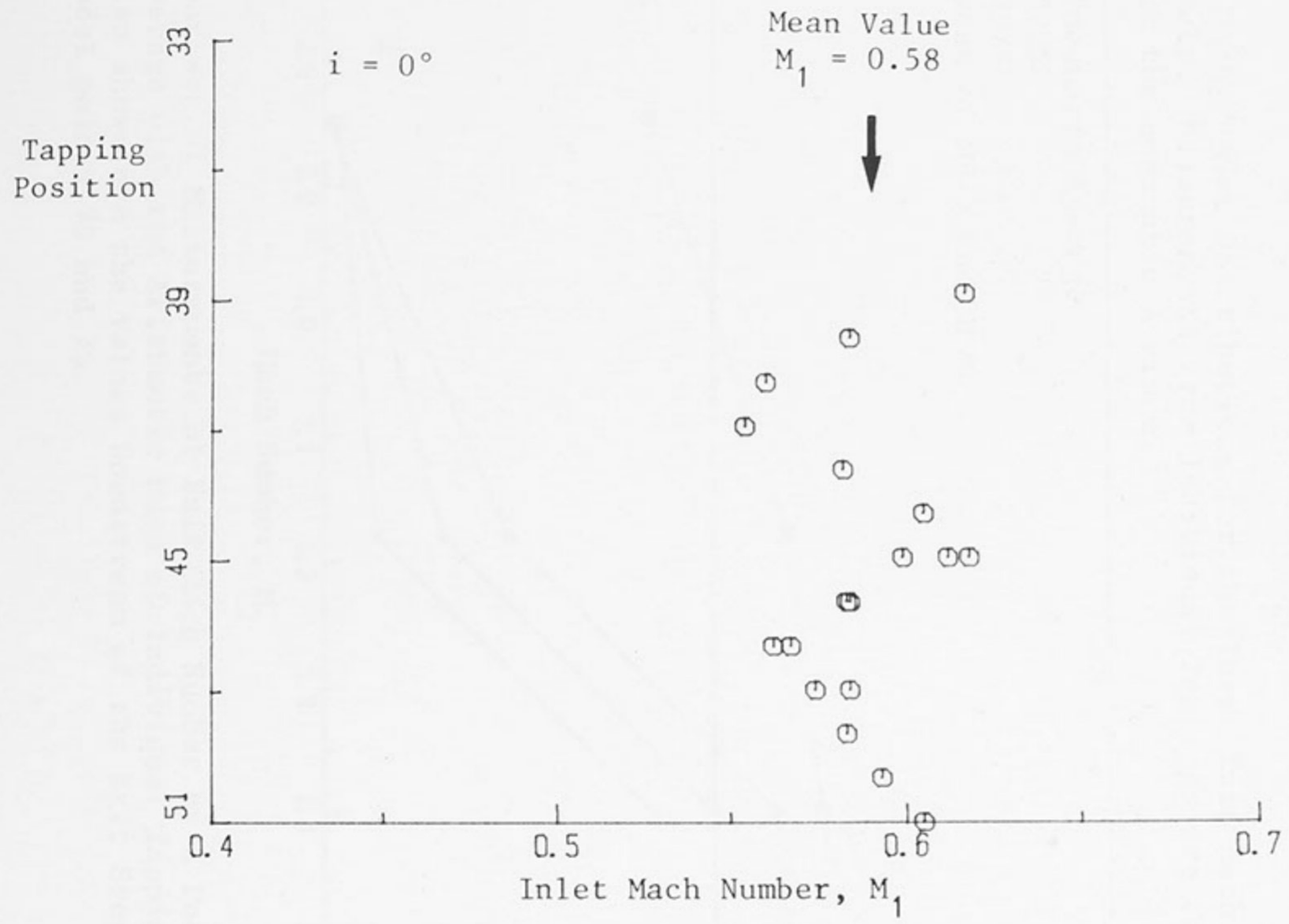

Fig. 3.10 Example of Inlet Mach Number Measurements and Positions of Sidewall Static Pressure Tappings.

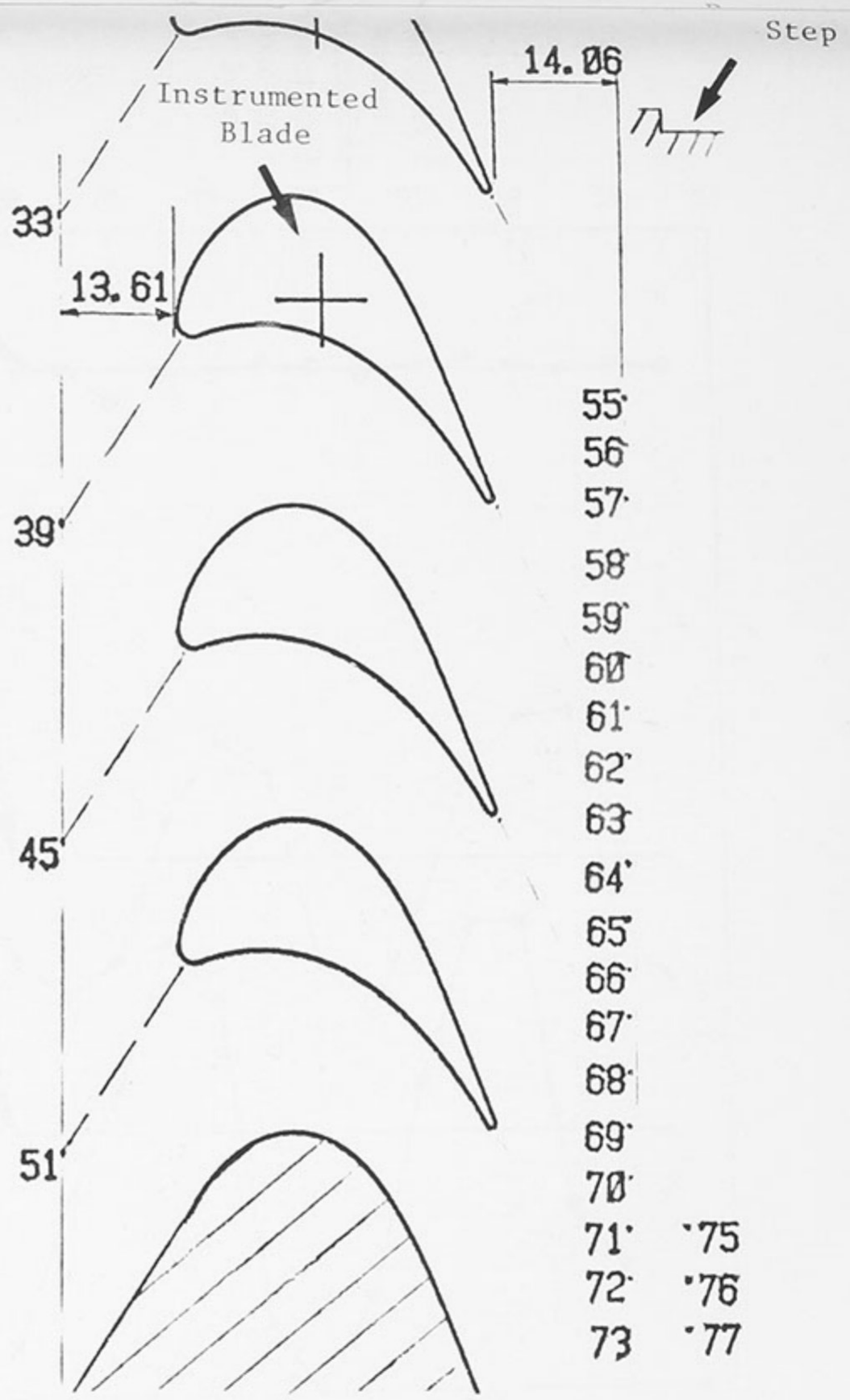

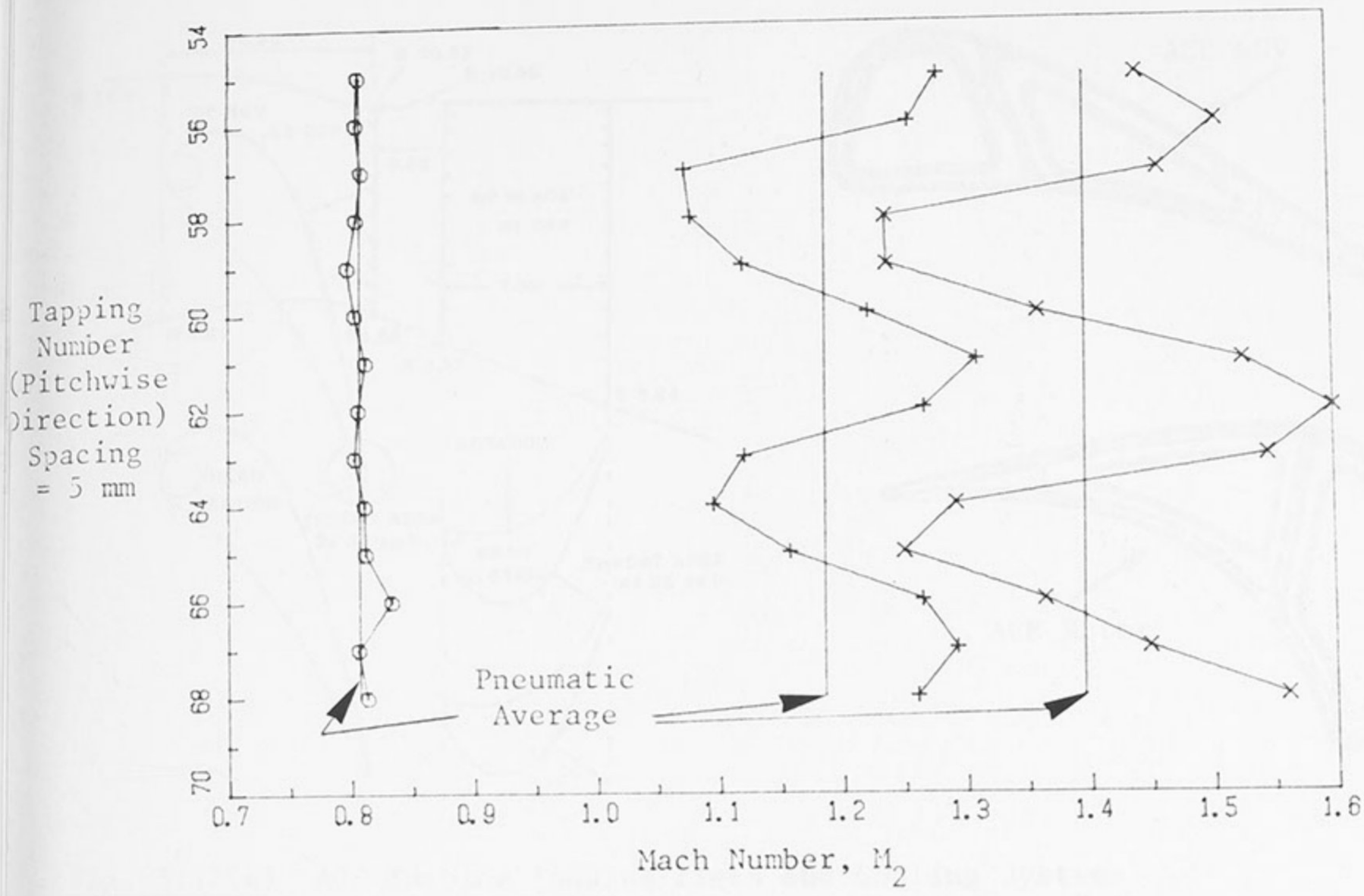

Fig. 3.11(a) Exit Mach Number Distributions for the Three Exit Mach Number Levels. Measurements from Individual Tappings are Compared with the Pneumatic Average.

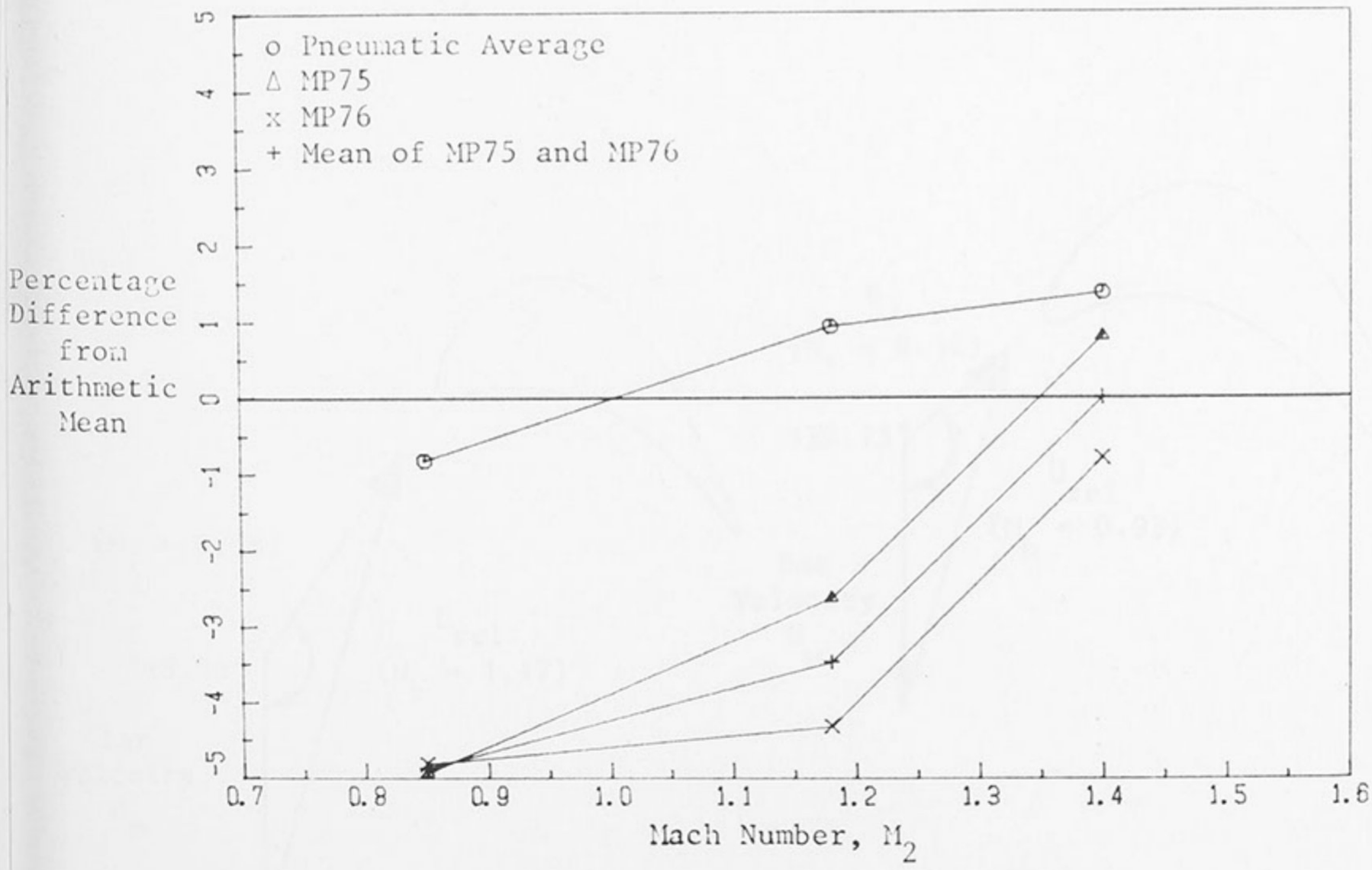

Fig. 3.11(b) Comparison of Measurements of Exit Mach Number by a Pneumatic Average with the Arithmetic Mean of Individual Tappings. Also shown are the Values Downstream of the Exit Step, model points 75 and 76.

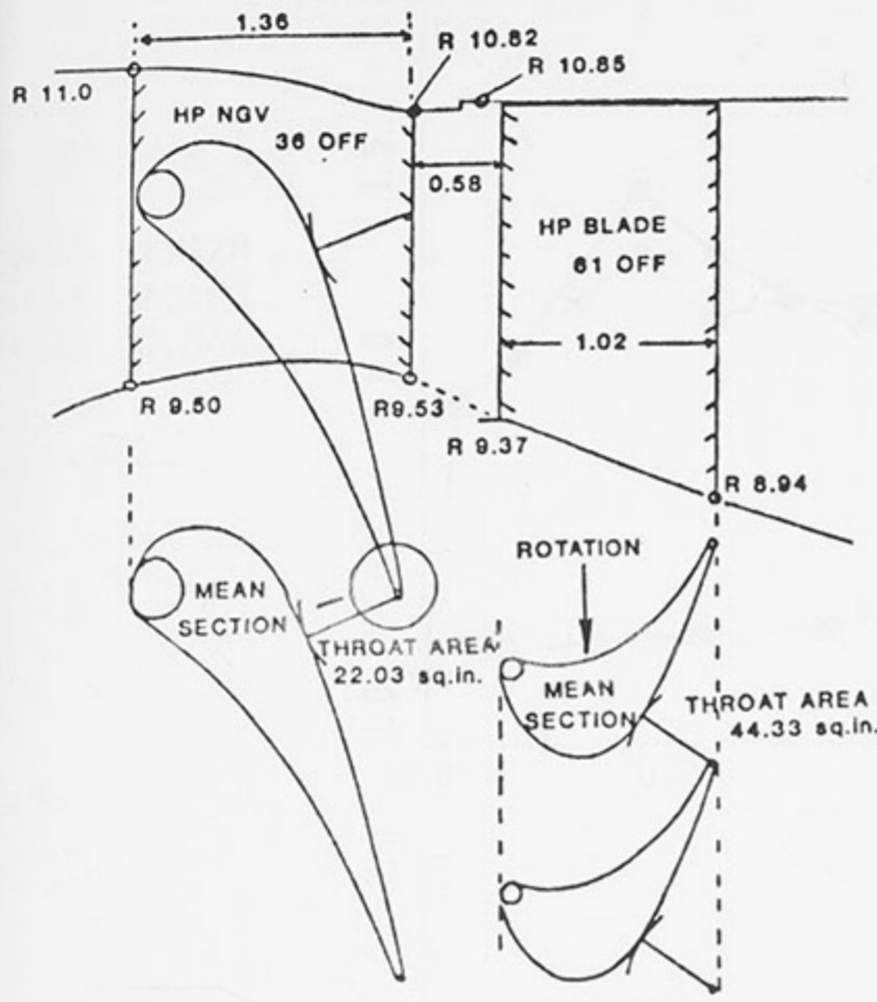

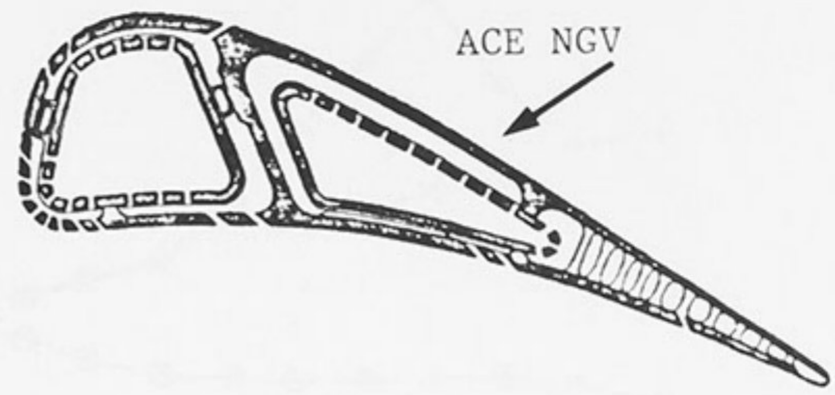

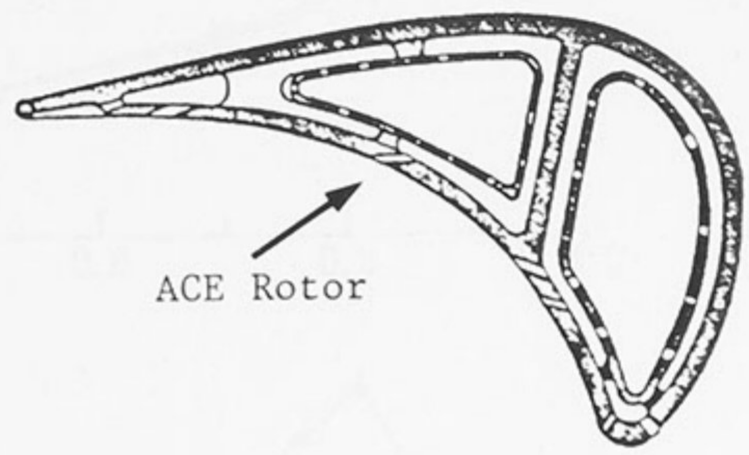

Fig. 3.12(a) ACE Turbine Annulus Lines and Cooling Systems (ROLLS-ROYCE[1983]).

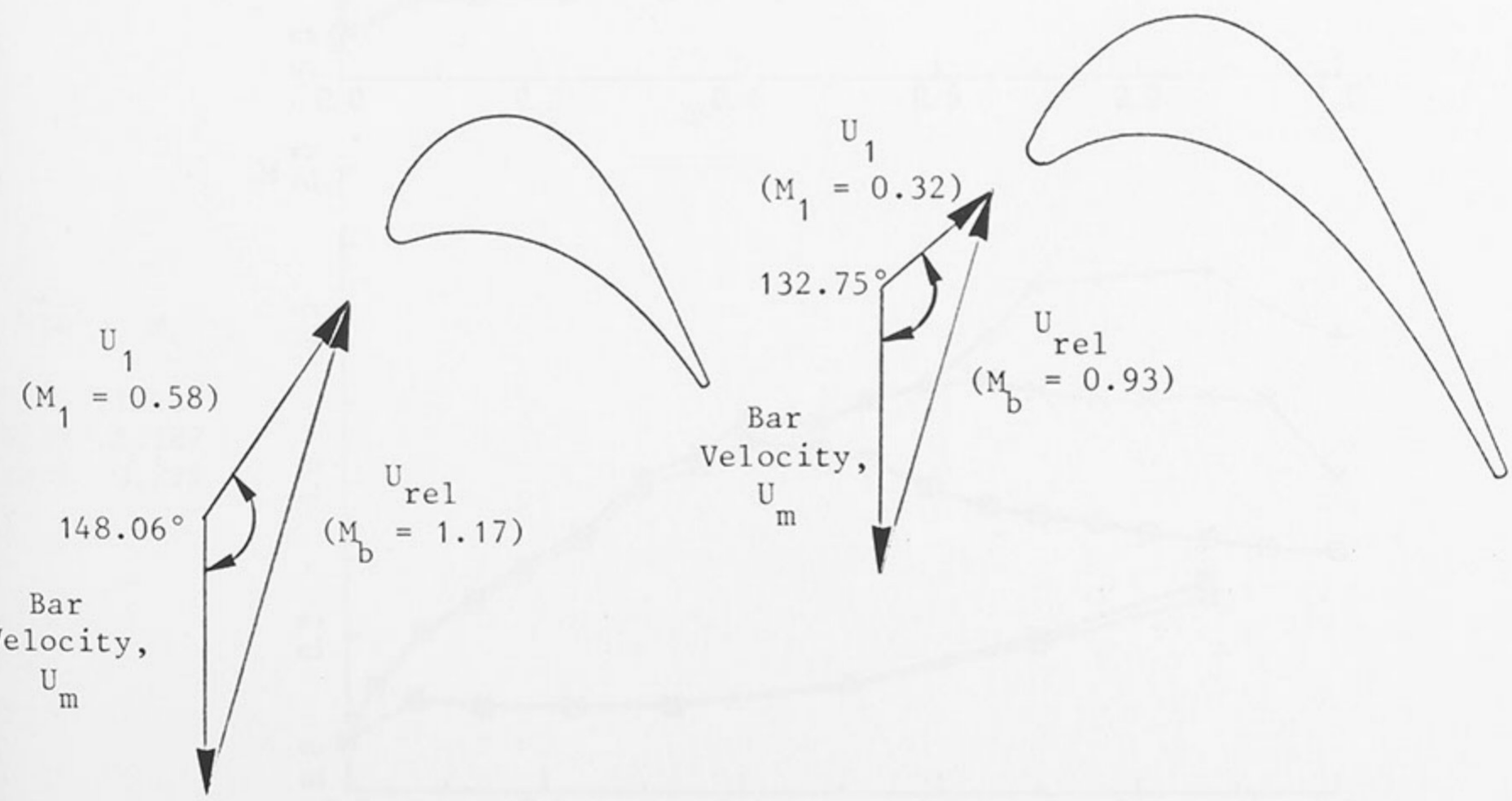

ACE Blade B22 Blade

Fig. 3.12(b) Comparison Between the ACE and B22 Rotor Profiles.

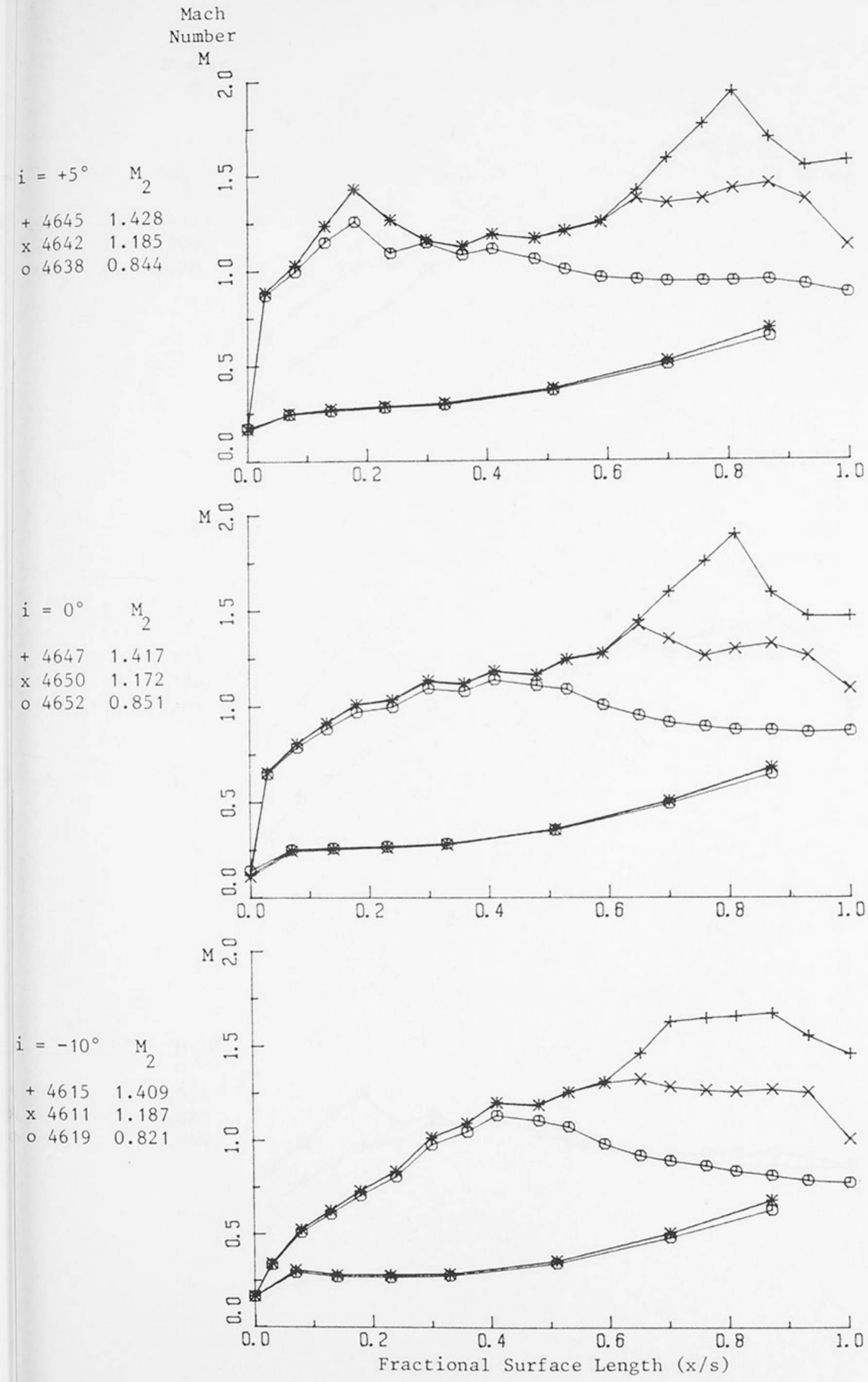

Fig. 4.1 Comparison of ACE Blade Mach Number Distributions with Variation in Exit Mach Number at Three Incidences.

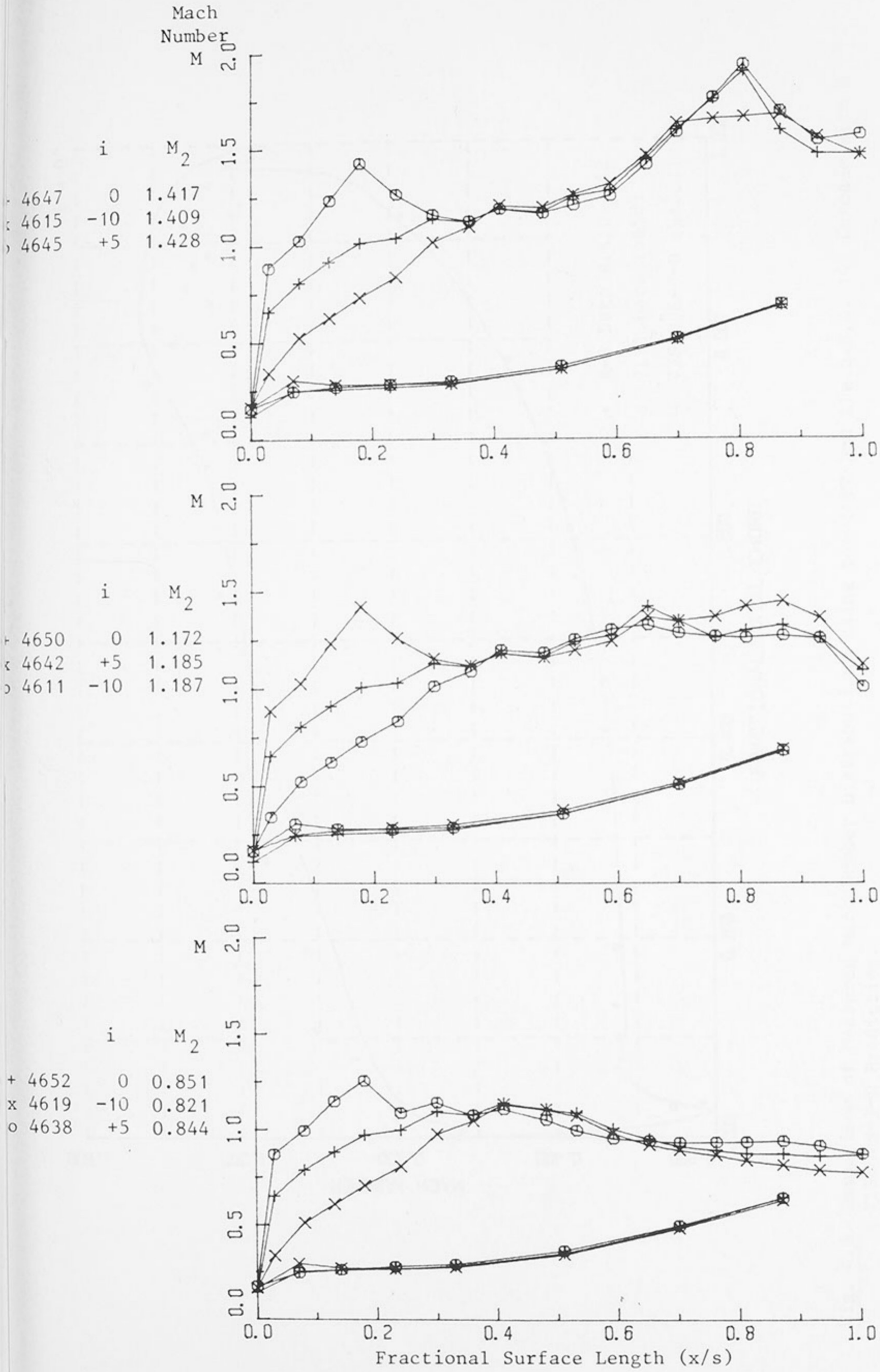

Fig. 4.2 Comparison of ACE Blade Mach Number Distributions with Variation of Incidence at Three Exit Mach Number Levels.

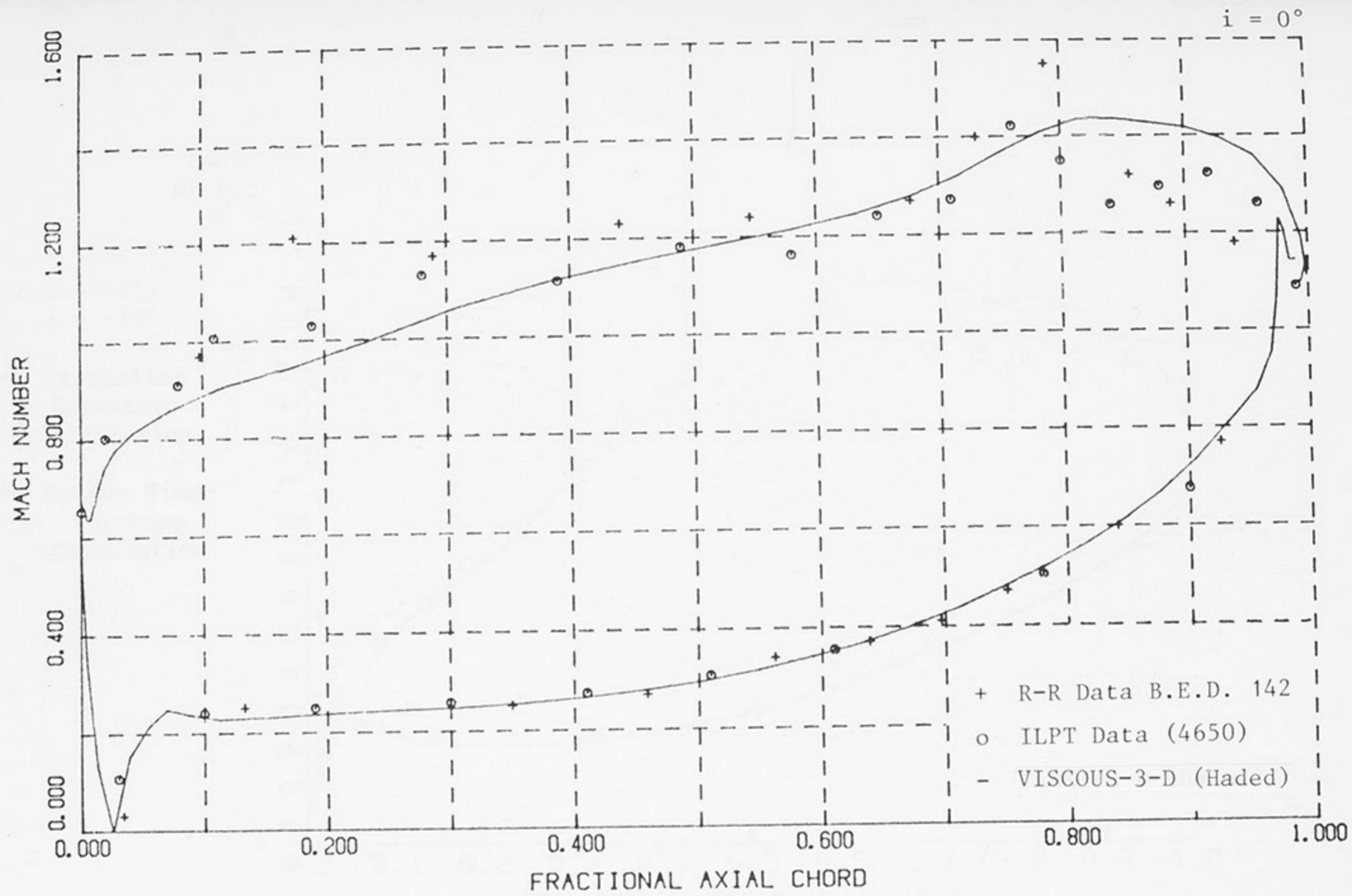

Fig. 4.3 Comparison of Measured Mach Number Distributions using the ILPT and the B.E.D. 142 Cascade with a VISCOUS-3-D Prediction.

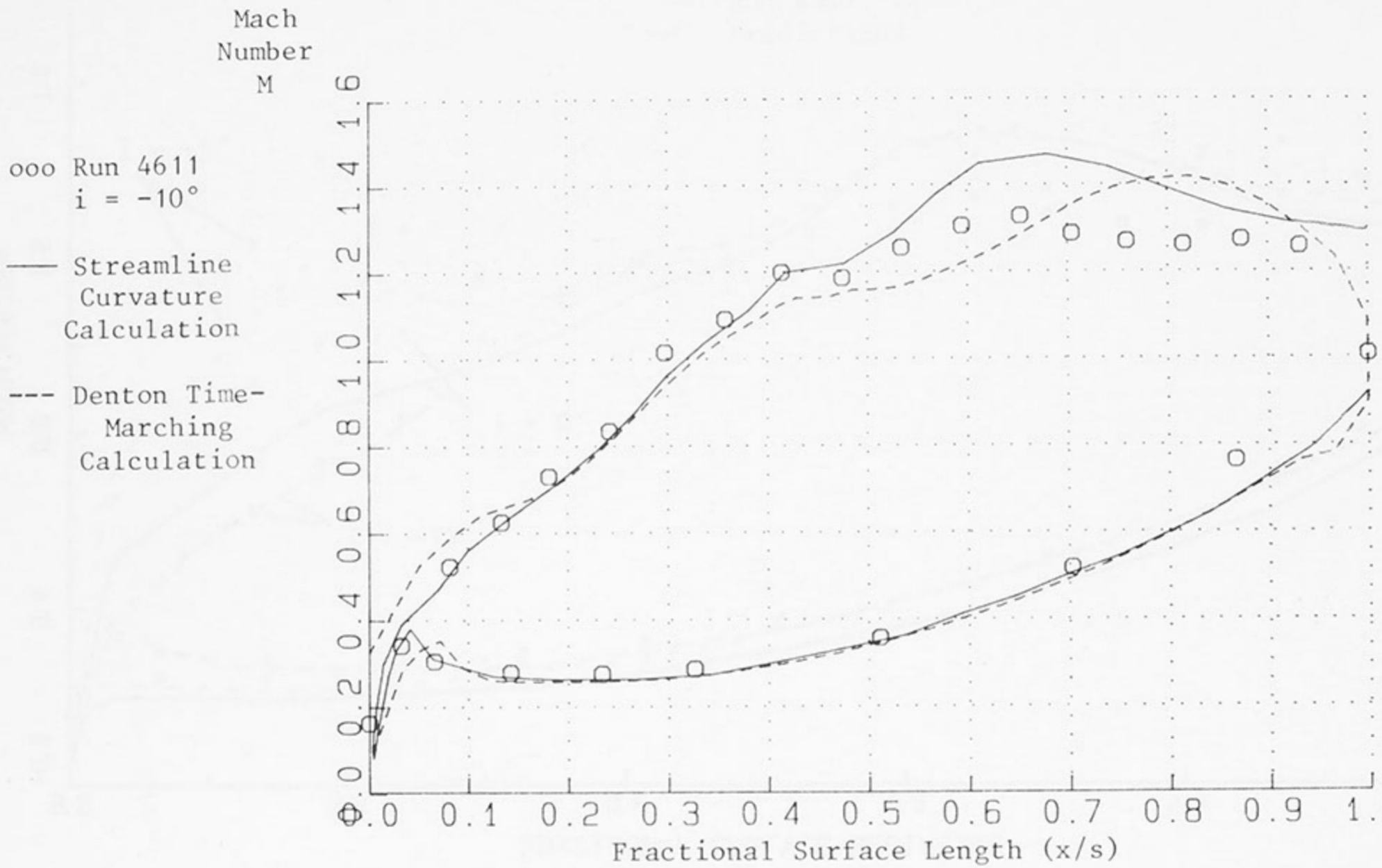

Fig. 4.4 Comparison of Measured Mach Number Distributions with Prediction at i = -10°.

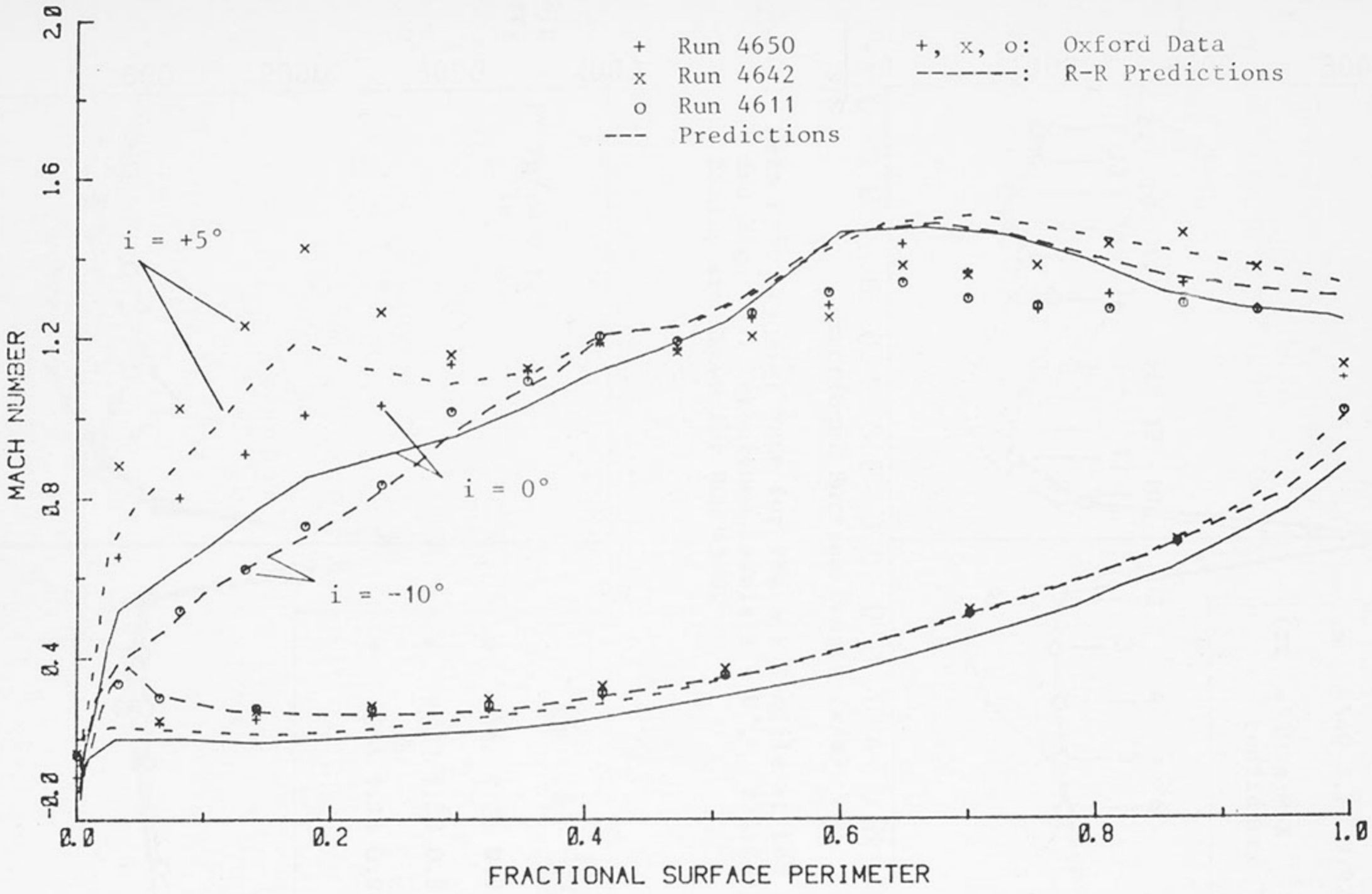

Fig. 4.5 Comparison of ILPT Mach Number Distributions with the Original Design Predictions for the ACE Profile at $M_2 = 1.18$.

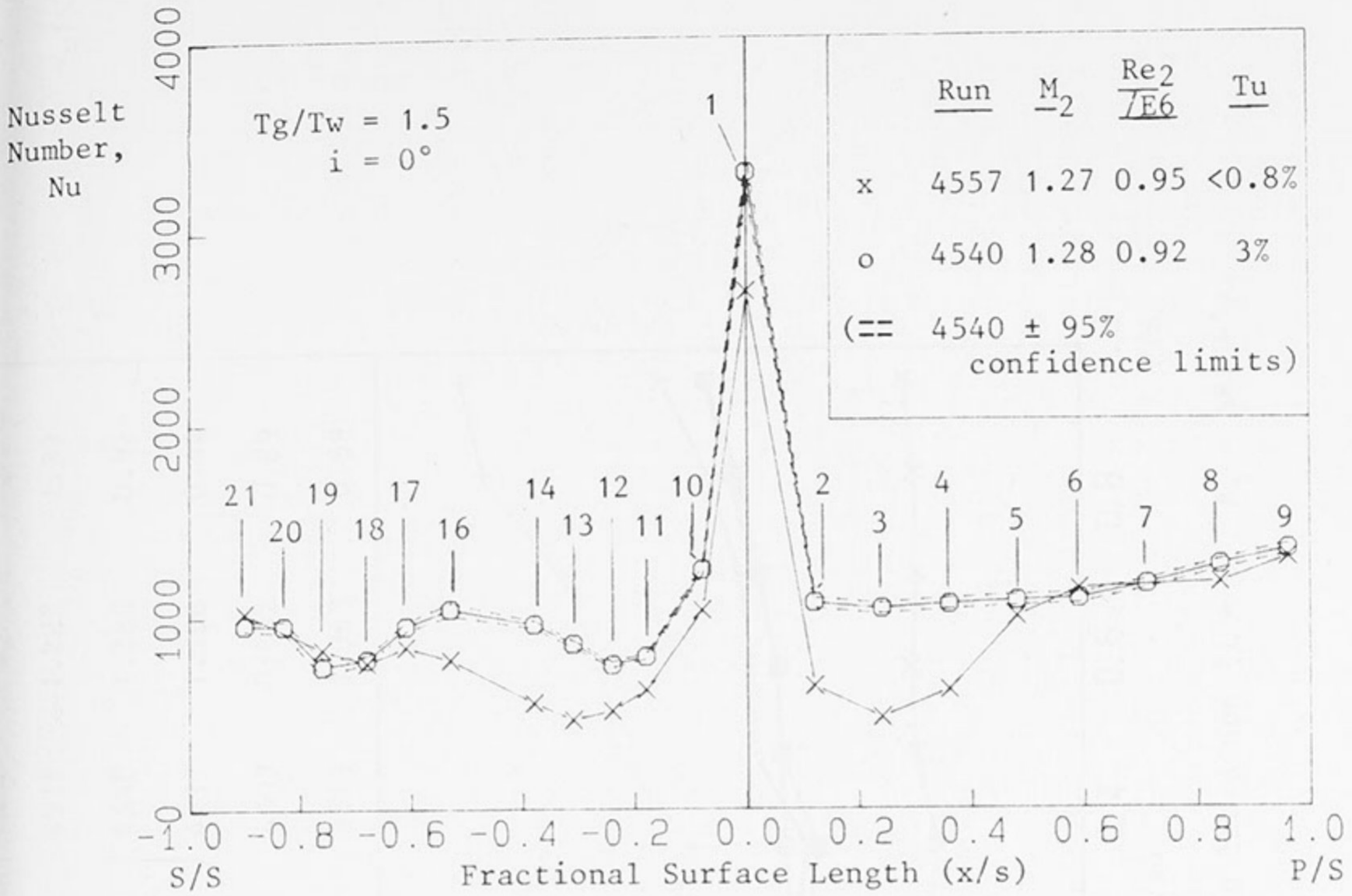

Fig. 4.6(a) Mean Heat Transfer Rate for the ACE Profile at Low (<0.8%) and High (3%) Turbulence Levels i = 0°, 95% Confidence Limits are Shown for Run 4540.

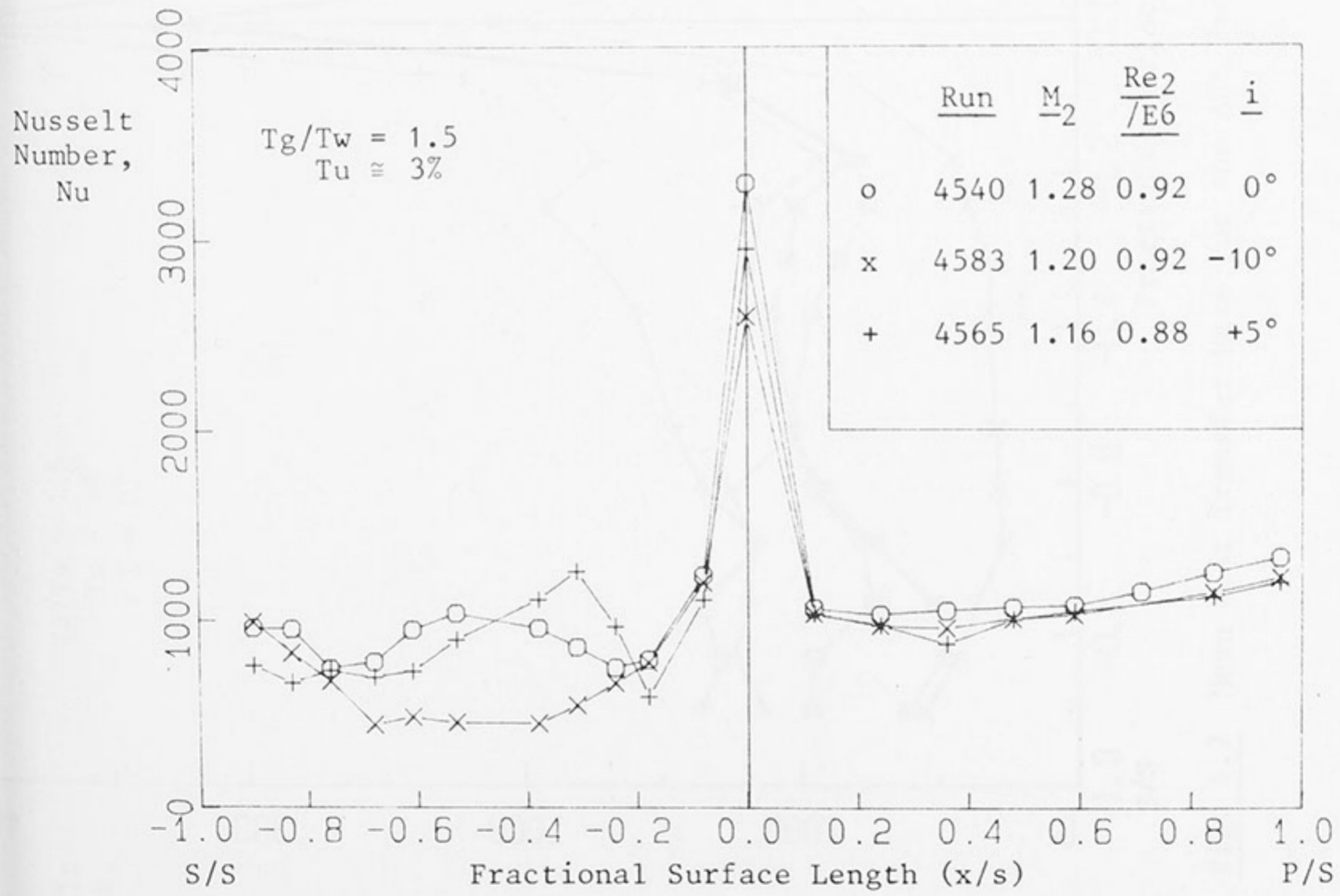

Fig. 4.6(b) Mean Heat Transfer Rate for the ACE Profile with Variation of Inlet Incidence. Design Inlet Angle (58.06°) Corresponds to i = 0°.

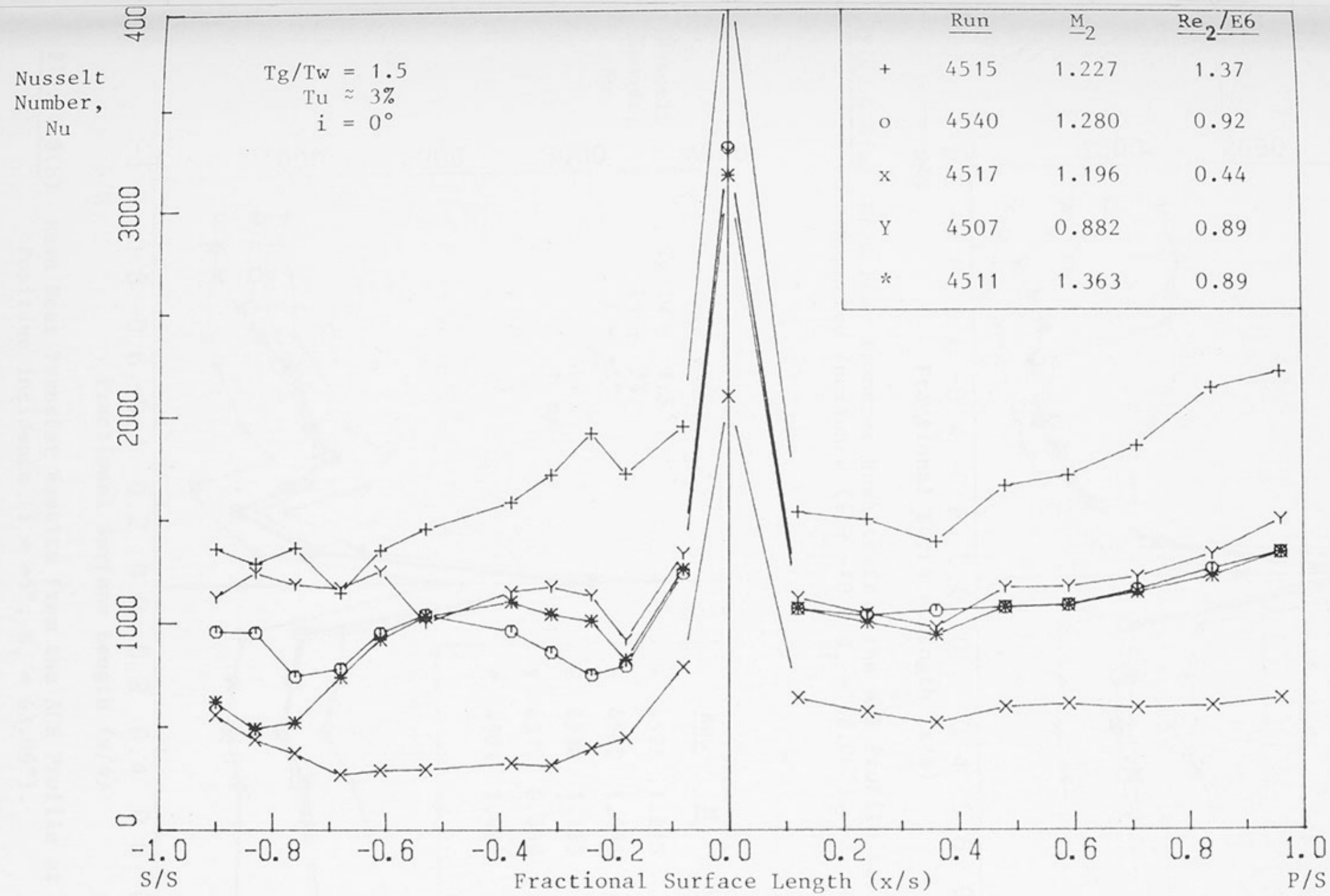

Fig. 4.7 Mean Heat Transfer Rate for the ACE Profile at Zero Incidence (i = 0°, β_1 = 58.06°).

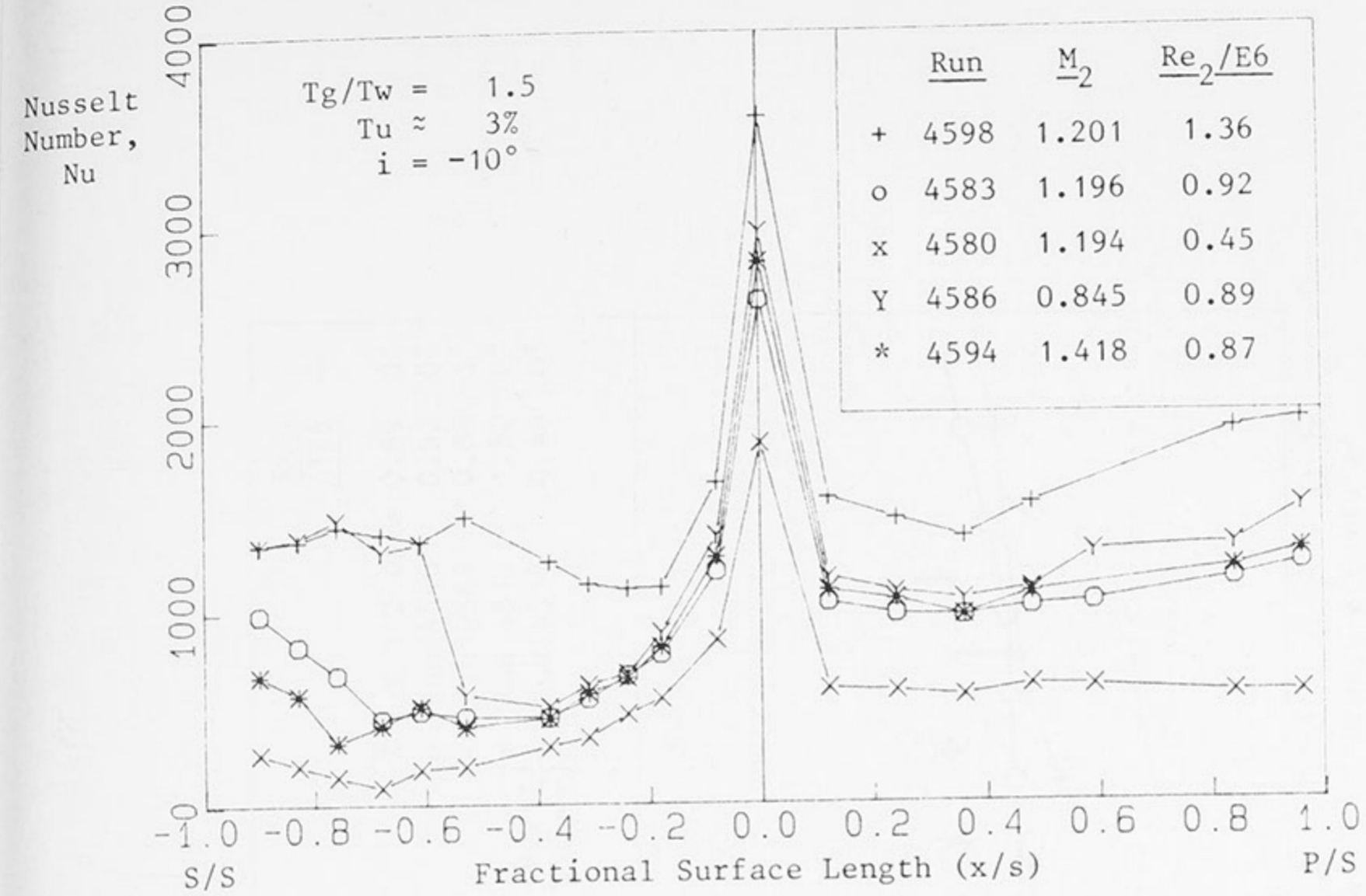

Fig. 4.8(a) Mean Heat Transfer Results from the ACE Profile at 10° of Negative Incidence ($i = -10°$, $\beta_1 = 48.06°$).

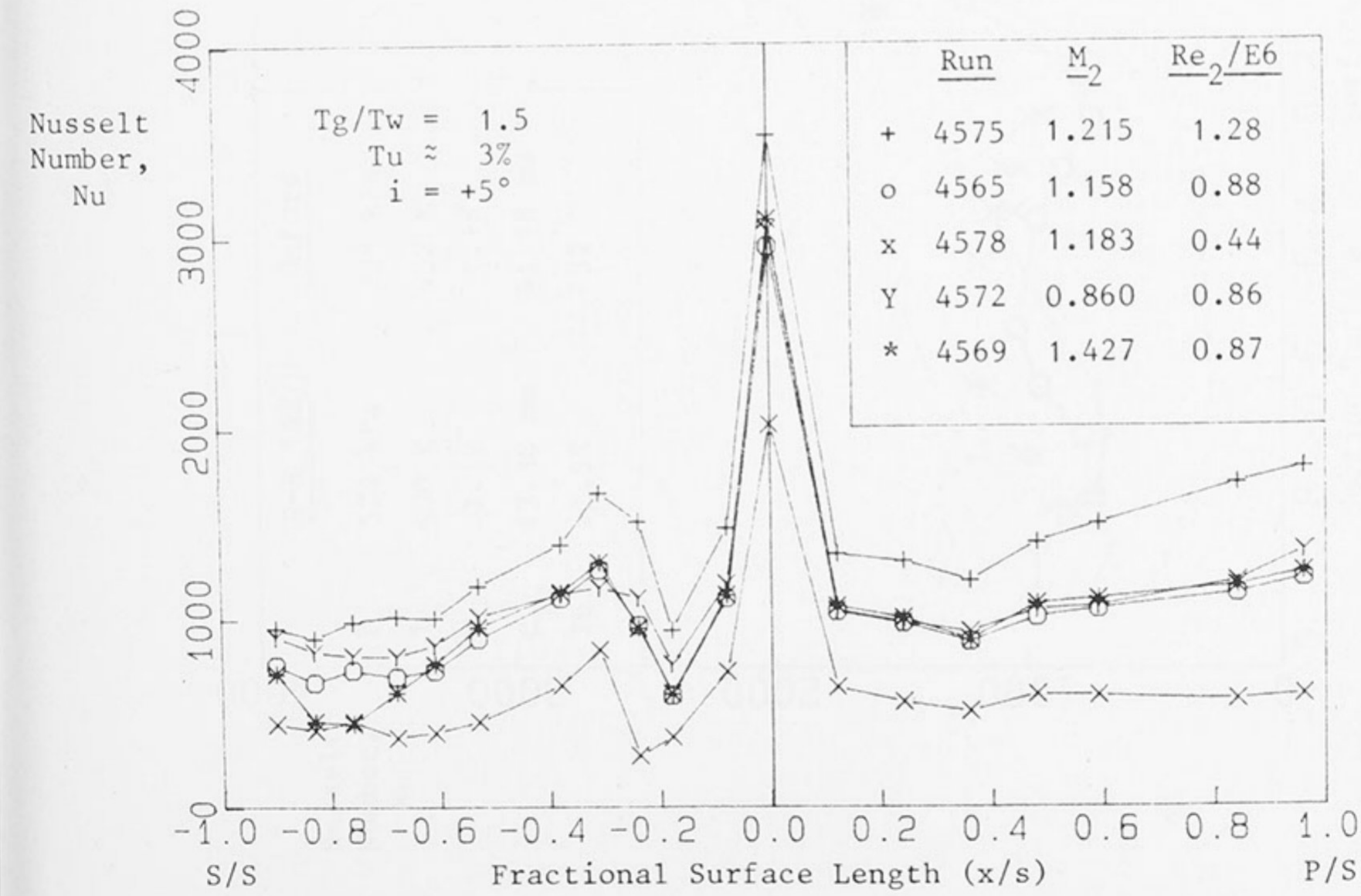

Fig. 4.8(b) Mean Heat Transfer Results from the ACE Profile at 5° of Positive Incidence ($i = +5°$, $\beta_1 = 63.06°$).

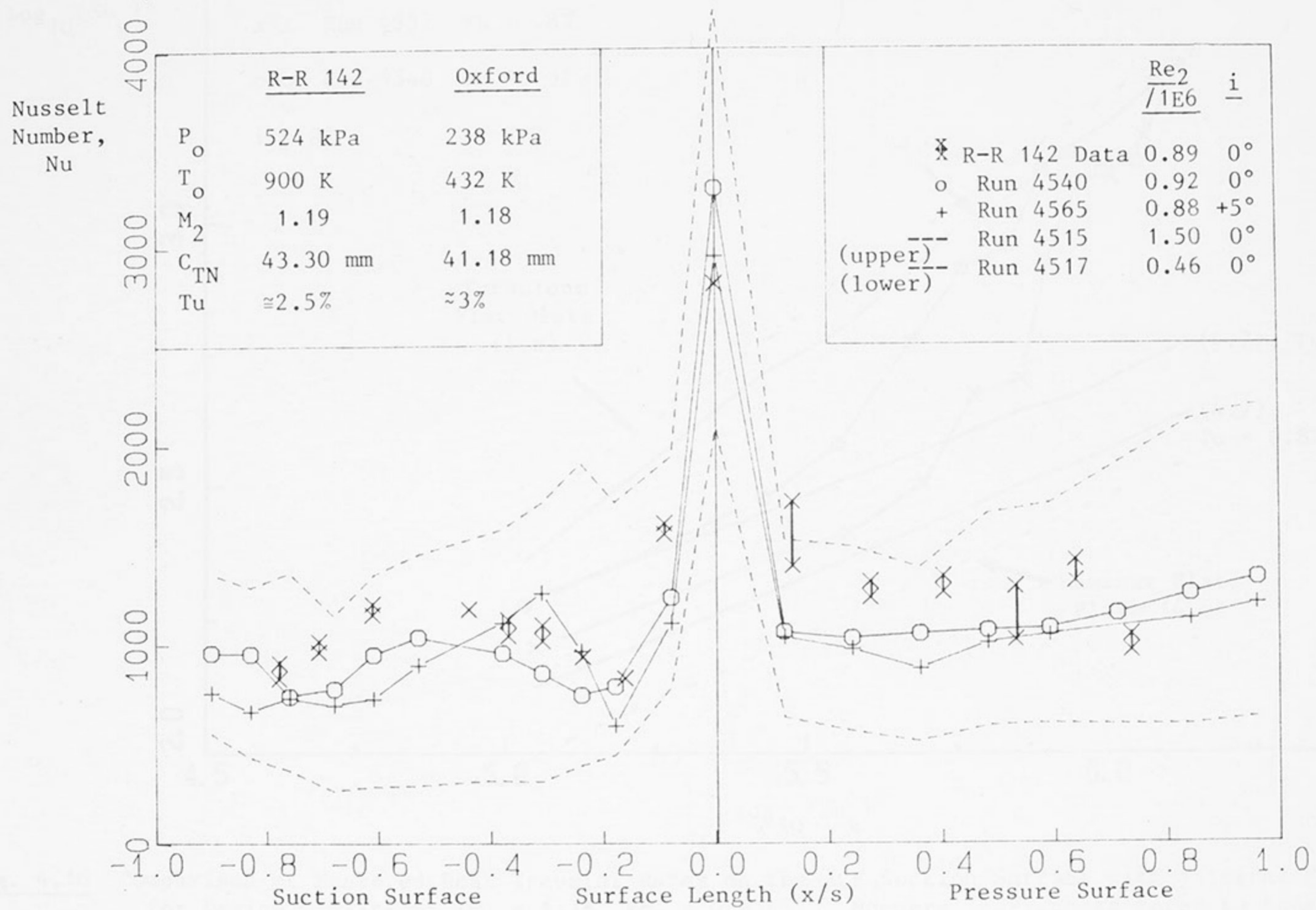

Fig. 4.9 Comparison of ACE Heat Transfer Data from the ILPT and R-R Rig 142.

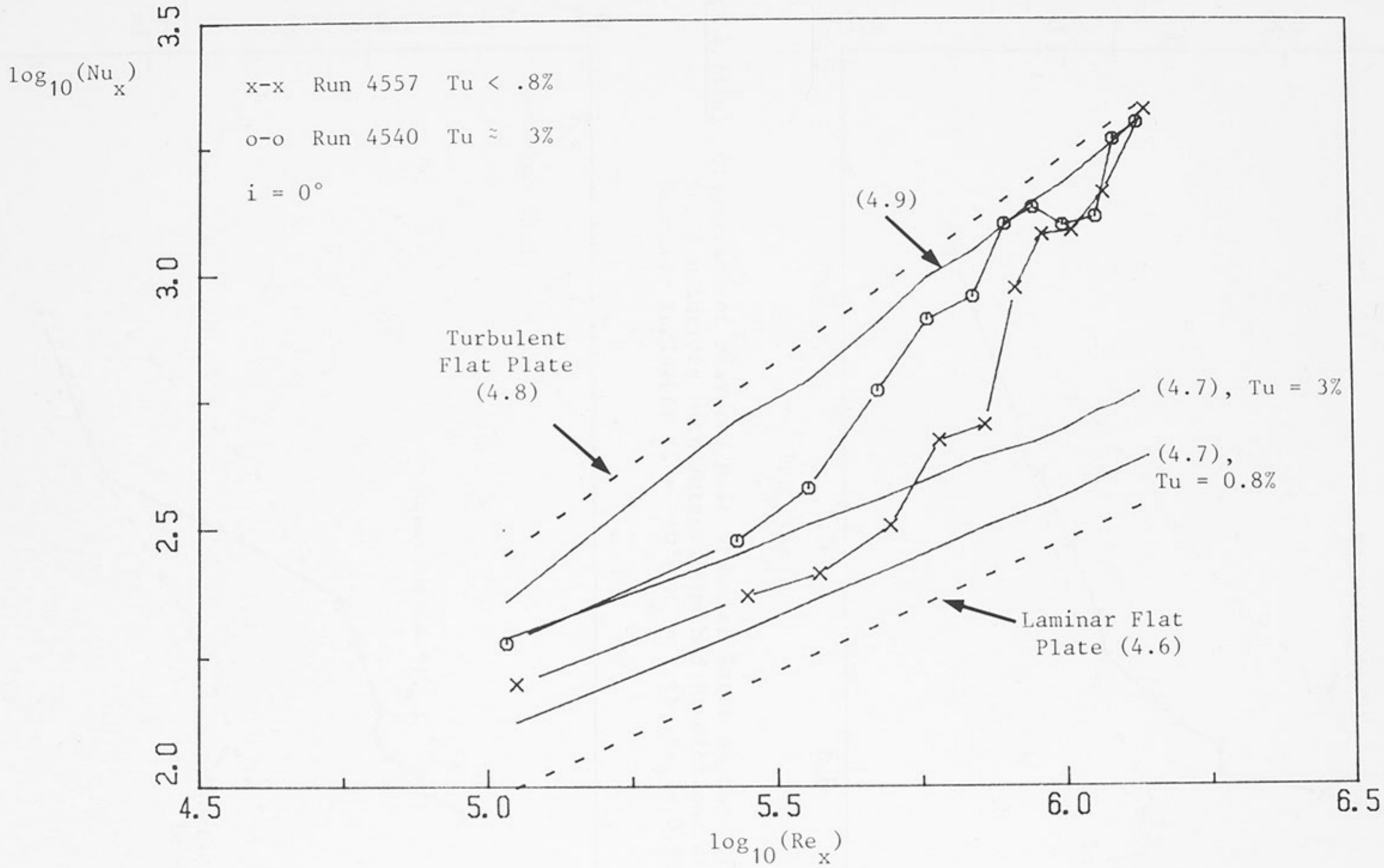

Fig. 4.10 Comparison of Measured Heat Transfer Rates on the ACE Suction Surface with Integral Method Predictions for Design Conditions (M_2 = 1.18, Re_2 = 0.92E6). Numbers in Brackets refer to Equations in Chapter IV.

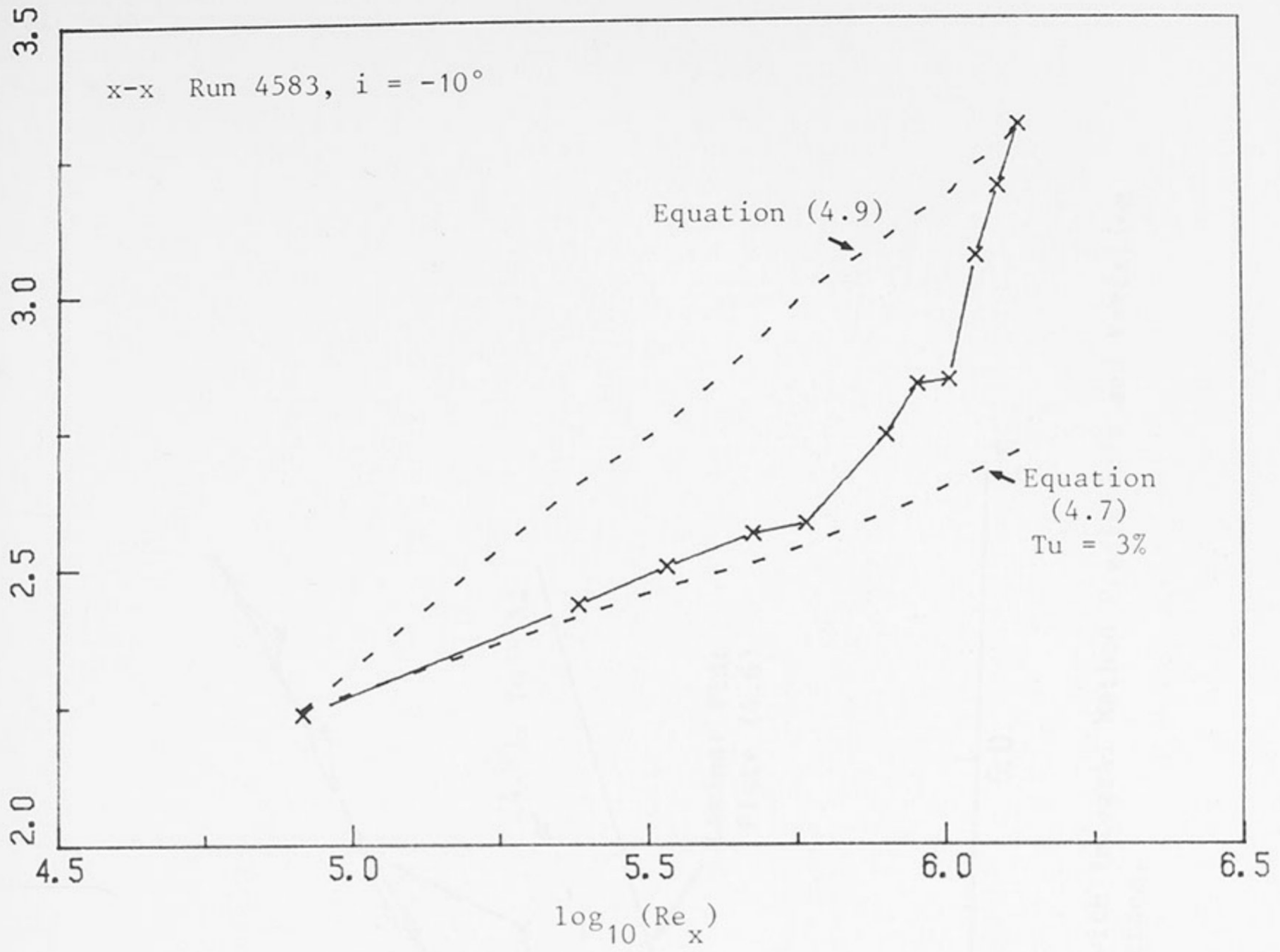

Fig. 4.11(a) Comparison of Measured Heat Transfer Rates on the ACE Suction Surface with Integral Method Predictions at Negative Incidence ($i = -10°$, $M_2 = 1.18$, $Re_2 = 0.92E6$).

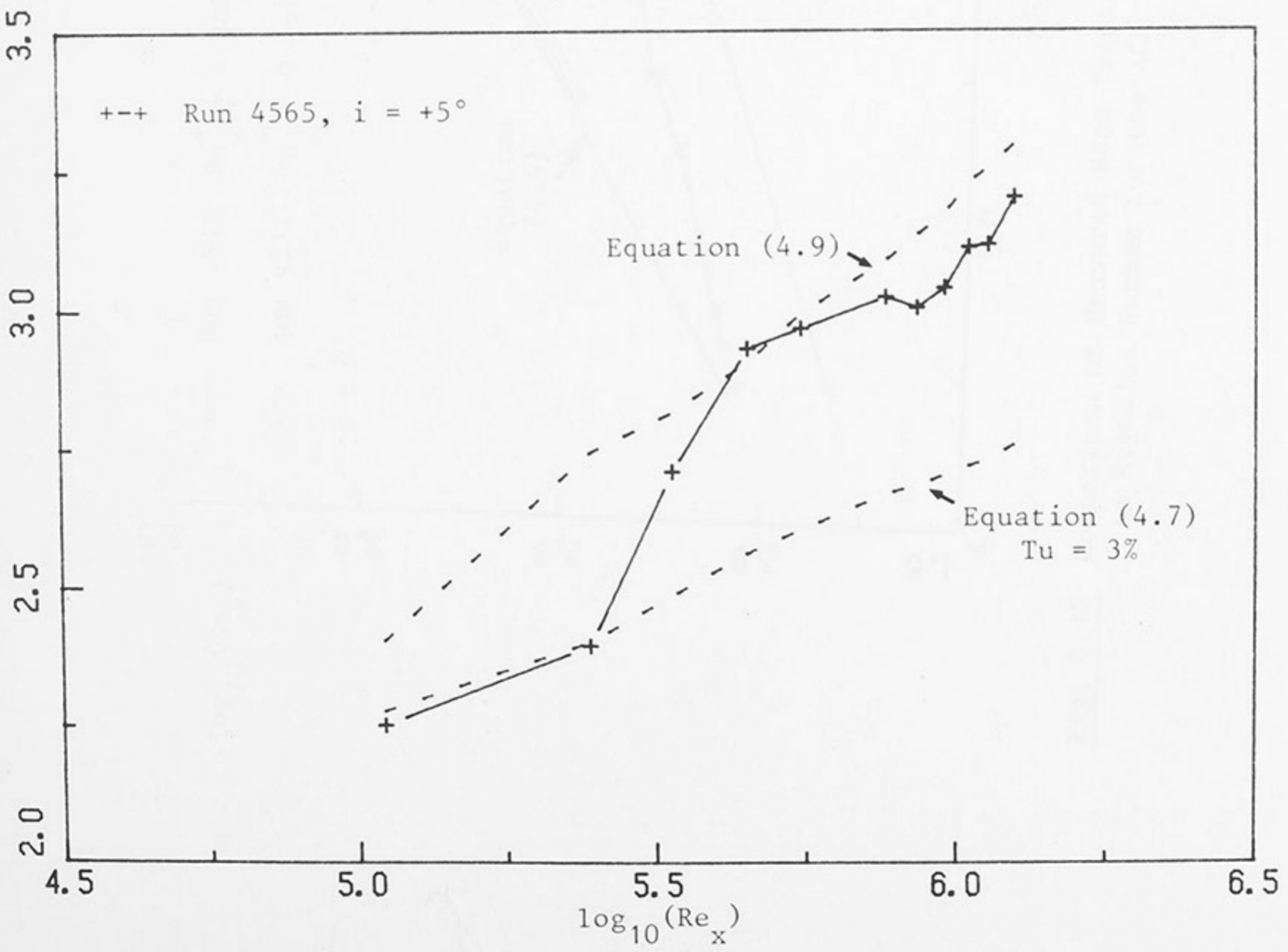

Fig. 4.11(b) Comparison of Measured Heat Transfer Rates on the ACE Suction Surface with Integral Method Predictions at Positive Incidence ($i = +5°$, $M_2 = 1.18$), $Re_2 = 0.92E6$).

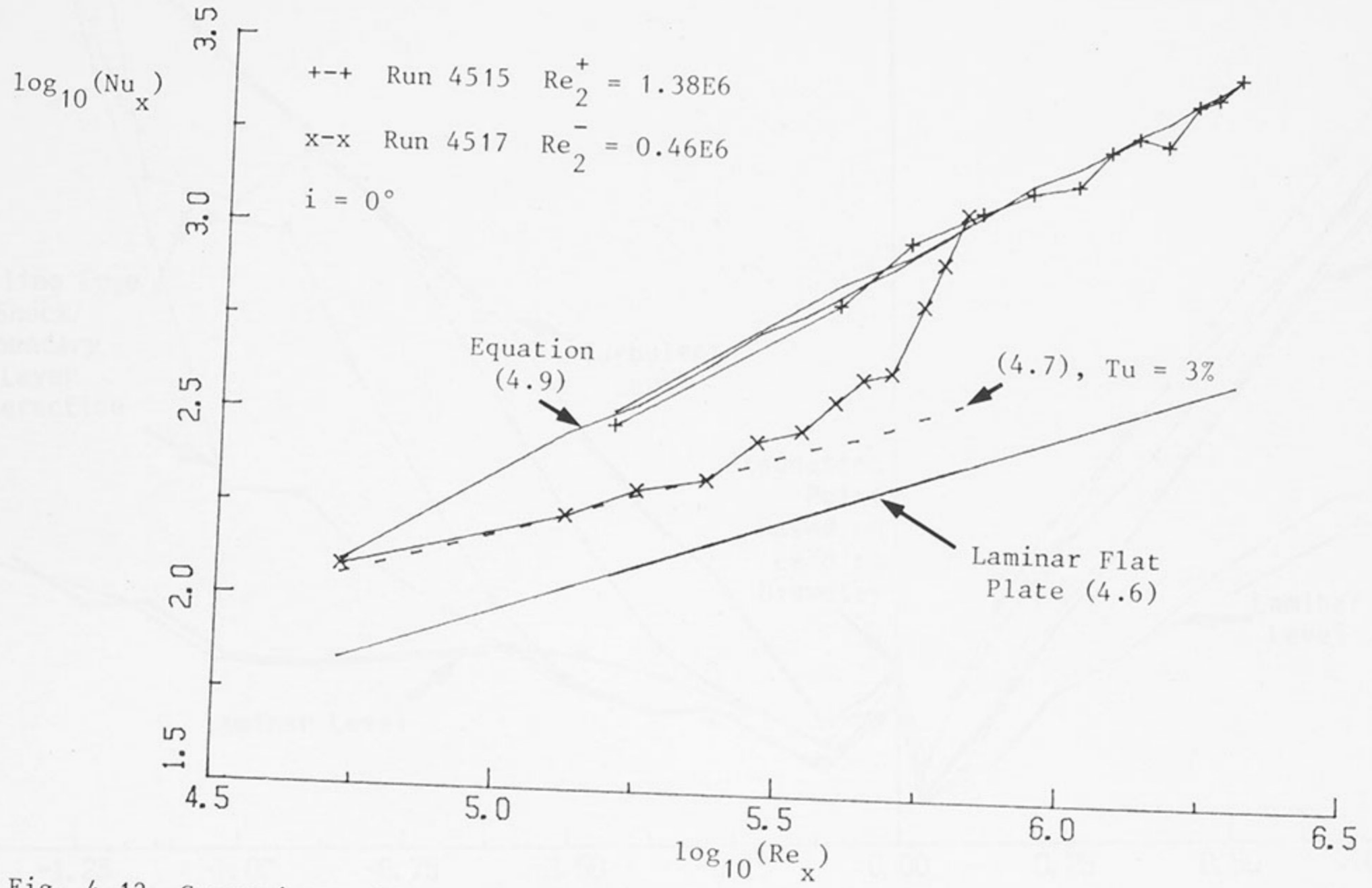

Fig. 4.12 Comparison of Measured Heat Transfer Rates with Integral Method Predictions and Variation in Reynolds Number for the ACE Suction Surface.

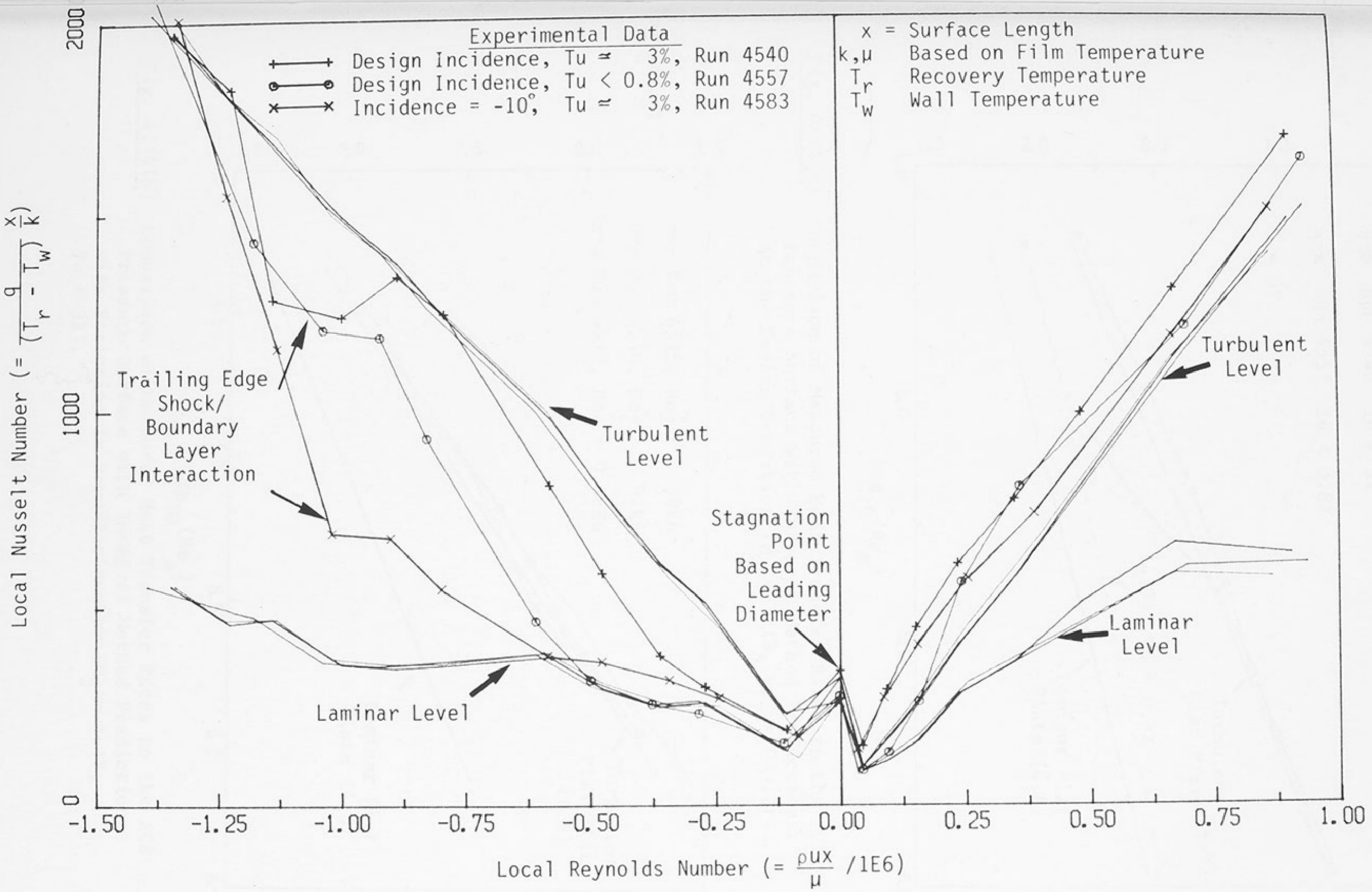

Fig.4.13 Comparison of Experimental Data and Integral Method Correlations: Surface Nusselt Numbers for Natural Transition on the ACE Profile.

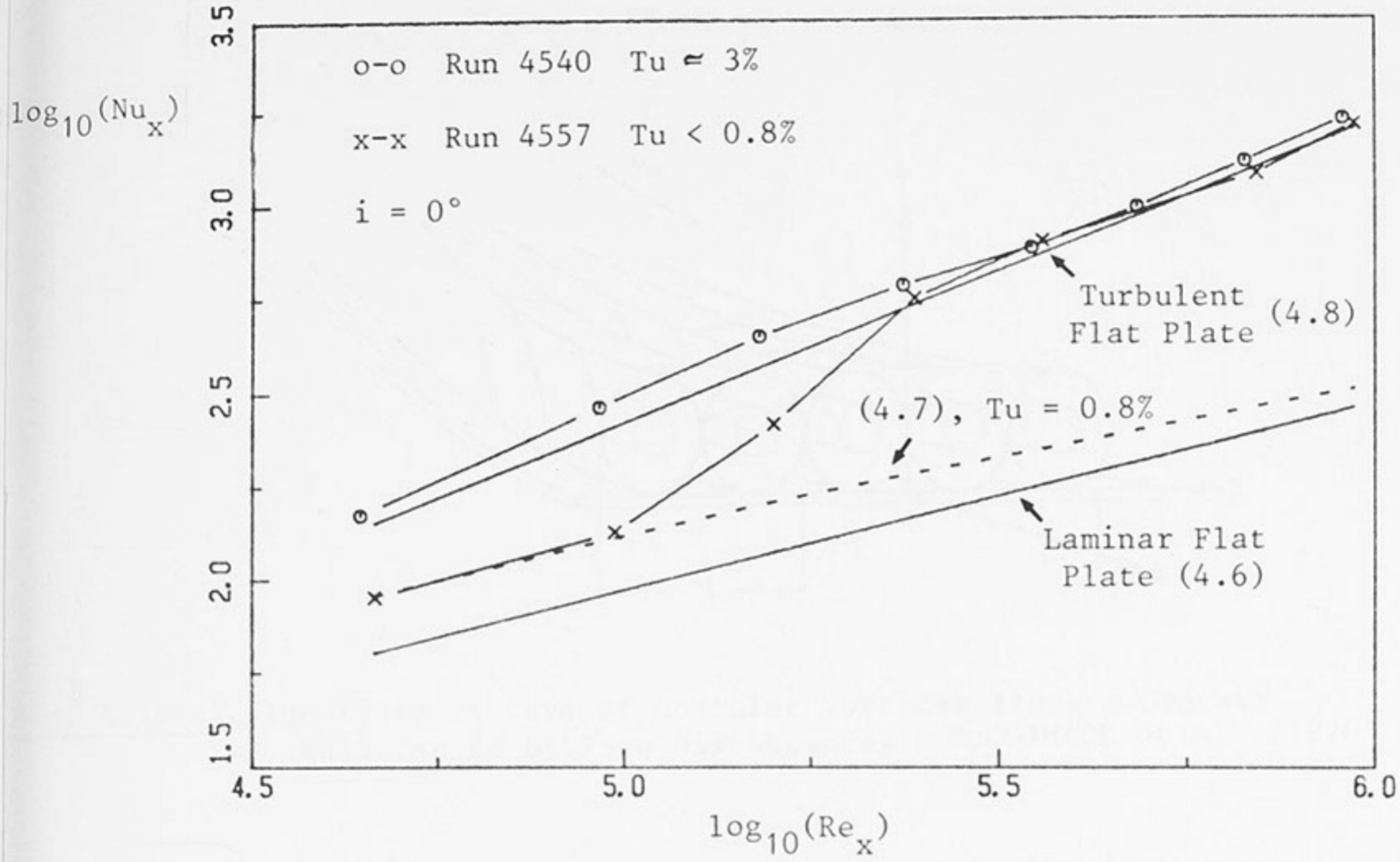

Fig. 4.14(a) Comparison of Measured Heat Transfer Rates to the ACE Pressure Surface with Integral Method Predictions: at the Design Condition (M_2 = 1.18, Re_2 = 0.92E6).

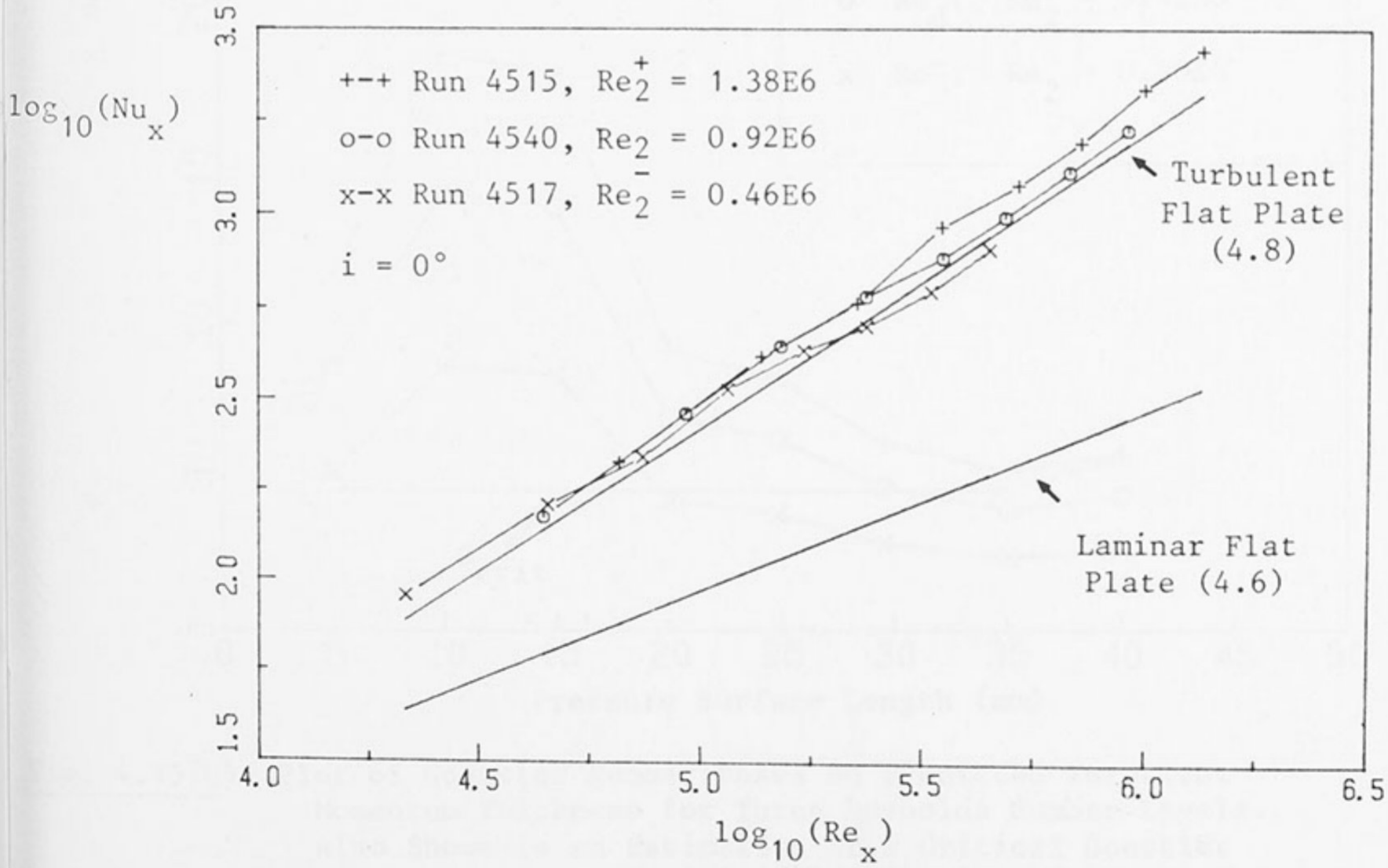

Fig. 4.14(b) Comparison of Measured Heat Transfer Rates to the ACE Pressure Surface with Integral Method Predictions with Variation in Reynolds Number (M_2 = 1.18, Tu ≅ 3%).

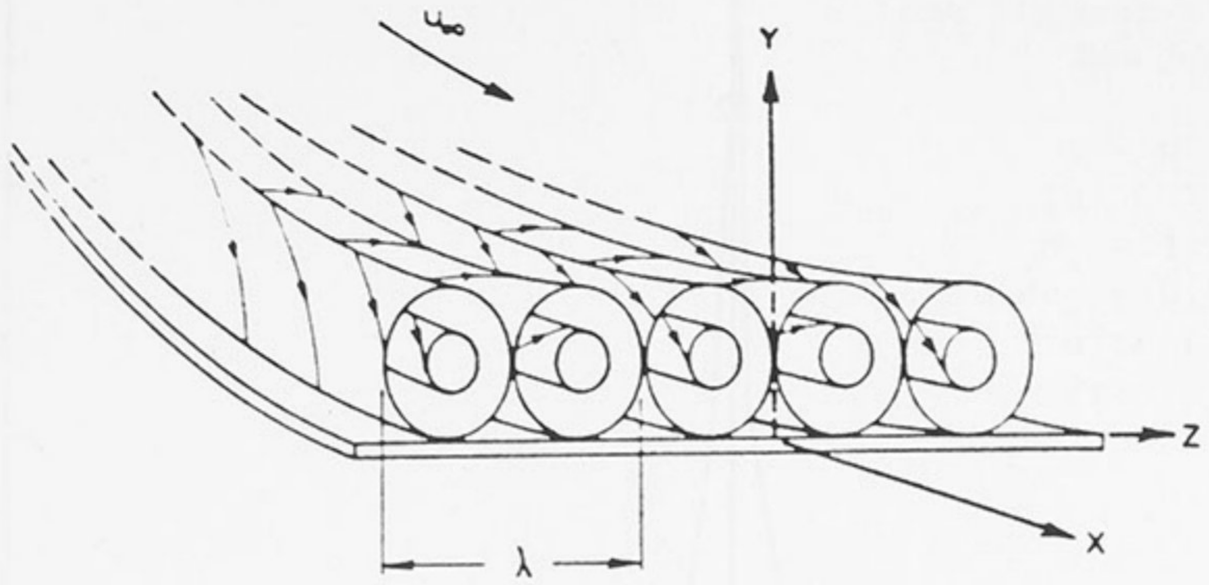

Fig. 4.15(a) Idealised Picture of Goertler Vortices Along a Concave Wall Caused by Flow Disturbances. McCORMACK et al. [1970]

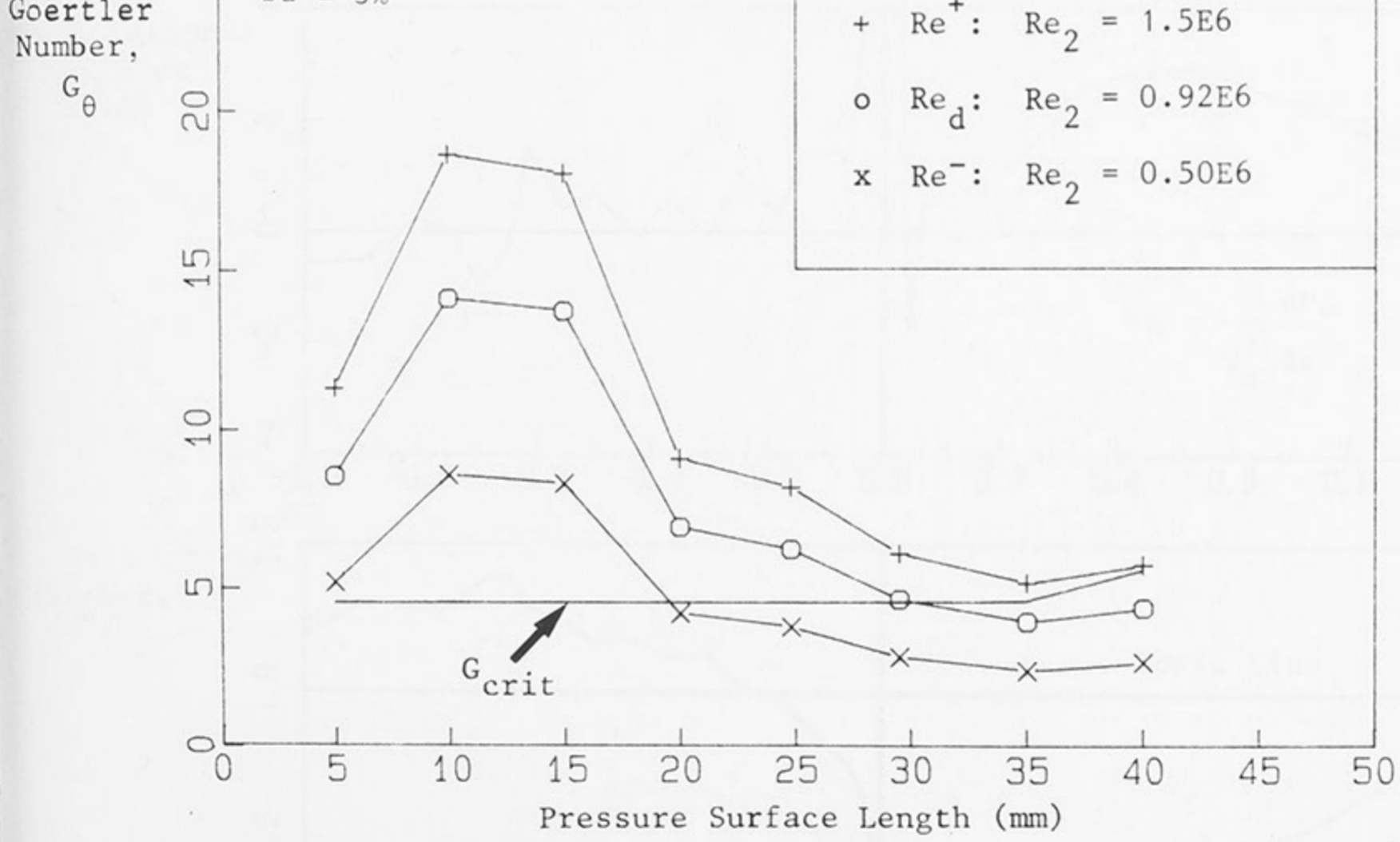

Fig. 4.15(b) Plot of Goertler Number Based on Predicted Turbulent Momentum Thickness for Three Reynolds Number Levels. Also Shown is an Estimation of a Critical Goertler Number based on FOREST[1977]. (Laminar Goertler Numbers Exceed Critical Values Prior to the First Measurement Point with High Freestream Turbulence Level.)

$$G_{crit} = 9 \exp(-17.3\ Tu_\ell)$$

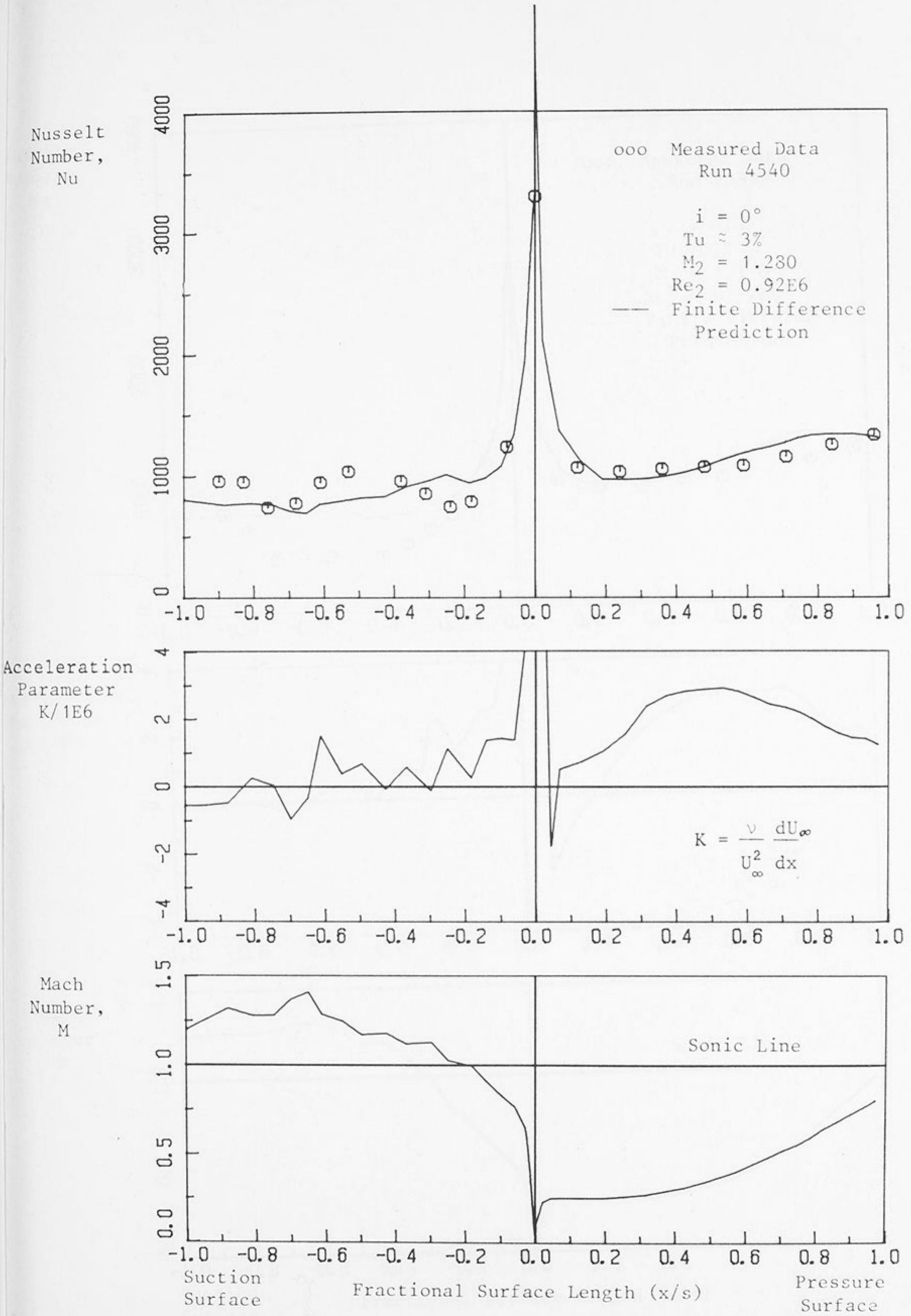

Fig. 4.16 Comparison of Measured Heat Transfer Rate for the ACE Profile at Zero Incidence (i = 0°) with Prediction. Also Shown are the Distributions of Acceleration Parameter and Mach Number derived from Measured Aerodynamic Data.

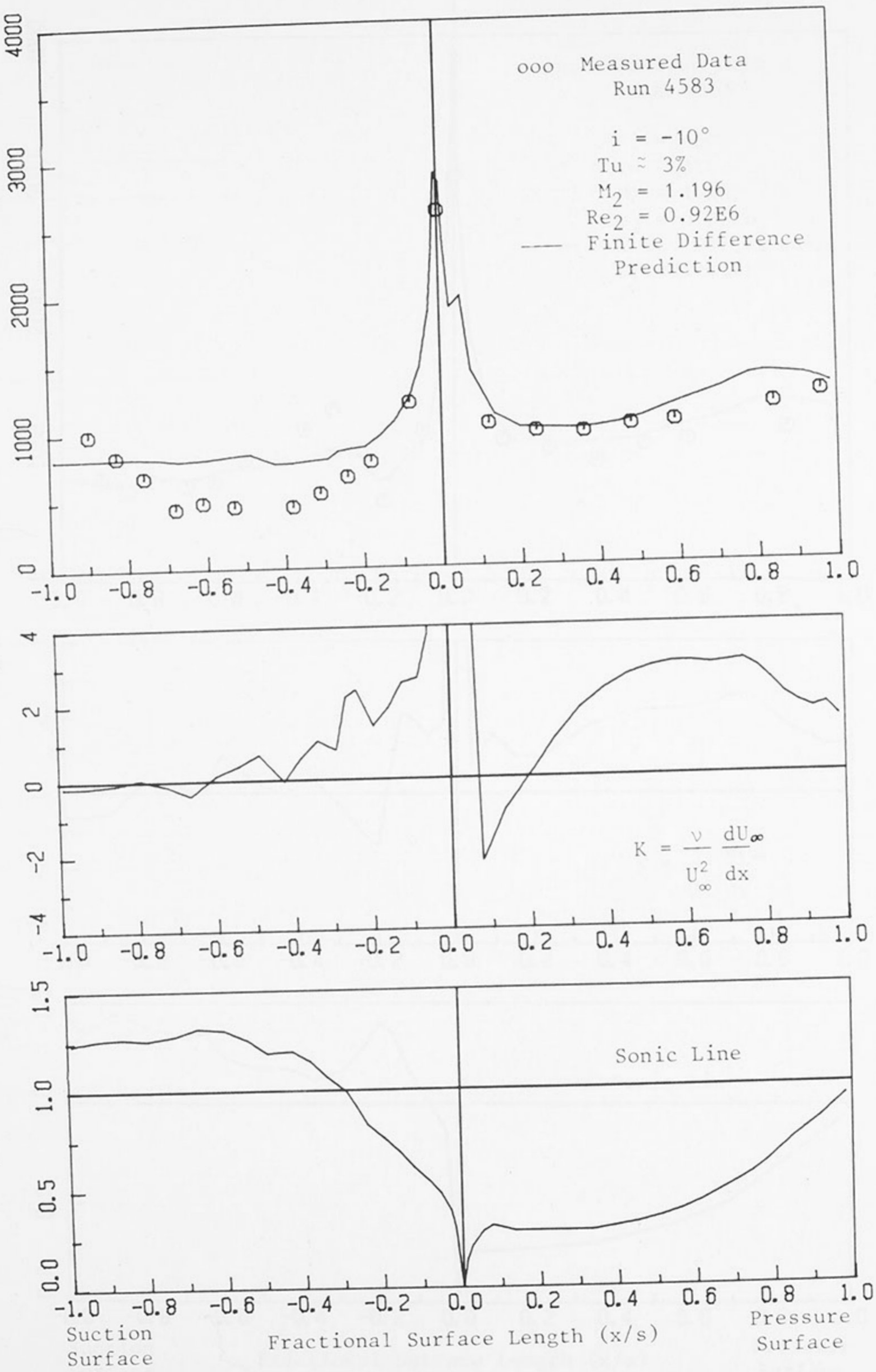

Fig. 4.17 Comparison of Measured Heat Transfer Rate for the ACE Profile at Negative Incidence (i = -10°) with Prediction. Also Shown are the Distribution of Acceleration Parameter and Mach Number derived from Measured Aerodynamic Data.

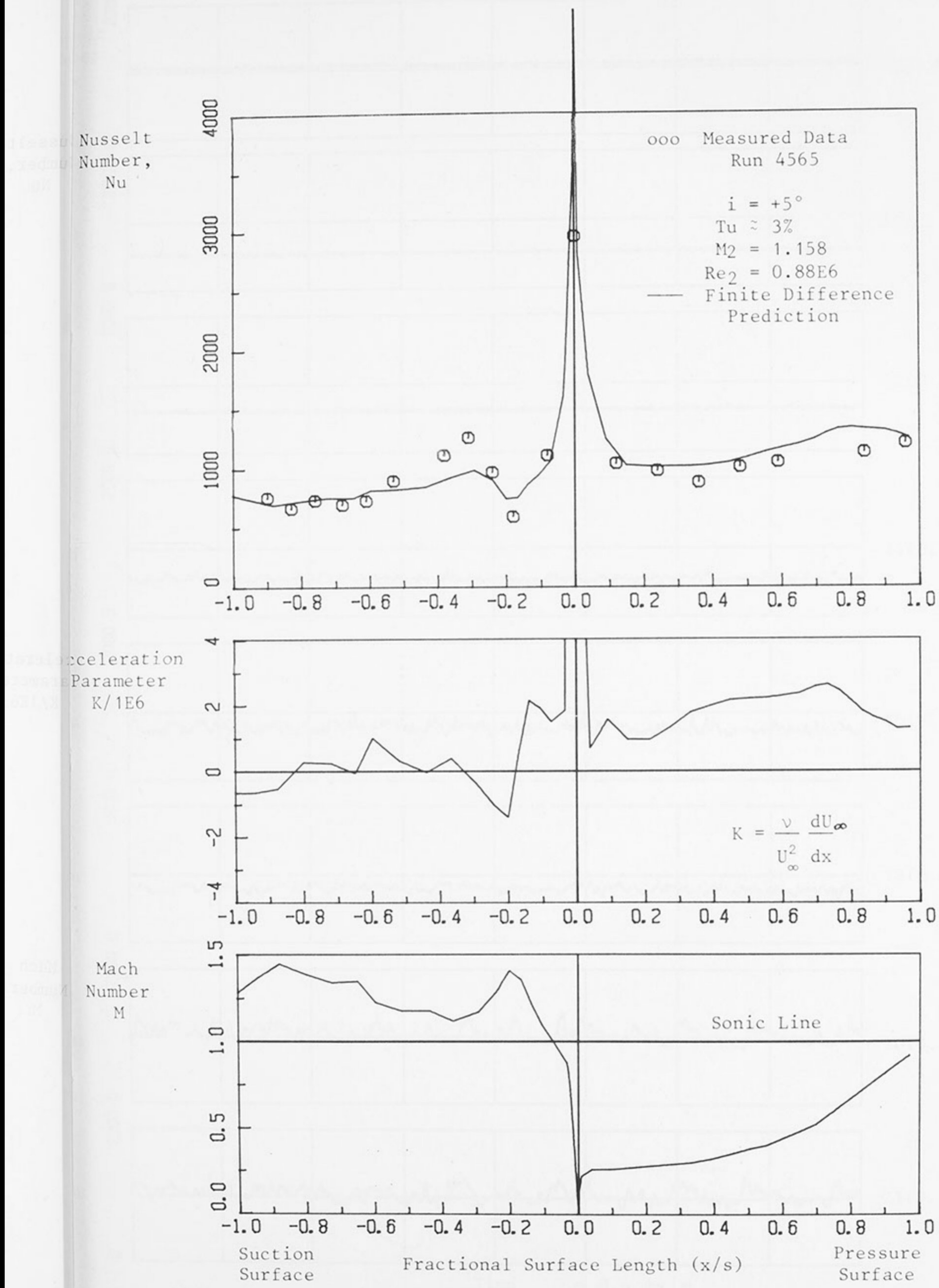

Fig. 4.18 Comparison of Measured Heat Transfer Rate for the ACE Profile at Positive Incidence (i = +5°) with Prediction. Also Shown are the Distributions of Acceleration Parameter and Mach Number derived from Measured Aerodynamic Data.

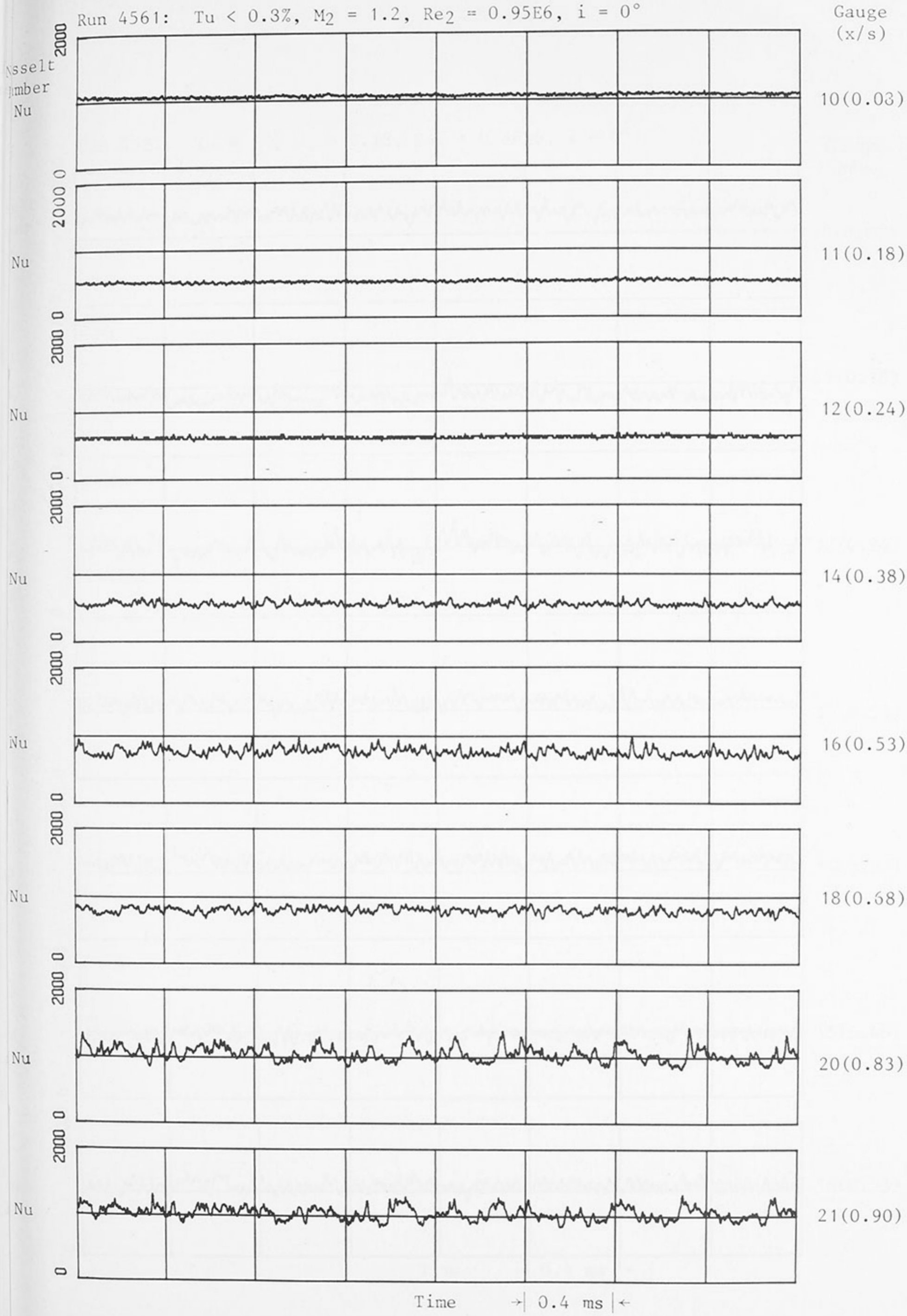

Fig. 4.19 Instantaneous Heat Transfer Data from the Suction Surface of the ACE Profile at Zero Incidence and Low Freestream Turbulence Level, Tu < 0.8%.

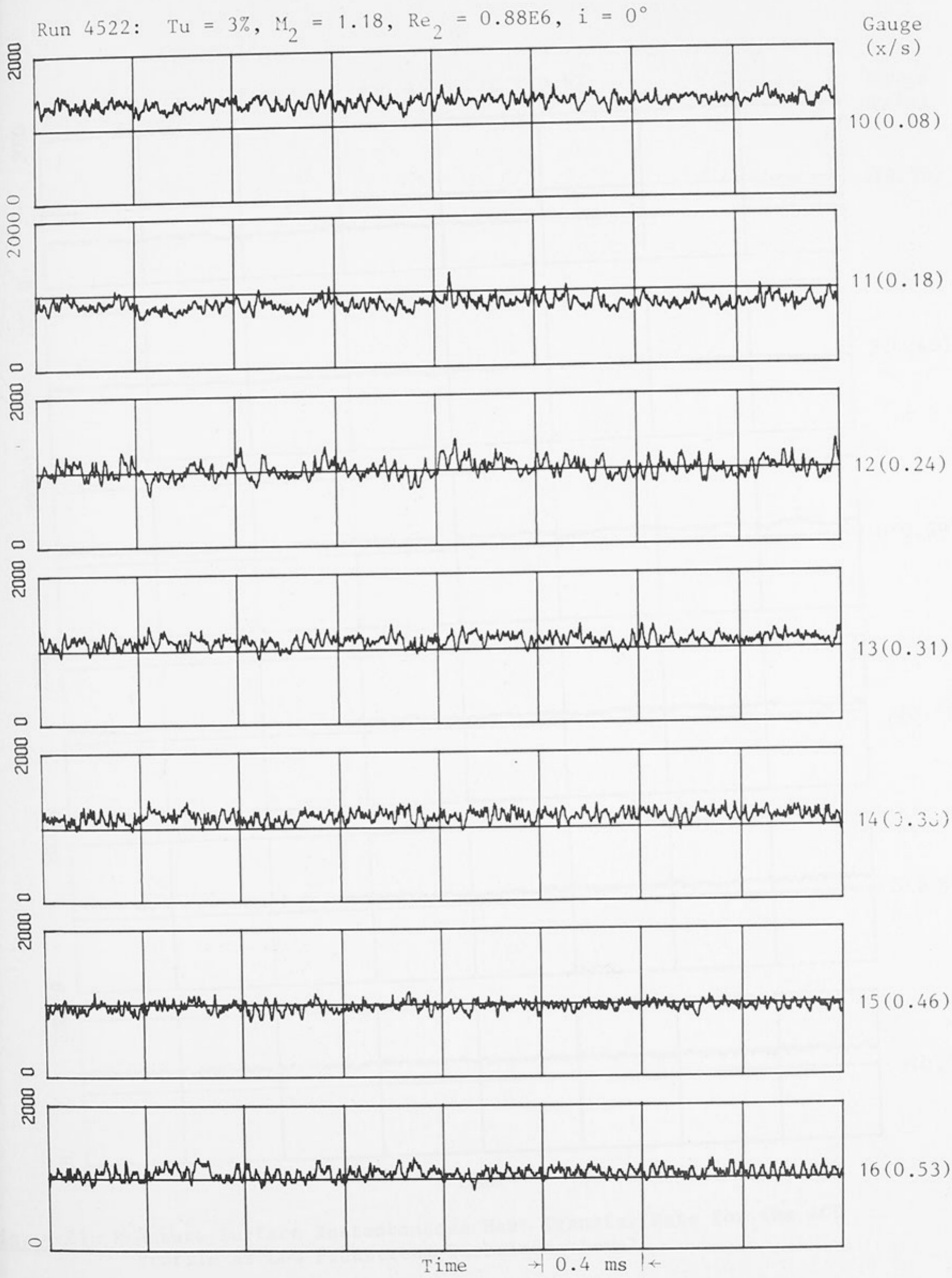

ig. 4.20 Instantaneous Heat Transfer Data from the Suction Surface of the ACE Profile at Zero Incidence and High Freestream Turbulence Level, Tu ≈ 3%.

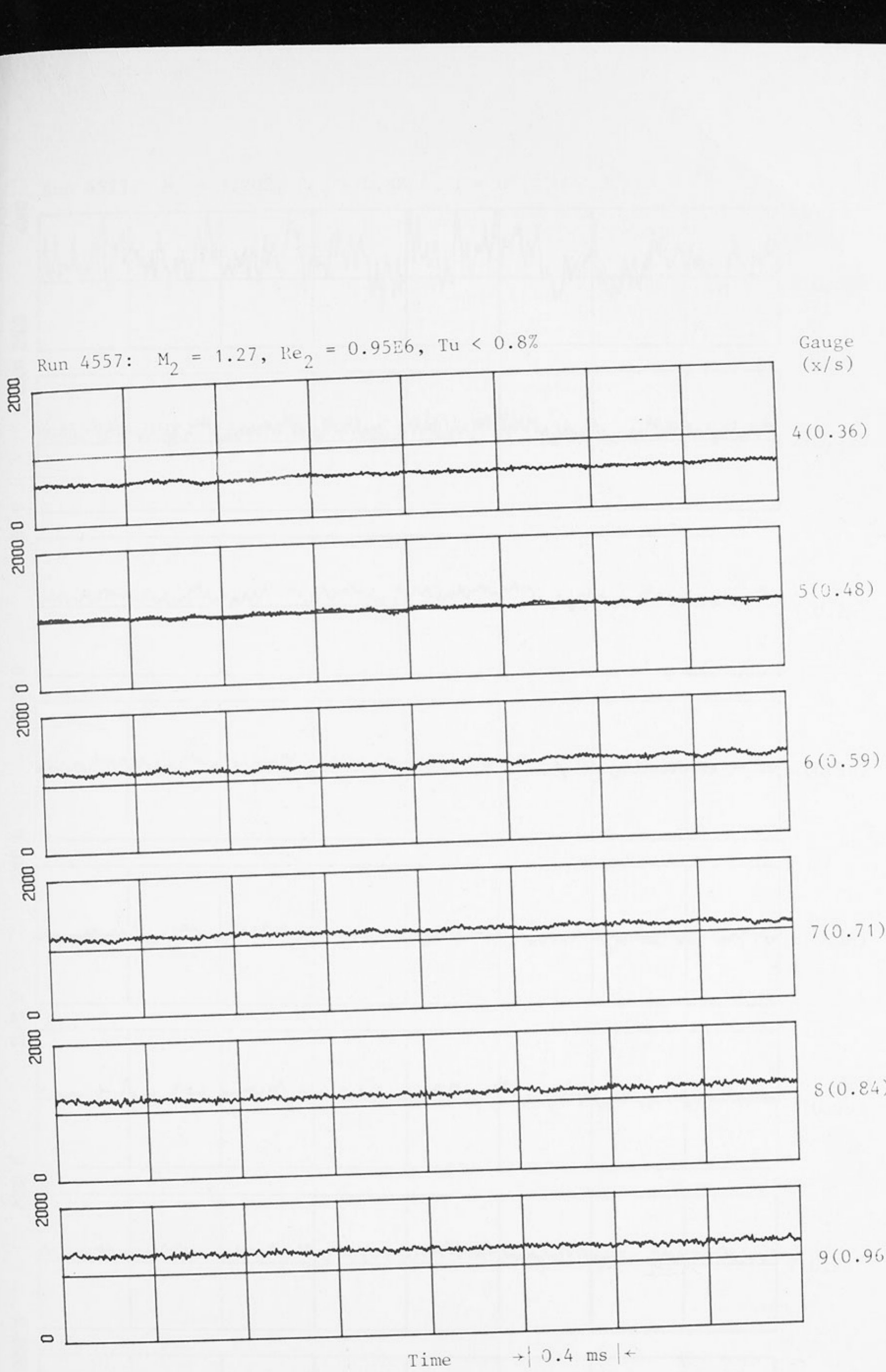

Fig. 4.21 Pressure Surface Instantaneous Heat Transfer Rate for the ACE Profile at Low Freestream Turbulence Level.

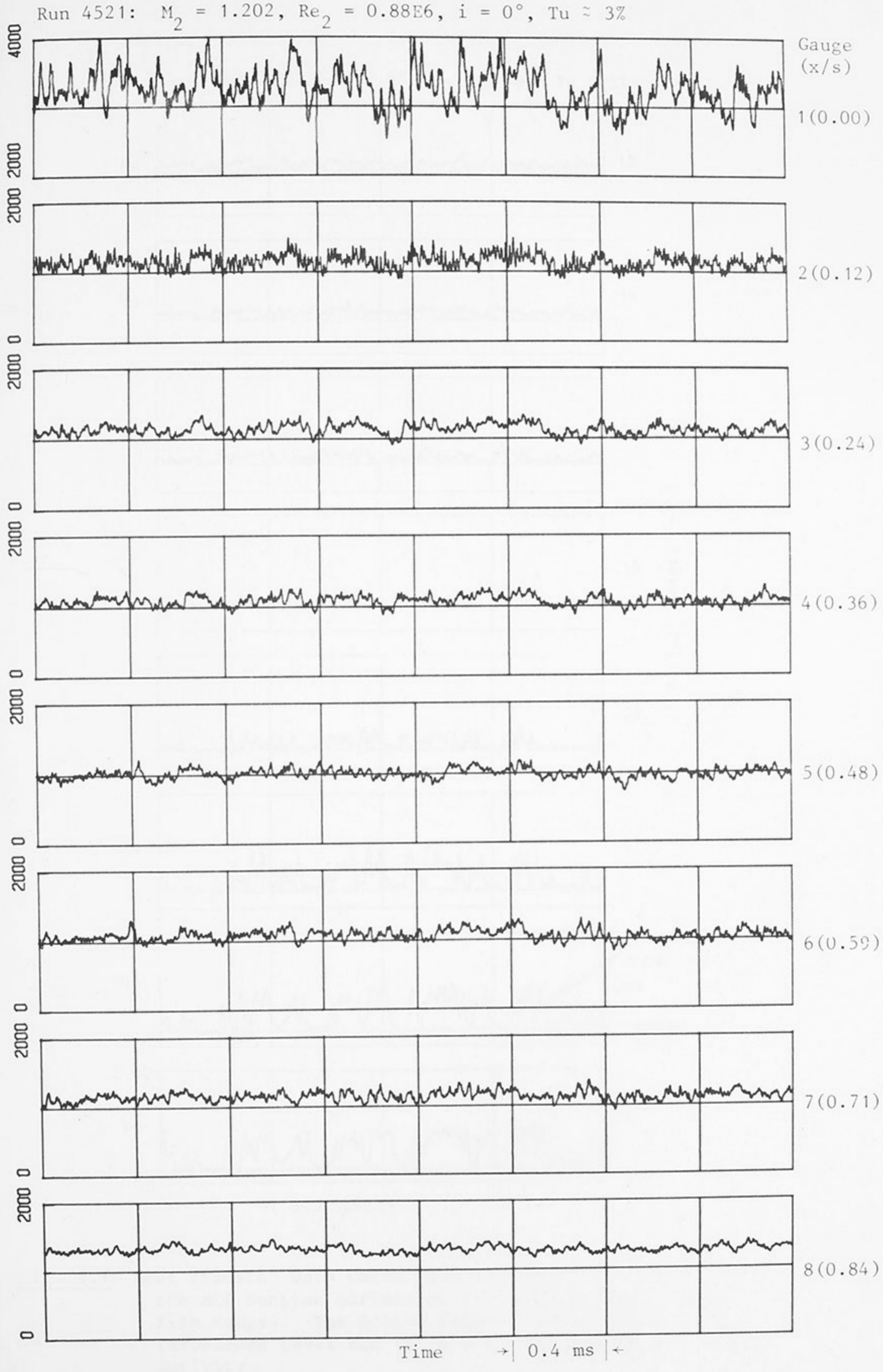

Fig. 4.22 Pressure Surface Instantaneous Heat Transfer Rate for the ACE Profile at High Freestream Turbulence Level.

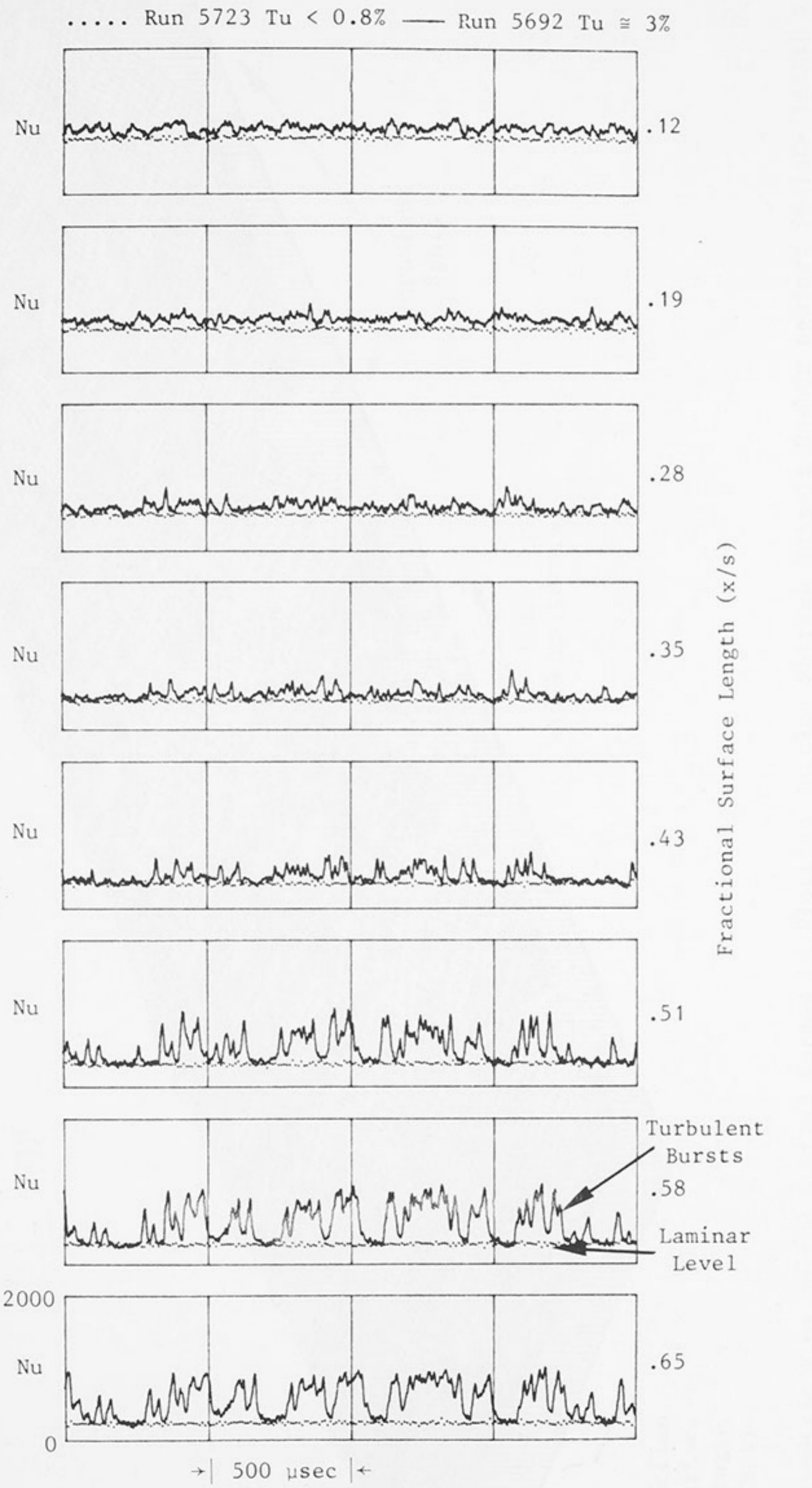

Fig. 5.1 Heat Transfer Data taken from the Second Series of Tests on the ACE Suction Surface at i = -10°, using 4 mm Wide Thin Film Gauges. The Dotted Values Correspond to a Low Turbulence Level Run (Tu < 0.8%) Exhibiting no Turbulent Activity.

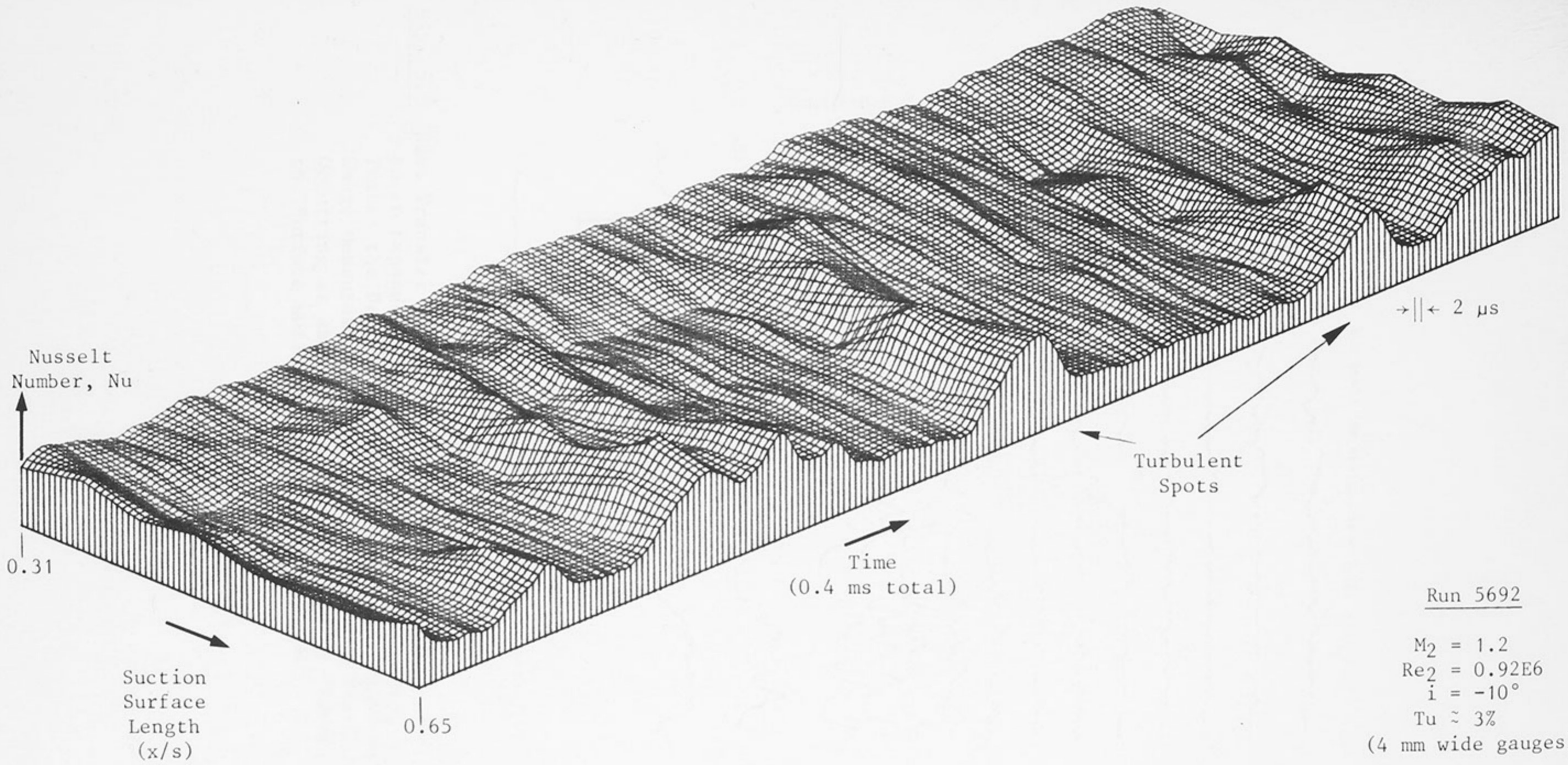

Fig. 5.2 Isometric View of the Surface formed by Plotting Suction Surface Nusselt Number against Surface Length for a Number of Successive Time Intervals. Each Data Point in the 400 μs Total Time is Plotted, Joined to the Next Surface Point Shifted in Time by 14 μs with 8 Intermediate Interpolated Positions between Gauges.

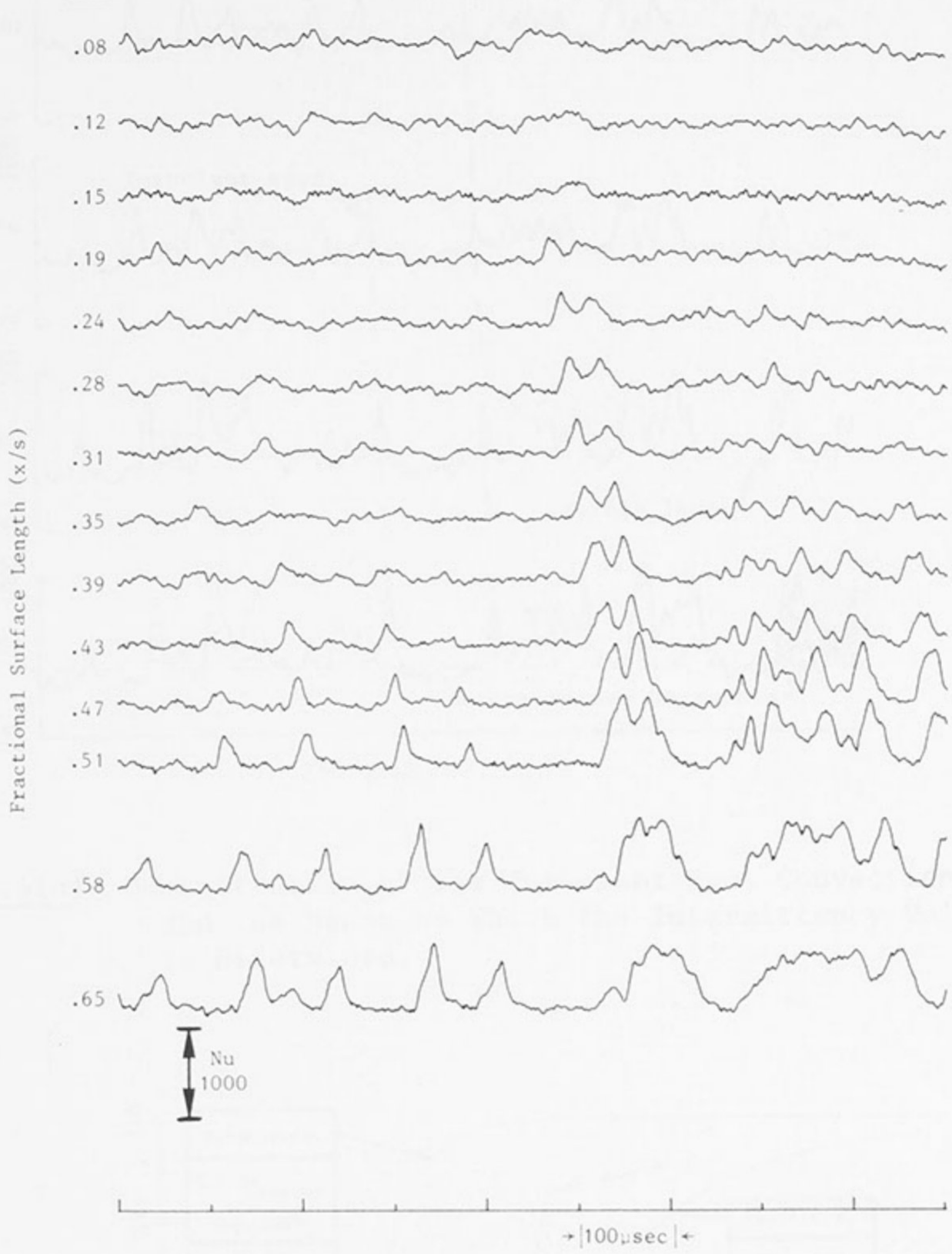

Fig. 5.3 Heat Transfer Measurements (as defined in Fig. 5.1) Drawn to an Expanded Time-Scale. By Closely Spacing Adjacent Traces the Degree of Similarity between Neighbouring Gauge Measurements is Evident. A Pair of Disturbances Occurring at about x/s 0.15 - 0.19 can be Tracked Along the Surface until they Merge by x/s = 0.65.

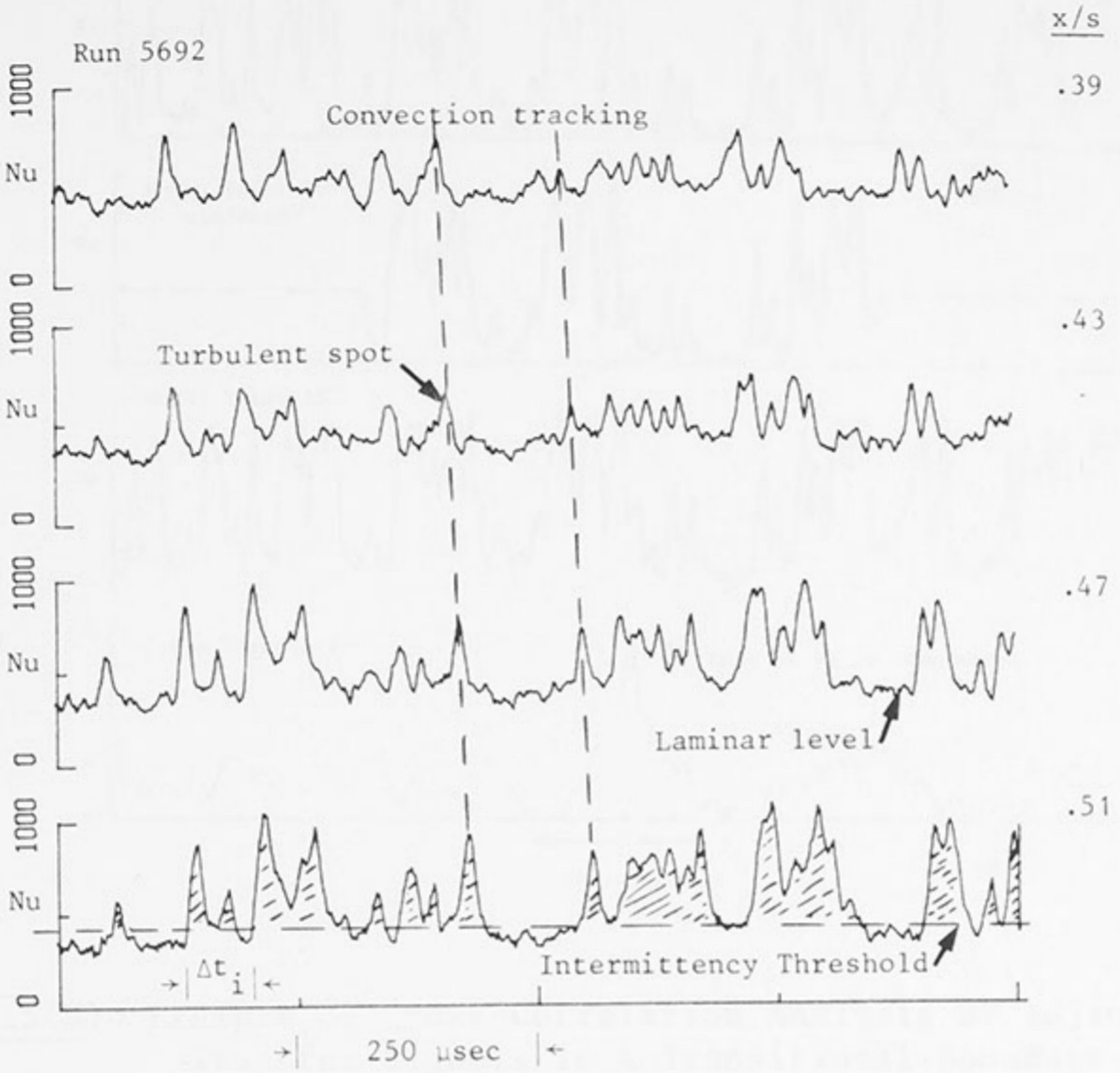

Fig. 5.4(a) Demonstration of the Turbulent Spot Convection Rate and the Means by Which the Intermittency Value γ is Determined.

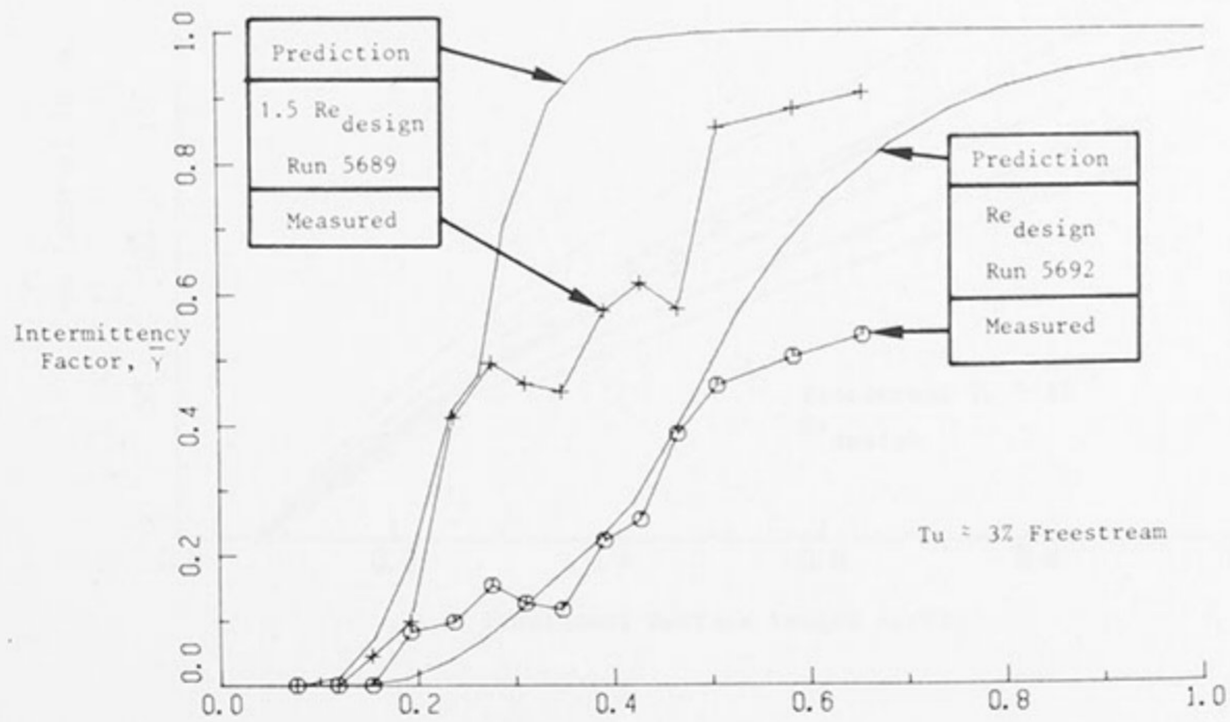

Fig. 5.4(b) Comparison between Measured Values of Intermittency Factor $\bar{\gamma}$ and Predictions for Natural Transition using the Method of FOREST[1977].

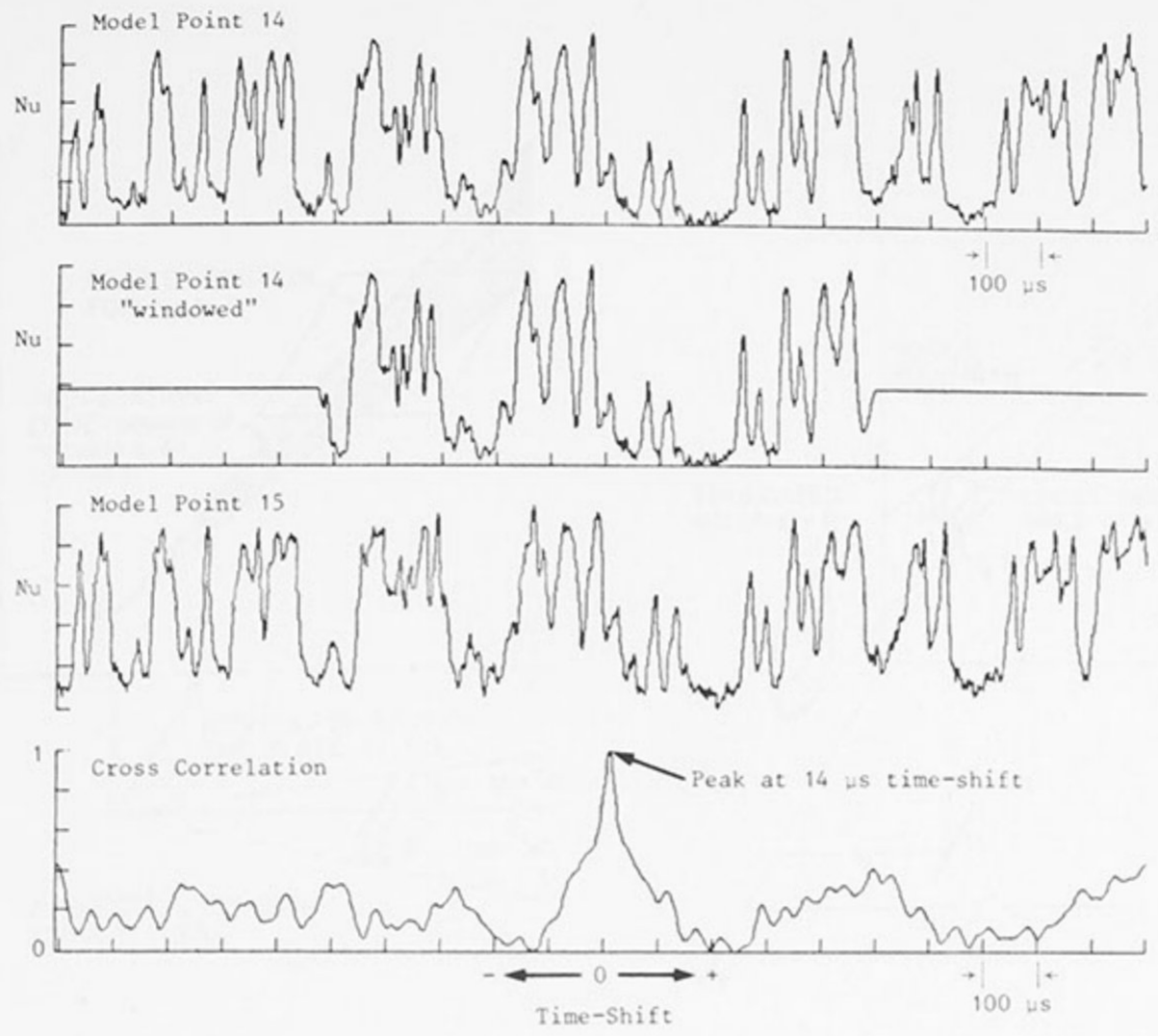

Fig. 5.5(a) Example of Cross-Correlation Analysis of Adjacent Heat Transfer Signals in a Transitional Boundary Layer.

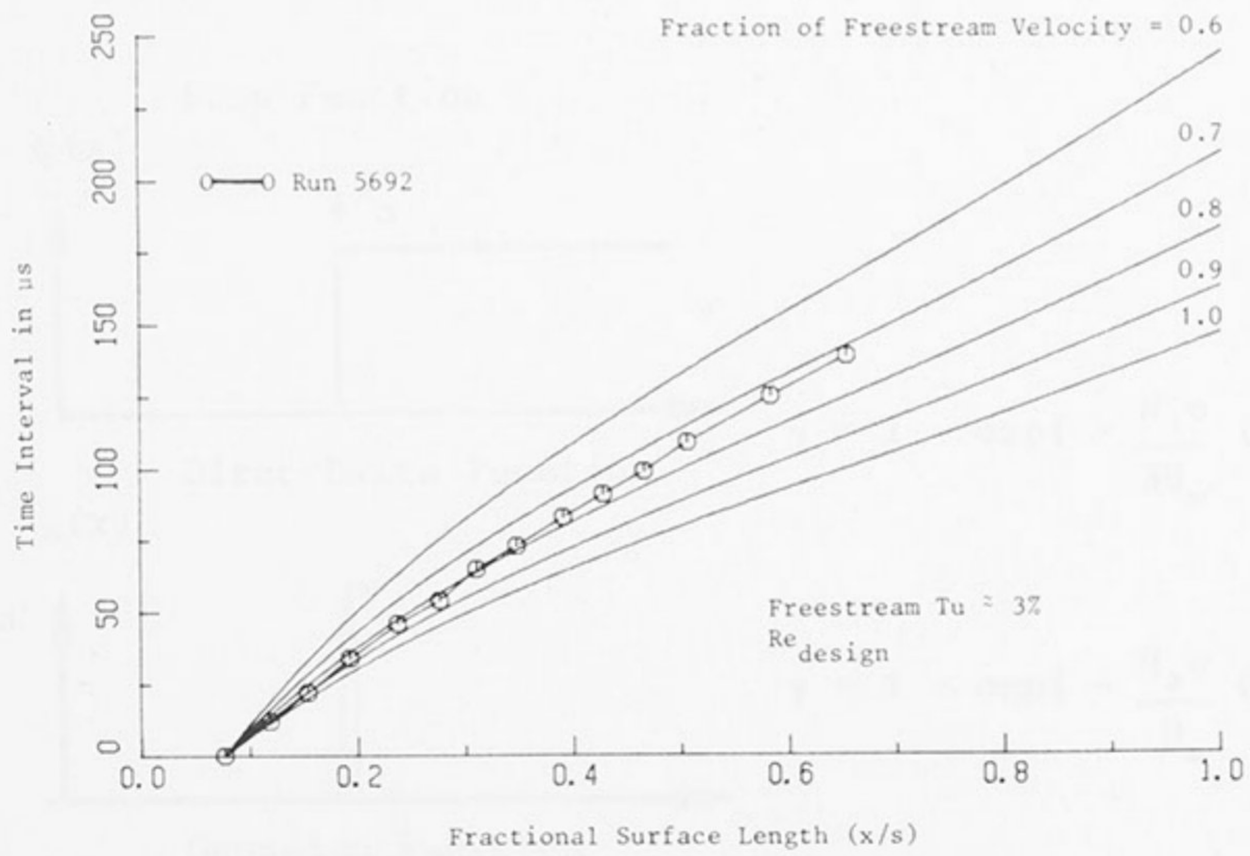

Fig. 5.5(b) Measured Mean Convection Rate of Turbulent Spots Derived from a Cross-Correlation Analysis and the Measured Freestream Conditions. Propagation Rates at Various Fractions of the Freestream Velocity for an Event Occurring at 0.08 x/s are also Shown.

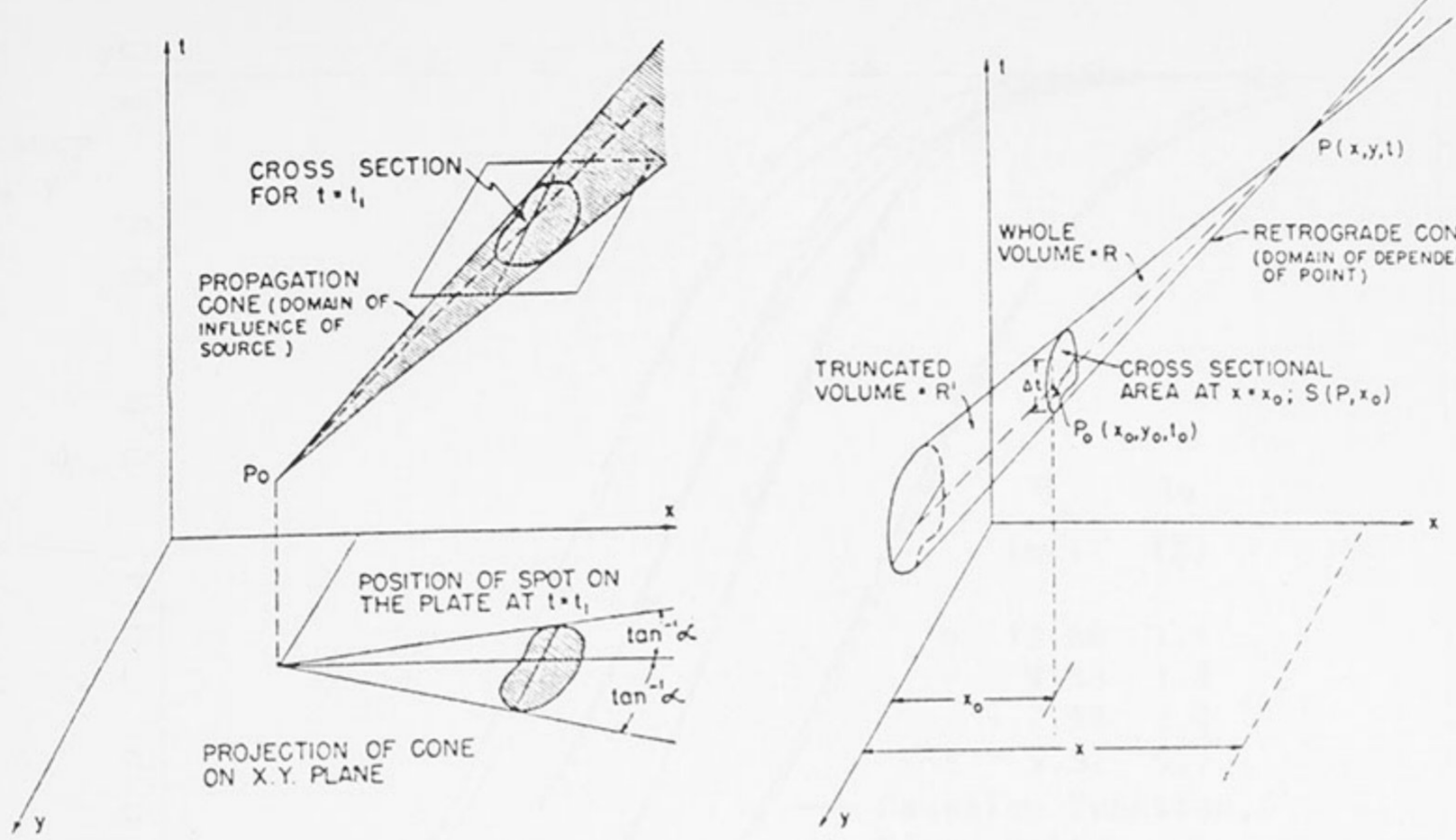

Fig. 5.6 (a & b) Definitions used in the Modelling of Turbulent Spot Growth by EMMONS[1951]:

(a) The Propagation Cone due to an Event Occurring at P_o;

(b) The Dependence Volume of a Point P(x,y,t).

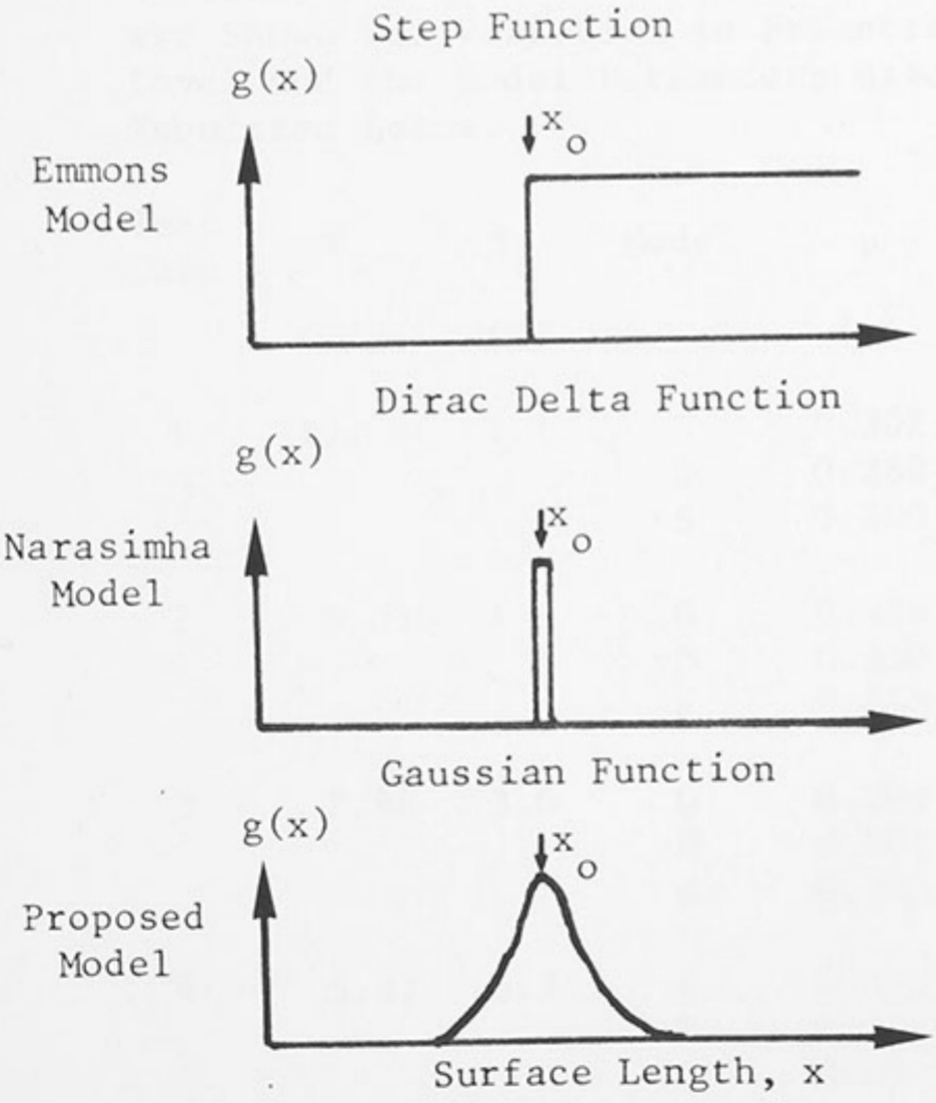

$$\gamma = 1 - \exp\{ - \frac{N_1 \sigma}{3U_\infty} (x - x_0)^3 \}$$

$$\gamma = 1 - \exp\{ - \frac{N_2 \sigma}{U_\infty} (x - x_0)^2 \}$$

$$\gamma = 1 - \exp\{ - \frac{\sigma}{U_\infty} \int_{x_0}^{x} g(x')(x - x')^2 dx' \}$$

Fig. 5.6(c) Comparison of the Three Types of Model Discussed for the Bursting Rate Function.

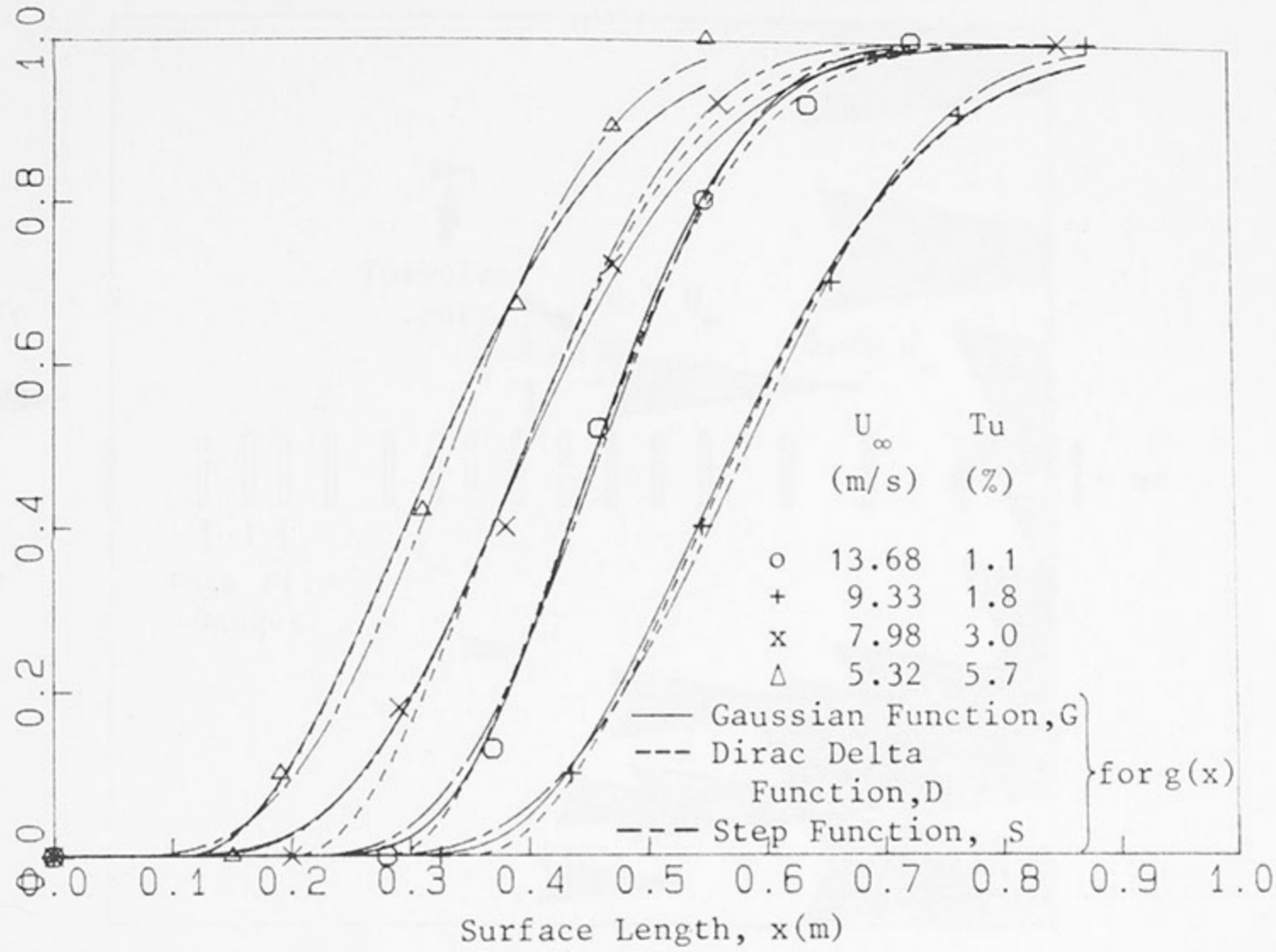

Fig. 5.7 Optimisation of Intermittency Models to Fit Experimental Data from GOSTELOW[1987]. Experimental data were taken by using an Intermittency Meter on Hot-Wire Measurements. The Freestream Velocity was Held Constant Over a Flat Plate Section. Results are Shown for Variation in Freestream Velocity and Turbulence Level and the Model Parameters used in Fitting to the Data Tabulated Below.

Test Case	U_∞ (m/s)	T_u (%)	Model	μ (m)	σ (m)	N (E3)	Δ (%)
1	13.68	1.1	G	0.302	0.044	2.3	1.21
			D	0.280	-	1.9	1.08
			S	0.200	-	10.0	1.91
2	9.33	1.8	G	0.350	0.035	0.8	1.28
			D	0.350	-	0.8	1.45
			S	0.240	-	3.3	1.26
3	7.98	3.0	G	0.201	0.060	0.8	1.73
			D	0.201	-	0.9	2.35
			S	0.103	-	4.0	2.27
4	5.32	5.7	G	0.110	0.005	0.5	2.15
			D	0.110	-	0.5	2.15
			S	0.050	-	3.0	2.17

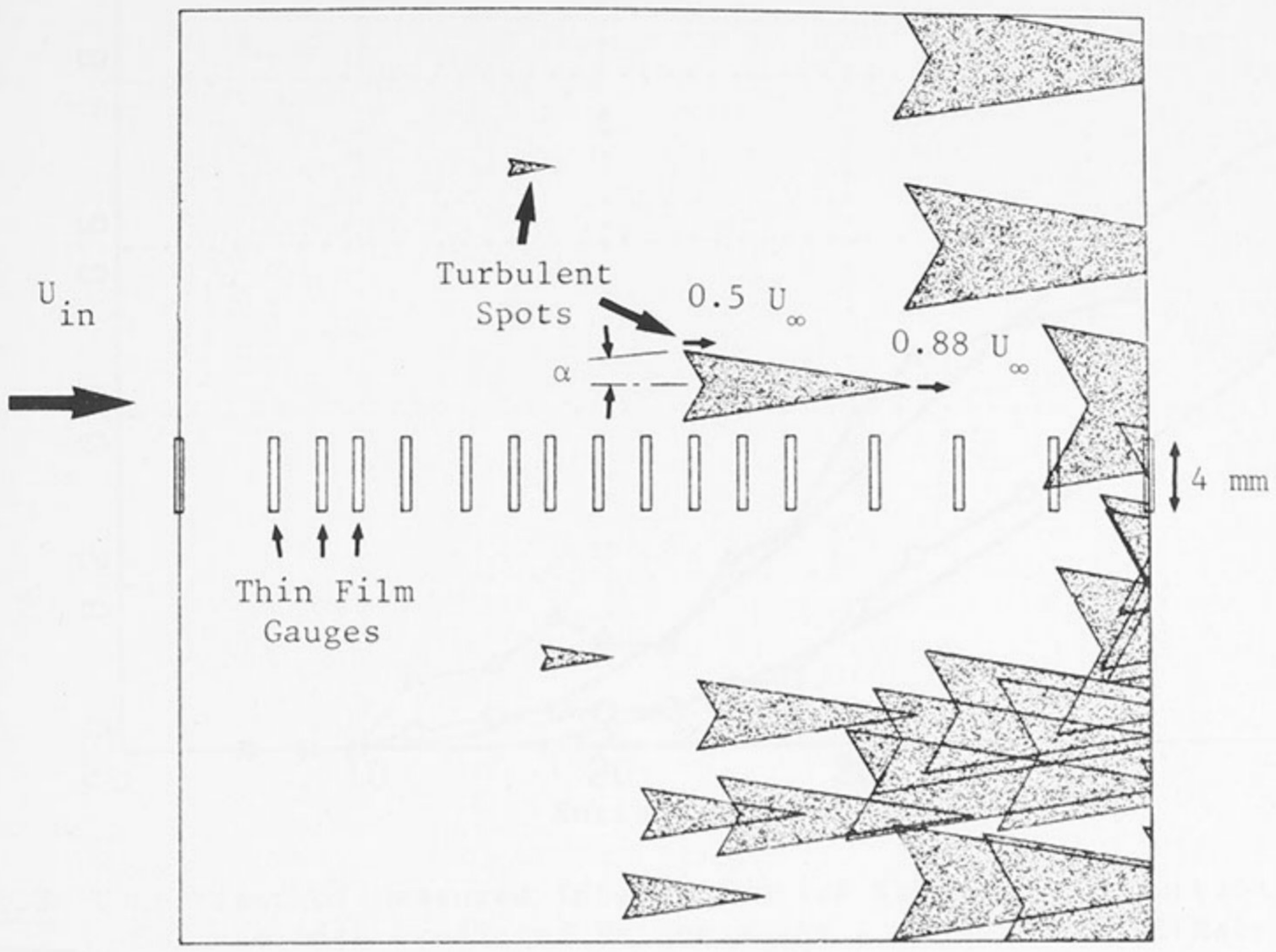

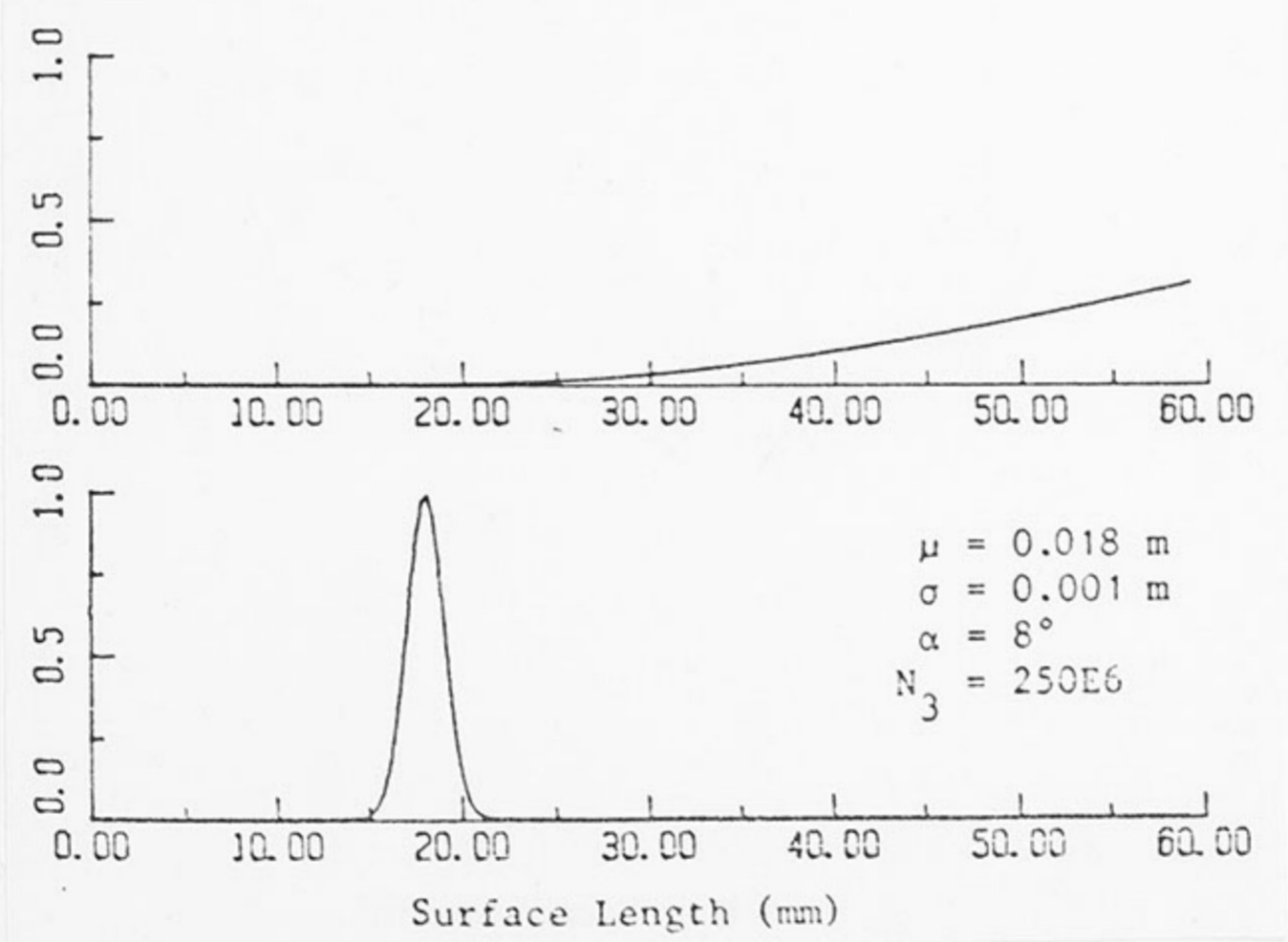

Fig. 5.8 Plan View of the Simulation of Transition on the ACE Suction Surface. Also Shown are the Average Calculated Intermittency Factor, γ, and the Burst Rate Probability Distribution.

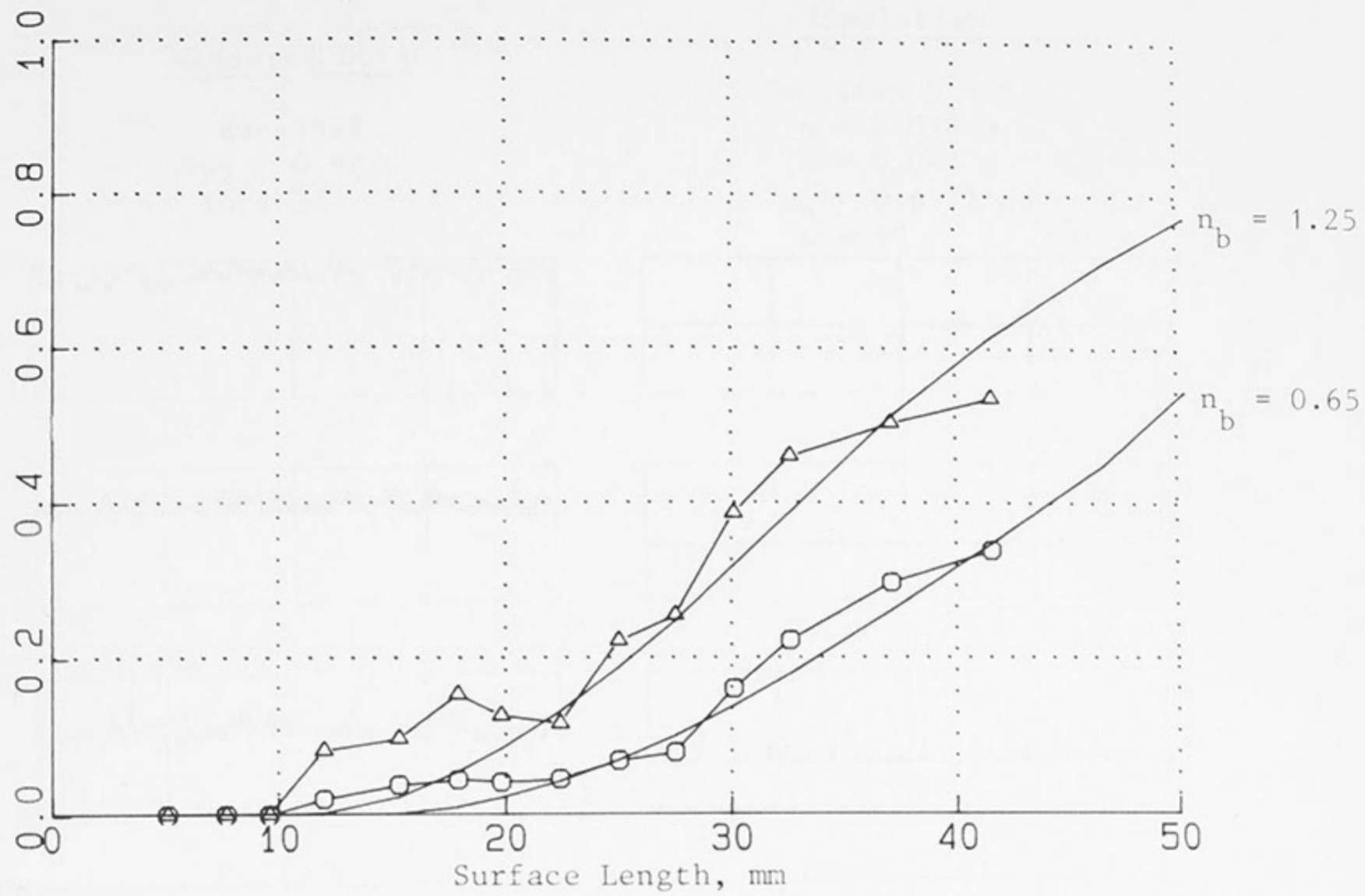

Fig. 5.9 Comparison of Measured Intermittencies from the ACE Suction Surface with Predicted Values using a Gaussian Burst Rate Distribution.

Mean value, μ = 18 mm

Standard deviation, σ = 1 mm

Δ-Δ-Δ Simple Threshold Value

o-o-o Area-Weighted Value

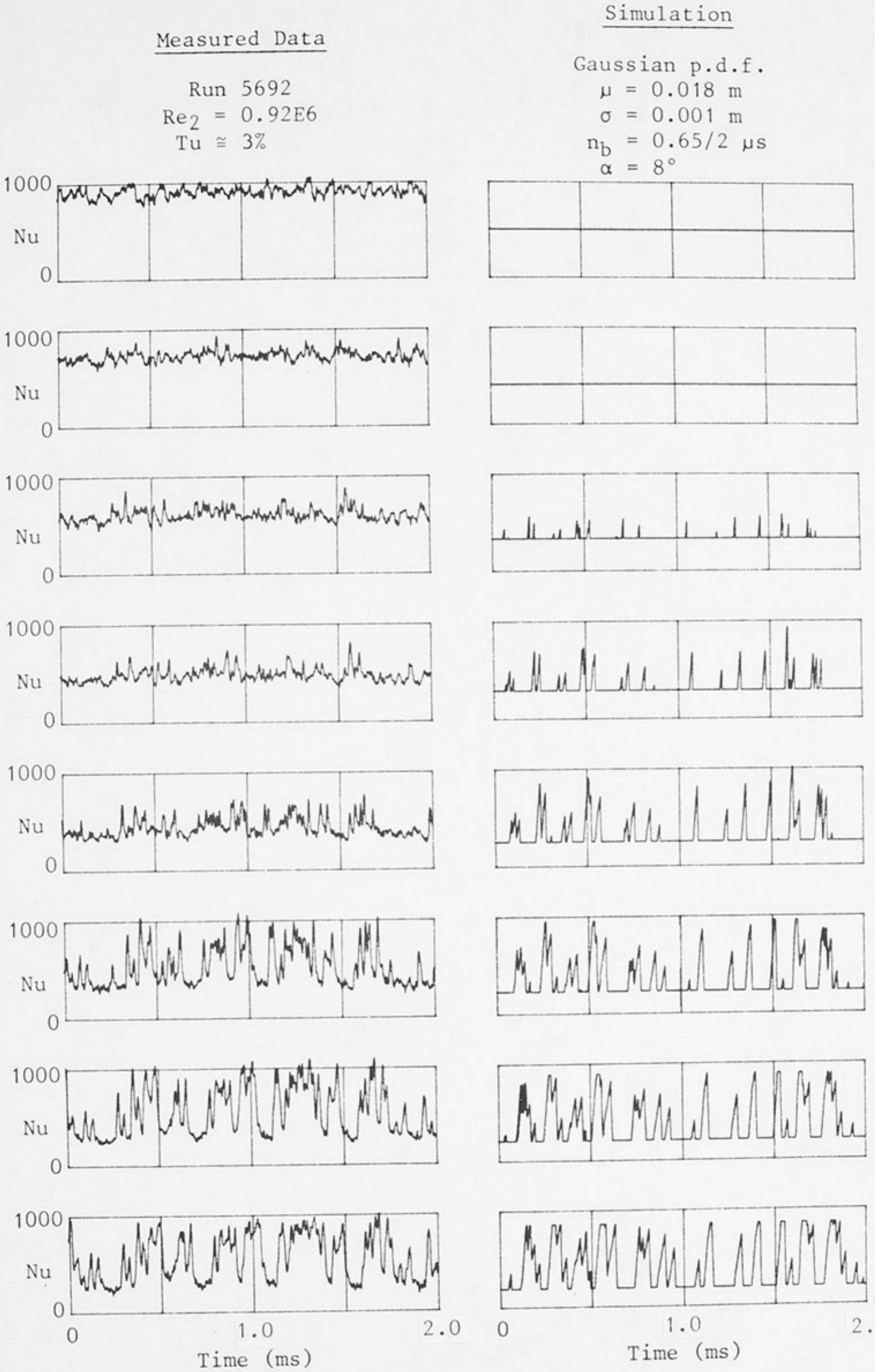

Fig.5.10 Comparison of a Simulation of Transitional Heat Transfer Traces on the ACE Suction Surface. Time-Averaged Intermittency Values are Consistent with the Model and Data but the Data shows a Slower Rate of Lateral Burst Growth up to Gauge 11. (No random fluctuations from the freestream are included in the simulation.)

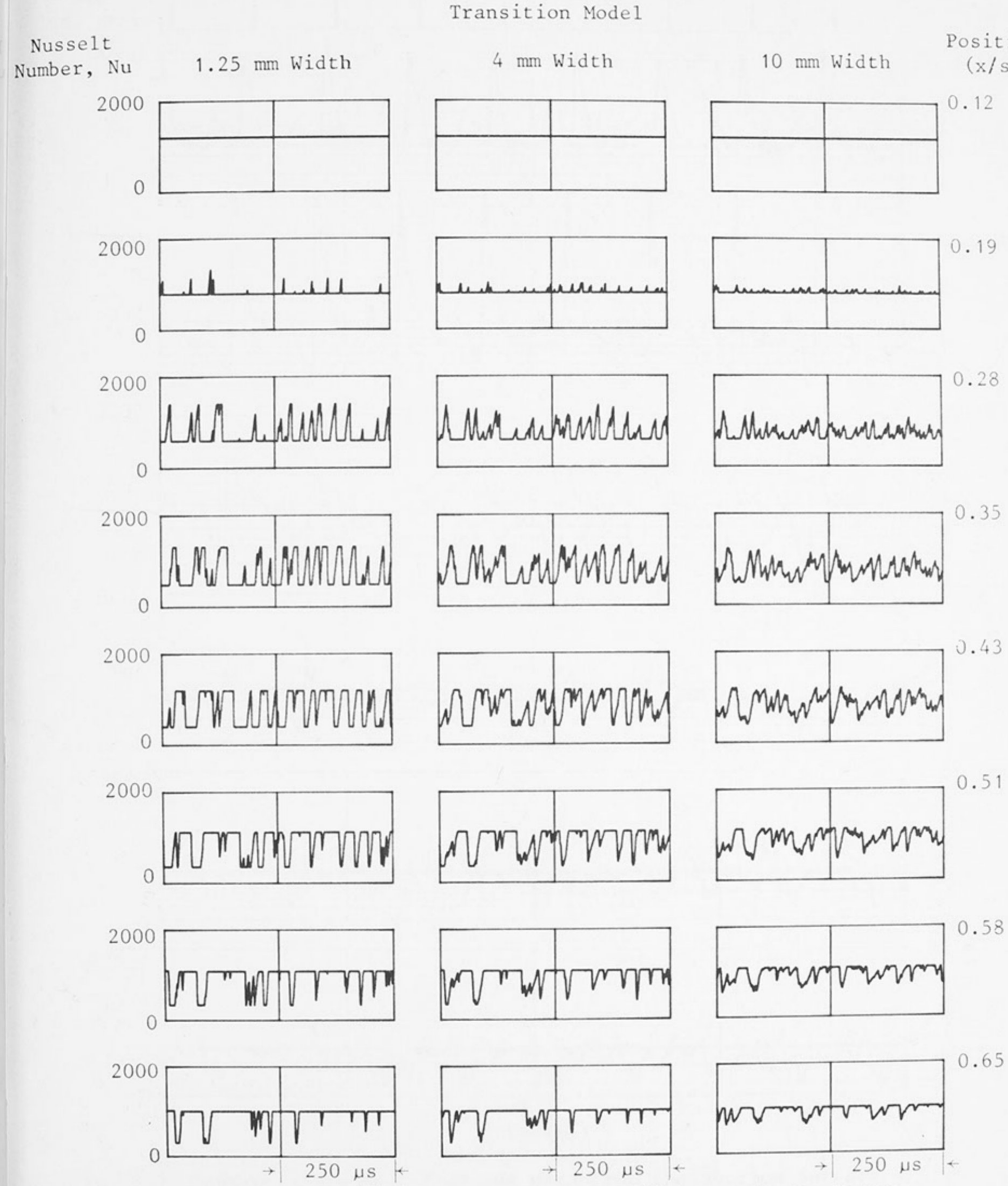

Fig. 5.11 Effect of Variation in Spanwise Gauge Width on the Predicted Instantaneous Values of Nusselt Number through Transition. Even the 'noise-less' Intermittency Signals Become Difficult to Interpret as the Gauge Width Increases to 10 mm due to the Effects of Spanwise Averaging.

Suction Surface - Run 4555

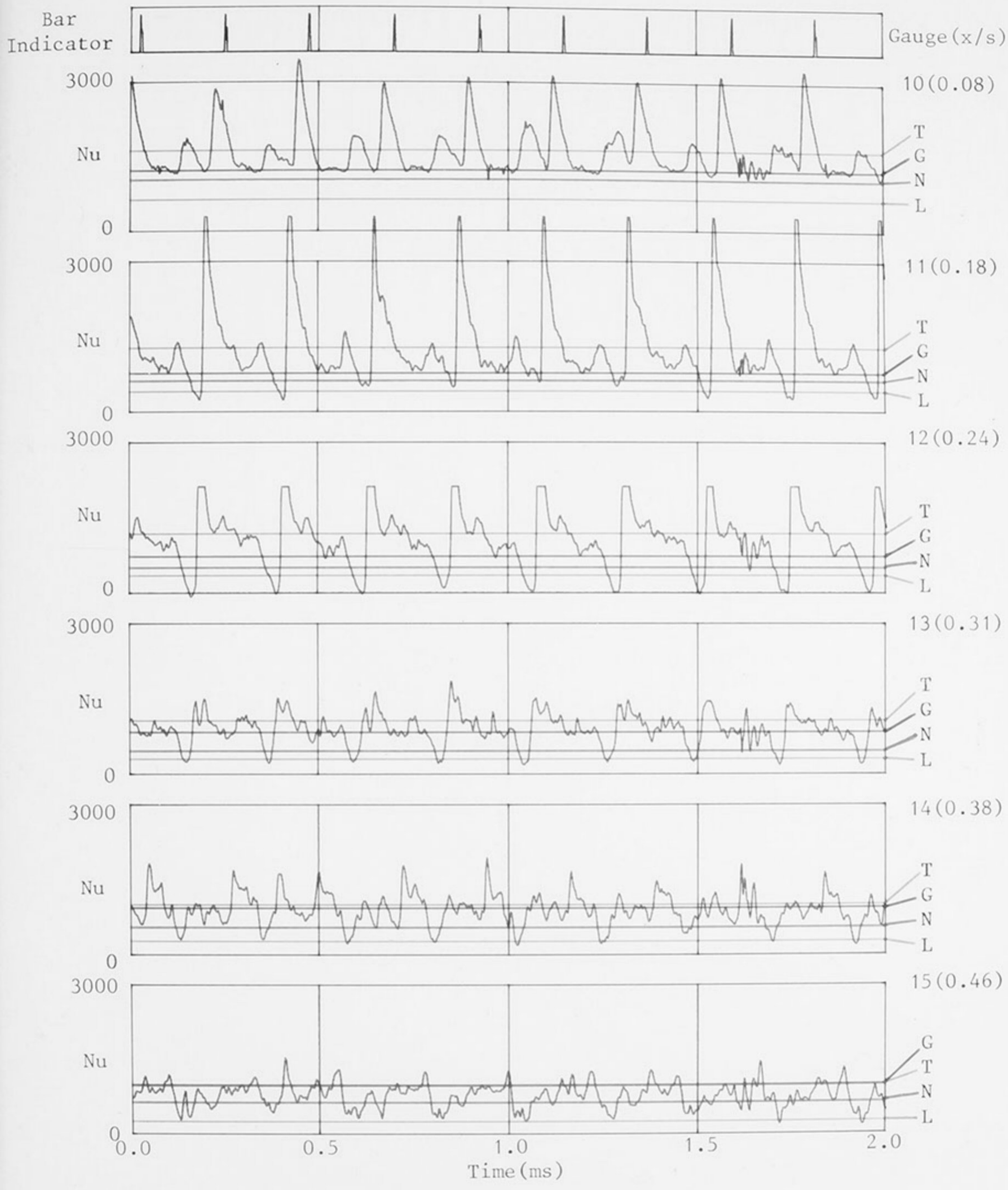

Fig. 6.1 Instantaneous Heat Transfer Data from the Suction Surface of the ACE Profile for the 16 Bar Case:

Bar Mach Number = 1.164, Tu < 0.8%
Design Operating Cond: M_2 = 1.28, Re_2 = 0.96E6, i = 0°

——— Run 4555 Instantaneous Data
——— Run 4557 Mean Level, No Bars, No Grid, Tu < 0.8% (N)
——— Run 4540 Mean Level, No Bars, Grid In, Tu ≅ 3% (G)
——— Laminar and Turbulent Predicted Levels (L and T).

Suction Surface - Run 4543

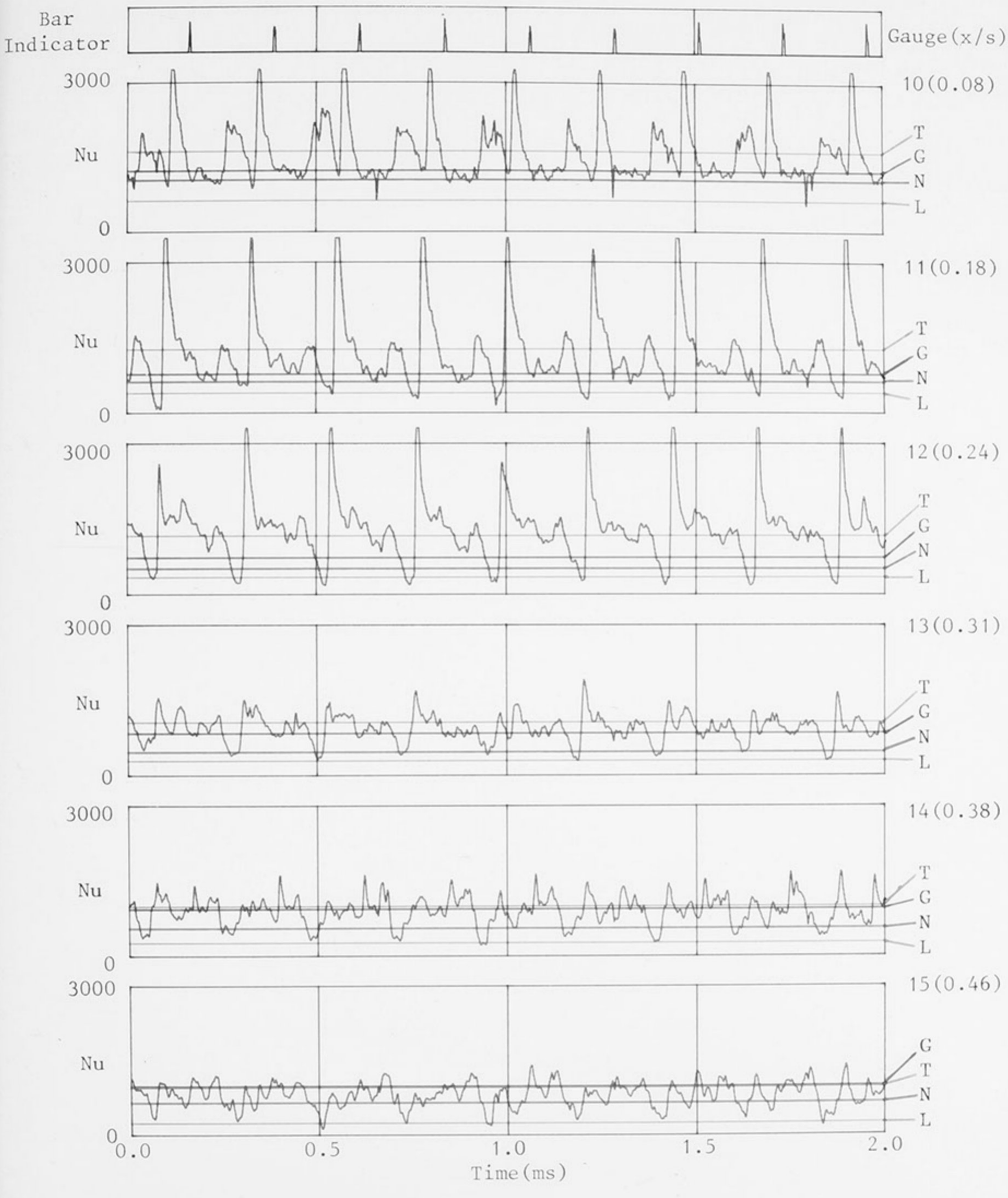

Fig. 6.2 Instantaneous Heat Transfer Data from the Suction Surface of the ACE Profile for the 16 Bar Case:

Bar Mach Number = 1.162, Tu ≅ 3%
Design Operating Cond: M_2 = 1.28, Re_2 = 0.92E6, i = 0°

——— Run 4543 Instantaneous Data
——— Run 4557 Mean Level, No Bars, No Grid, Tu < 0.8% (N)
——— Run 4540 Mean Level, No Bars, Grid In, Tu ≅ 3% (G)
——— Laminar and Turbulent Predicted Levels (L and T).

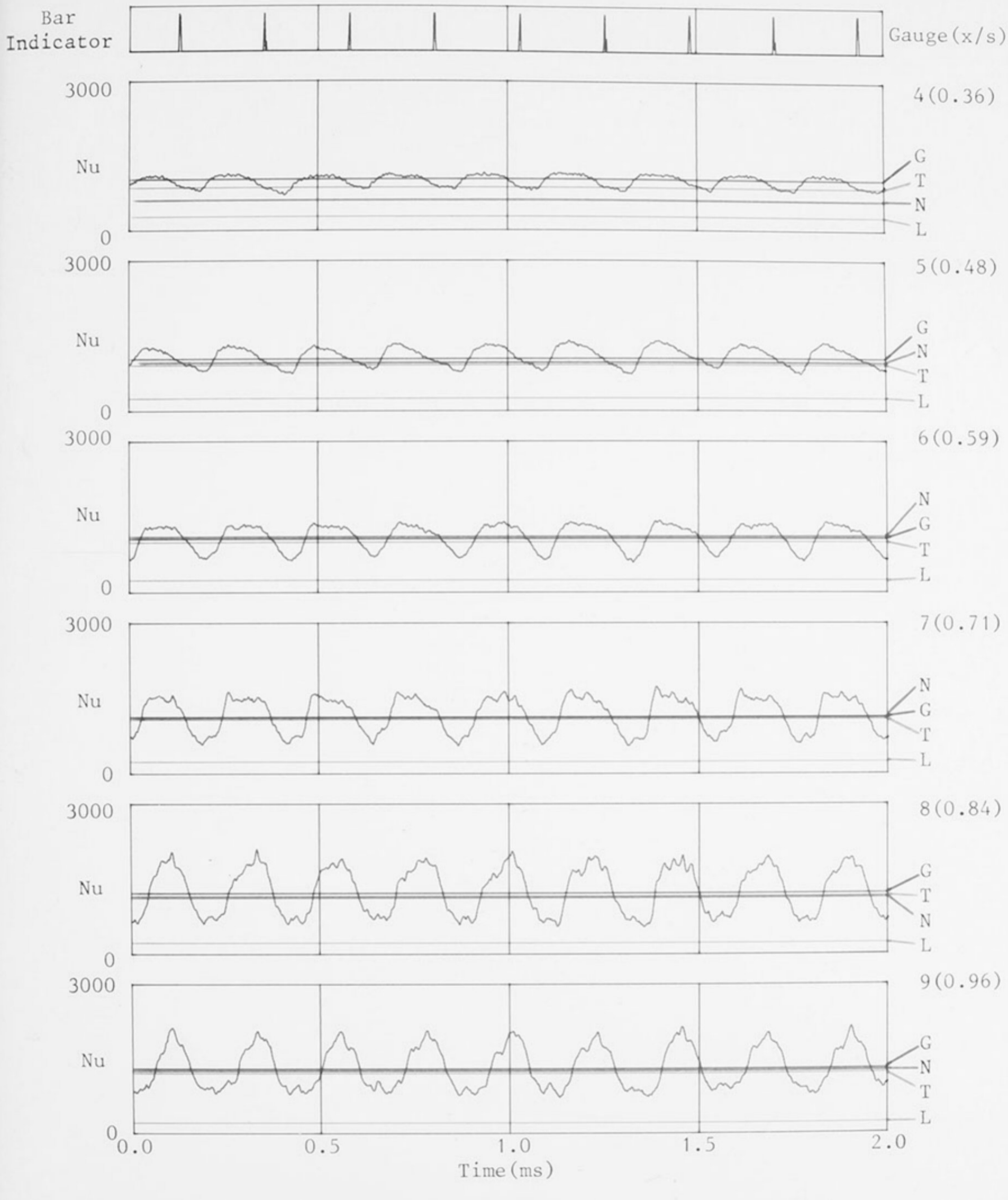

Fig. 6.3 Instantaneous Heat Transfer Data from the Pressure Surface of the ACE Profile for the 16 Bar Case:

Bar Mach Number = 1.162, Tu < 0.8%
Design Operating Cond: M_2 = 1.28, Re_2 = 0.95E6, i = 0°

——— Run 4556 Instantaneous Data
——— Run 4557 Mean Level, No Bars, No Grid, Tu < 0.8% (N)
——— Run 4540 Mean Level, No Bars, Grid In, Tu ≅ 3% (G)
——— Laminar and Turbulent Predicted Levels (L and T).

Pressure Surface - Run 4546

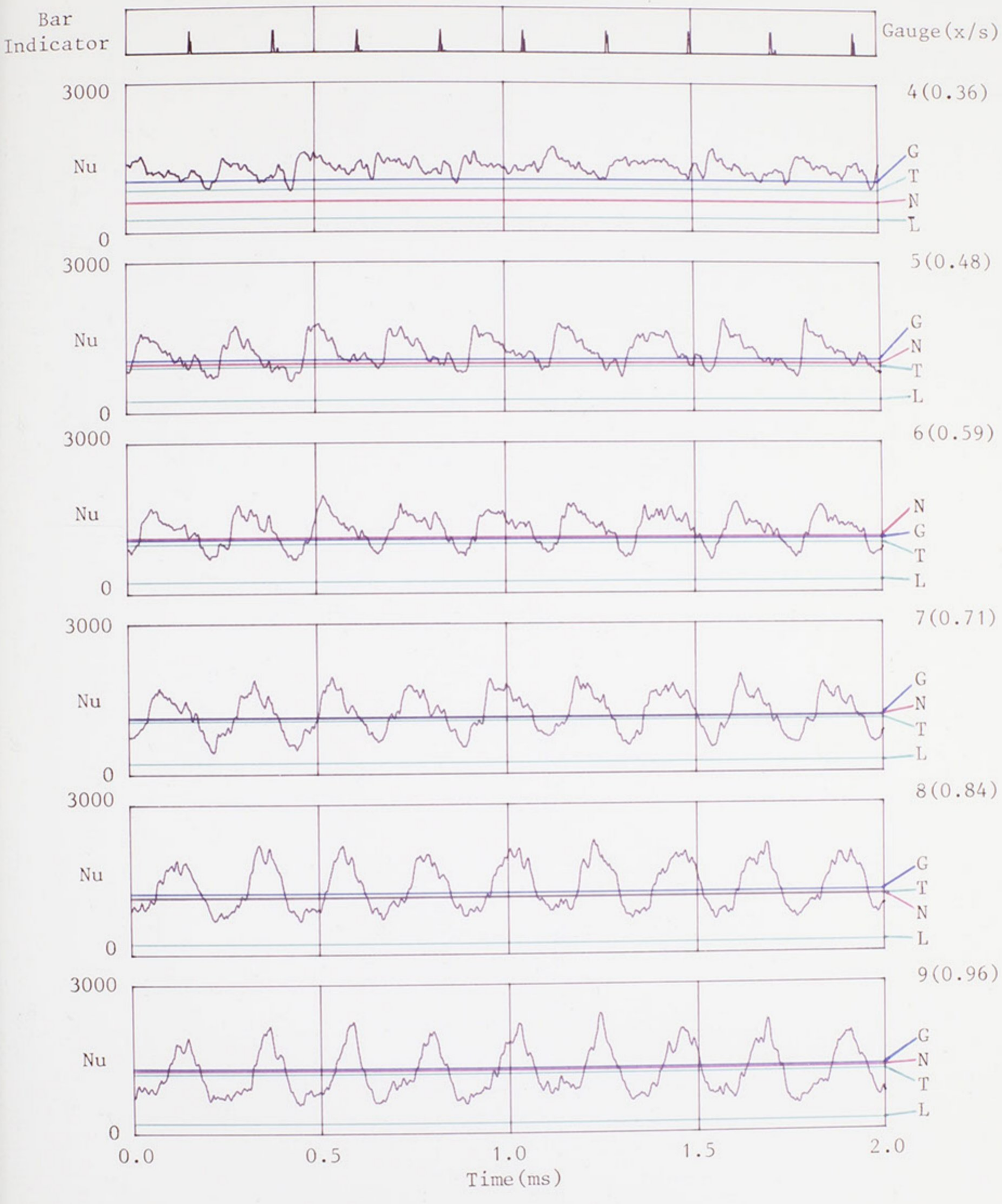

Fig. 6.4 Instantaneous Heat Transfer Data from the Pressure Surface of the ACE Profile for the 16 Bar Case:

Bar Mach Number = 1.173, Tu ≅ 3%
Design Operating Cond: M_2 = 1.28, Re_2 = 0.91E6, i = 0°

Run 4546 Instantaneous Data
Run 4557 Mean Level, No Bars, No Grid, Tu < 0.8% (N)
Run 4540 Mean Level, No Bars, Grid In, Tu ≅ 3% (G)
Laminar and Turbulent Predicted Levels (L and T).

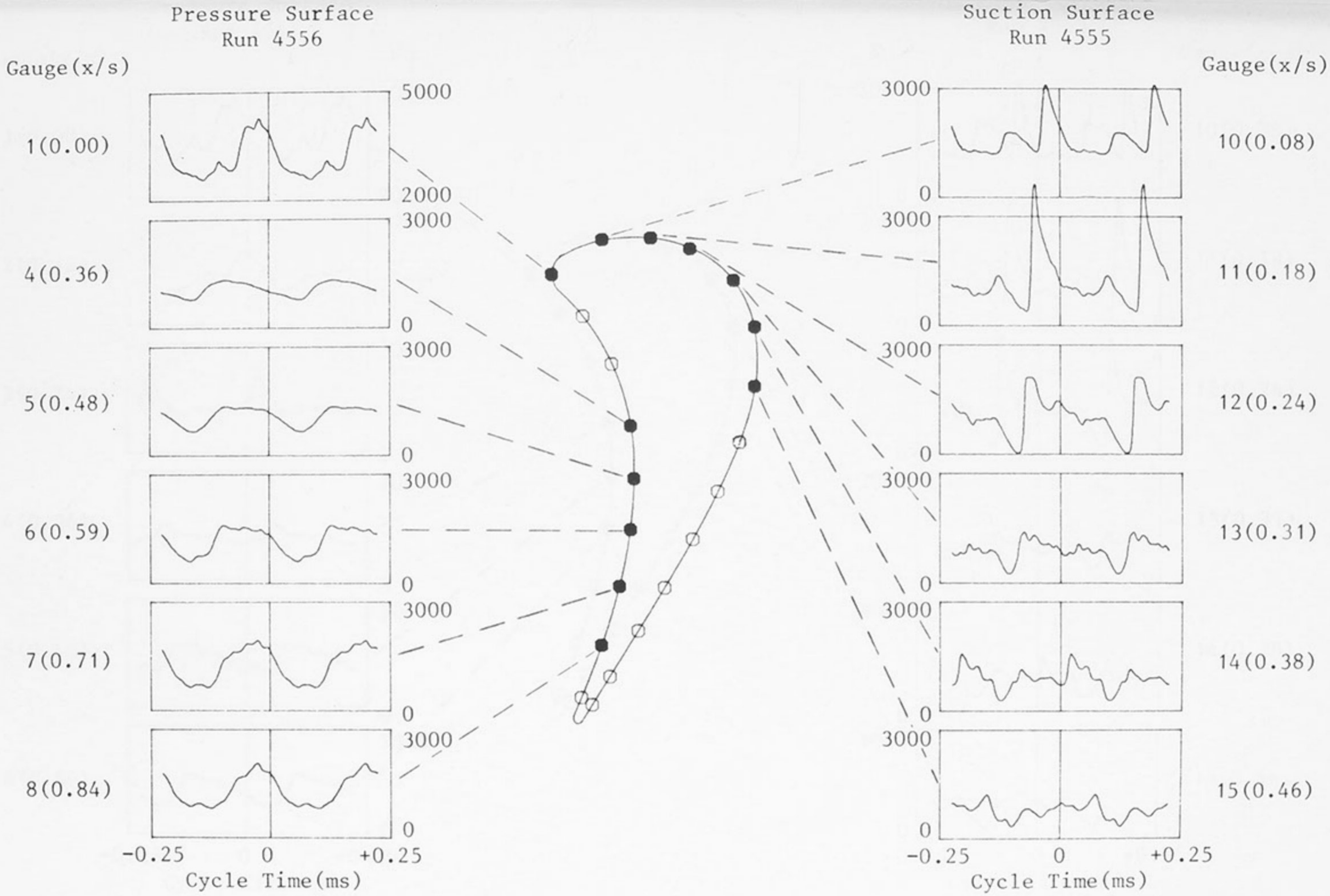

Fig. 6.5 Ensemble-Averaged Heat Transfer Results for the ACE Profile for the 16 Bar Case with no Turbulence Grid Fitted (Tu < 0.8%). (Operating Conditions are given in Figs. 6.1 and 6.3.) 2 Cycle Periods are Shown of the Average of 10 Bar-Passing Cycles.

Cycle Time = 0.23 ms, b.p.f. = 4350 Hz.

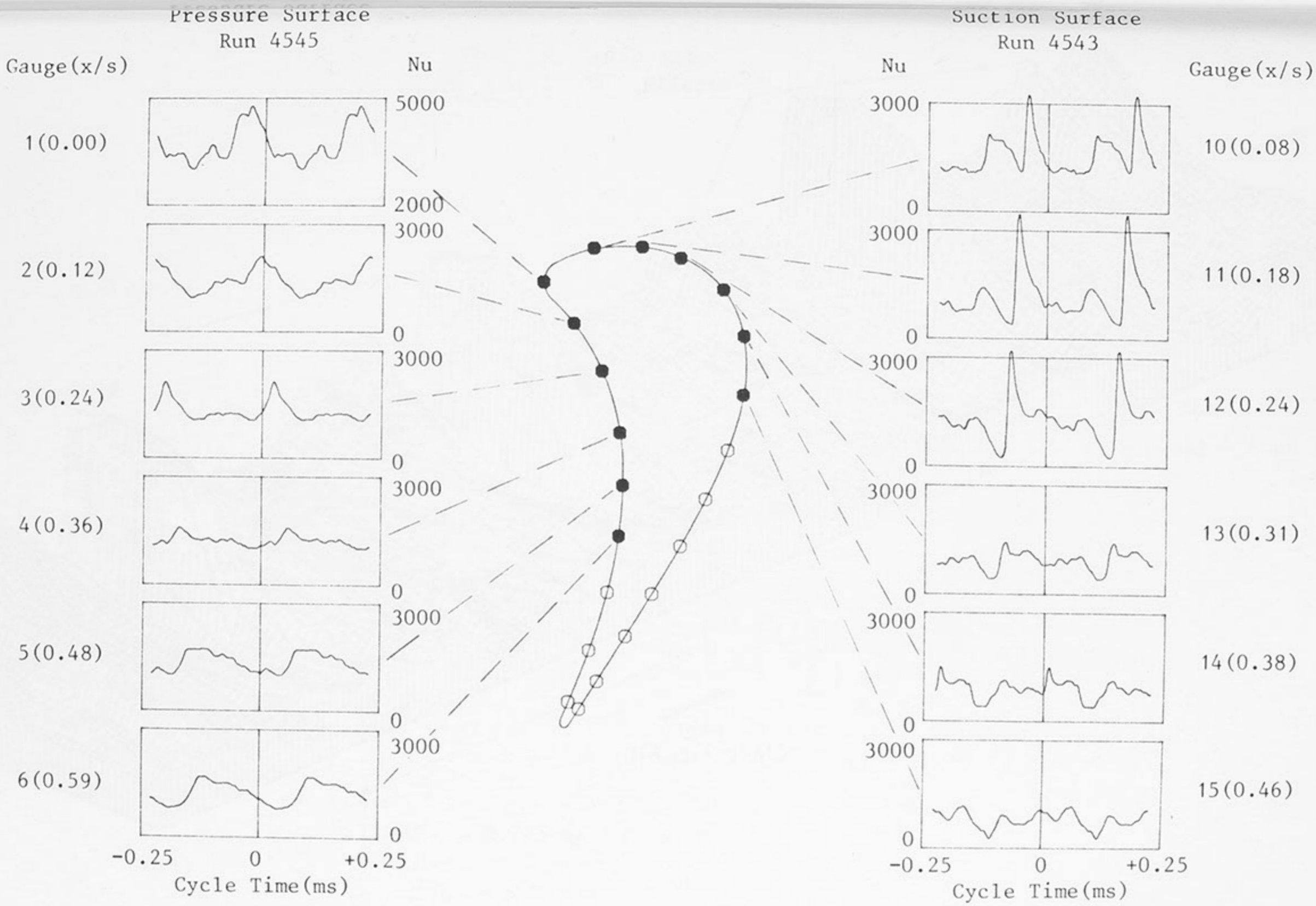

Fig. 6.6 Ensemble-Averaged Heat Transfer Results for the ACE Profile for the 16 Bar Case with the Turbulence Grid Fitted (Tu ≅ 3%). (Operating Conditions are given in Figs. 6.2 and 6.4.) 2 Cycle Periods are Shown of the Average of 10 Bar-Passing Cycles.

Cycle Time = 0.23 ms, b.p.f. = 4350 Hz.

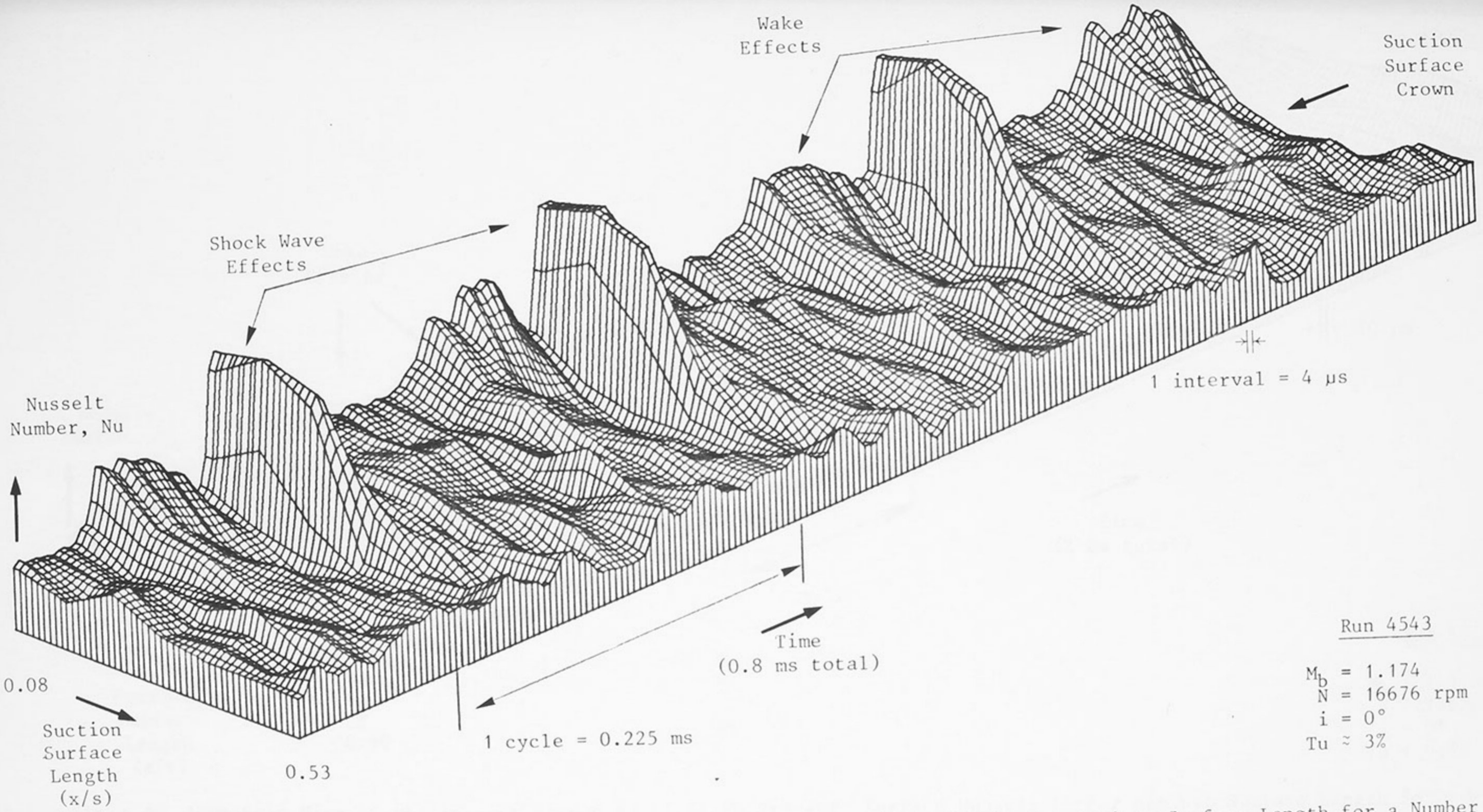

Run 4543

M_b = 1.174
N = 16676 rpm
i = 0°
Tu ≈ 3%

Fig. 6.7 Isometric View of the Surface formed by Plotting Suction Surface Nusselt Number against Surface Length for a Number of Successive Time Intervals. Every Third Data Point is Plotted, Joined to the Next Surface Point Shifted in Time by =-8 μs with 7 Interpolated Intermediate Positions between Gauges.

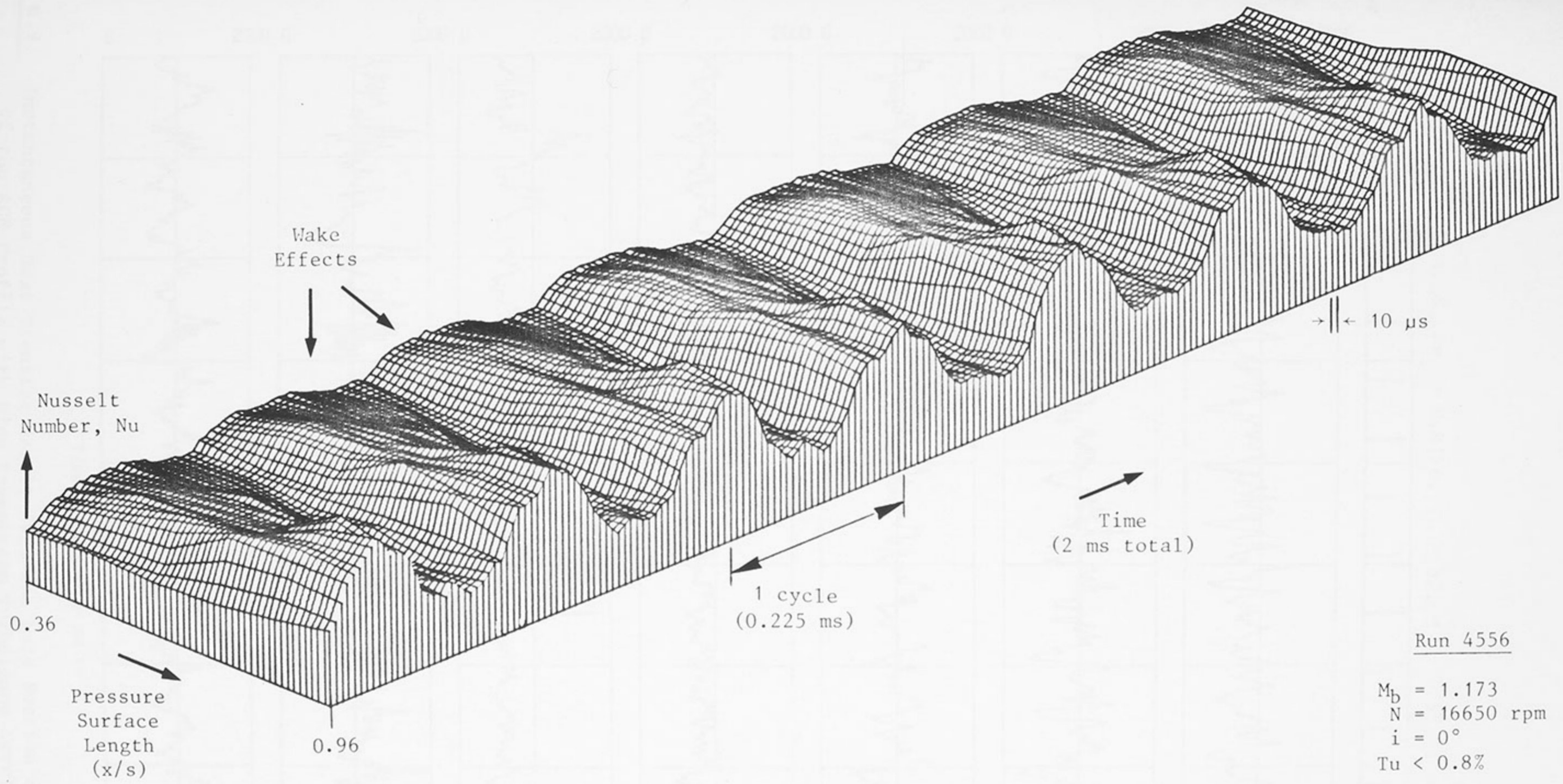

Fig. 6.8 Isometric View of the Surface formed by Plotting Pressure Surface Nusselt Number against Surface Length for a Number of Successive Time Intervals. Every Fifth Data Point is Plotted, Joined to the Next Surface Point Shifted in Time by 6 μs, with 8 Intermediate Interpolated Positions between Gauges.

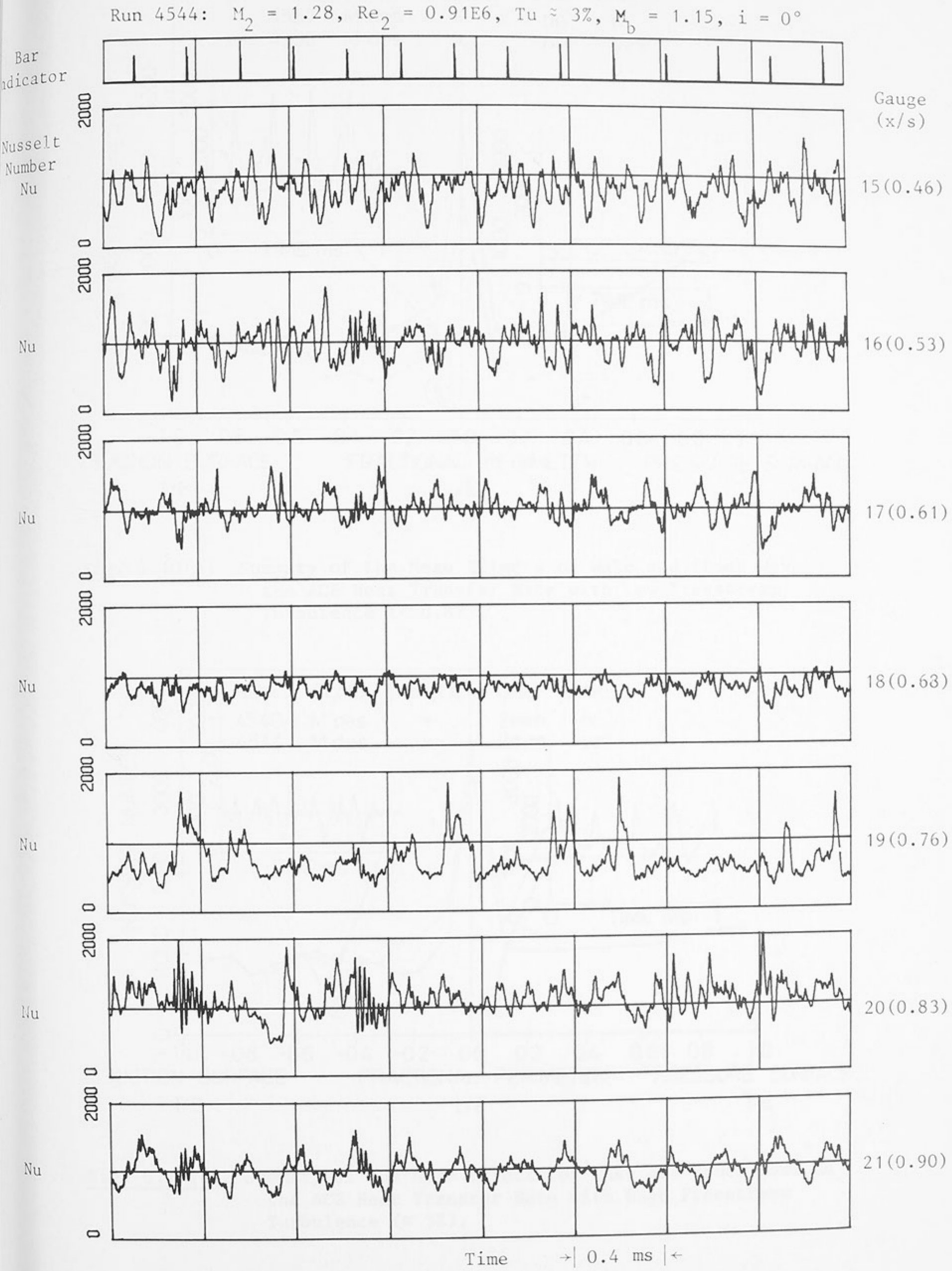

Fig. 6.9 Instantaneous Heat Transfer Result from the Late Suction Surface of the ACE Profile with High Freestream Turbulence Level, Tu ≈ 3%.

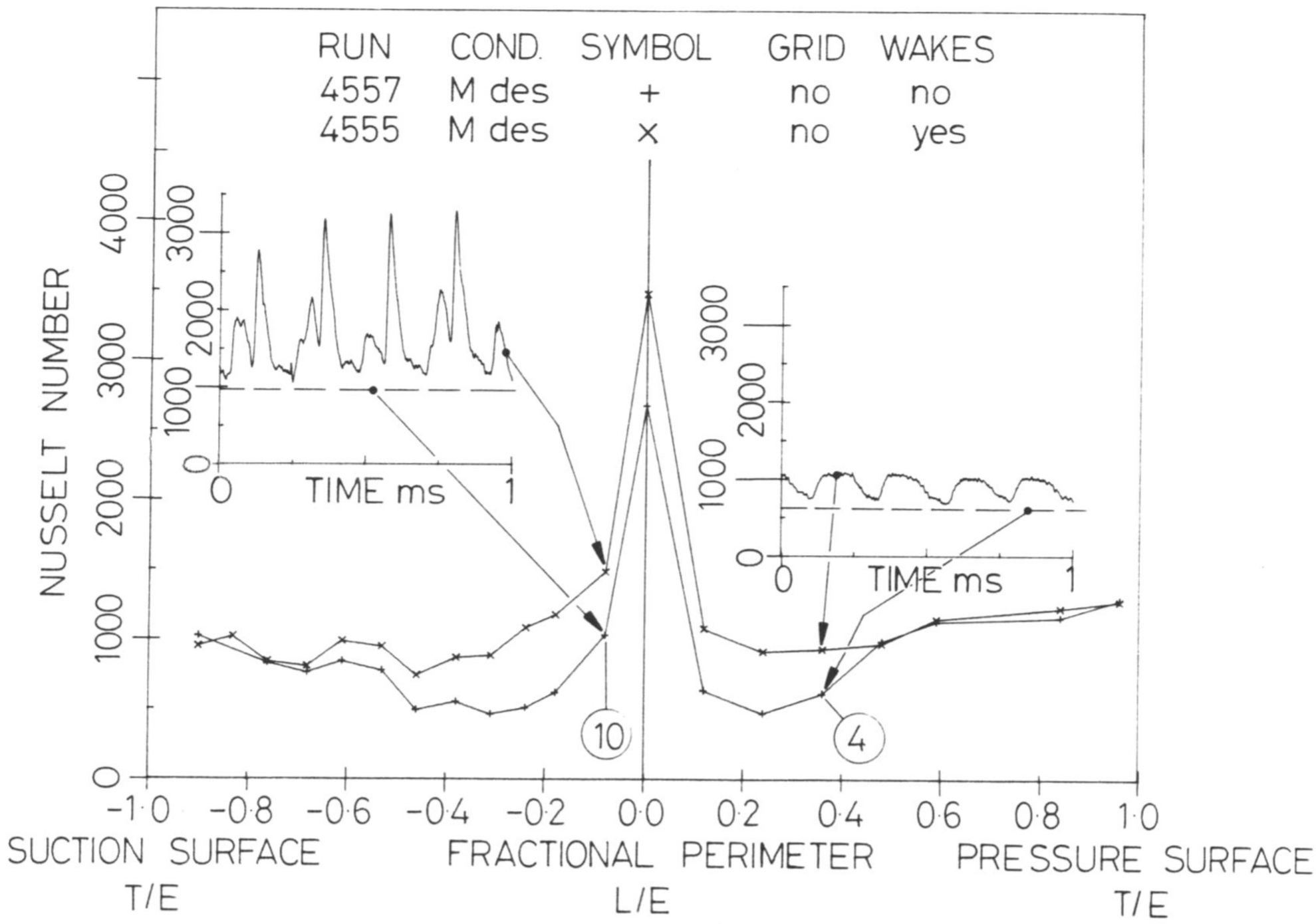

Fig. 6.10(a) Summary of the Mean Effects of Wake and Shock Wave on the ACE Heat Transfer Rate with Low Freestream Turbulence (< 0.8%).

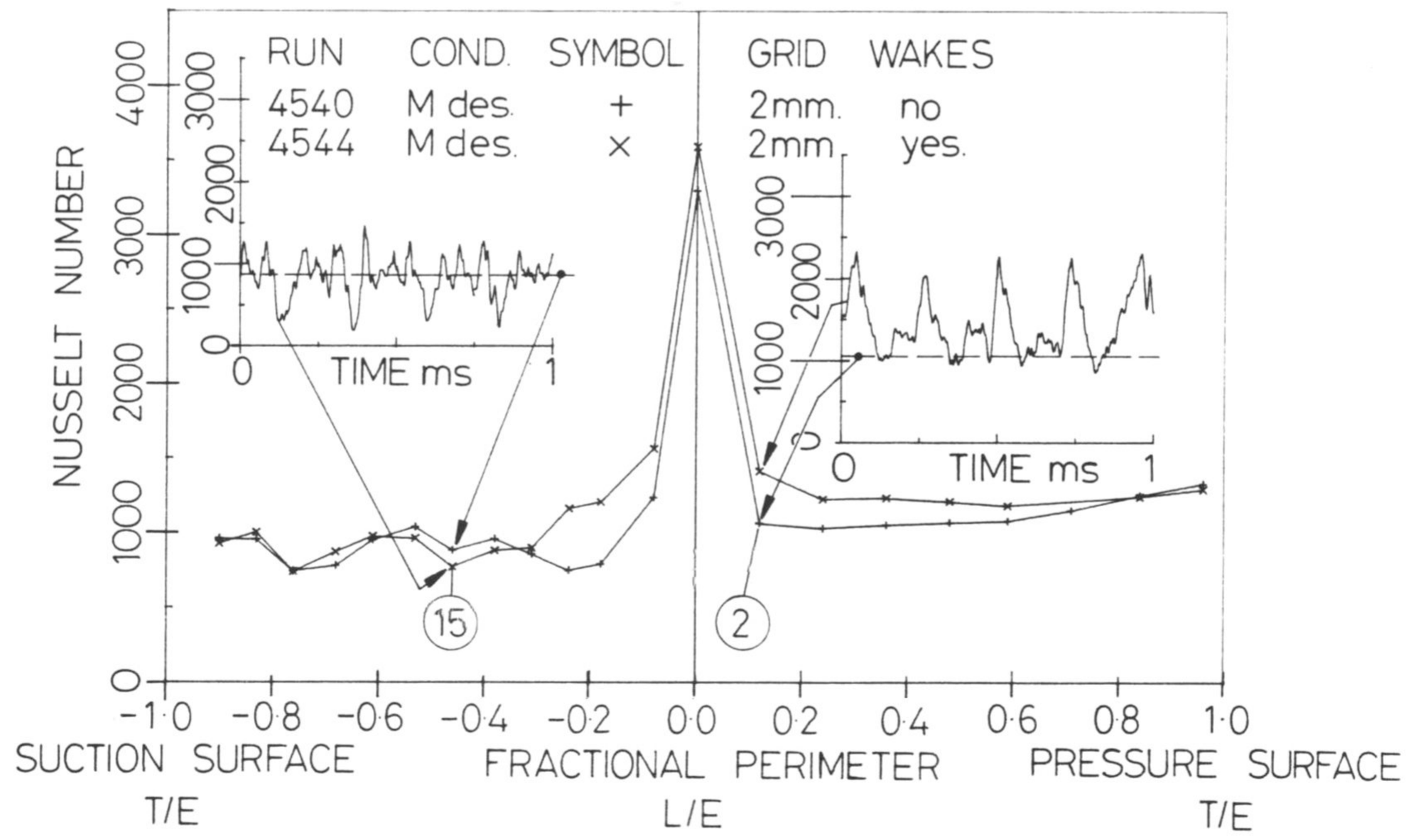

Fig. 6.10(b) Summary of the Mean Effects of Wake and Shock Wave on the ACE Heat Transfer Rate with High Freestream Turbulence (≅ 3%).

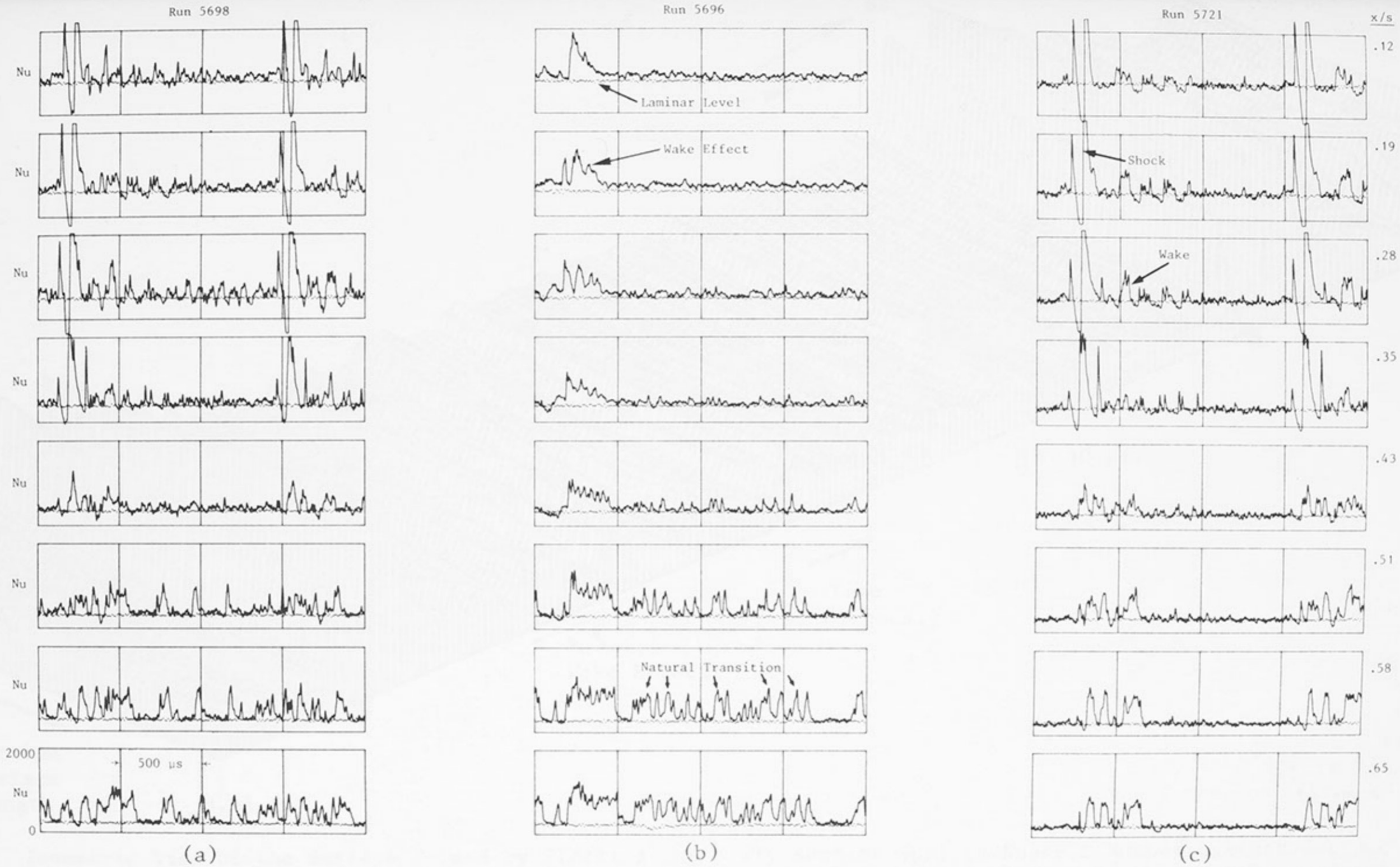

Fig. 6.11 Unsteady Heat Transfer Measurements from the Second Series of Tests using the Narrow (4 mm wide) Gauges and 2 Bars:

(a) Run 5698 M_b = 1.17, Tu ≈ 3%

(b) Run 5696 M_b = 0.83, Tu ≈ 3% ... Run 5723 No Bars, Tu < 0.8%.

(c) Run 5721 M_b = 1.17, Tu < 0.8%.

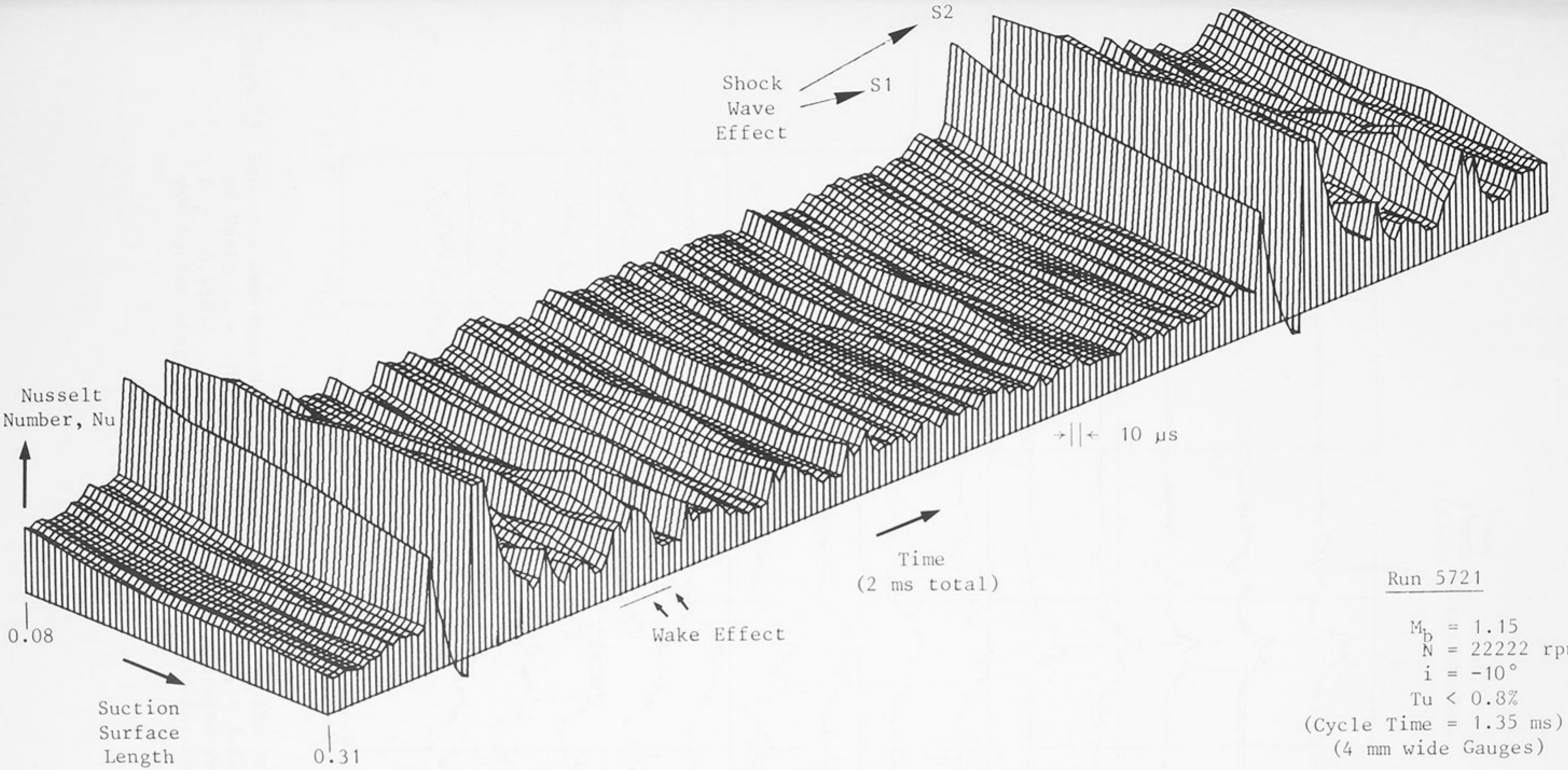

Fig.6.12 Isometric View of the Surface Formed by Plotting the Early Suction Surface Nusselt Number against Surface Length for a Number of Successive Time Intervals. Every Fifth Data Point is Plotted, Joined to the Next Point in Time Shifted by - 6 μs with 7 Intermediate Interpolated Positions between Gauges.

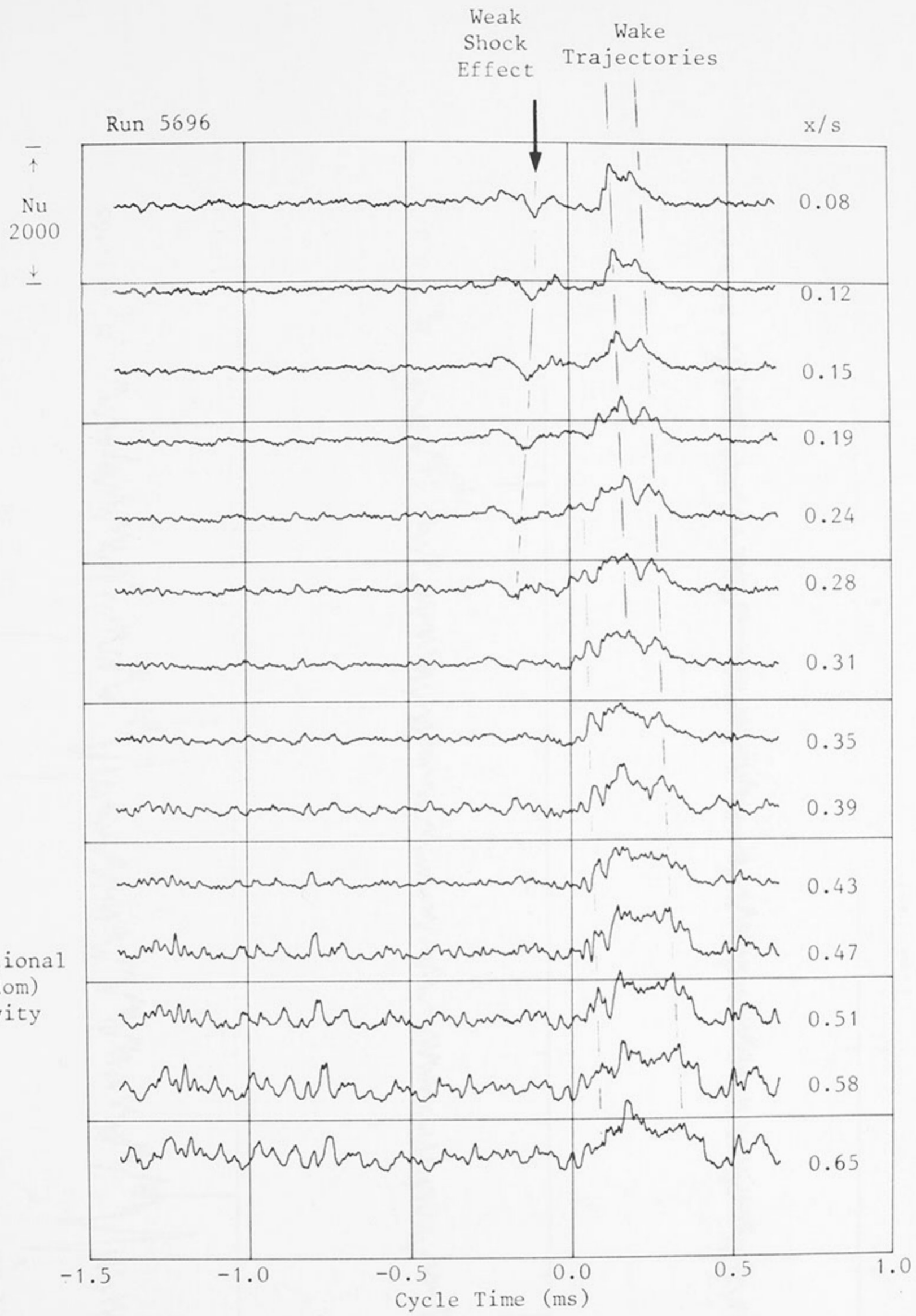

Fig.6.13 Ensemble-Averaged Heat Transfer Results from the Second Series of Tests ($i = -10°$, $Tu \approx 3\%$, $M_b = 0.83$, $M_2 = 1.20$, $Re_2 = 0.95E6$). Results Could only be Averaged Over 3 Cycles due to the Long Cycle Time at the Subsonic Bar Condition.

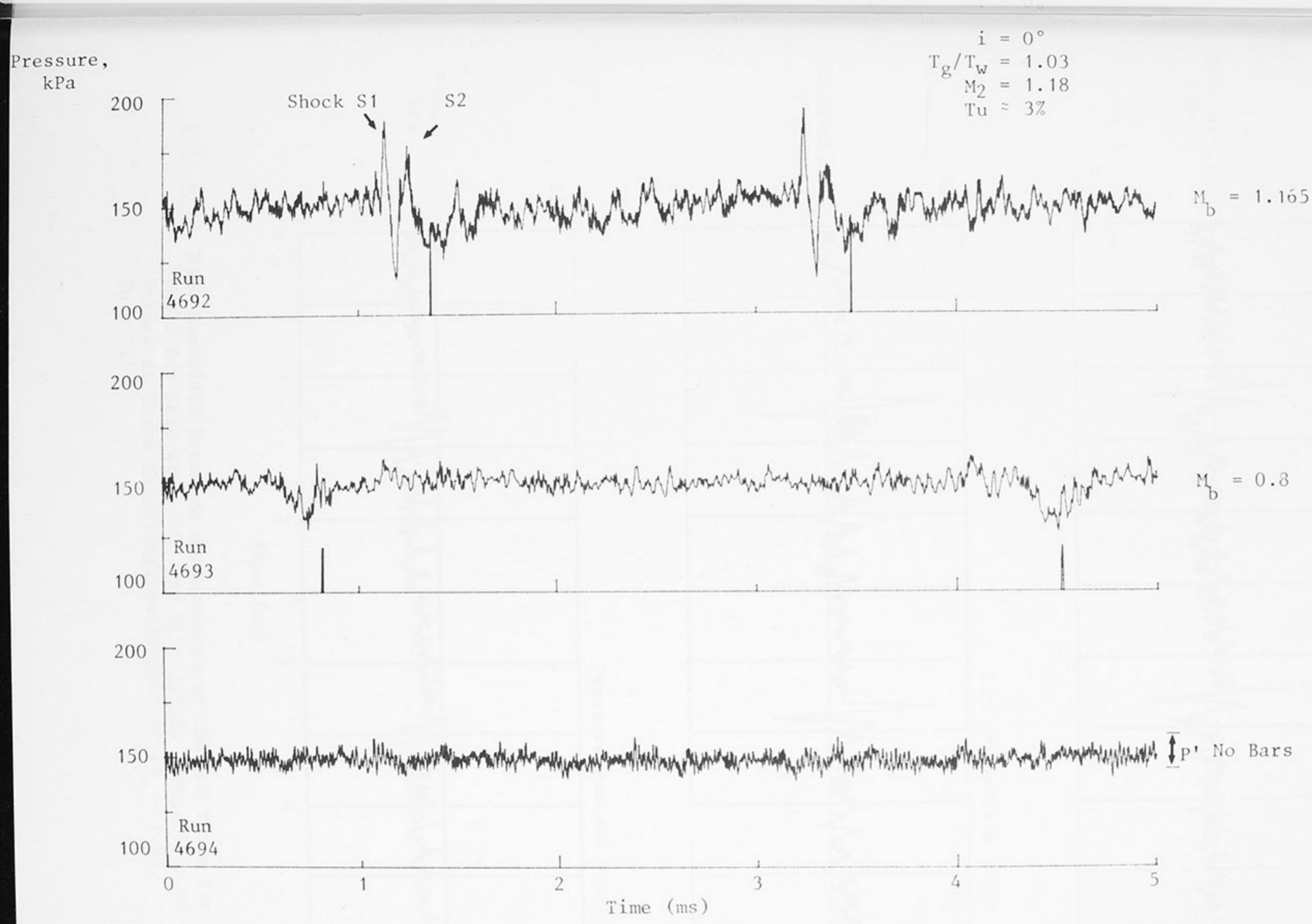

Fig. 6.14 High Bandwidth Pressure Measurements from the Leading Edge Position on the ACE Blade. Comparison of Results with Variation in Bar Speed for the 2 Bar Case and with no Bars Fitted.

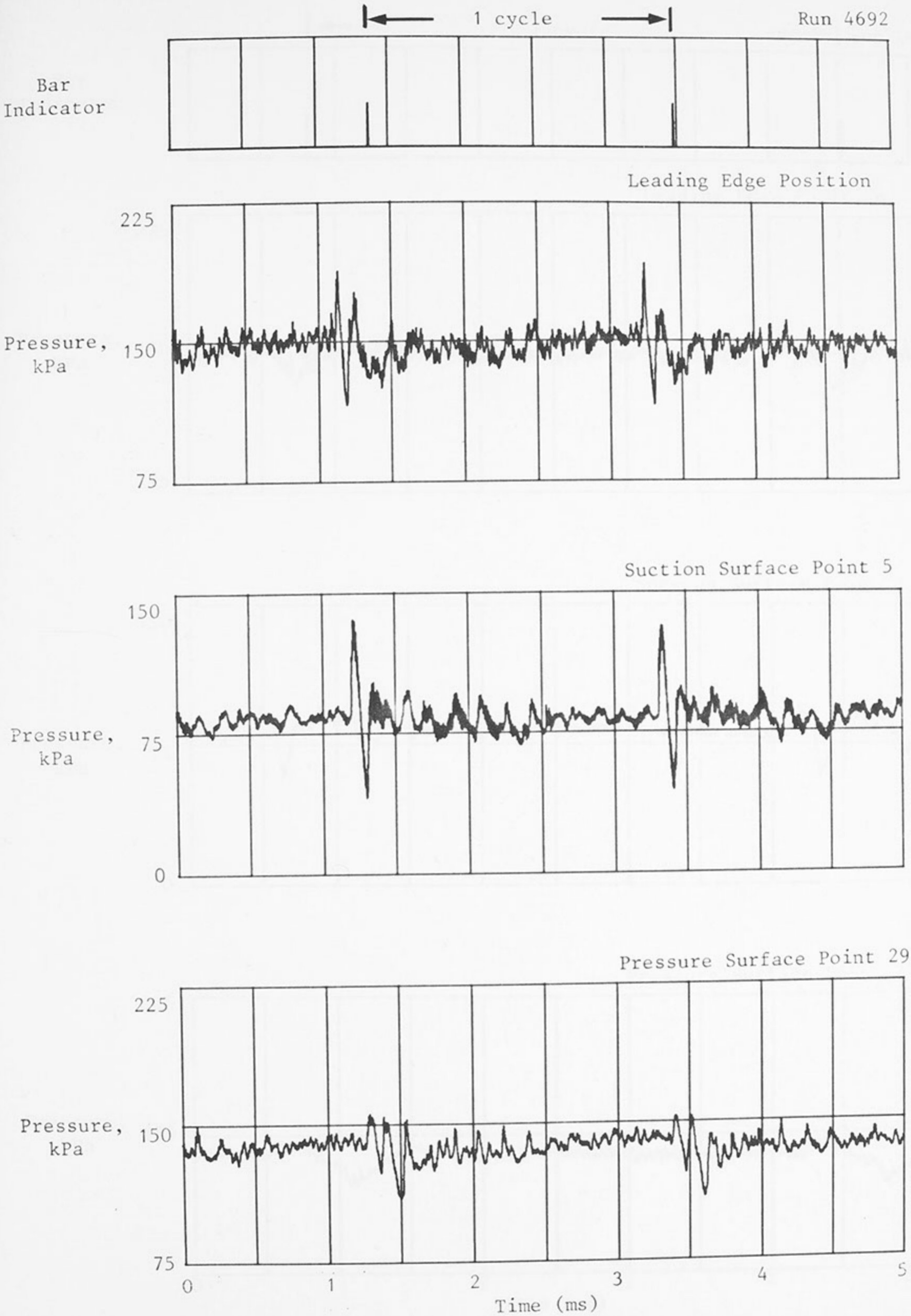

Fig. 6.15 High Bandwidth Pressure Measurements on the ACE Blade for the 2 Bar Case at i = 0° and M_b = 1.165. Comparison of Values at Three Measuring Locations. (T_g/T_w = 1.03, Tu = 3%)

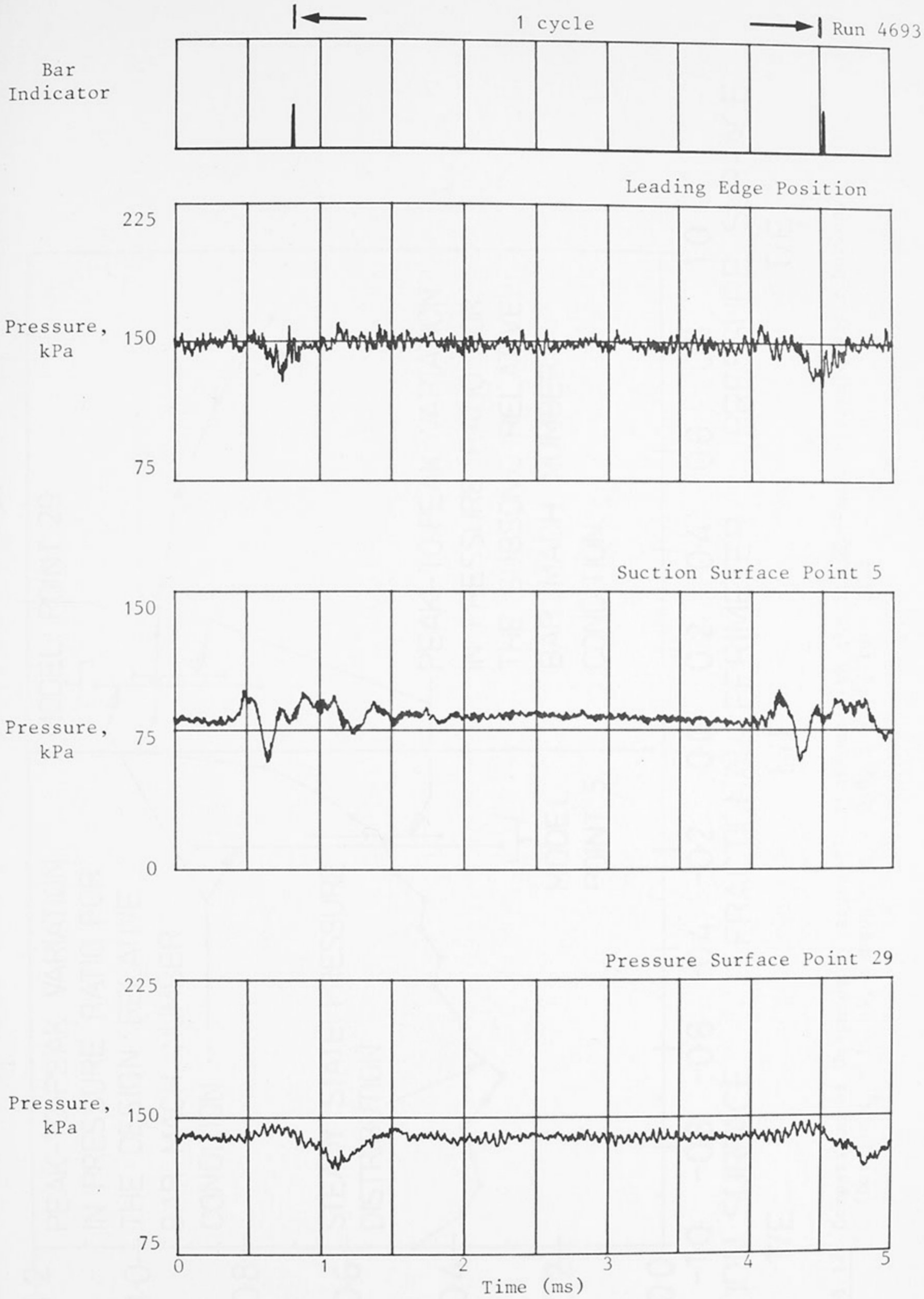

Fig. 6.16 High Bandwidth Pressure Measurements on the ACE Blade for the 2 Bar Case at i = 0° and M_b = 0.80. Comparison of Values at Three Measuring Locations. (T_g/T_w = 1.03, Tu = 3%)

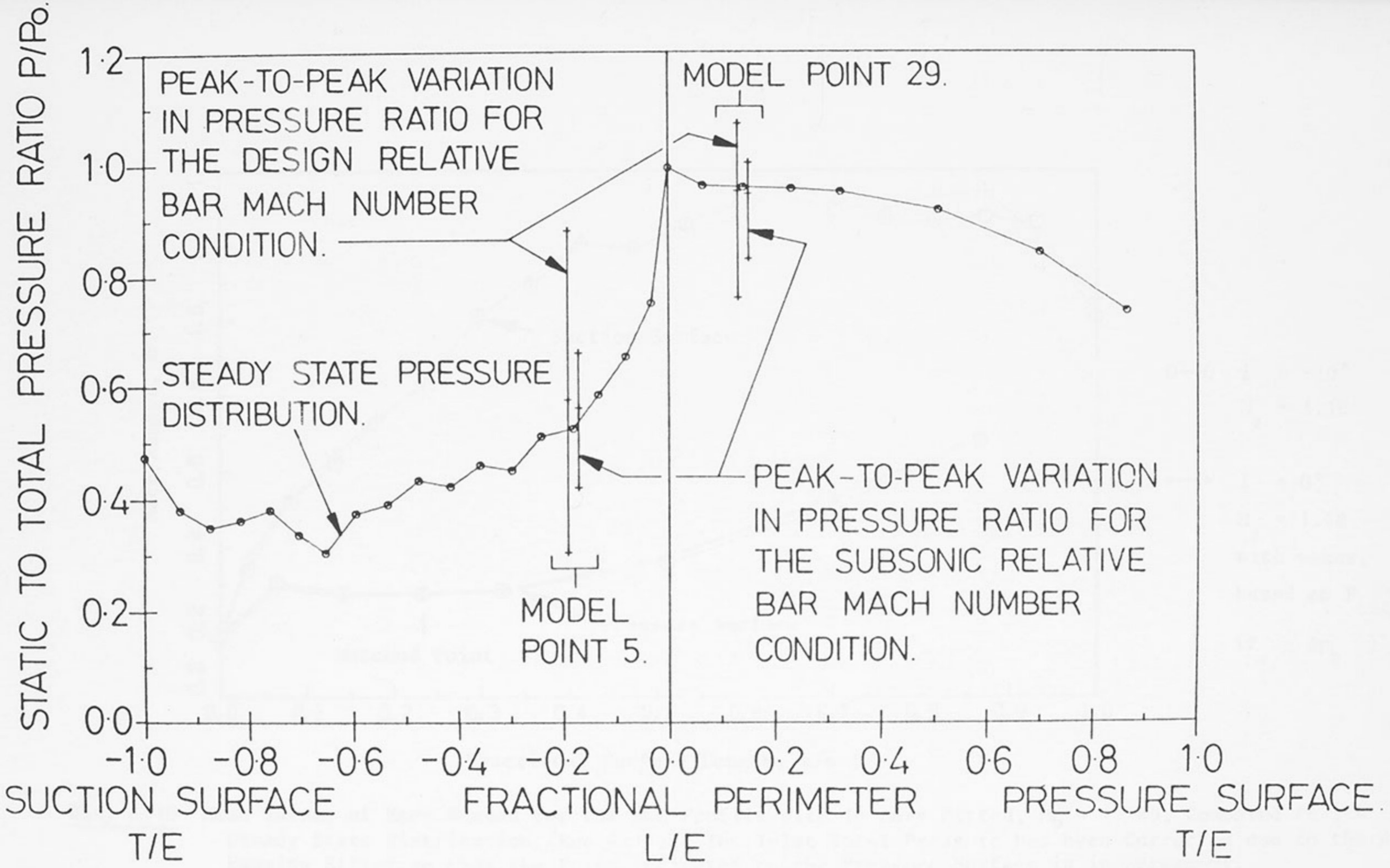

Fig. 6.17 Comparison of Unsteady Pressure Fluctuations with the Steady-State Pressure Distribution. (Design M_b = 1.165, subsonic M_b = 0.8, i = 0°, Tu = 3%.)

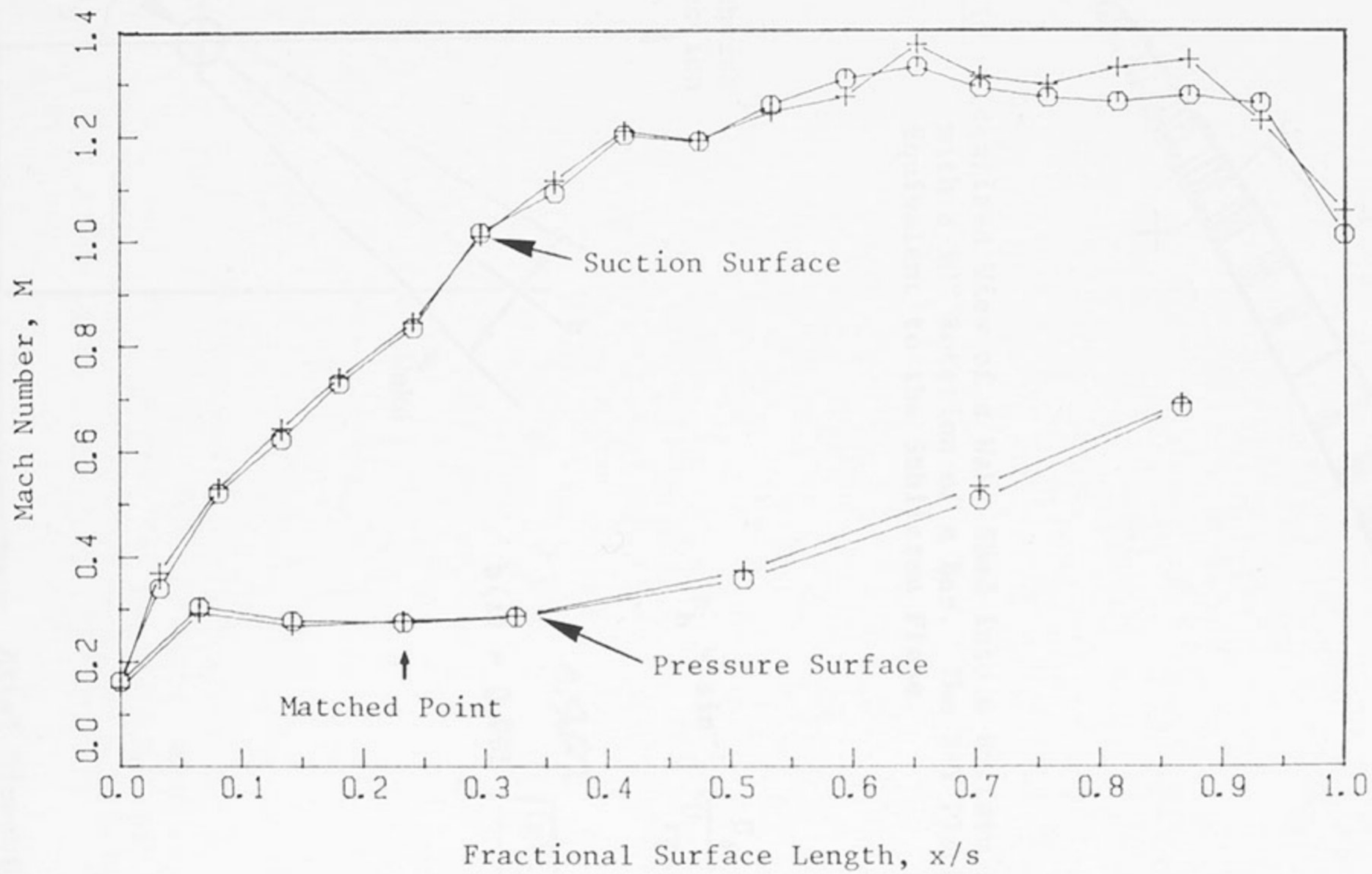

Fig. 6.18 Mean Values of Mach Number for the ACE Profile with 16 Bars Fitted, M_b = 1.165, Compared to i = -10° Steady State Distribution (Run 4611). The Inlet Total Pressure has been Corrected due to the Bar-Passing Effect so that the Point Indicated on the Pressure Surface is in Agreement.

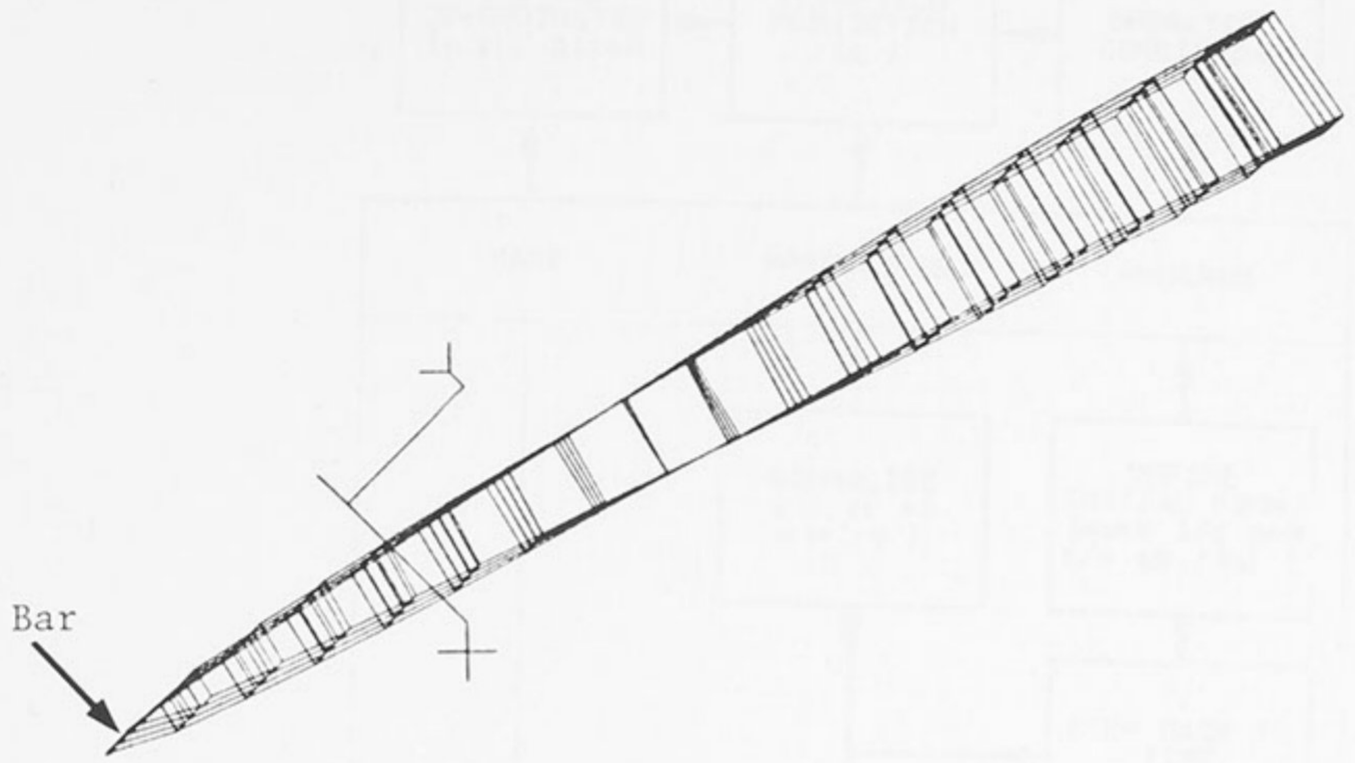

Fig. 7.1(a) Idealised View of a Wake Shed into a Uniform Flowfield with a 90° Rotation of a Bar. The X-Y Plane Equivalent to the Schlieren Plane.

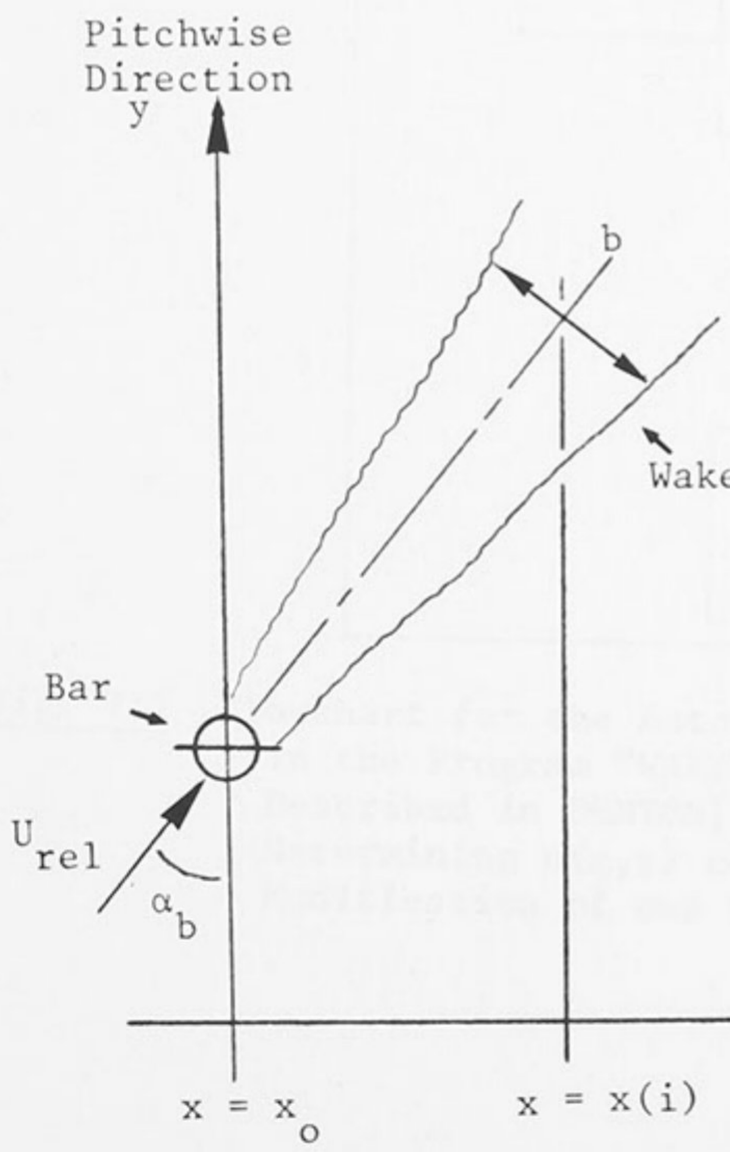

$$\alpha_b = \sin^{-1}\left(\frac{U_1}{U_{rel}} \cos \beta_1\right)$$

$$b(i) = 0.033 \sqrt{\frac{(x(i) - x_o)C_D d}{\sin \alpha_b}}$$

Fig. 7.1(b) Nomenclature used in the Wake Model.

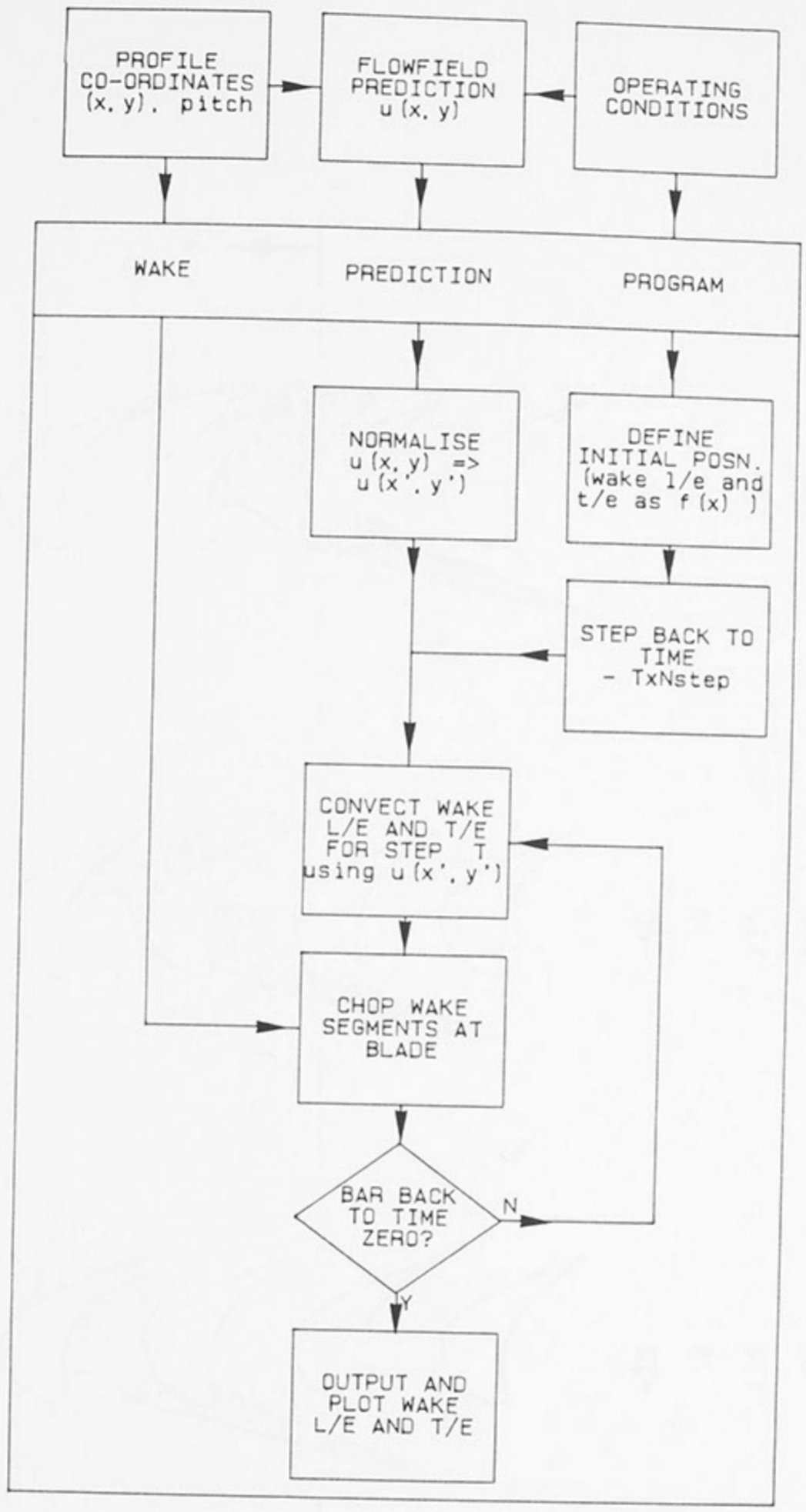

Fig. 7.2 Flowchart for the Automated Striped-Air Prediction Embodied in the Program "WAKE". The Flowfield Prediction used is Described in DENTON[1983] though other Methods for Determining u(x,y) could be used, only Requiring Modification of one Subroutine (INPUT).

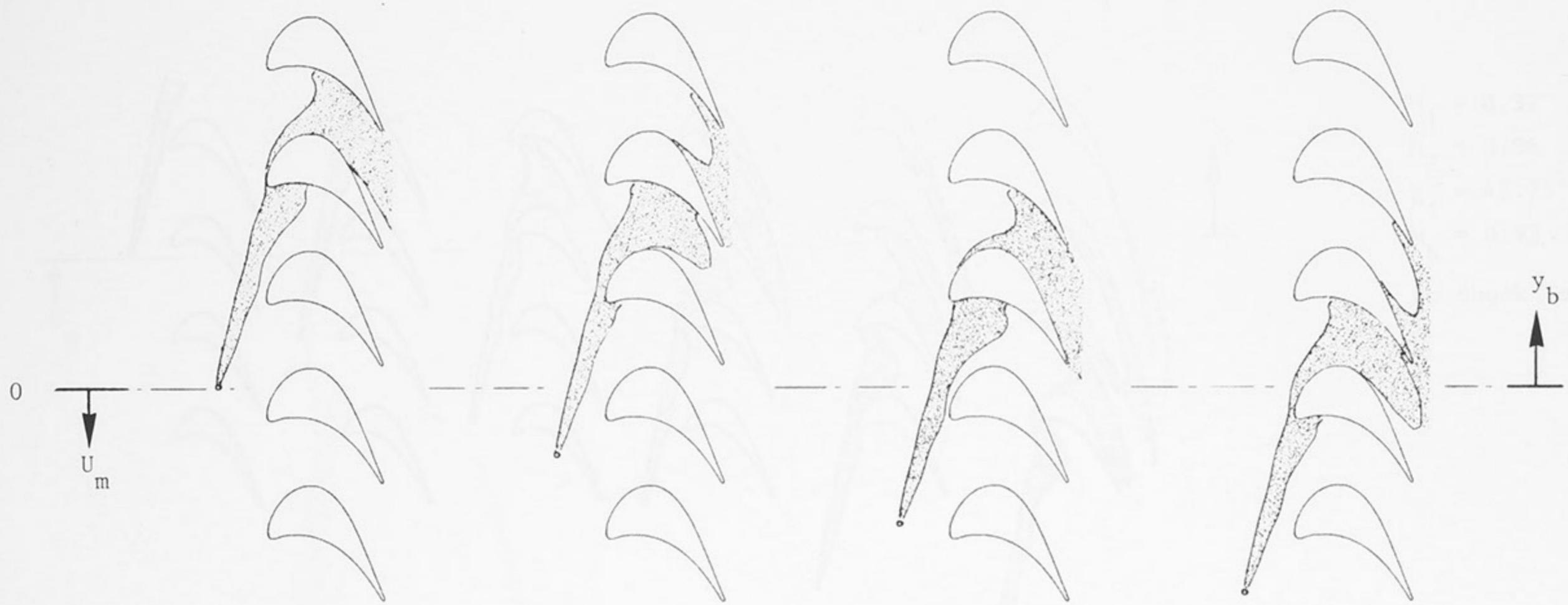

y_b (mm)	0	-20	-40	-60
θ_b (°)	0	8	16	24
Δt_c (μs)	0	116	235	356
Δt_h (μs)	0	97	196	298

Fig. 7.3 Predicted Positions for the Wake as Calculated by the Striped-Air Model Corresponding to the Operating Conditions of Run 5696, i = -10°, M_b = 0.82. (Δt_c and Δt_h are the time intervals corresponding to 'cold' (T_o = 315 K) and 'hot' (T_o = 450 K) Running Conditions Respectively.)

$M_1 = 0.32$
$M_2 = 0.96$
$\beta_1 = 42.75°$
$M_b = 0.93$

No Shock Waves Included

Fig. 7.4 Positions of the Wake in the B22 Cascade as Predicted by the Striped-Air Calculation (Program "WAKE"). The Wake is Shown for Six Equal 50 mm Increments of the Bar Below the Datum Position, $y_b = 0$ mm.

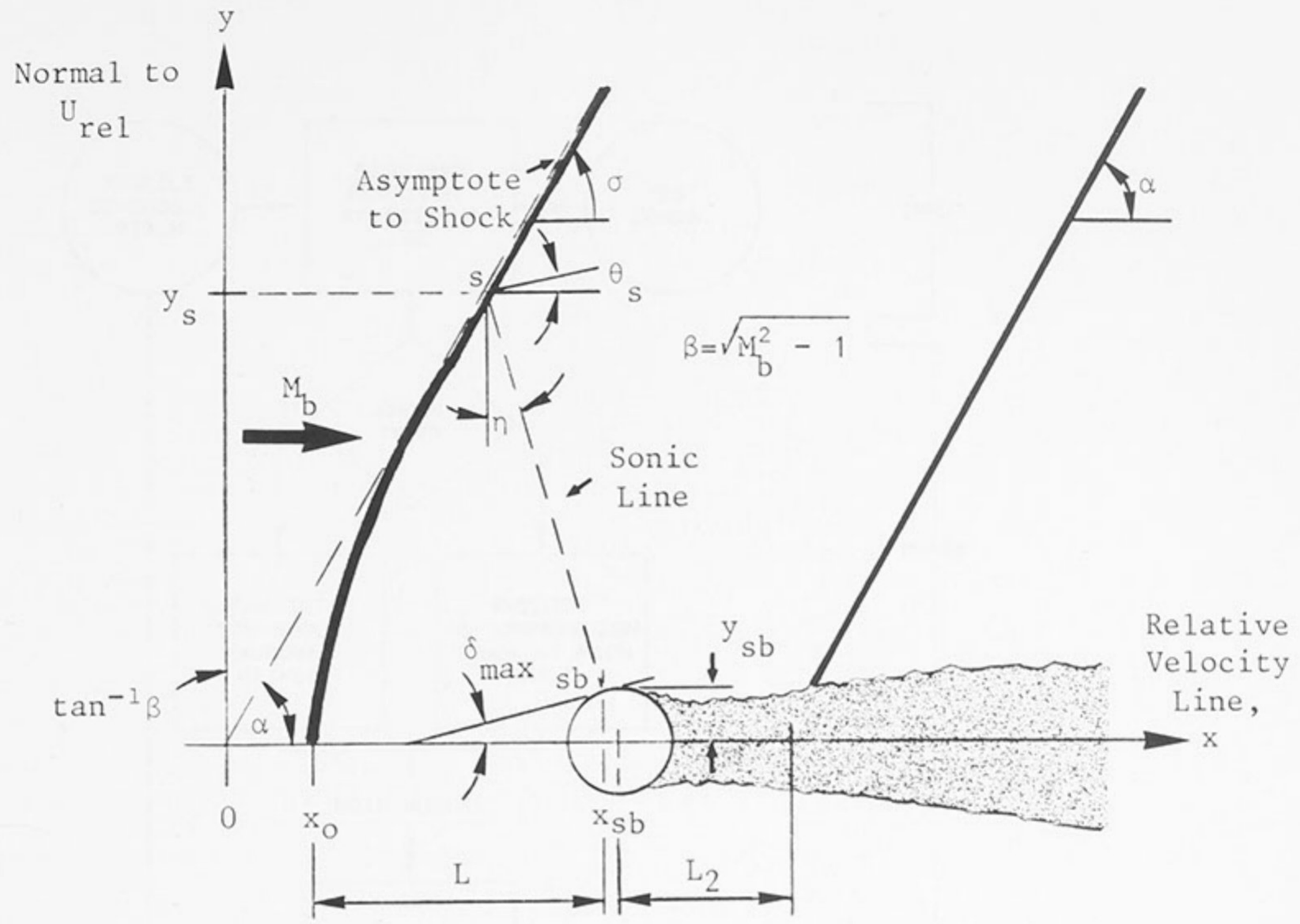

Fig. 7.5(a) Nomenclature for Approximate Analysis of Bow and Recompression Shock Locations.

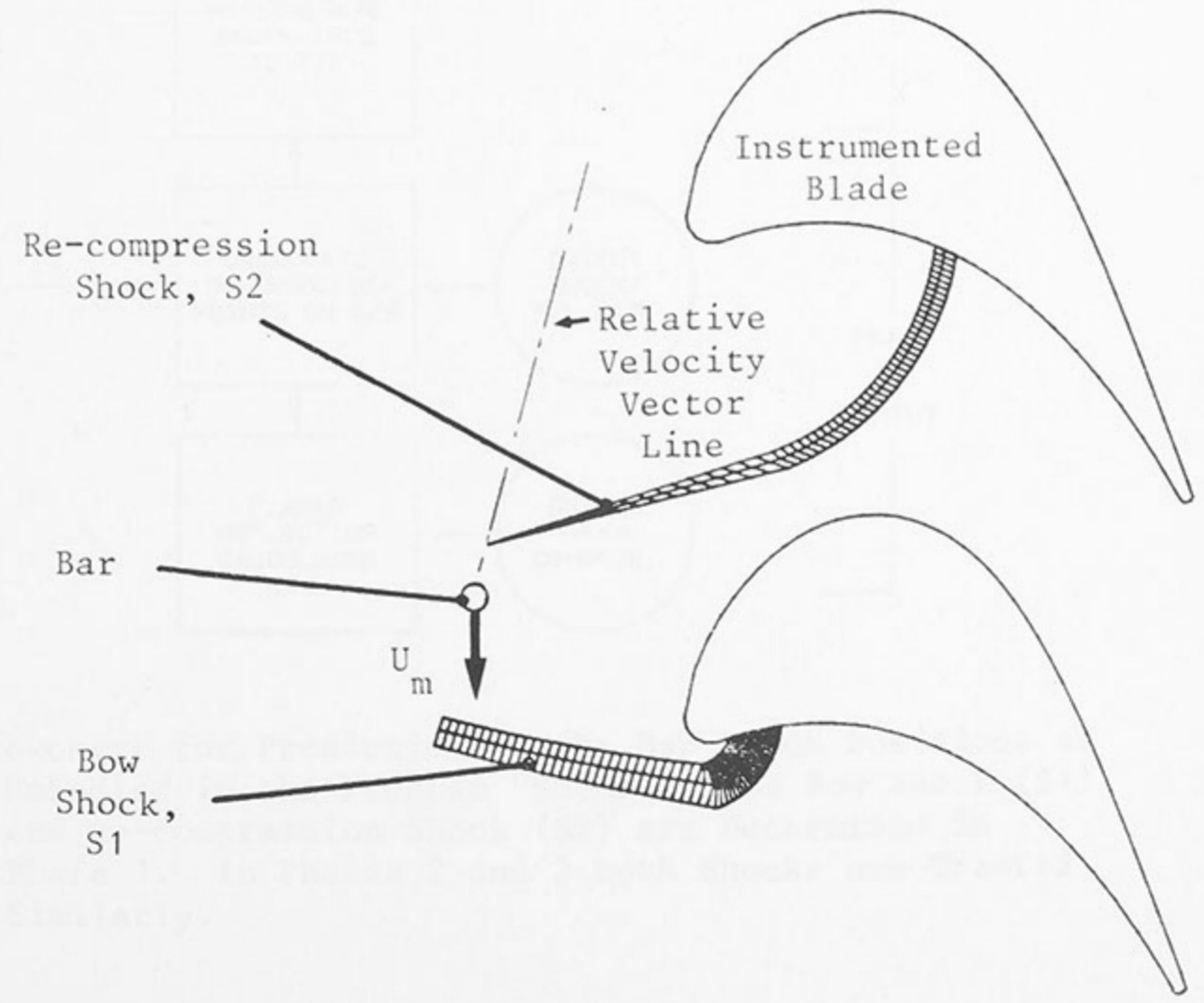

Fig. 7.5(b) Example of the Shock Prediction at Mid-Height, with the Bar Normal to the Cascade Sidewall. View in the Schlieren Plane.

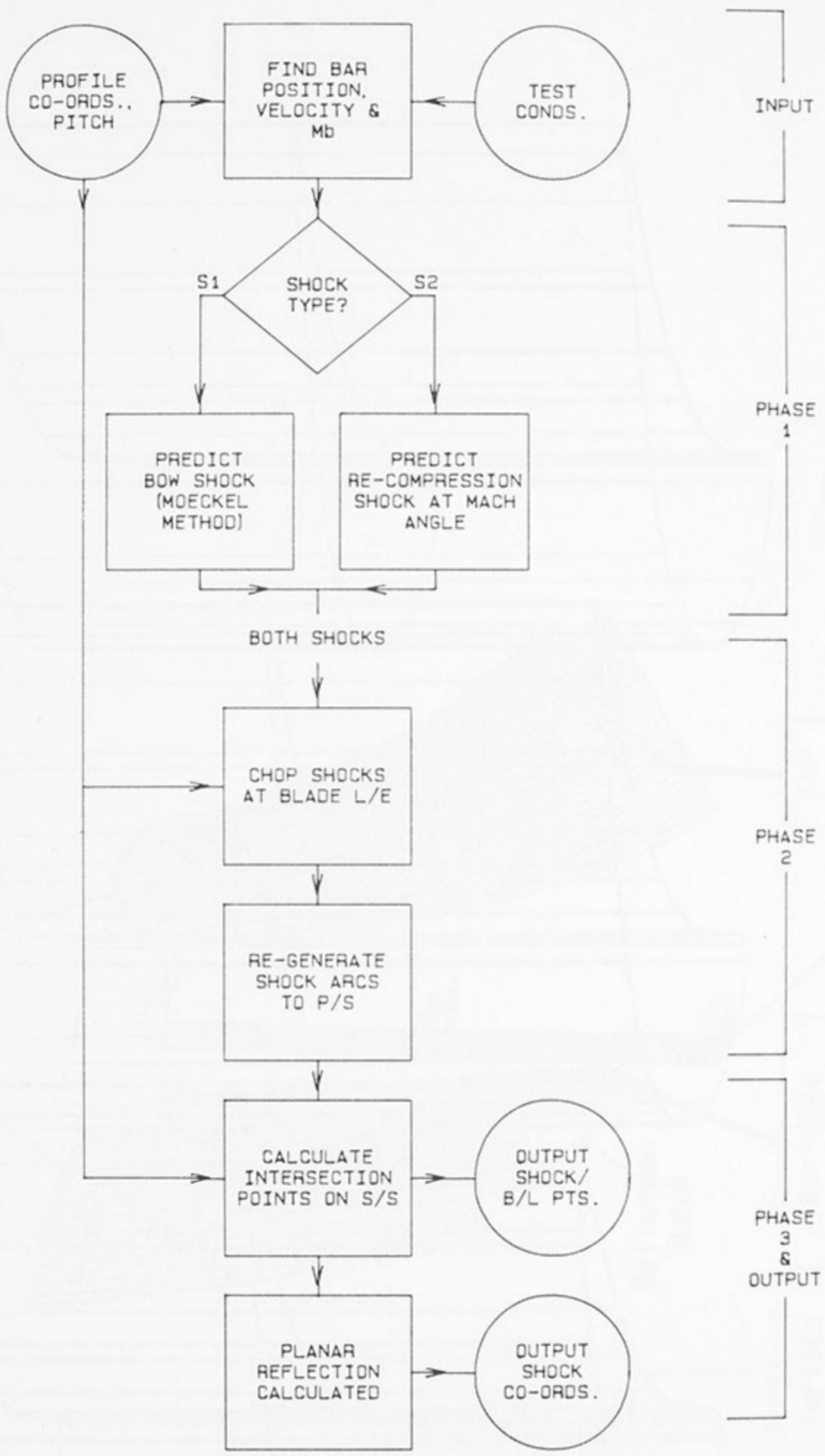

Fig. 7.6 Flowchart for Prediction of the Bar Shock Positions as Embodied in the Program "SHOCK". The Bow Shock (S1) and Re-compression Shock (S2) are Determined in Phase 1. In Phases 2 and 3 both Shocks are Treated Similarly.

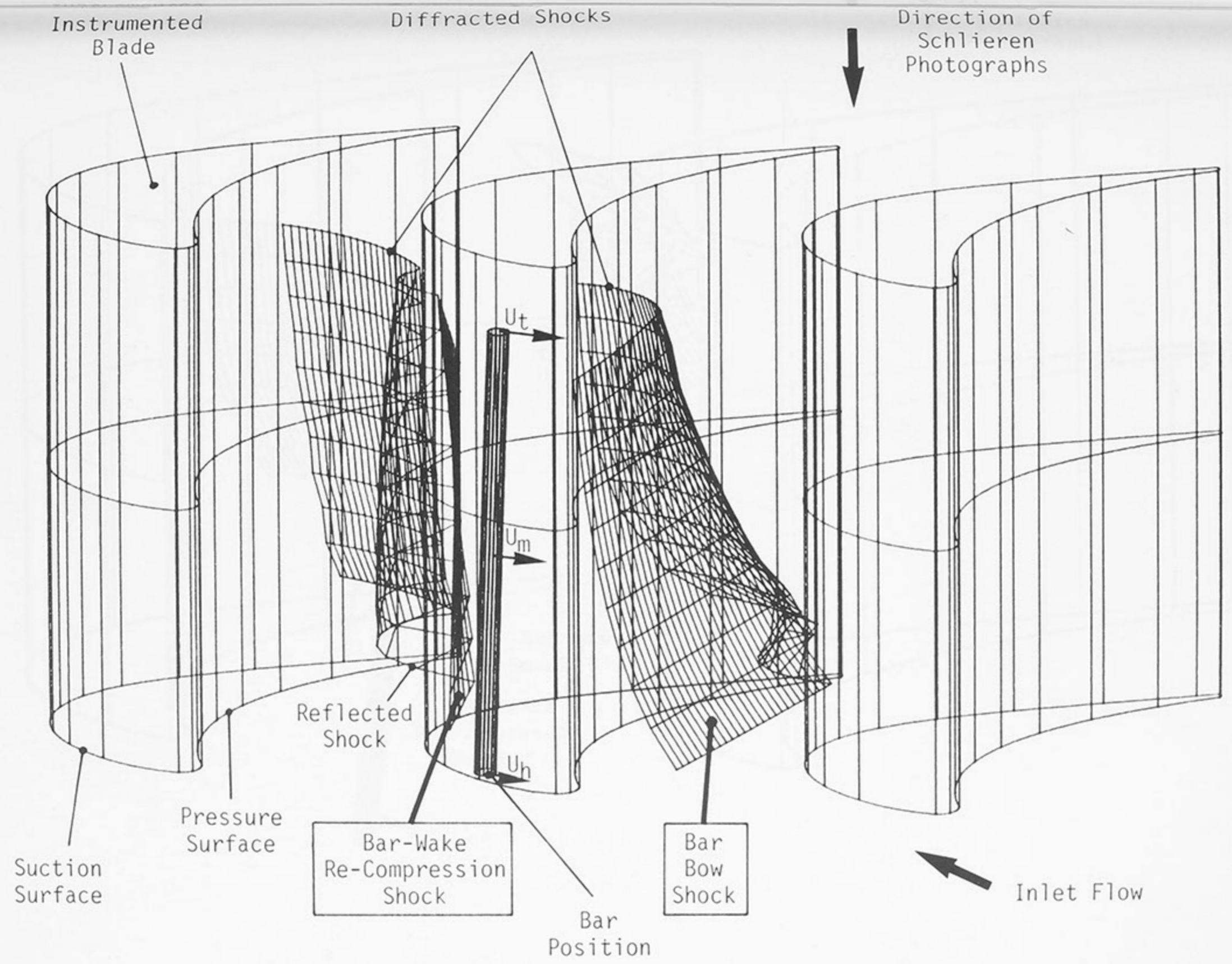

Fig. 7.7 Predicted Positions of the Bar Shocks for the ACE Test with the Bar at 2° to the Normal to the Cascade Sidewall. Only the Halves of the Shocks Downstream of the Relative Velocity Vector Line are Shown. The Bar Rotates in a Clockwise Direction in this View. Design Operating Conditions (i = 0°, M_b = 1.16).

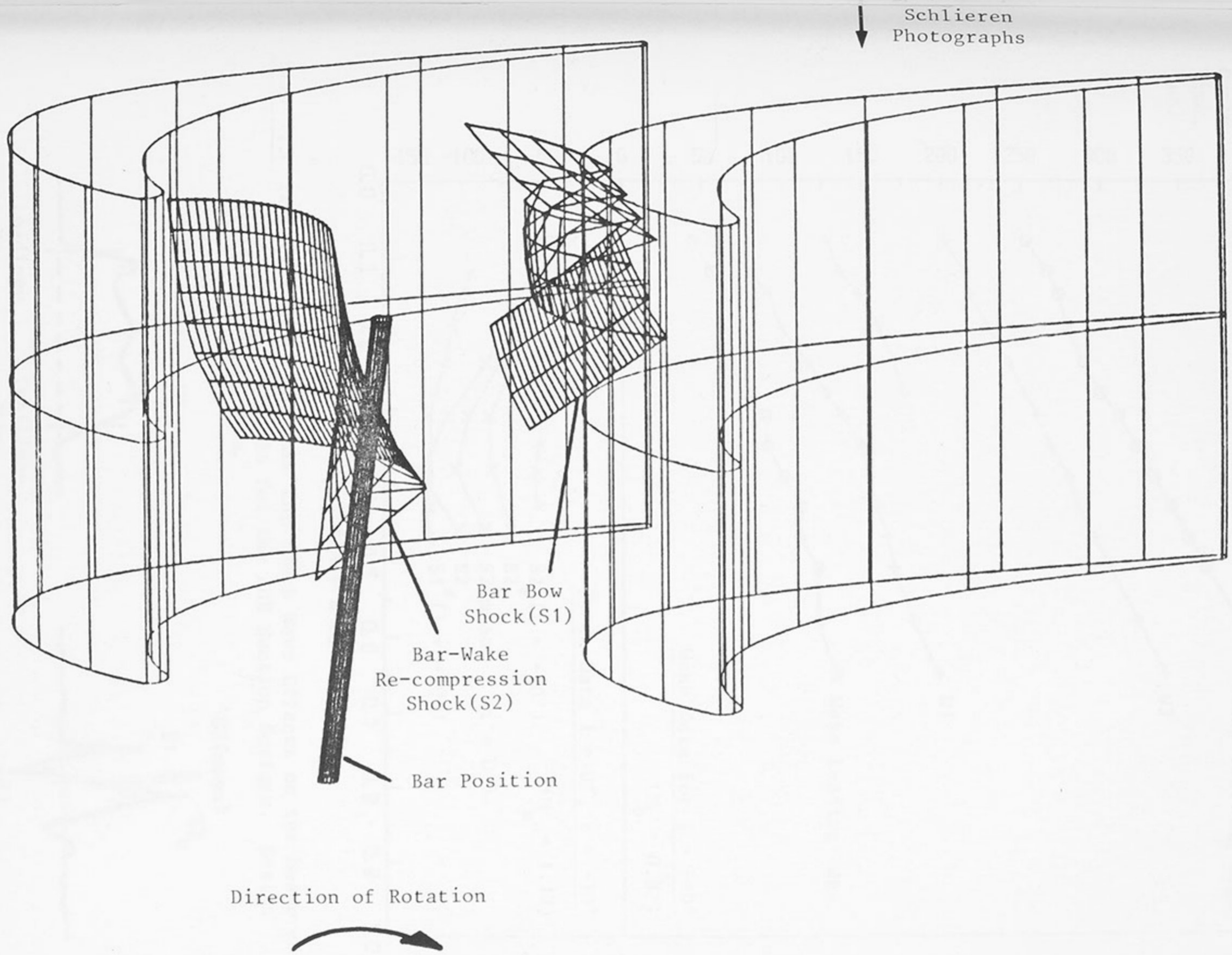

Fig. 7.8 Predicted Positions of the Bar Shocks for the B22 Test with the Bar at 6.5° to the Normal to the Cascade Sidewall. Only the Halves of the Shocks Downstream of the Relative Velocity Vector Line are Shown. The Bar Rotates in a Clockwise Direction in this View. Design Operating Conditions (M_b = 0.92, M_1 = 0.32, β_1 = 42.75°).

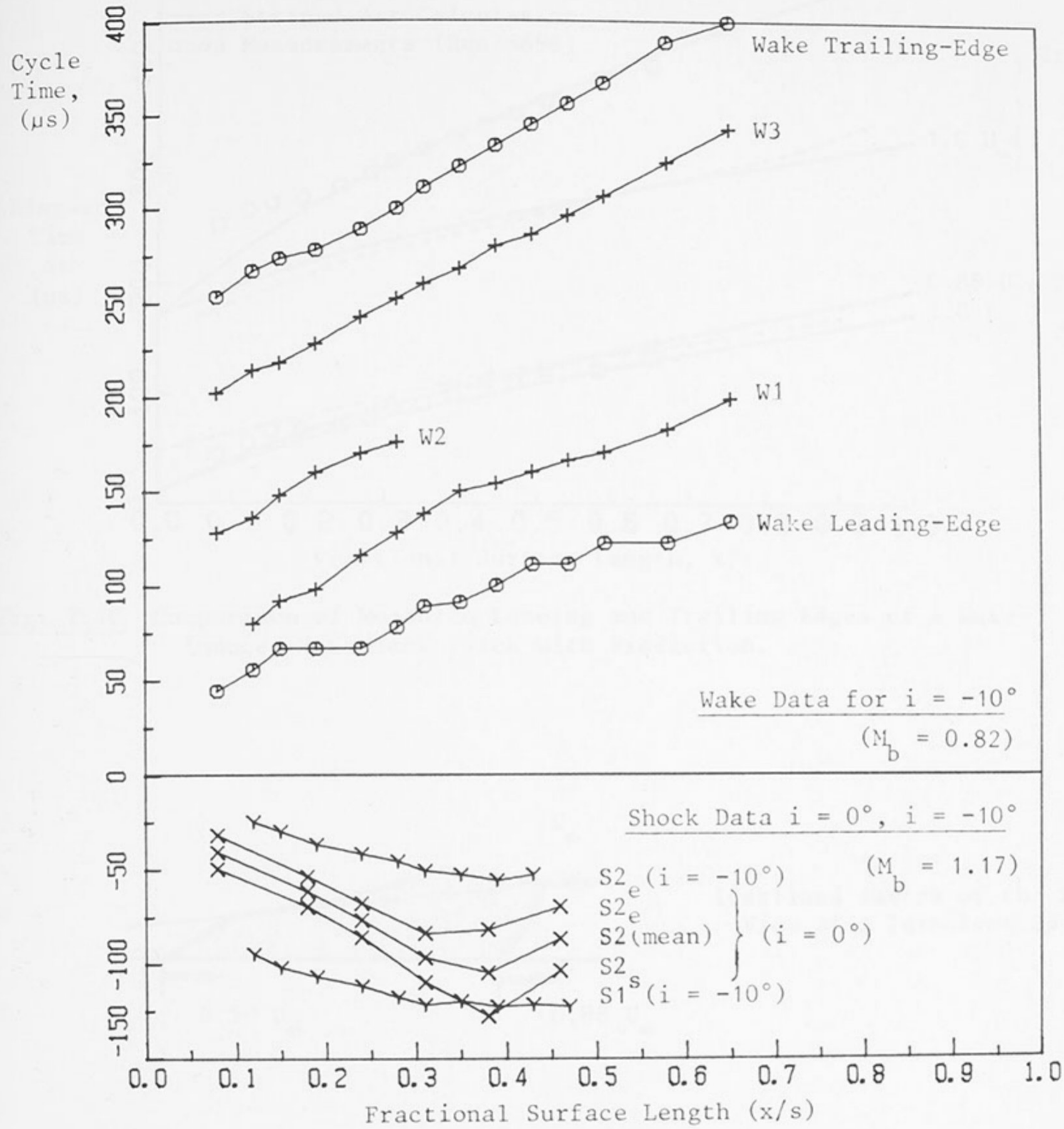

Fig. 7.9 Trajectories of the Wake and Shock Wave Effects on the Measured Heat Transfer Signals for the ACE Suction Surface. Design Operating Conditions.

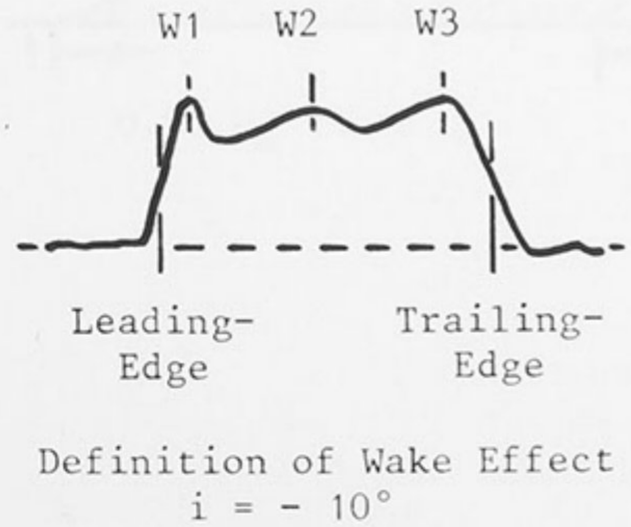

Definition of Wake Effect
i = - 10°

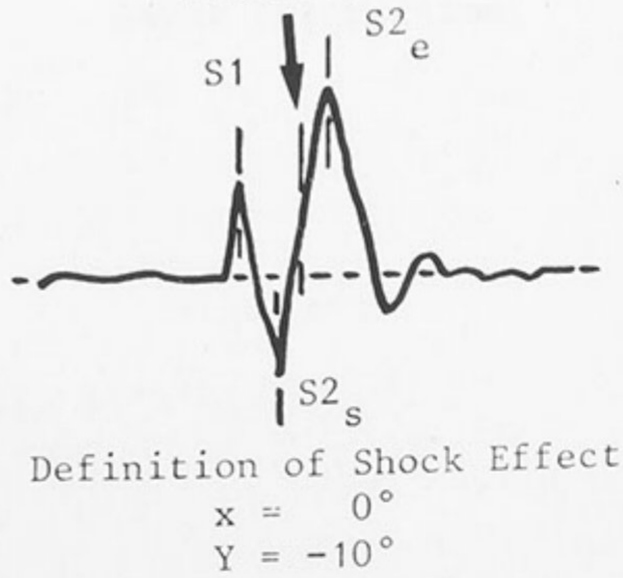

Definition of Shock Effect
x = 0°
Y = -10°

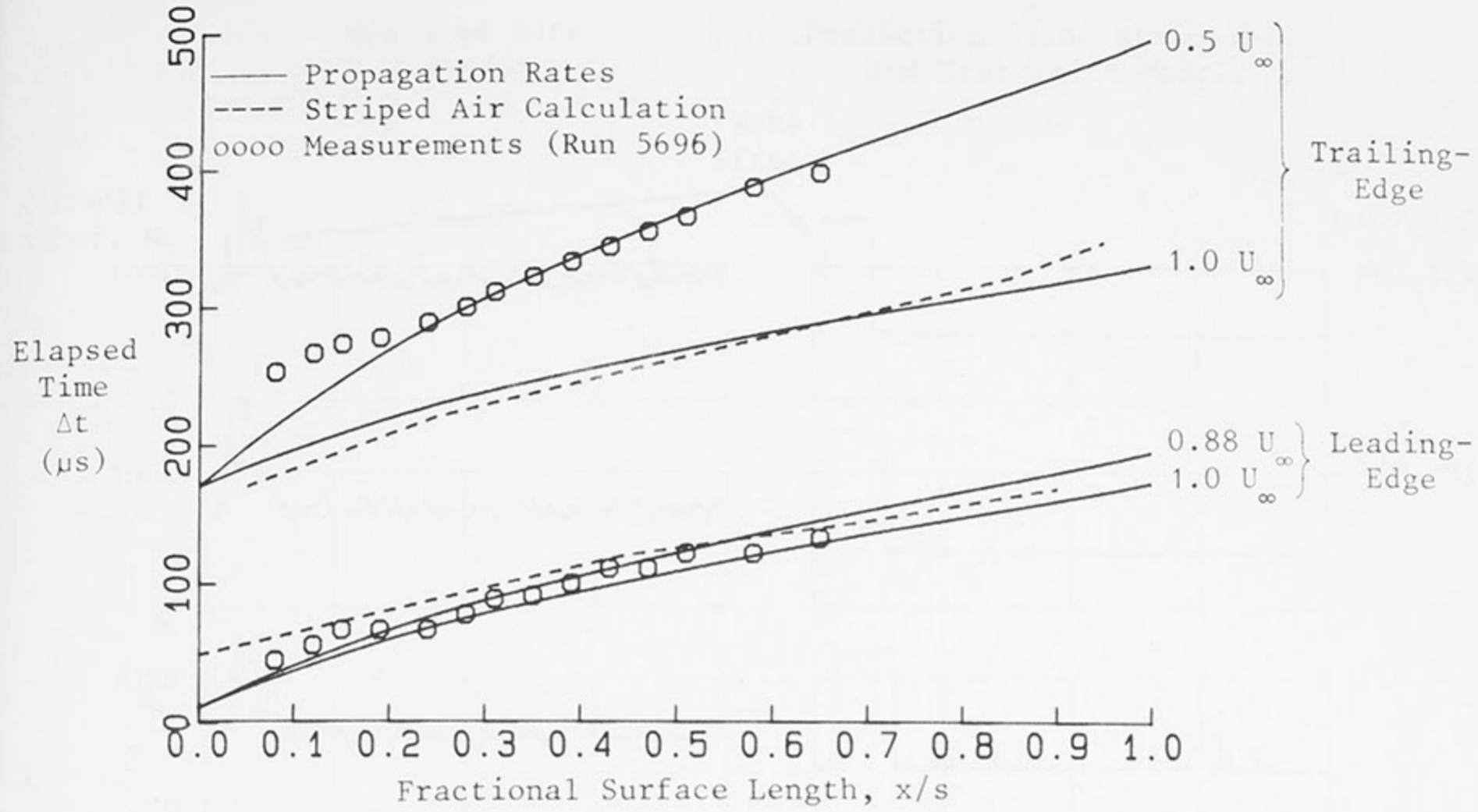

Fig. 7.10 Comparison of Measured Leading and Trailing Edges of a Wake-Induced Turbulent Patch with Prediction.

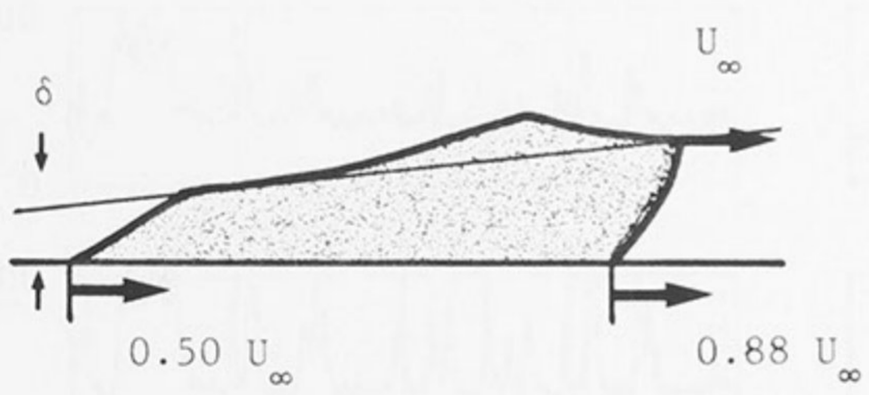

Idealised Sketch of the Side View of a Turbulent Spot.

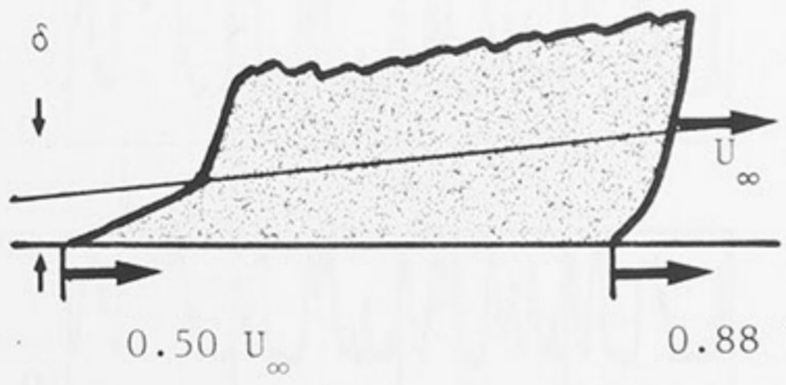

Idealised Sketch of the Side View of a Wake/Boundary Layer Interaction.

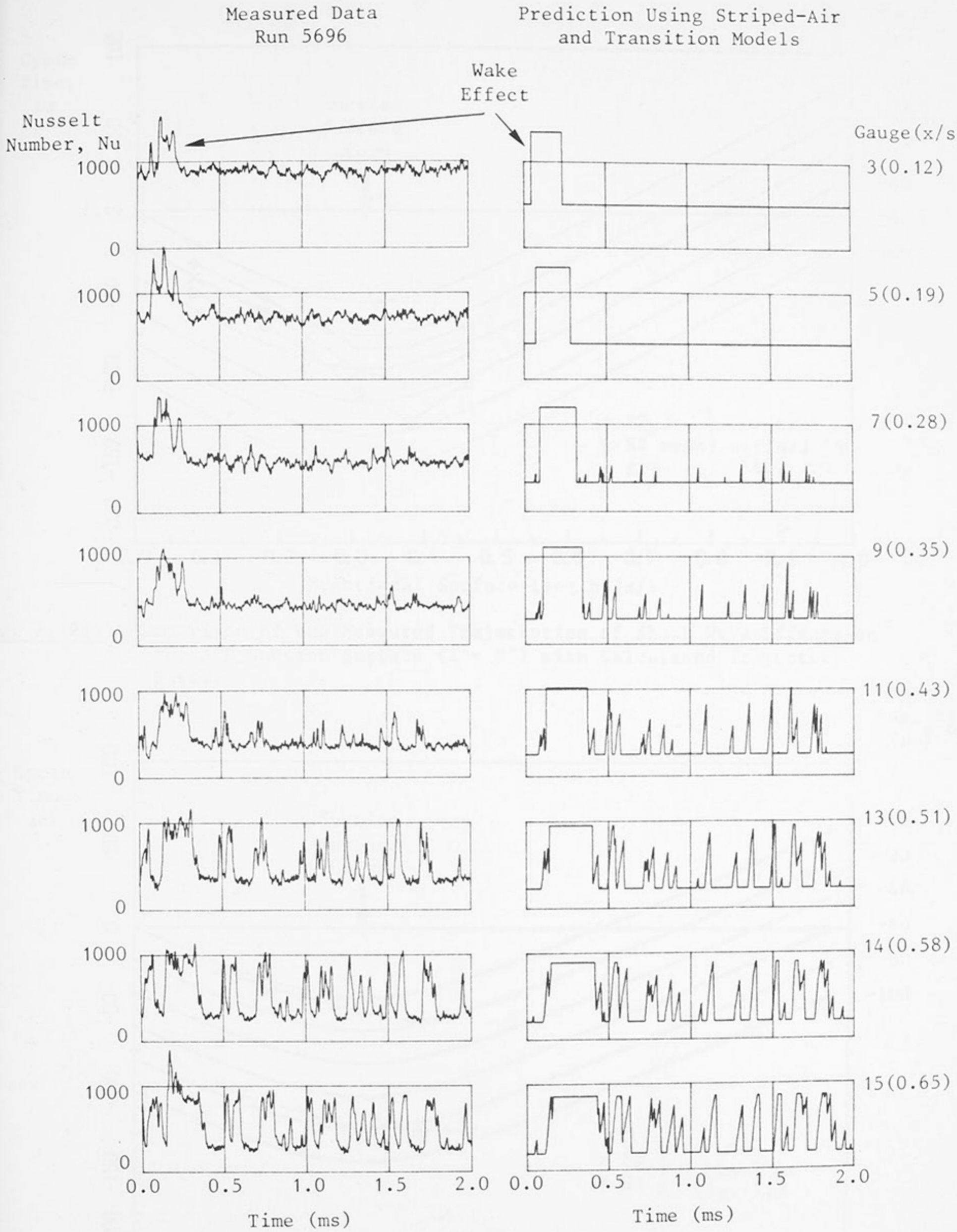

Fig. 7.11 Instantaneous Data from the ACE Blade with Wake-Passing Compared with Predicted Values. Data is taken from the Second Series of Tests using 4 mm Wide Gauges ($i = -10°$, $Tu \cong 3\%$, Sub-sonic $M_b = 0.82$, $M_2 = 1.18$).

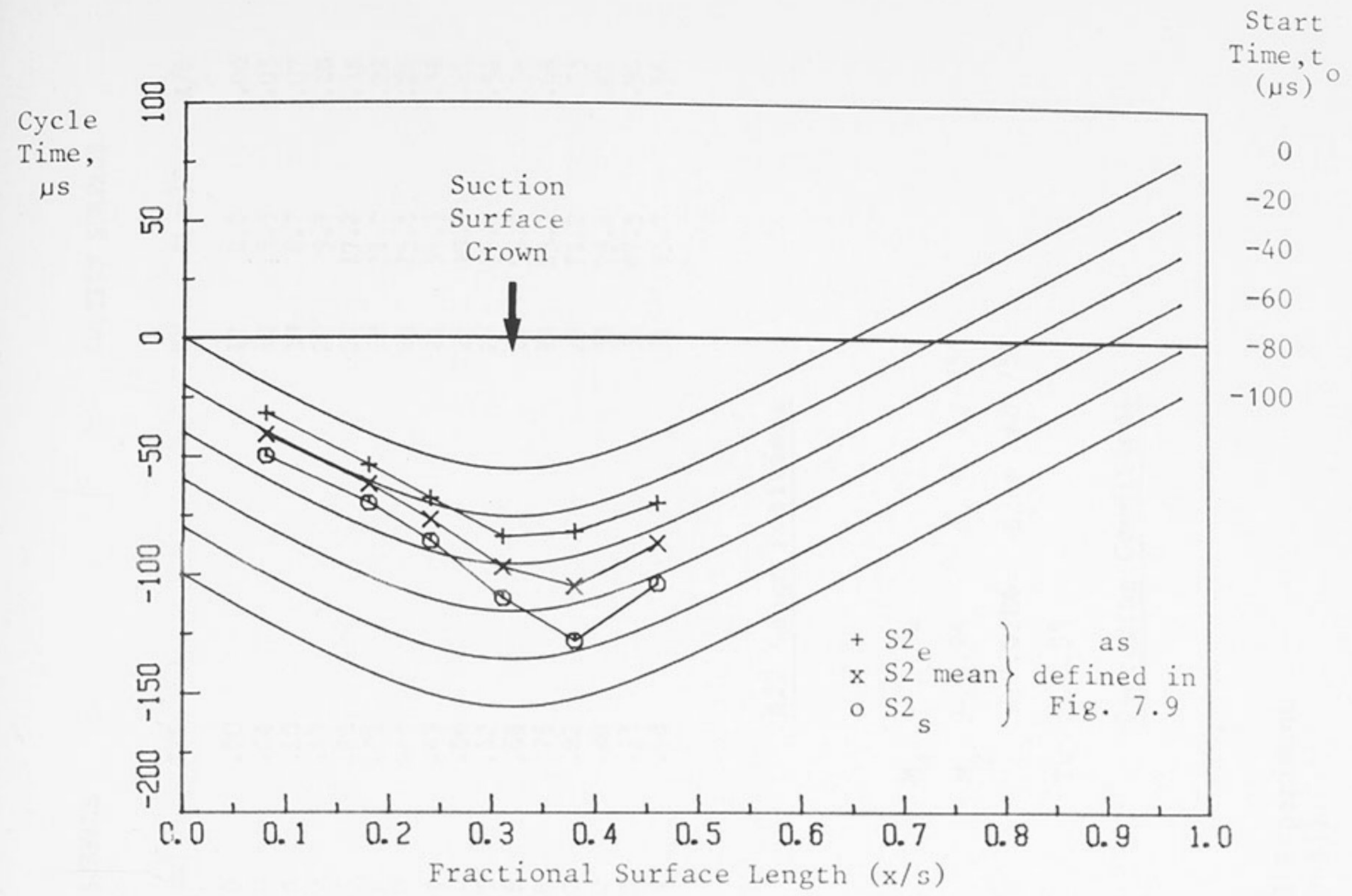

Fig. 7.12(a) Comparison of the Measured Trajectories of Shock Wave Effects on the ACE Suction Surface (i = 0°) with Calculated Trajectory Rates.

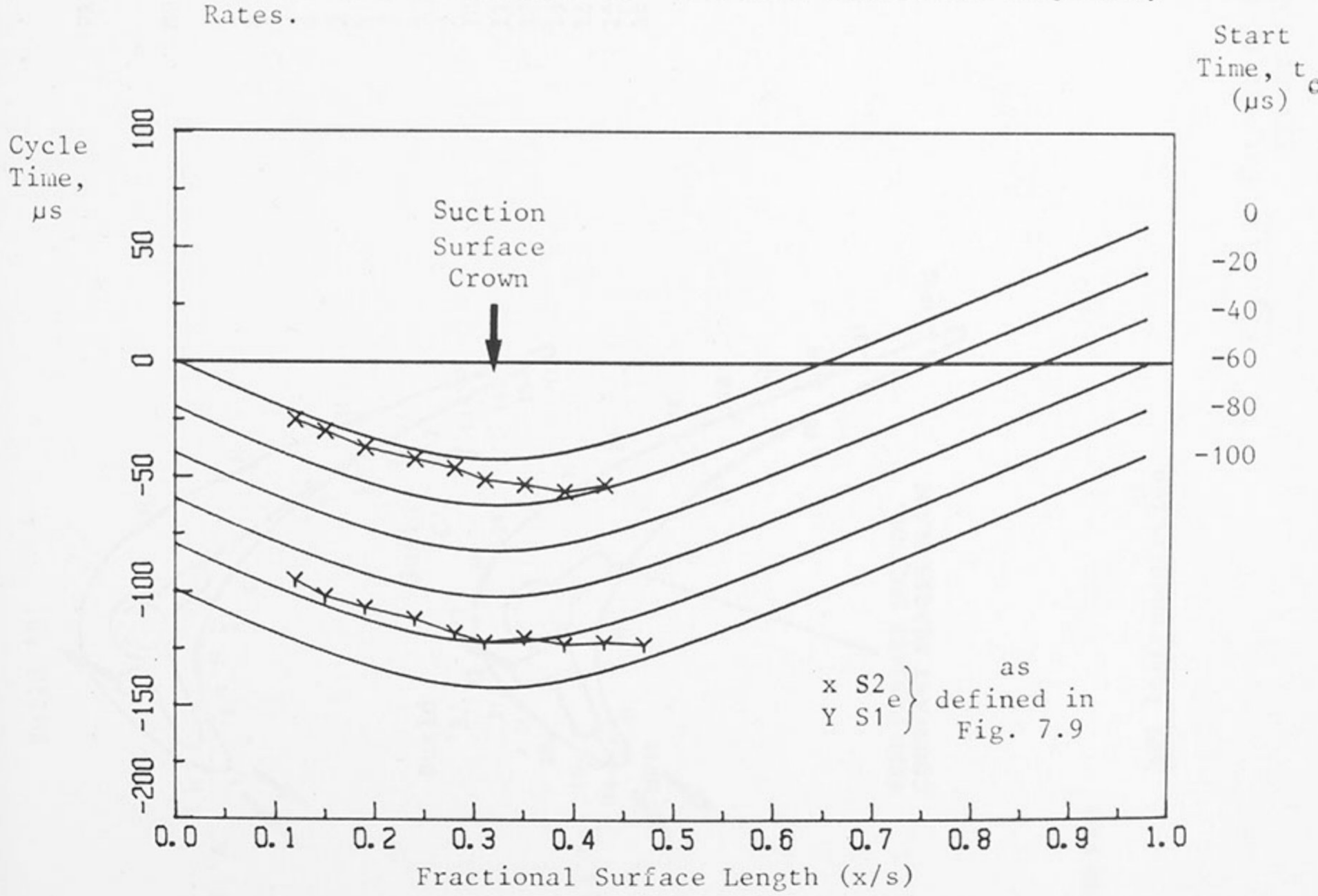

Fig. 7.12(b) Comparison of the Measured Trajectories of Shock Wave Effects on the ACE Suction Surface (i = -10°) with Calculated Trajectory Rates.

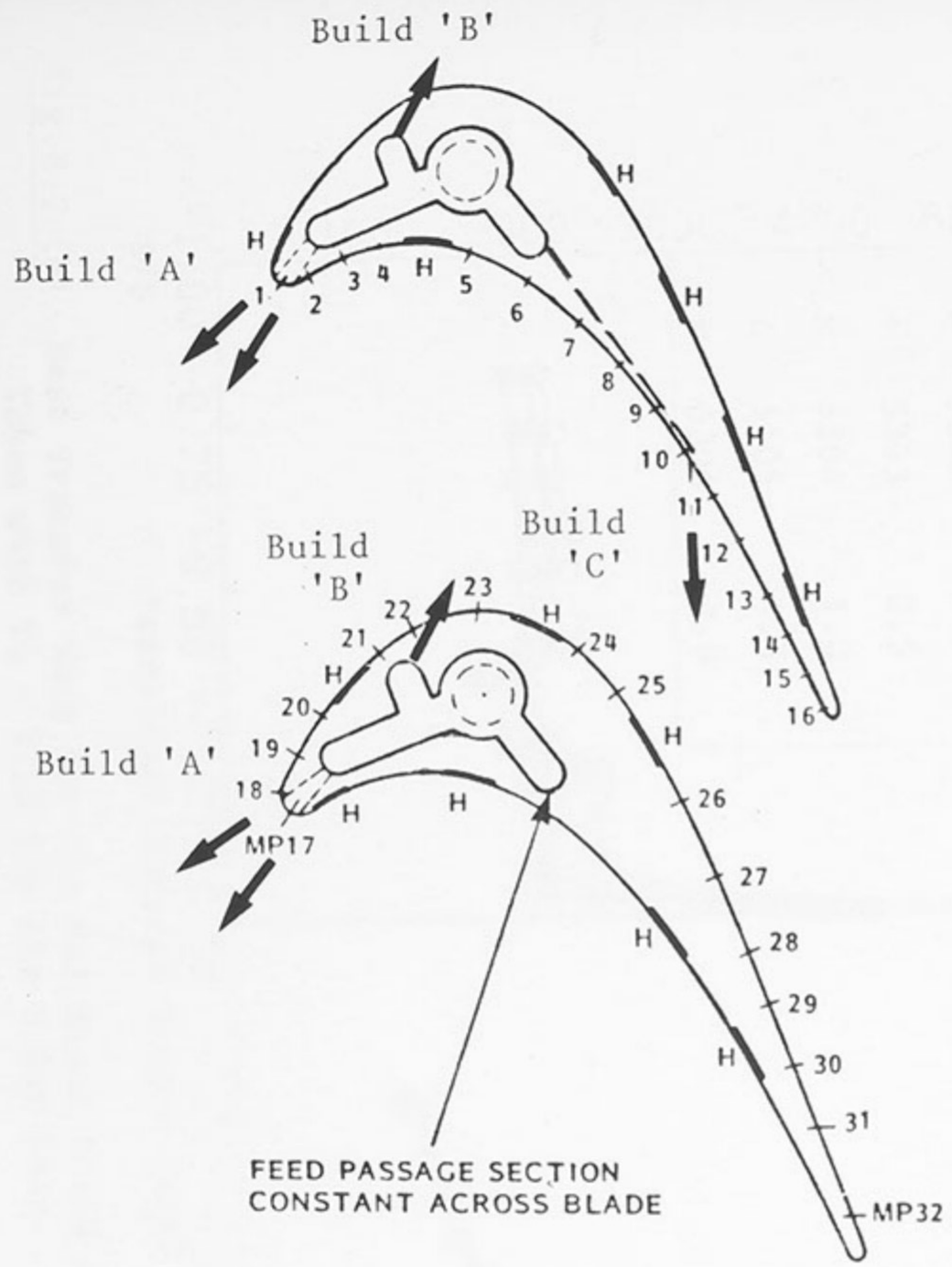

H = HEATER PAD

B22 Instrumentation

PRESSURE SURFACE

MP	X(mm)	X/S
1	0.0	.00
2	3.0	.04
3	7.0	.10
4	11.2	.15
5	20.3	.28
6	25.6	.32
7	31.0	.43
8	35.4	.49
9	40.8	.56
10	45.3	.62
11	49.6	.68
12	54.8	.75
13	60.0	.82
14	64.0	.88
15	67.8	.93
16	71.4	.98

SUCTION SURFACE

MP	X(mm)	X/S
17	0.0	.00
18	3.3	.03
19	6.7	.07
20	9.7	.10
21	17.2	.18
22	21.0	.22
23	25.3	.26
24	35.3	.36
25	40.2	.41
26	50.8	.52
27	56.7	.58
28	63.7	.66
29	71.2	.73
30	79.2	.82
31	87.5	.90
32	93.7	.96

B22 Gauge Positions

M_1 = 0.32

M_2 = 0.96 β_1 = 42.75°

Re_2 = 2.02E6 β_2 = -68.75°

Tu ≅ 2.5%

Operating Conditions

Fig. 8.1 Details of the B22 Experiment (after HORTON[1985]).

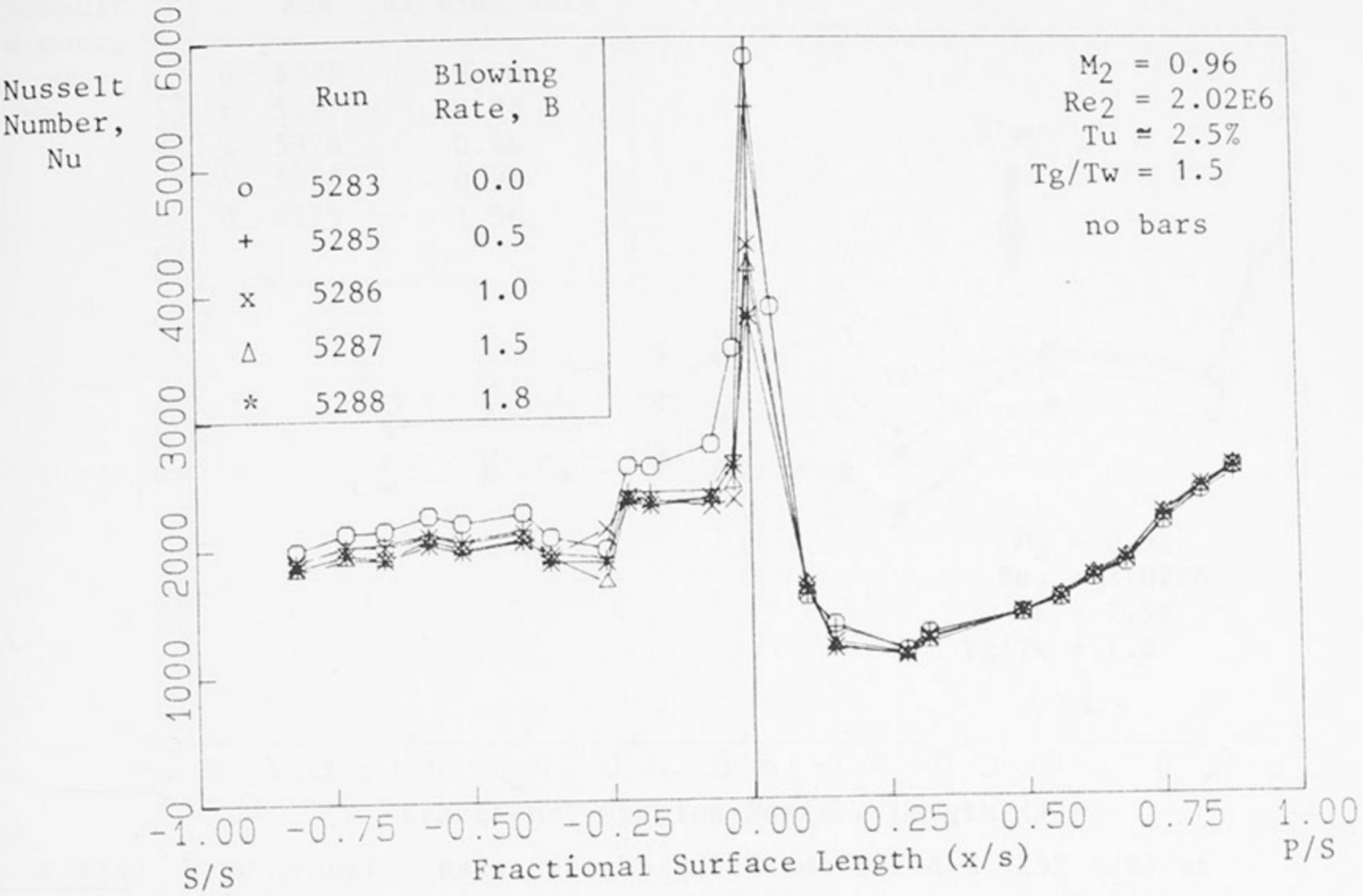

Fig. 8.2 (a) Heat Transfer Rate for the B22 Blade Build A (L/E). Datum Case with no Bars and Tu ≃ 2.5% with Variation in Blowing Rate.

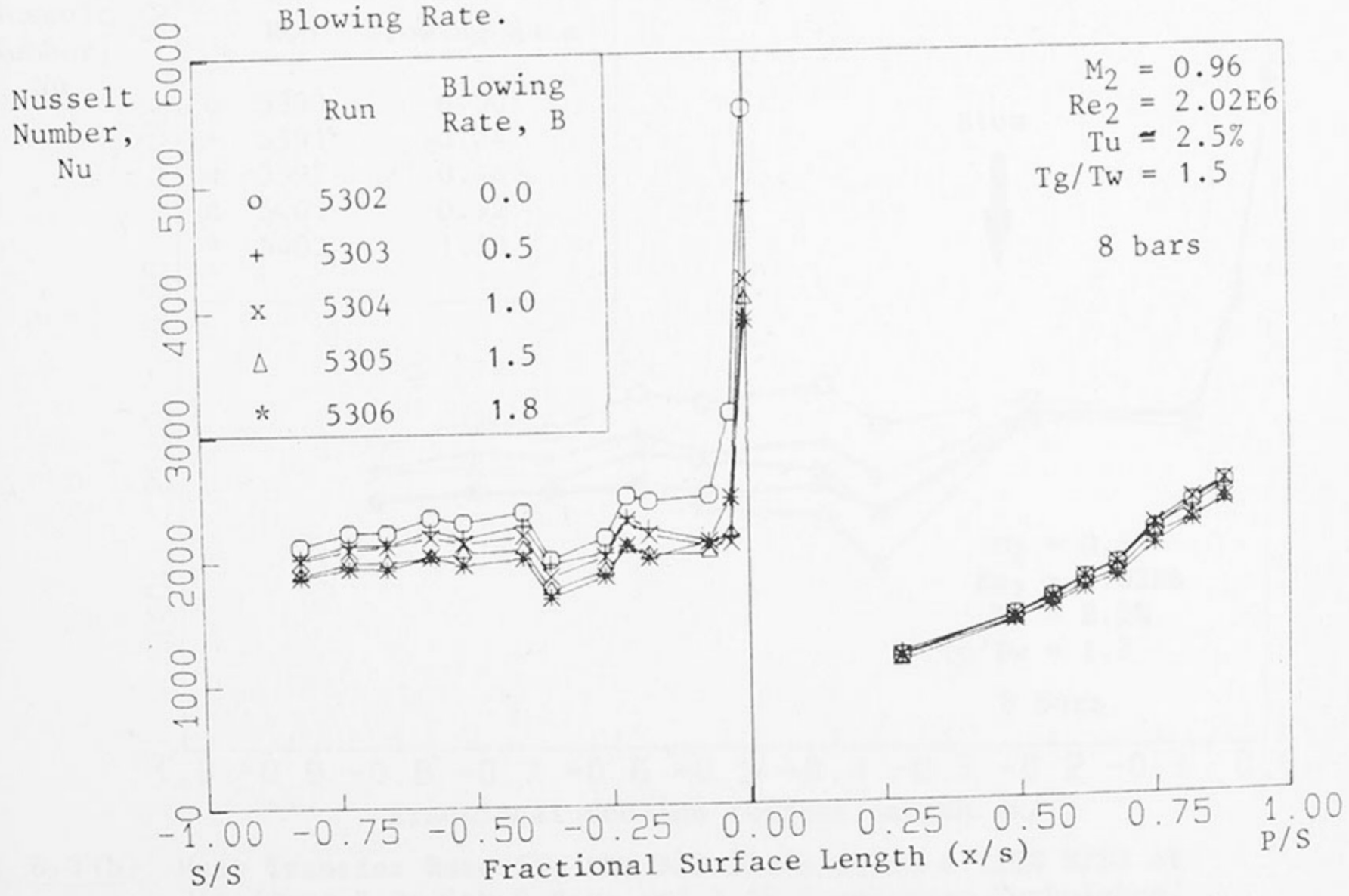

Fig. 8.2 (b) Heat Transfer Rate for the B22 Blade Build A (L/E). Data Taken with Tu ≃ 2.5% for the 8 Bar Case.

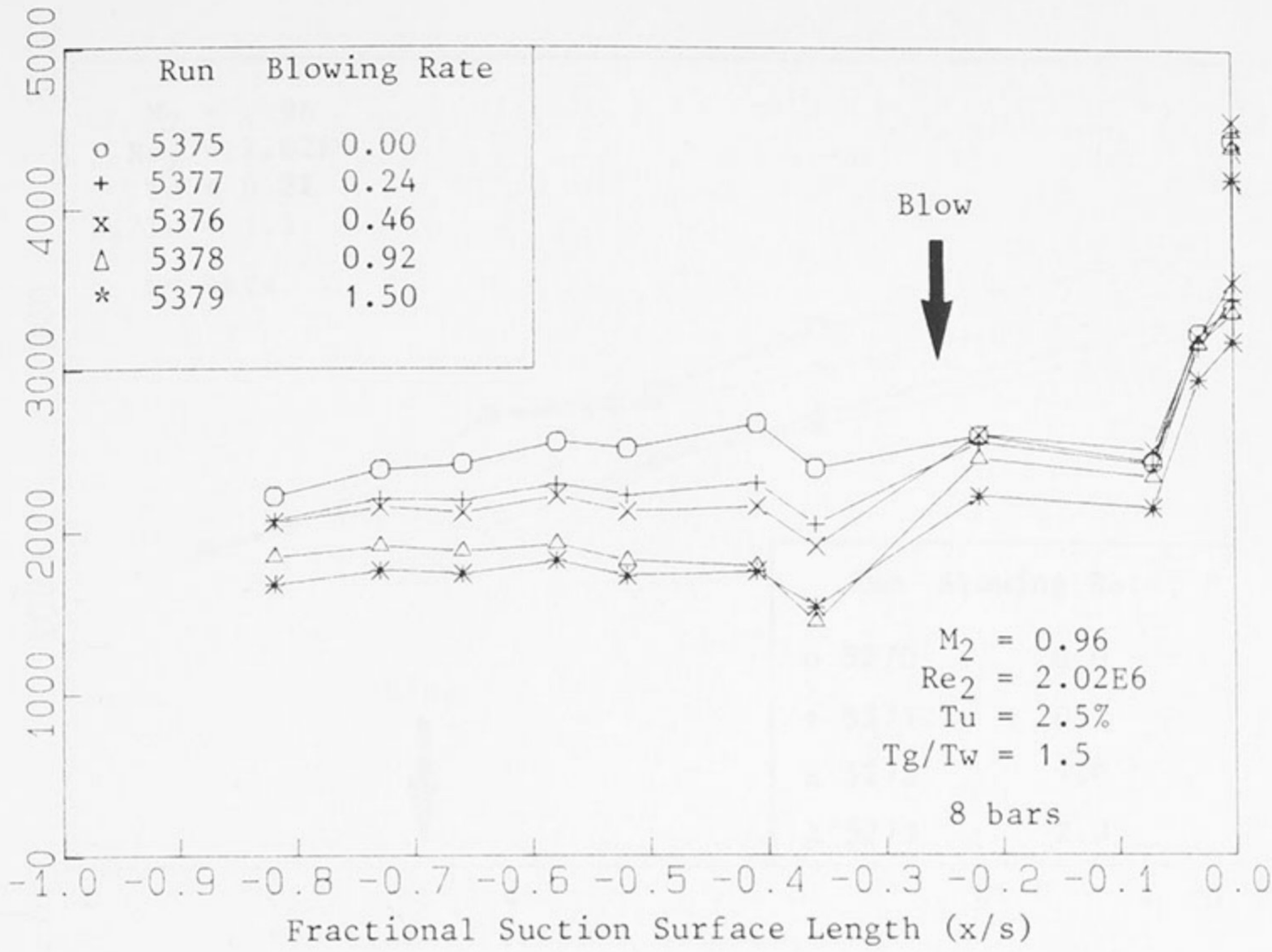

Fig. 8.3(a) Heat Transfer Rate for the B22 Blade Build B (25% S/S) at Tg/Tw = 1.5 with 8 Bars and 2.5% Freestream Turbulence.

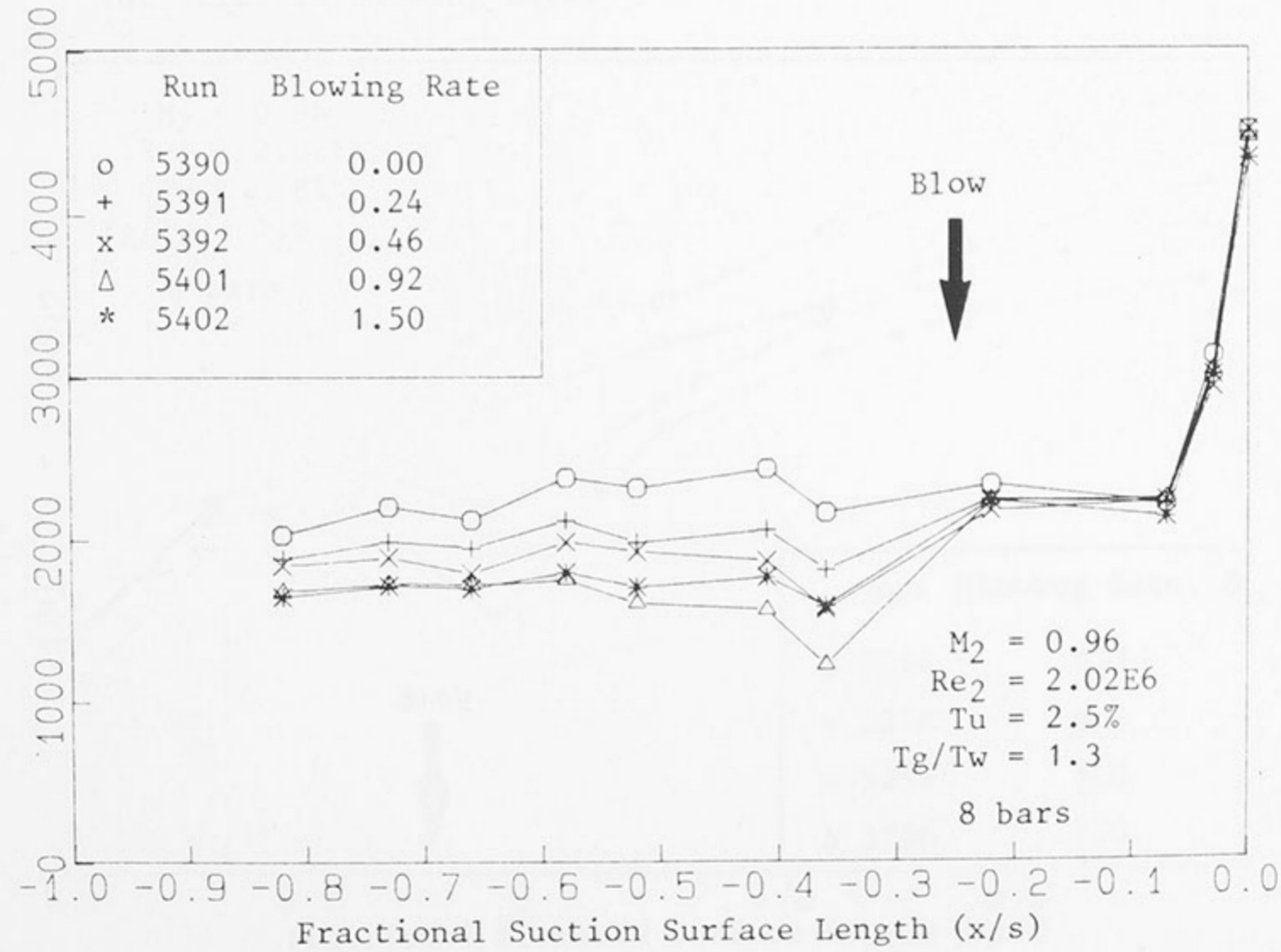

Fig. 8.3(b) Heat Transfer Rate for the B22 Blade Build B (25% S/S) at Tg/Tw = 1.3 with 8 Bars and 2.5% Freestream Turbulence.

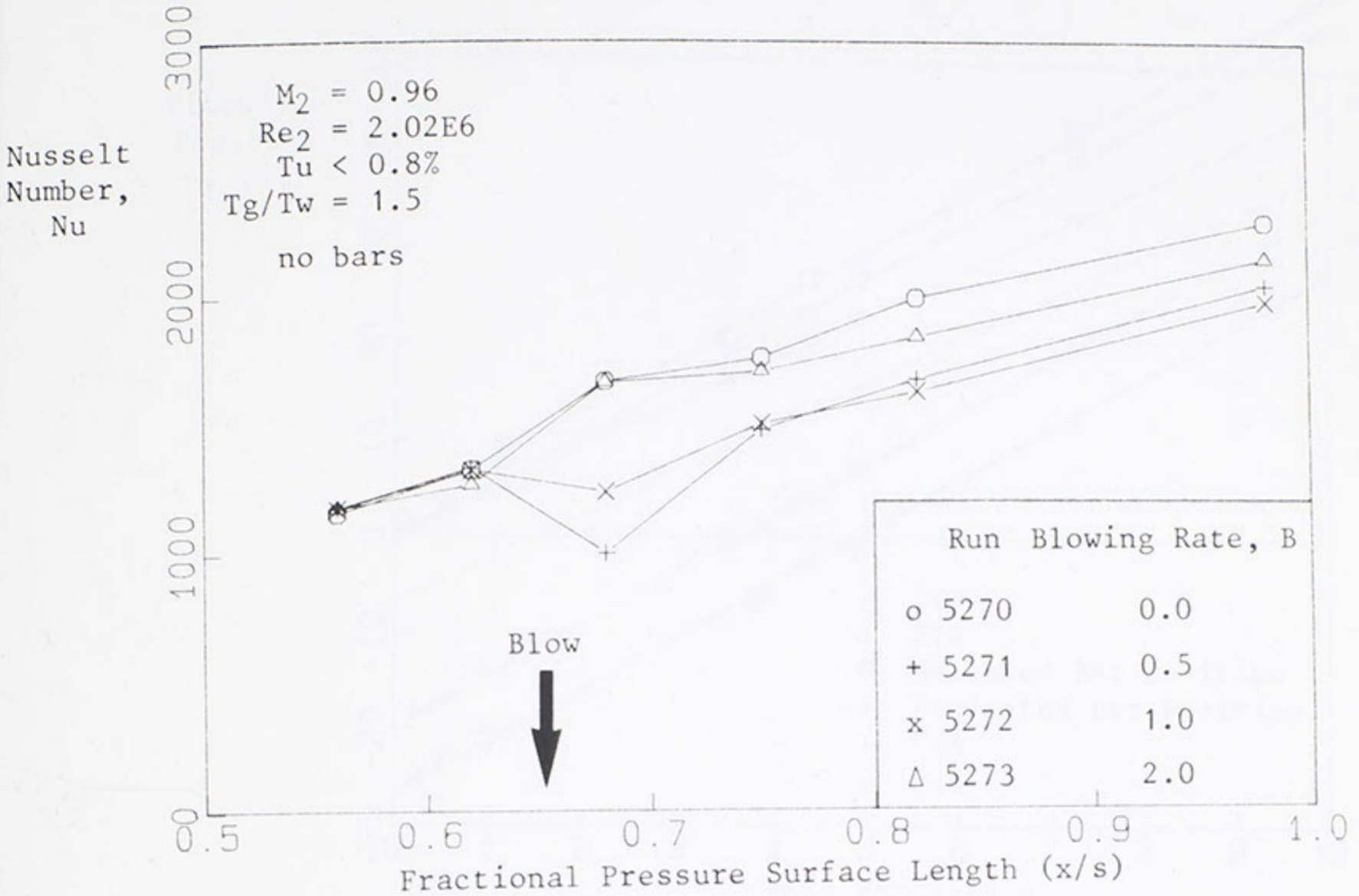

Fig. 8.4 (a) Heat Transfer Rate for the B22 Blade Build C (65% P/S). Datum Case with no Bars and Low Turbulence Level (< 0.8%) with Variation in Blowing Rate.

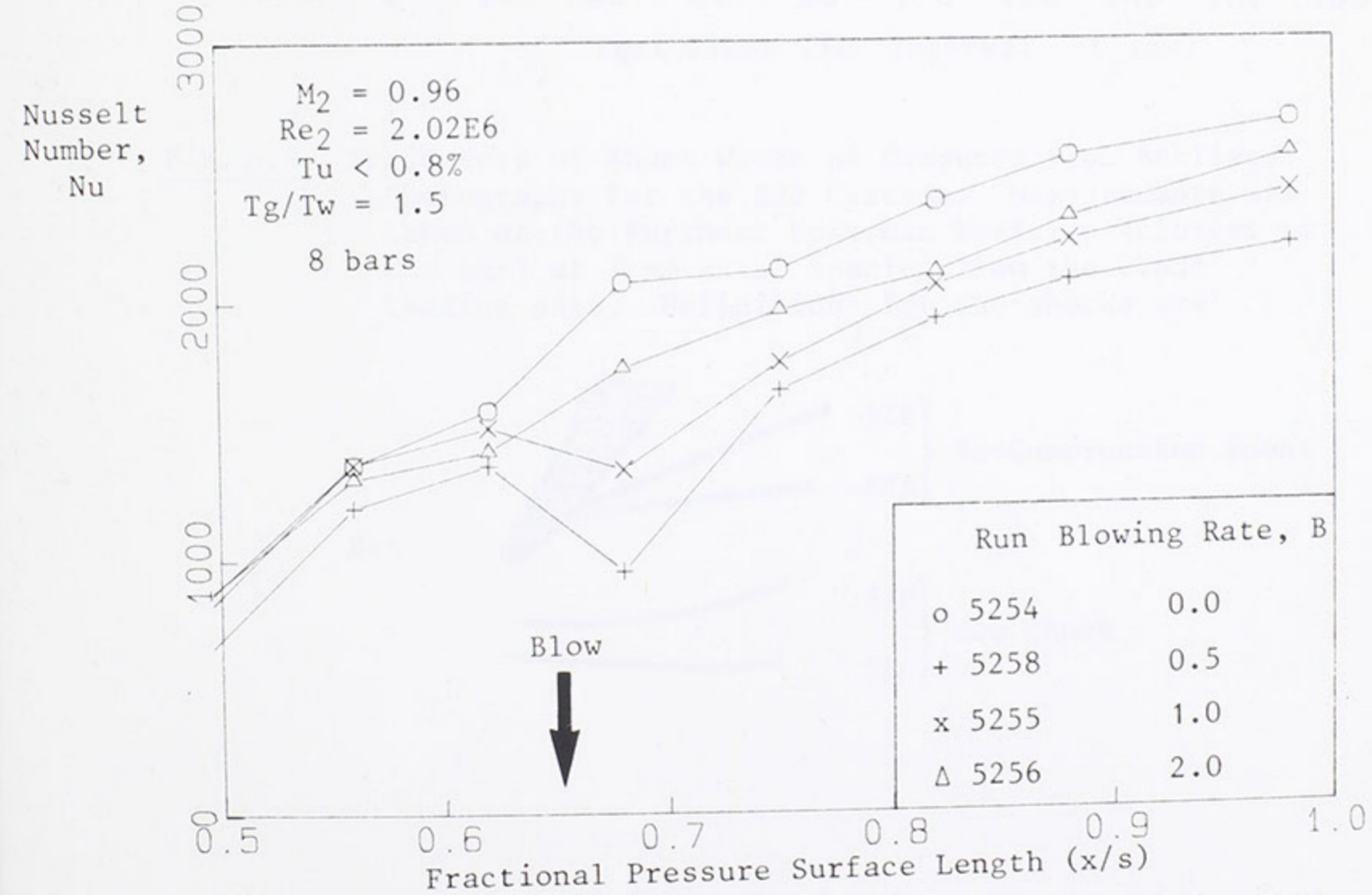

Fig. 8.4 (b) Heat Transfer Rate for the B22 Blade Build C (65% P/S). Data taken at Low Turbulence Level (< 0.8%) for the 8 Bar Case, M_b = 0.92.

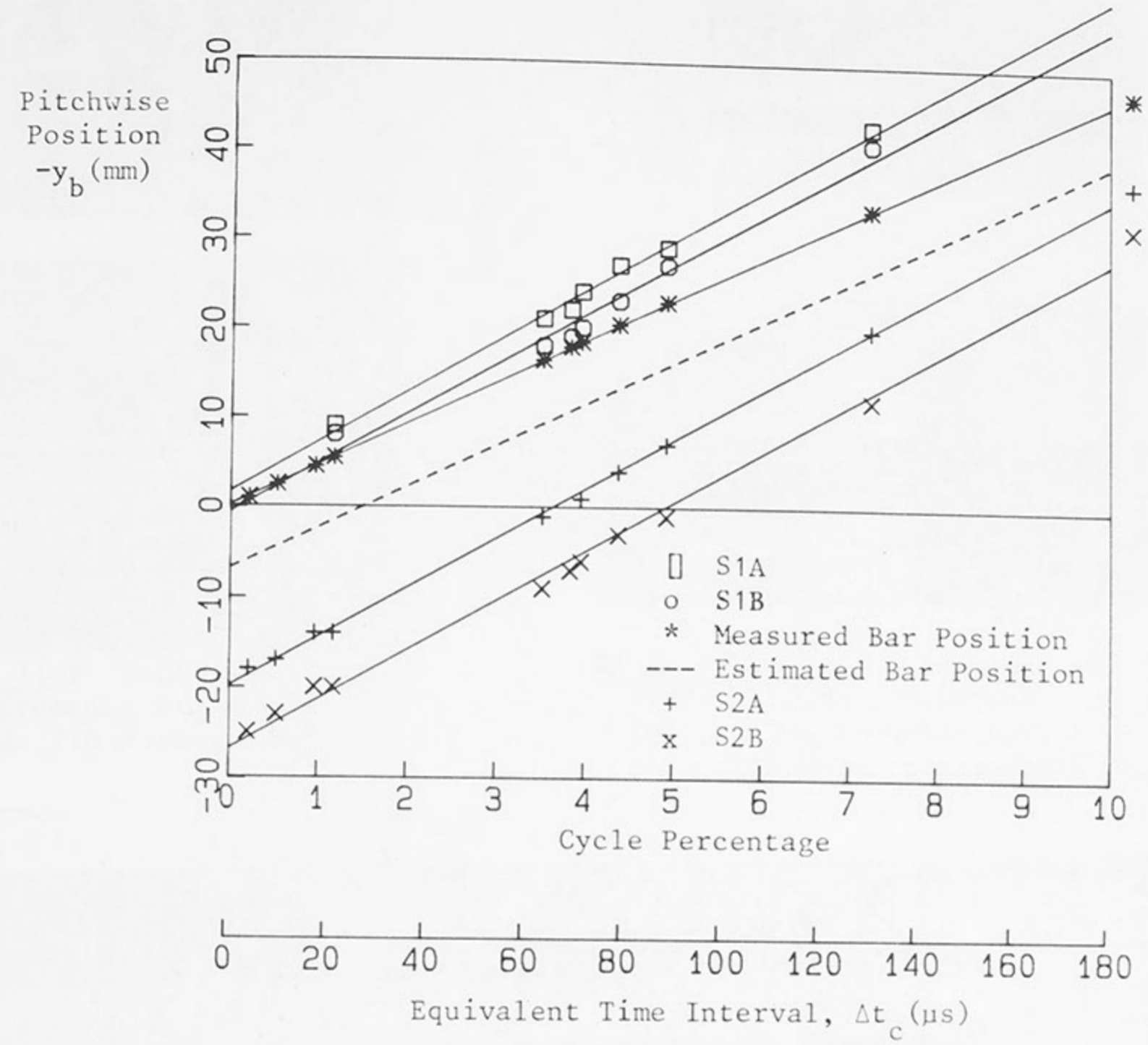

Fig. 8.5 Trajectory of Shock Waves as Measured from Schlieren Photographs for the B22 Cascade. Measurements are taken at the Furthest Upstream Position (closest to the bar) at 7 mm axial spacing from the blade leading edge. Definitions for the shocks are:

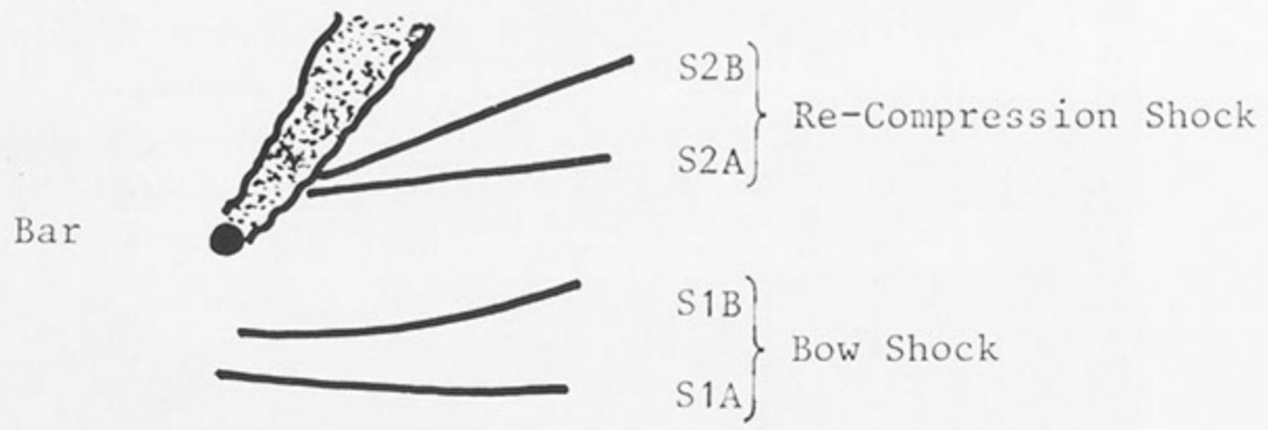

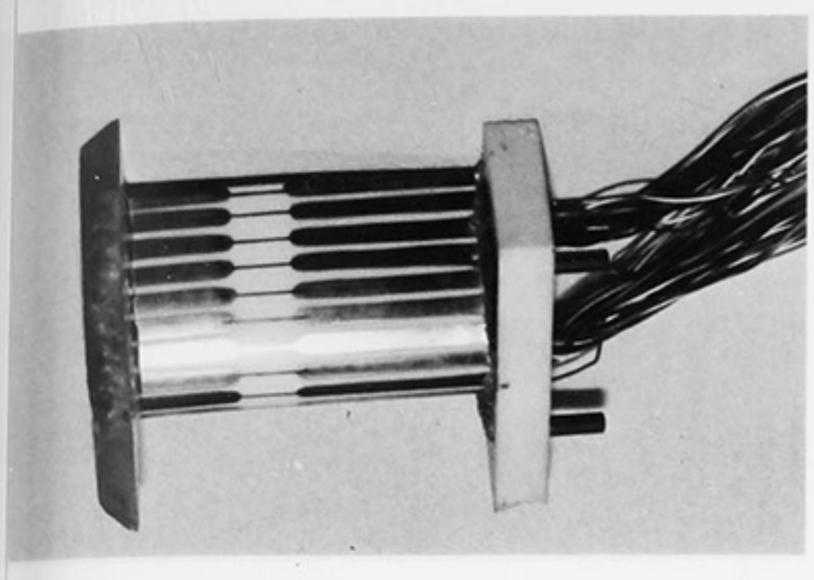

← Suction Surface →

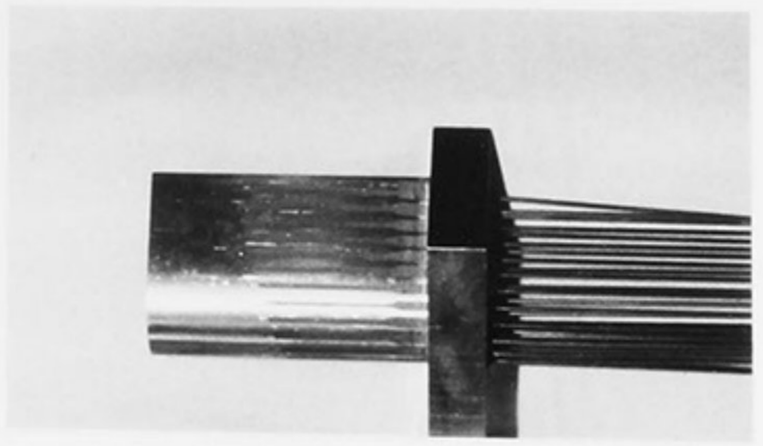

Plate 1(a) Thin Film Gauge Instrumentation on the ACE Blade (10 mm Gauge Width).

← Pressure Surface →

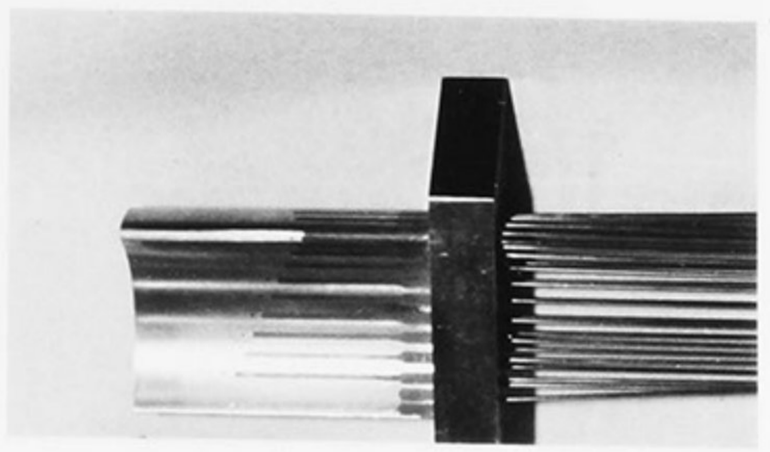

Plate 1(b) Pressure-Tapped ACE Blade Showing Hypodermic Tubes. The trenches have been filled-in subsequently.

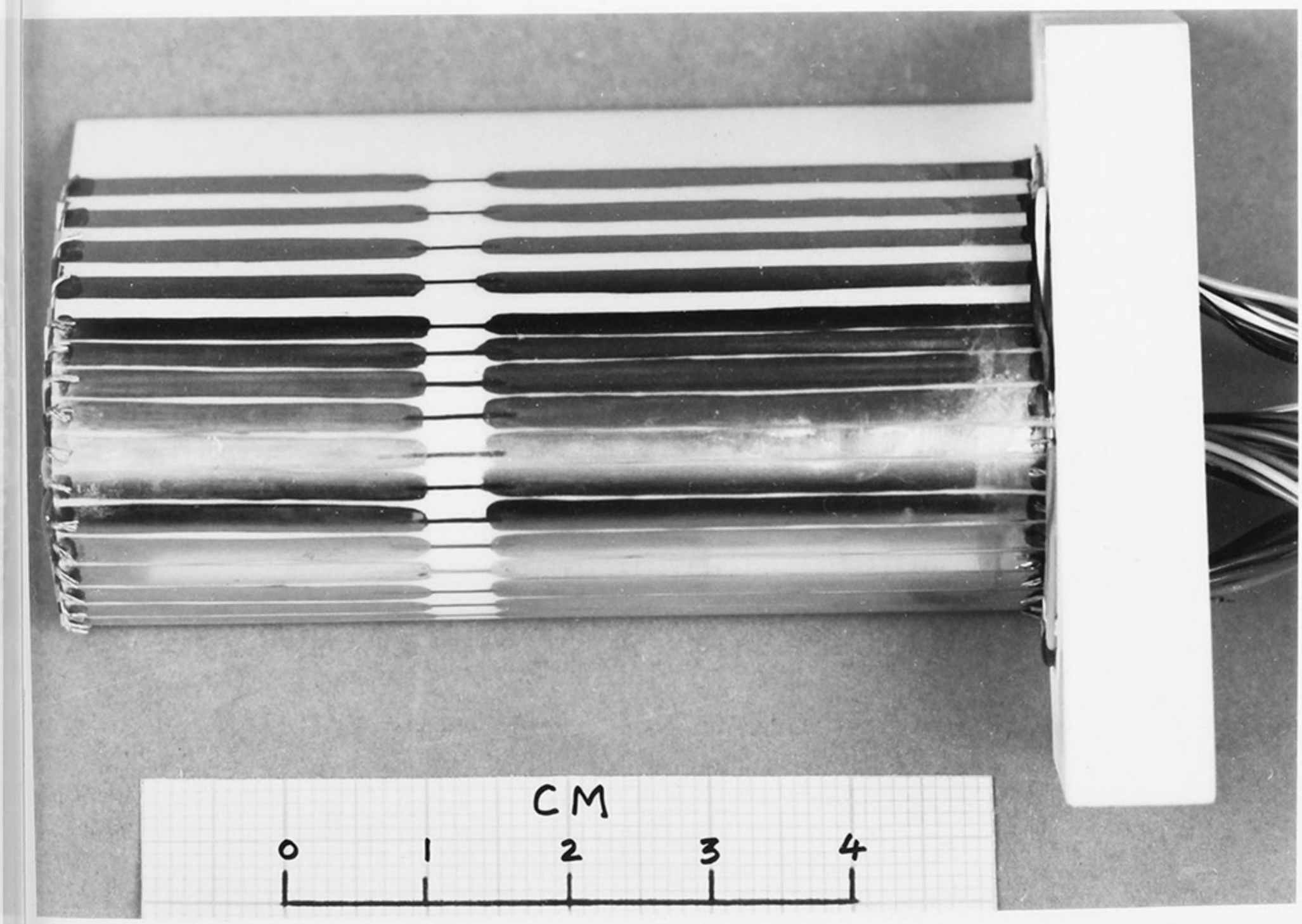

Plate 1(c) Thin Film Gauge Instrumentation on the ACE Suction Surface as Used in the Second Series of Tests (4 mm Gauge Width).

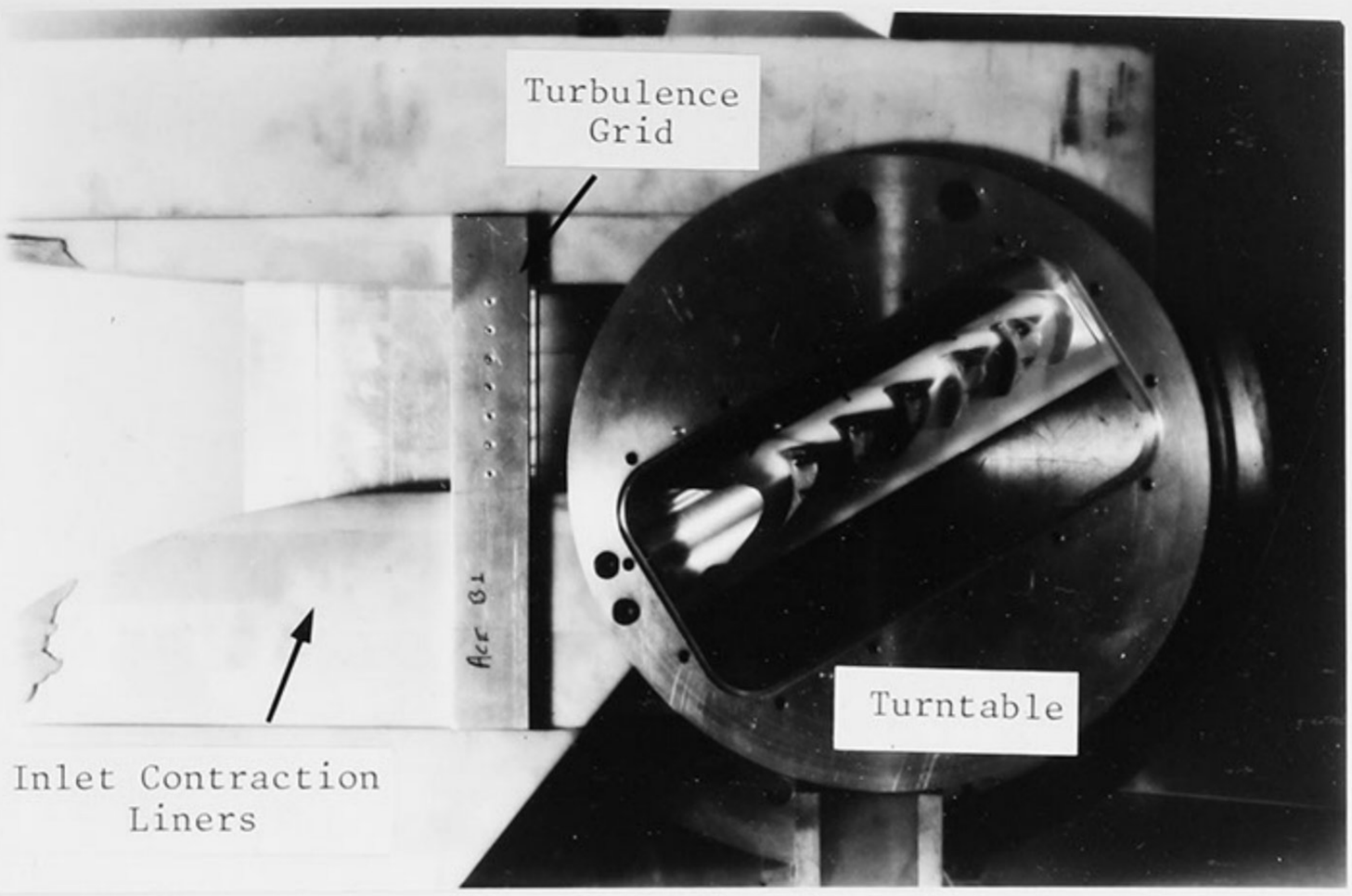

(a)

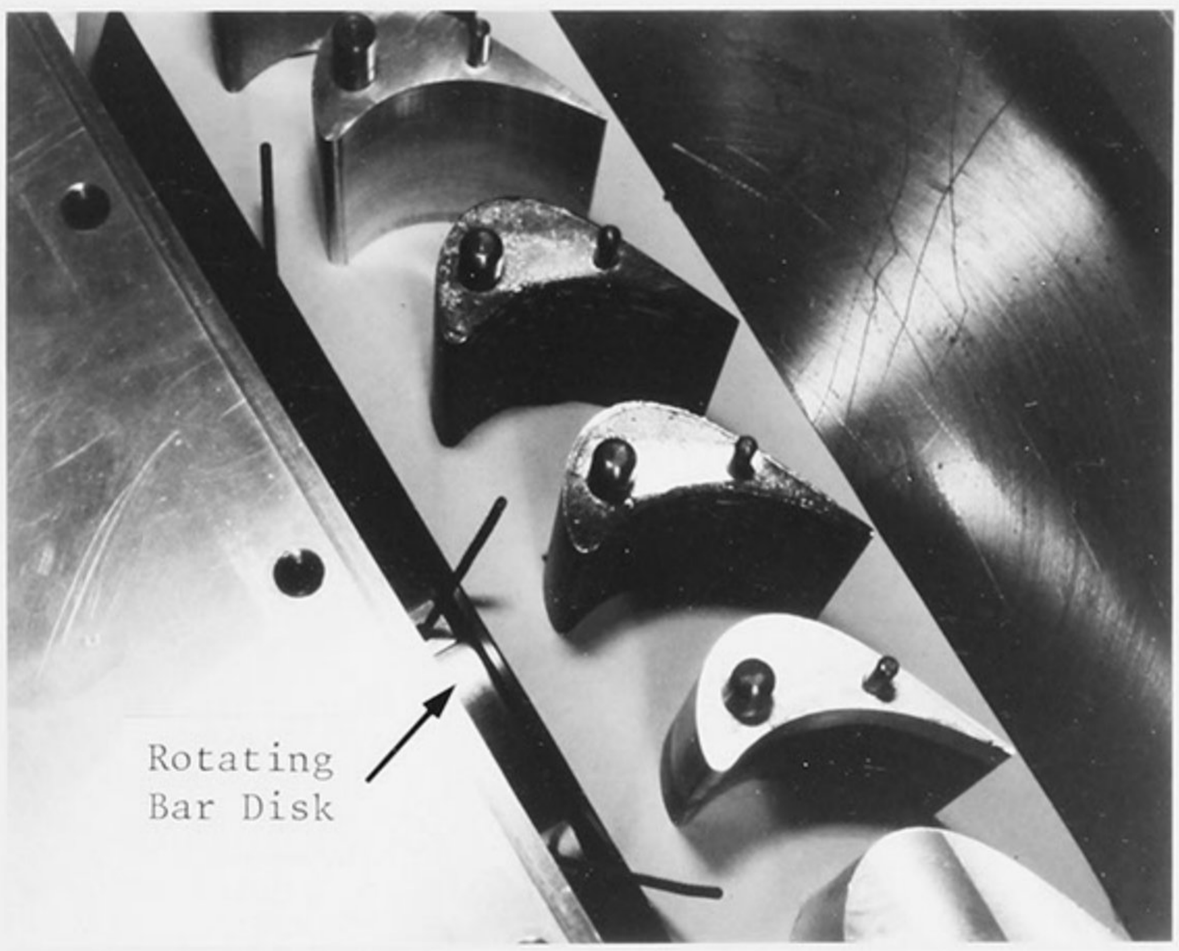

(b)

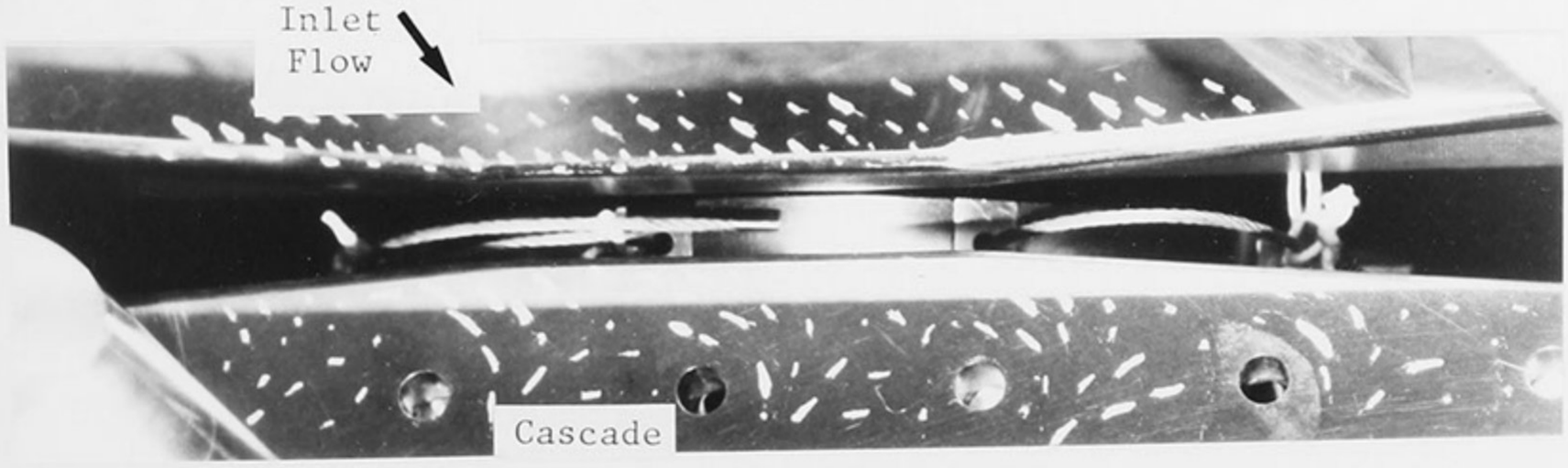

(c)

Plate 2 Views of the ILPT ACE Build:

(a) Side view at i = 0° showing the inlet contraction, turbulence grid and the turntable;

(b) View of the cascade showing the wake generator bars;

(c) Oil-dot flow visualisation on the endwall upstream and downstream of the rotating disk opening.

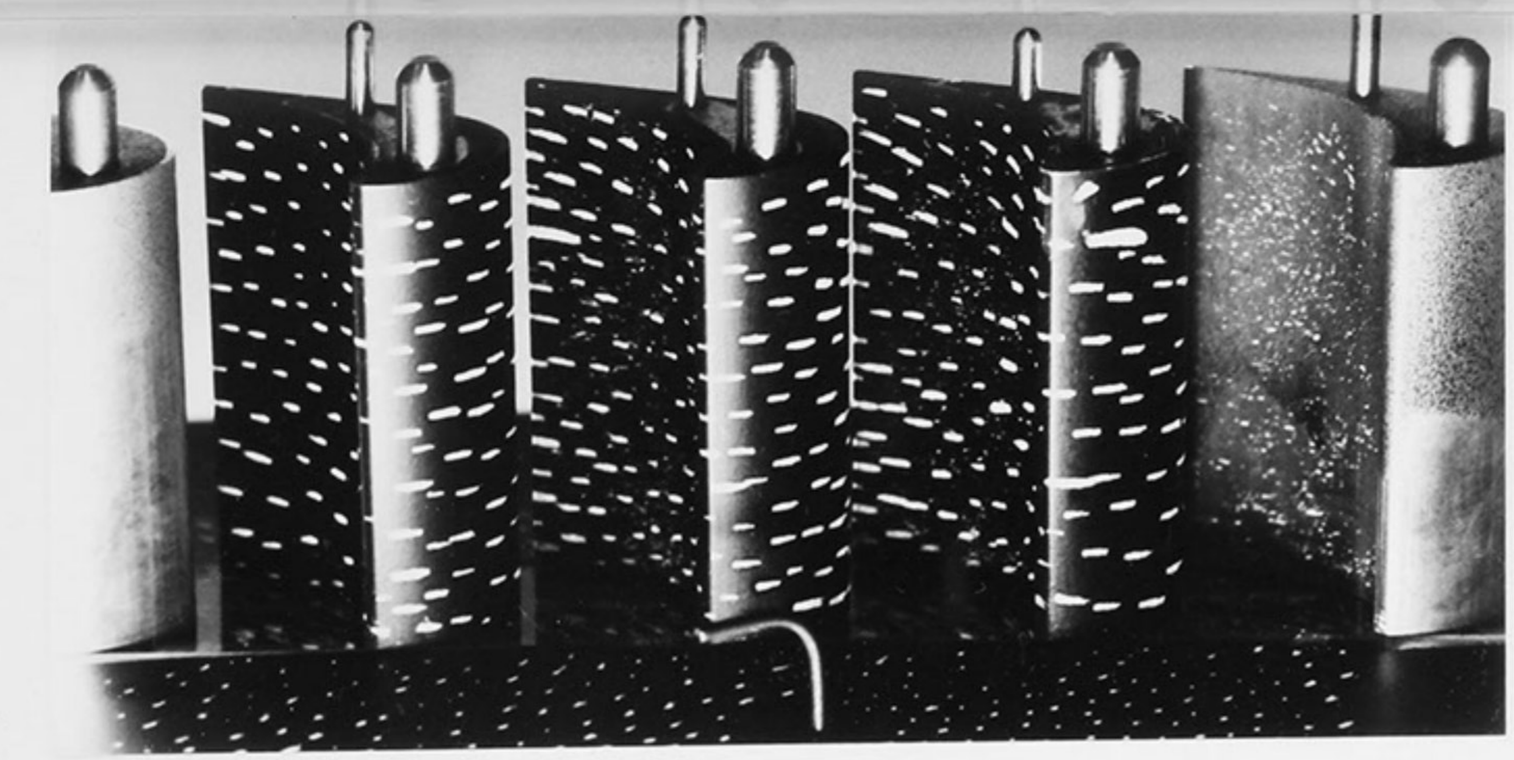

(a)

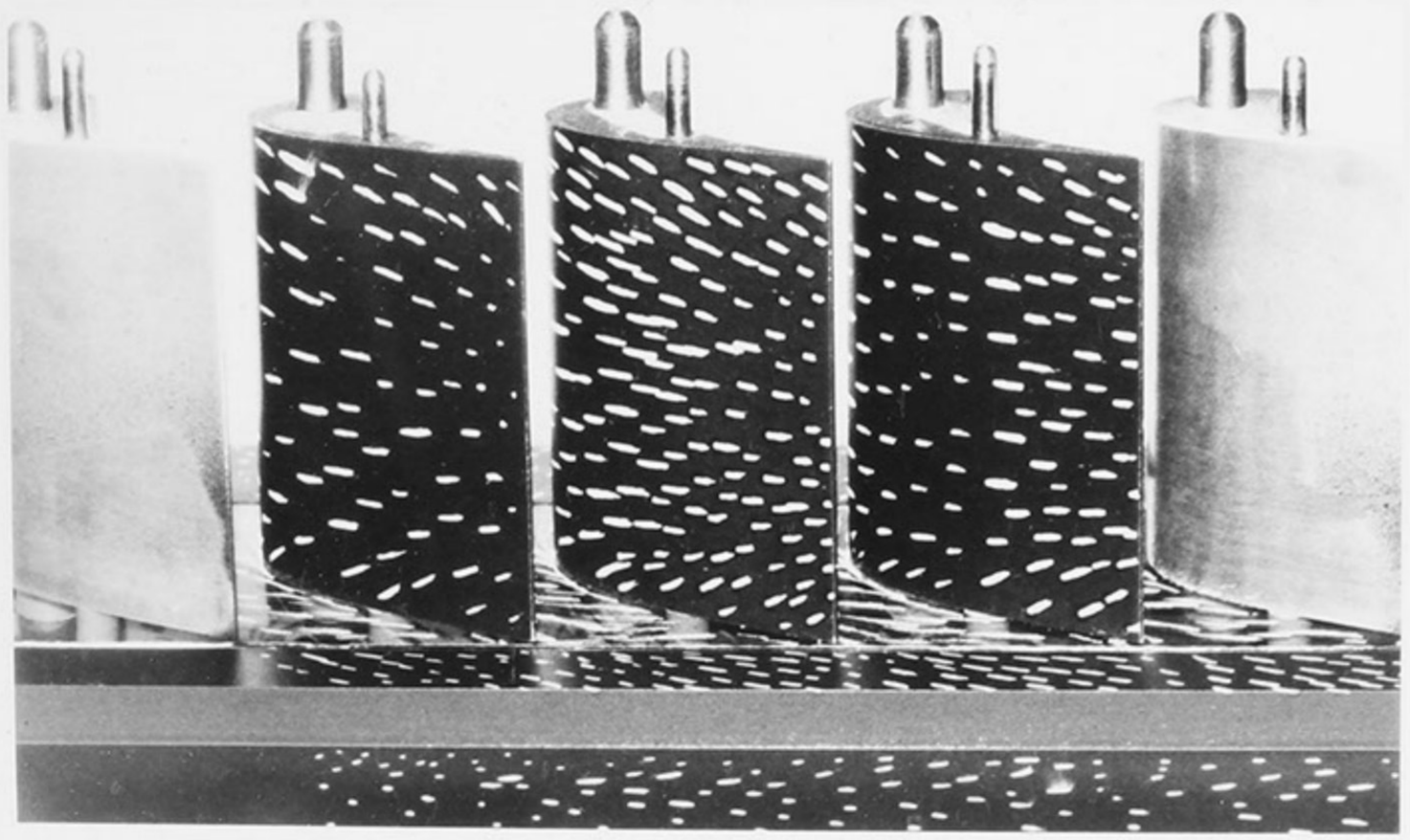

(b)

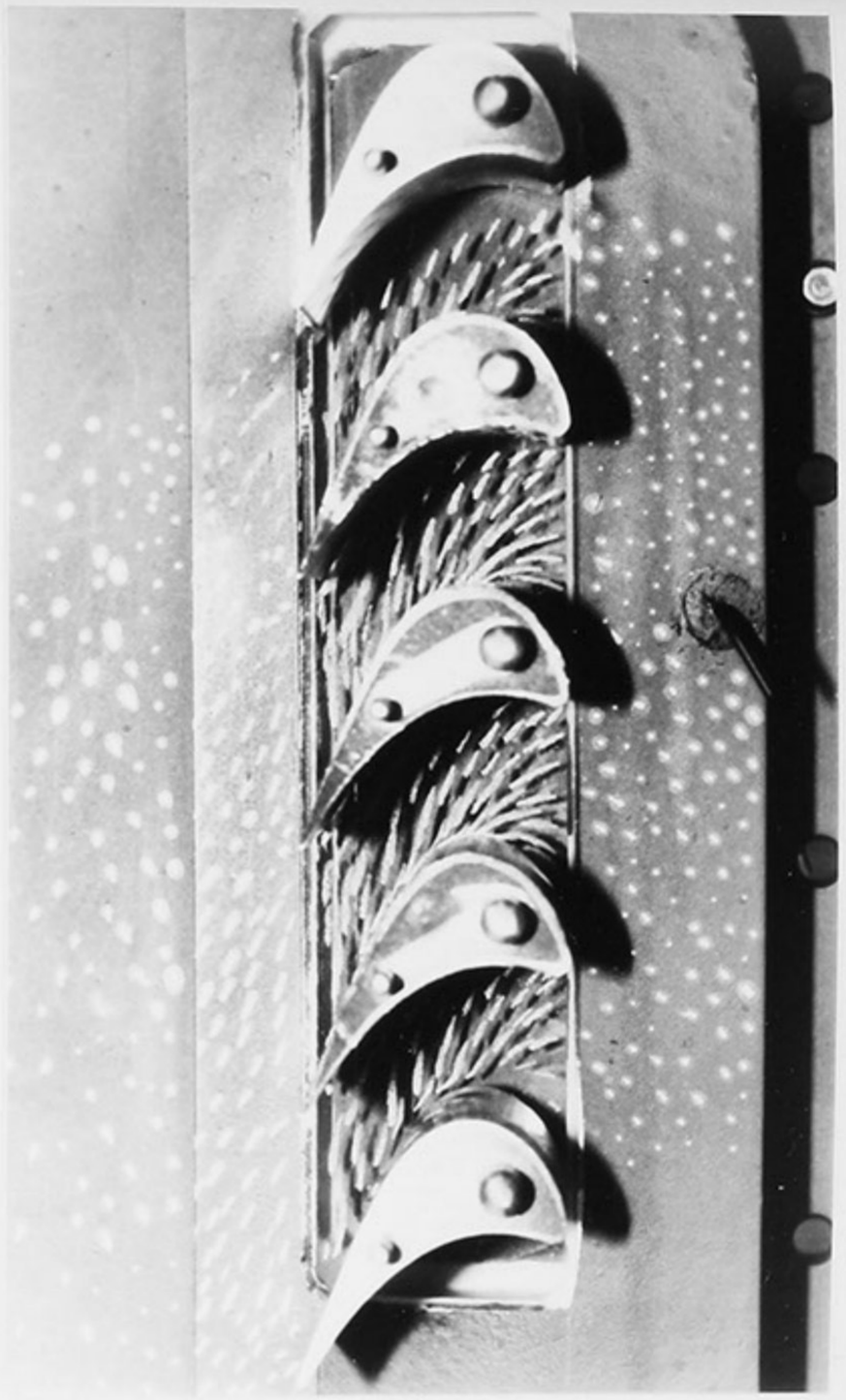

(c)

Plate 3 Oil-dot Flow Visualisation of the ACE Cascade for the 16 Bar Case:

(a) View towards the inlet plane from upstream;
(b) View towards the exit plane from downstream;
(c) View of the endwall showing the gas-path surface on the schlieren window.

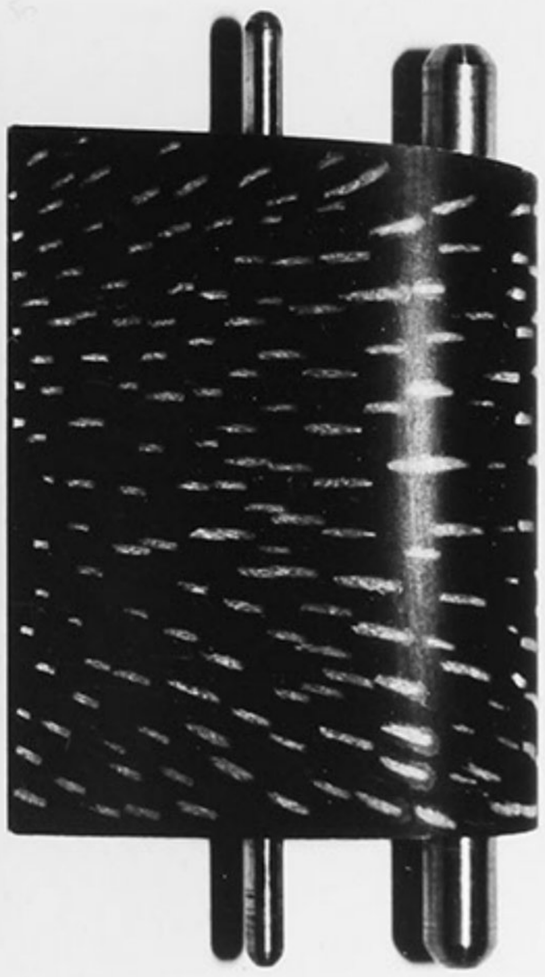

(a)

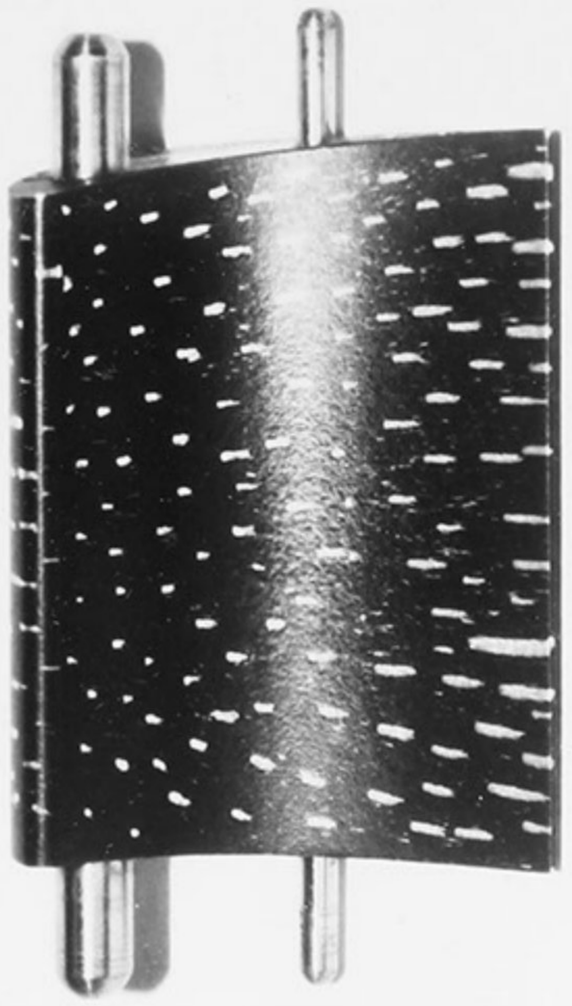

(b)

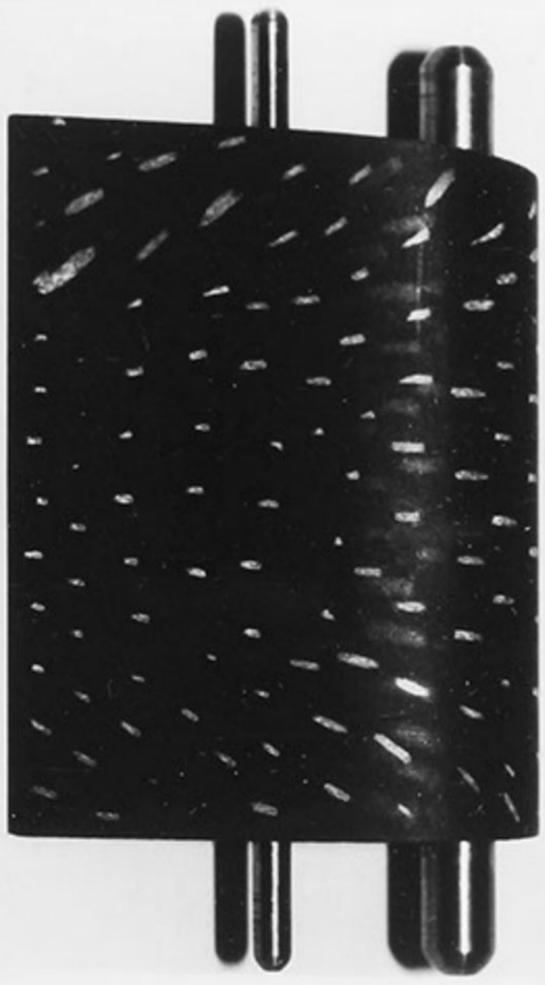

(c)

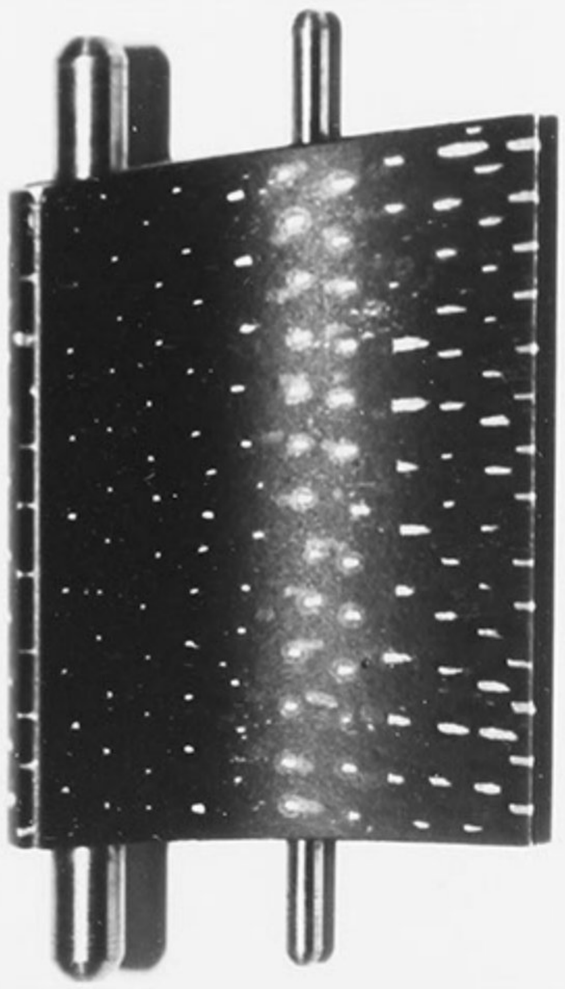

(d)

Plate 4 Oil-dot Flow Visualisation on the ACE Blade - Tu ~ 3%, Design Operating Conditions:

(a) Suction surface
(b) Pressure surface
} 16 bars

(c) Suction surface
(d) Pressure surface
} no bars

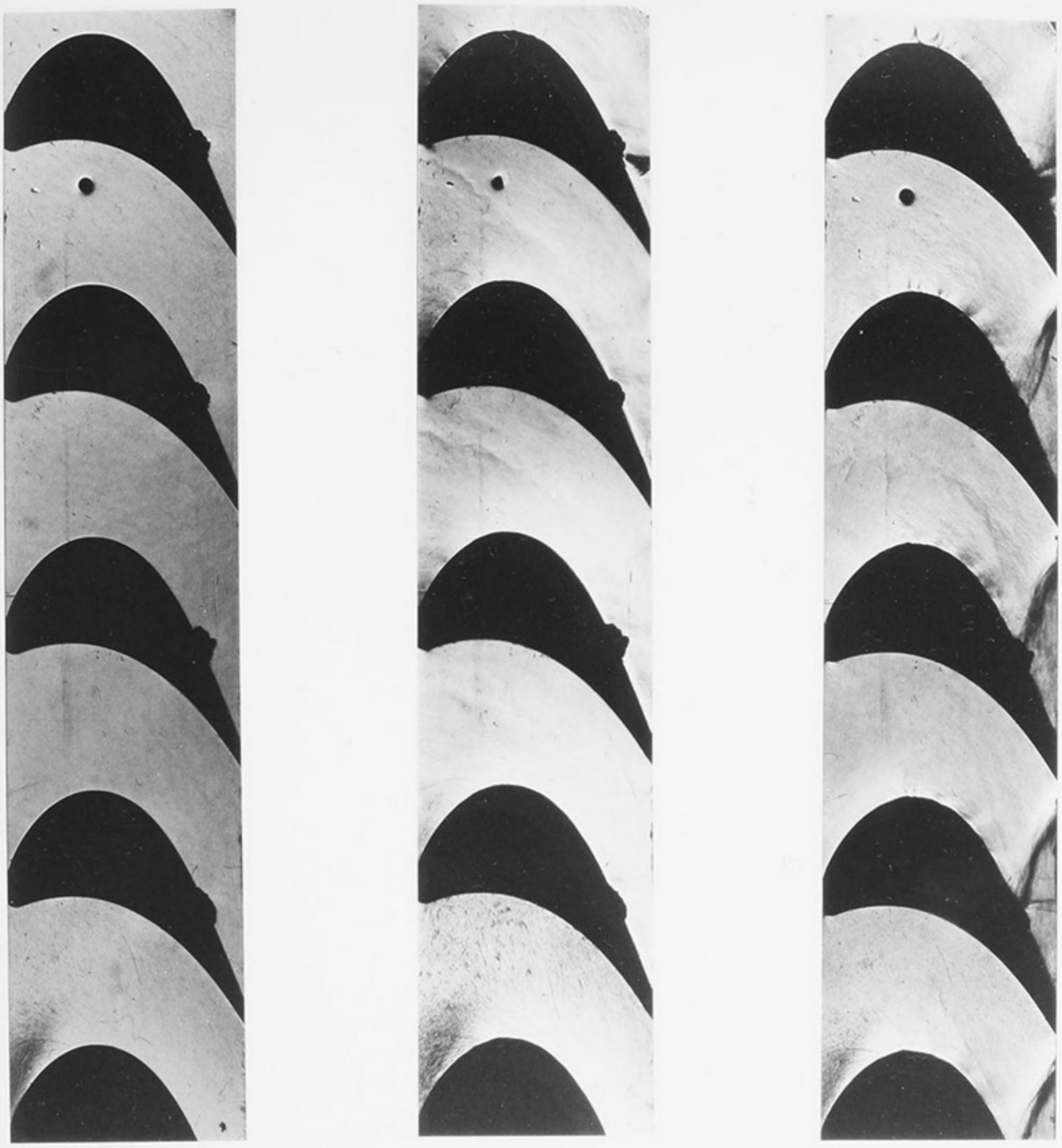

(a)
(Run 4704)

(b)
Run 4704

(c)
Run 4701

Plate 5 Schlieren Photographs of the ACE Cascade:

(a) No flow;

(b) Steady conditions (no bars) M_d, Re_d, Tu $\sim$ 3%, schlieren knife-edge horizontal;

(c) As (b) but with schlieren knife-edge vertical.

(Scale 1:1)

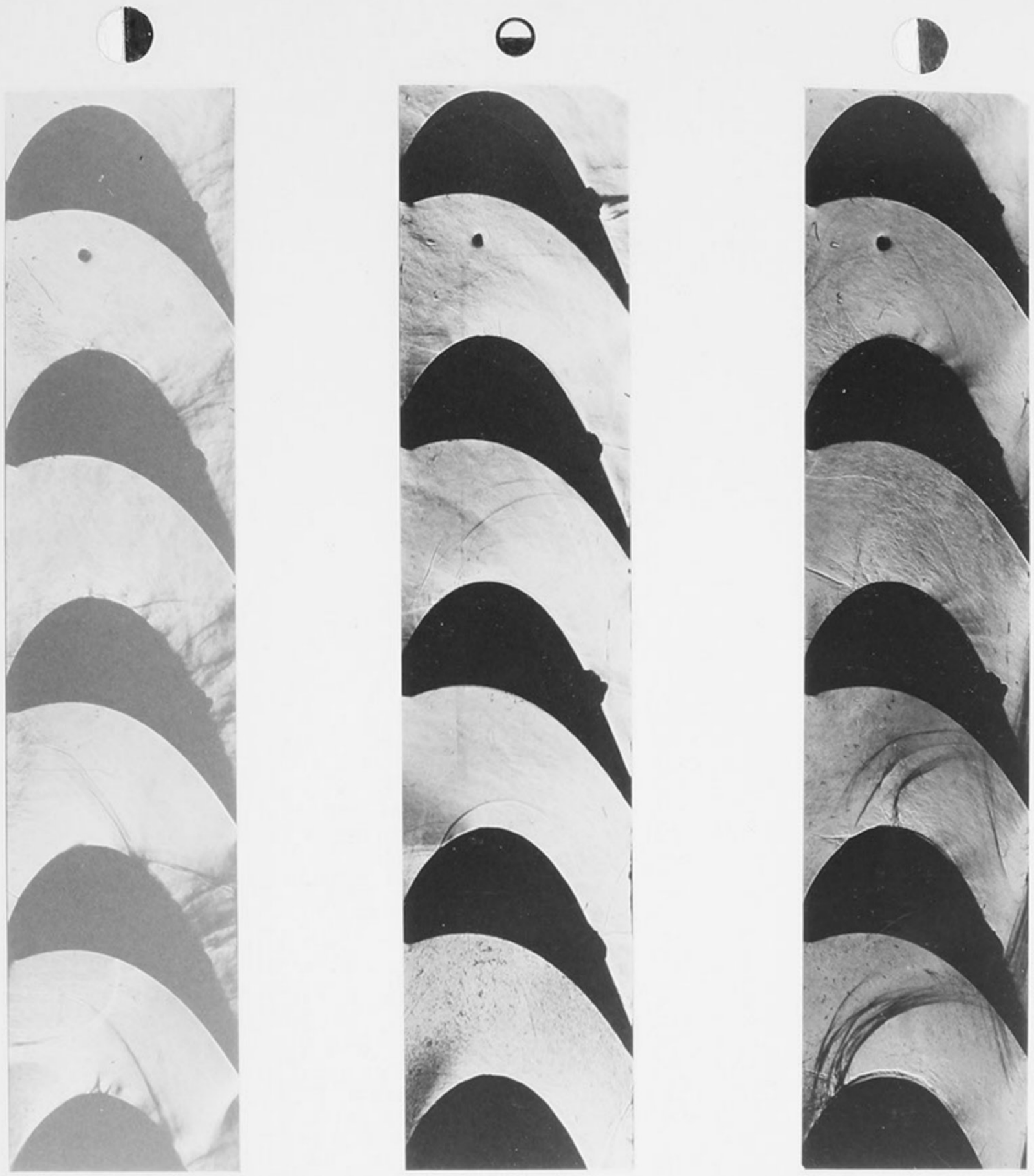

(a)
Run 4731

(b)
Run 4703

(c)
Run 4728

Plate 6 Schlieren Photographs of the ACE Cascade for the 2 Bar Case, M_b = 1.165 (nominal mid-span) with Variation in Exit Mach Number:

(a) M_2 = 0.84;

(b) M_2 = 1.18;

(c) M_2 = 1.38.

(Scale 1:1)

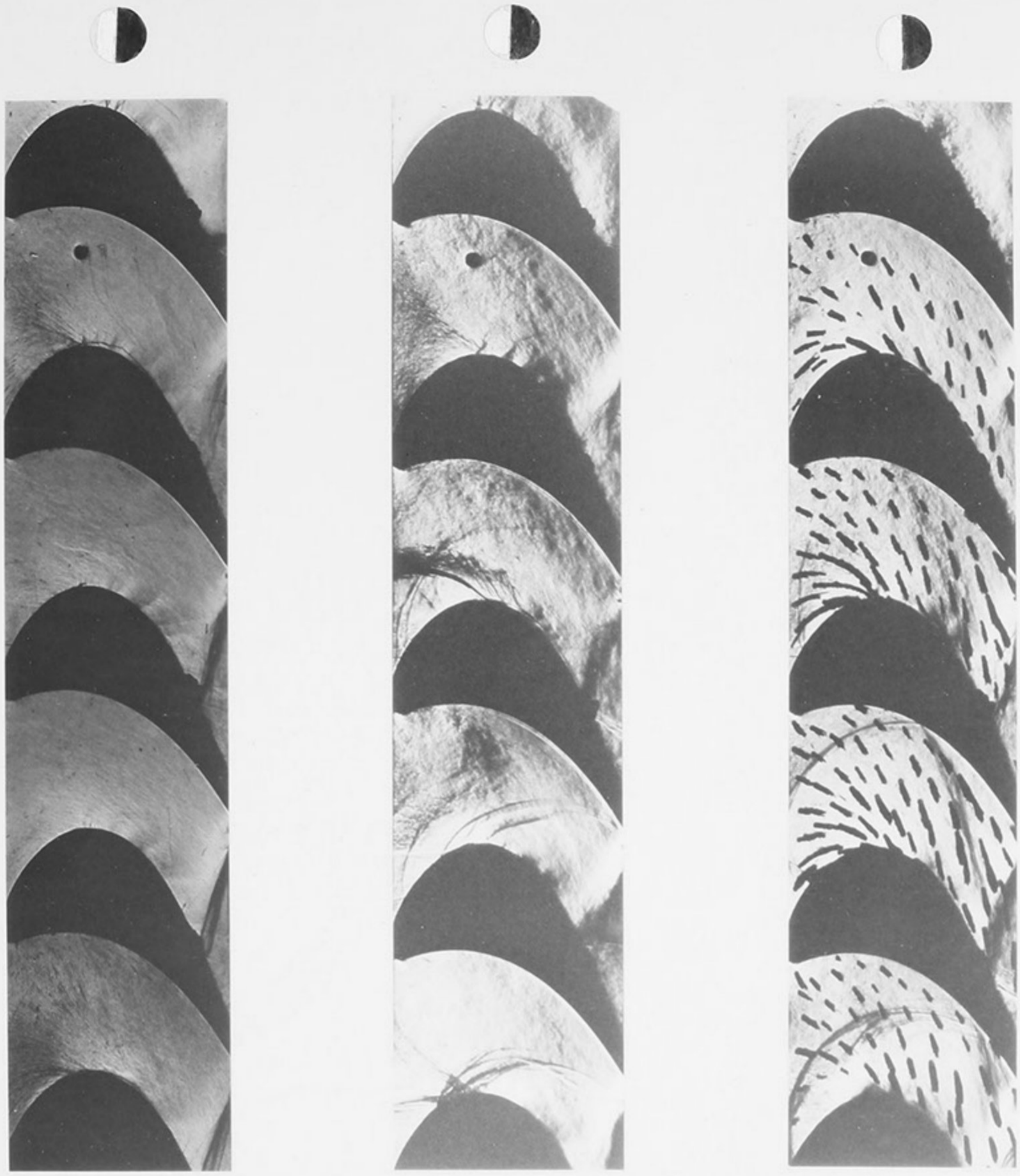

(a)
Run 4726

(b)
Run 4757

(c)
Run 4761

Plate 7 Schlieren Photographs of the ACE Cascade at Design Exit Mach Number (M_2 = 1.18):

(a) 2 bars, subsonic M_b = 0.82 (mid-span);

(b) 16 bars, M_b = 1.165 (mid-span);

(c) As (b) plus oil-dots on the schlieren window.

(Scale 1:1)

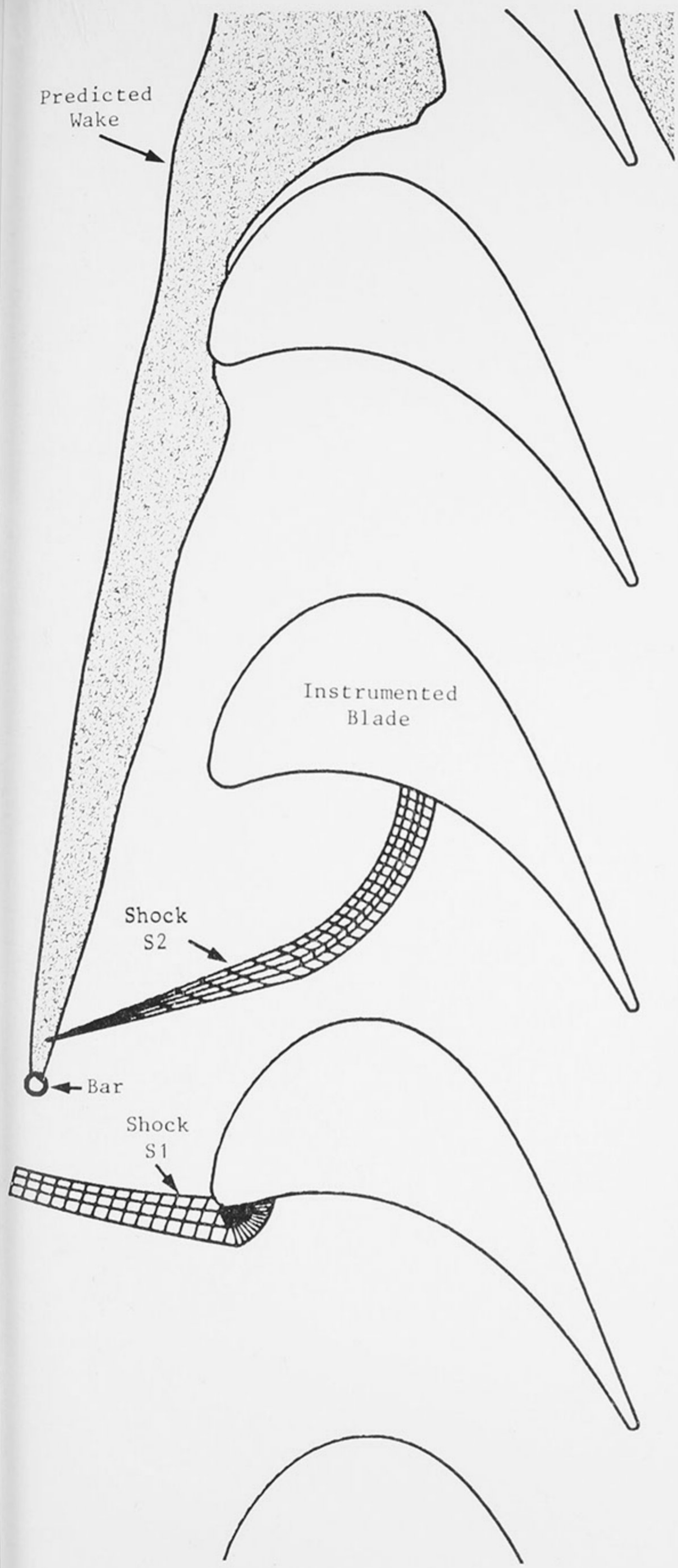

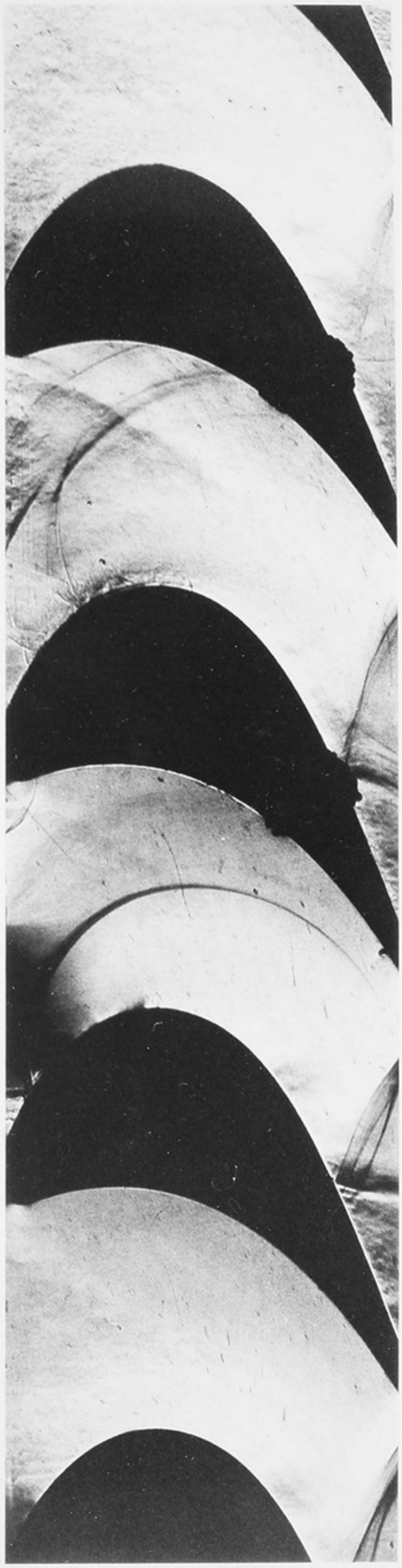

Plate 8 Schlieren Photograph for Run 5438 and Prediction for the Wake and Shock Positions:

Δt_c = 5 μs (0.23% cycle)

M_b = 1.225 (N = 14035 rpm)

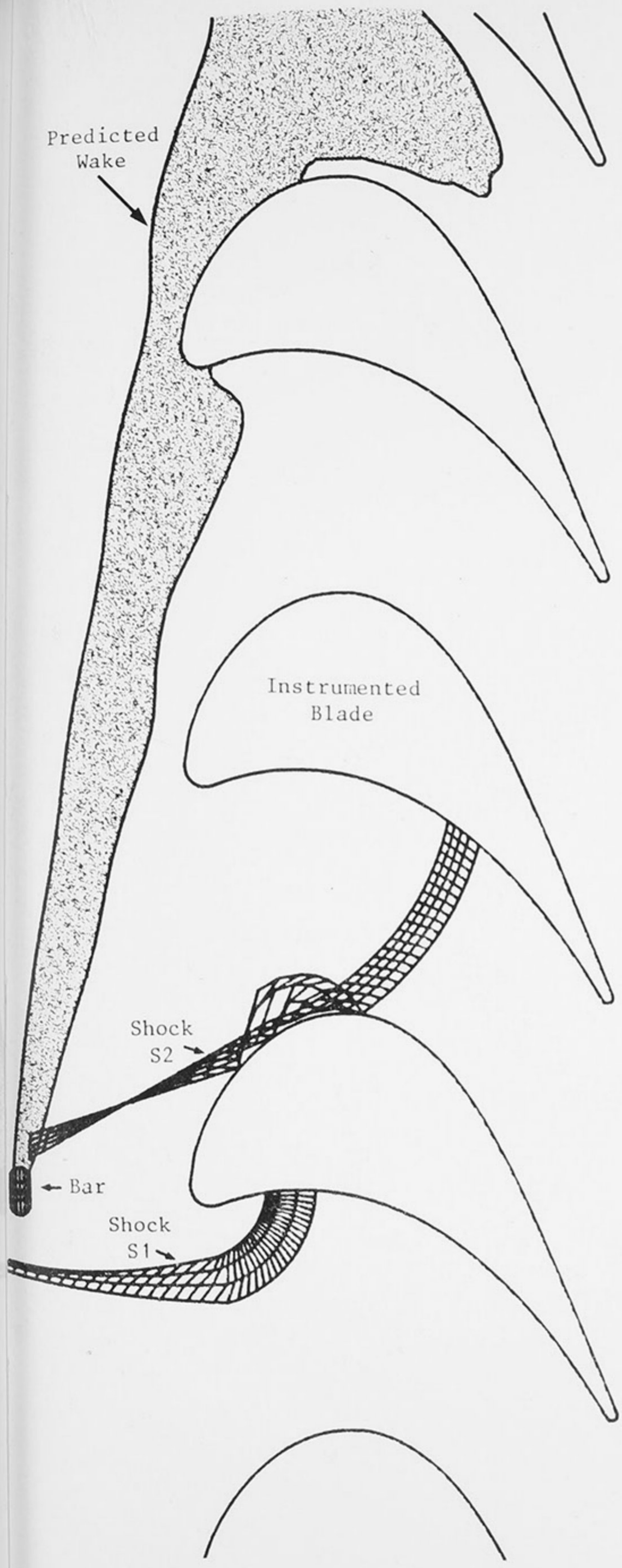

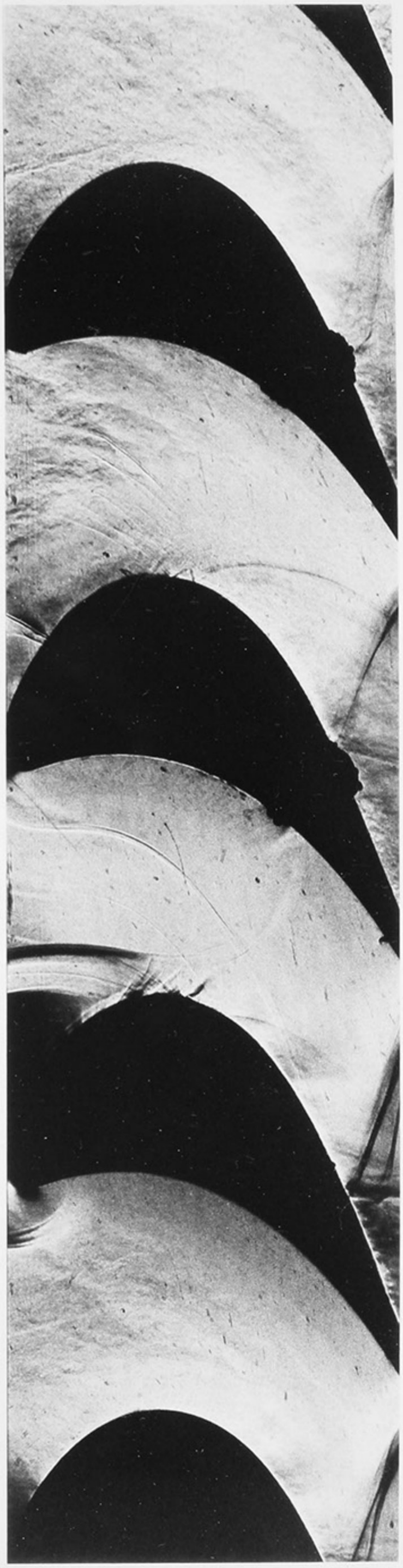

Plate 9 Schlieren Photograph for Run 5437 and Prediction for the Wake and Shock Positions:

Δt_c = 50 μs (2.34% cycle)

M_b = 1.222 (N = 14043 rpm)

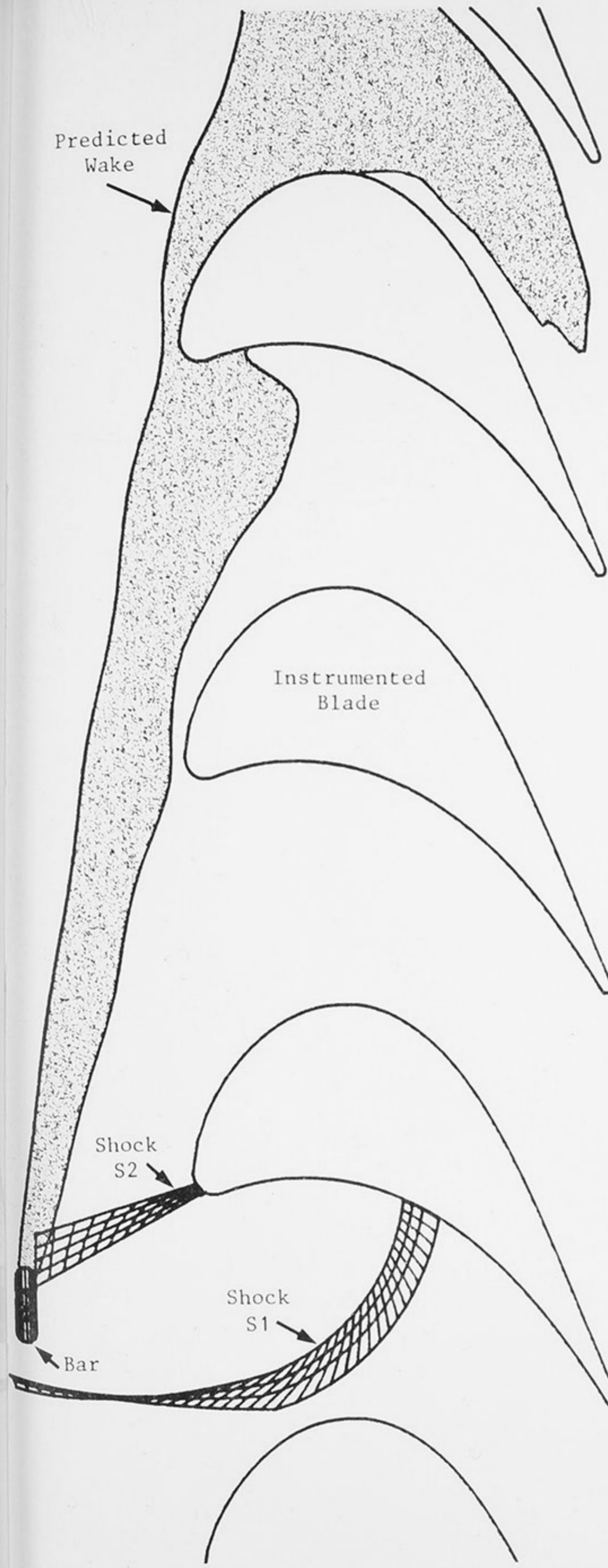

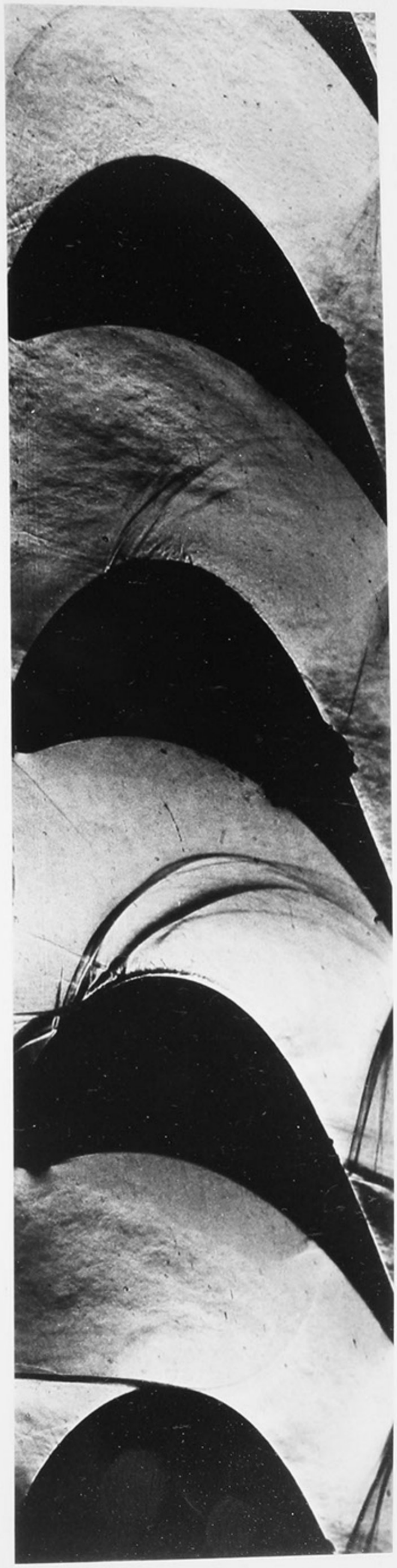

Plate 10 Schlieren Photograph for Run 5435 and Prediction for the Wake and Shock Positions:

Δt_c = 95 μs (4.43% cycle)

M_b = 1.215 (N = 13978 rpm)

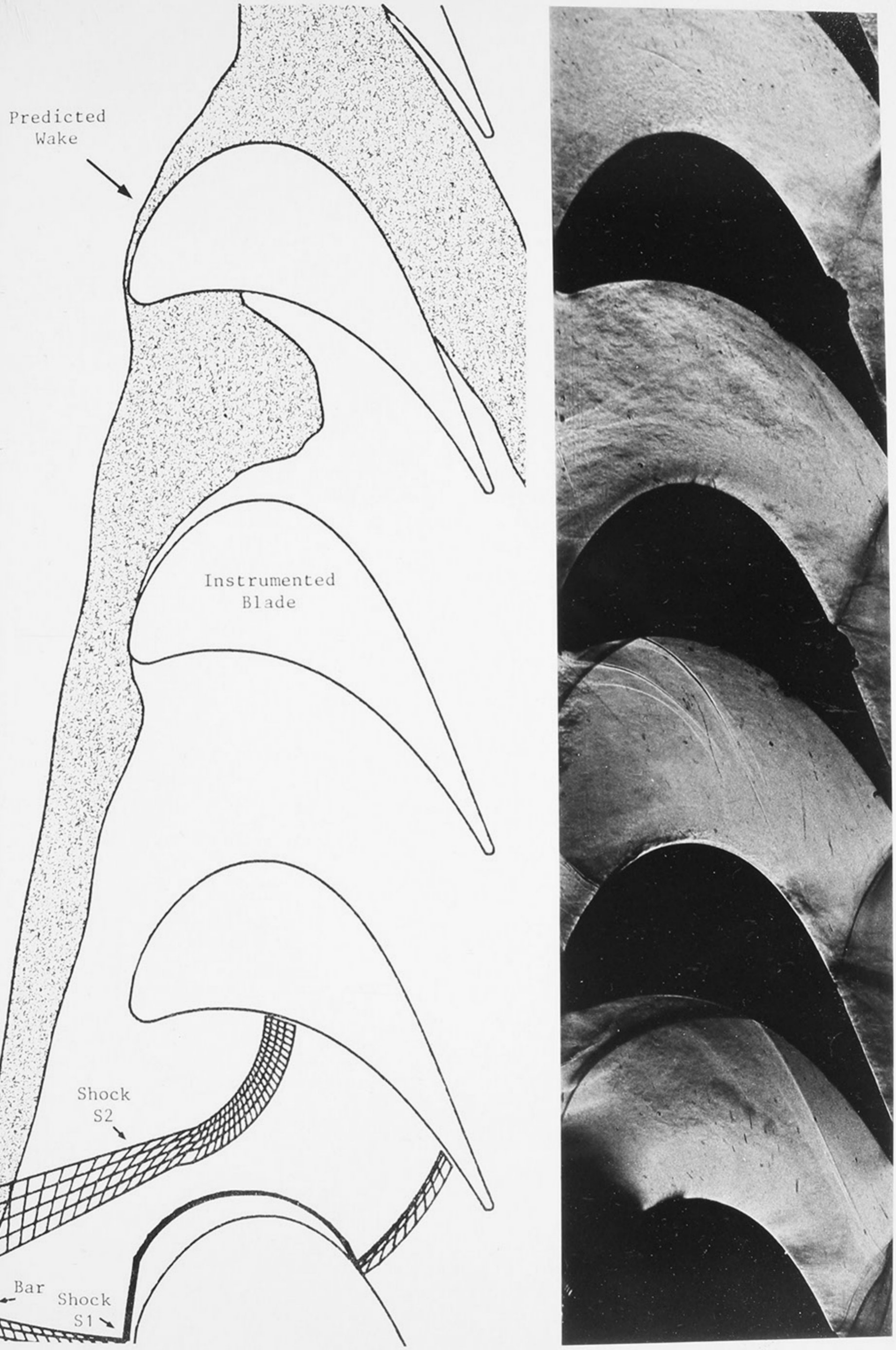

Plate 11 Schlieren Photograph for Run 5440 and Prediction for the Wake and Shock Positions:

Δt_c = 160 μs (7.50% cycle)

M_b = 1.213 (N = 14064 rpm)

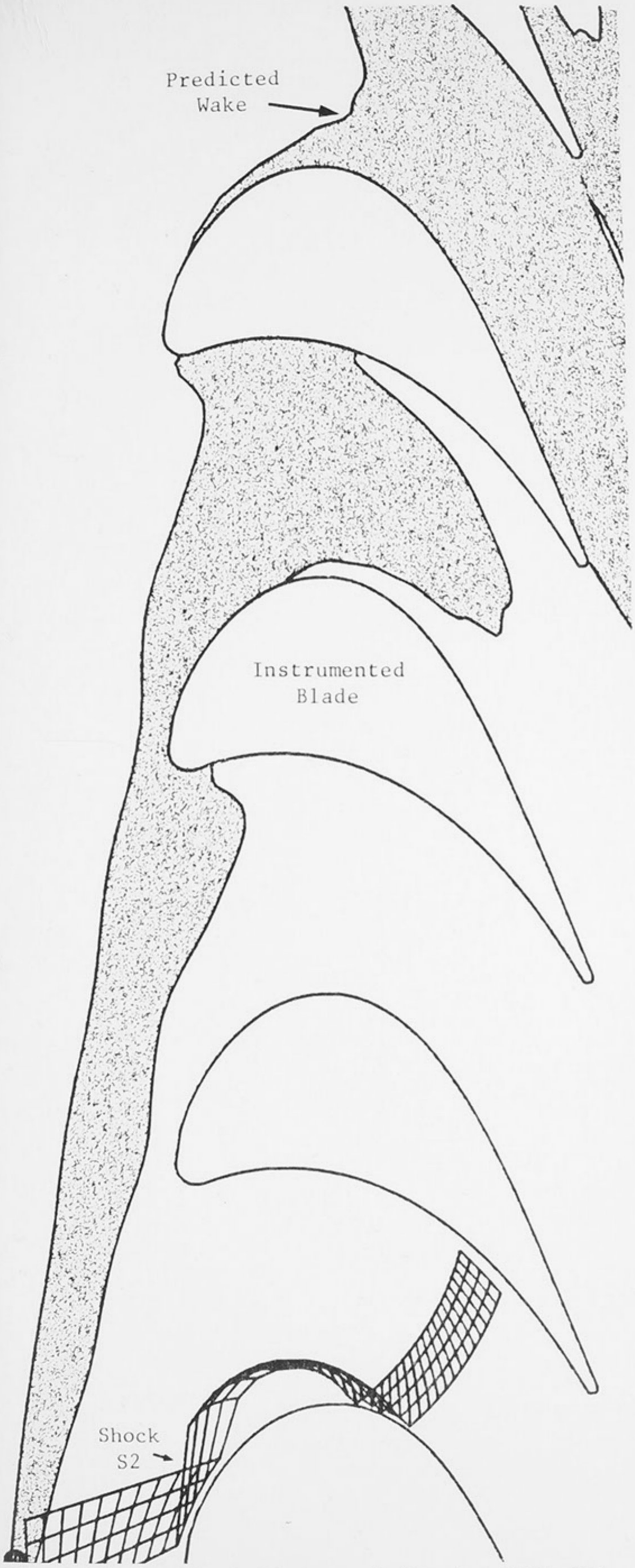

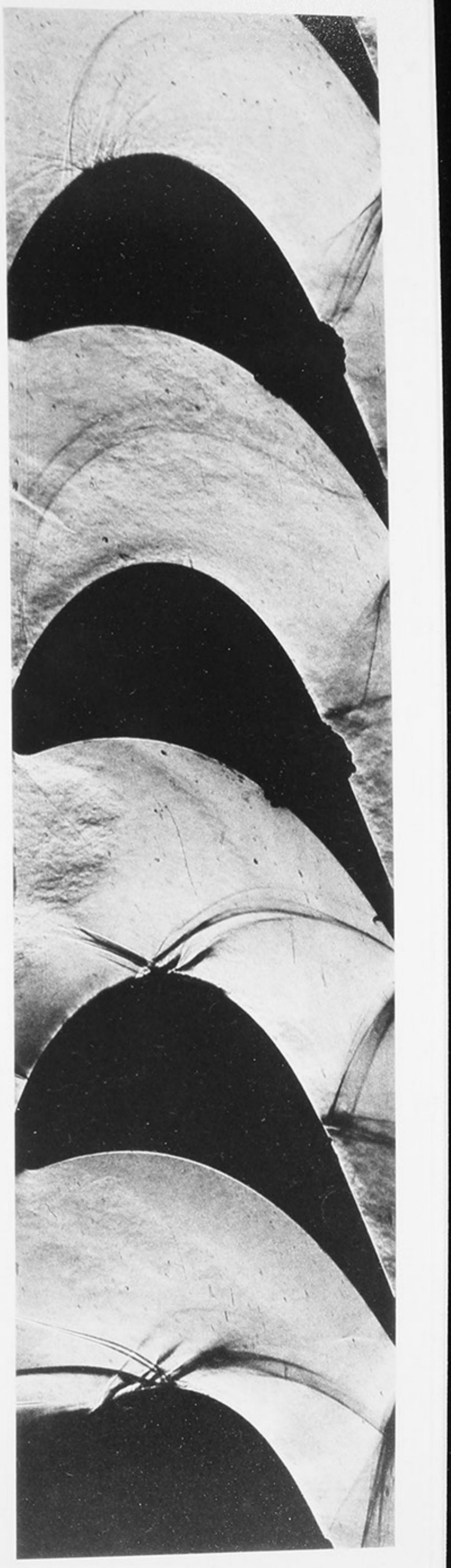

Plate 12 Schlieren Photograph for Run 5439 and Prediction for the Wake and Shock Positions:

Δt_c = 220 μs (10.30% cycle)

M_b = 1.216 (N = 14039 rpm)

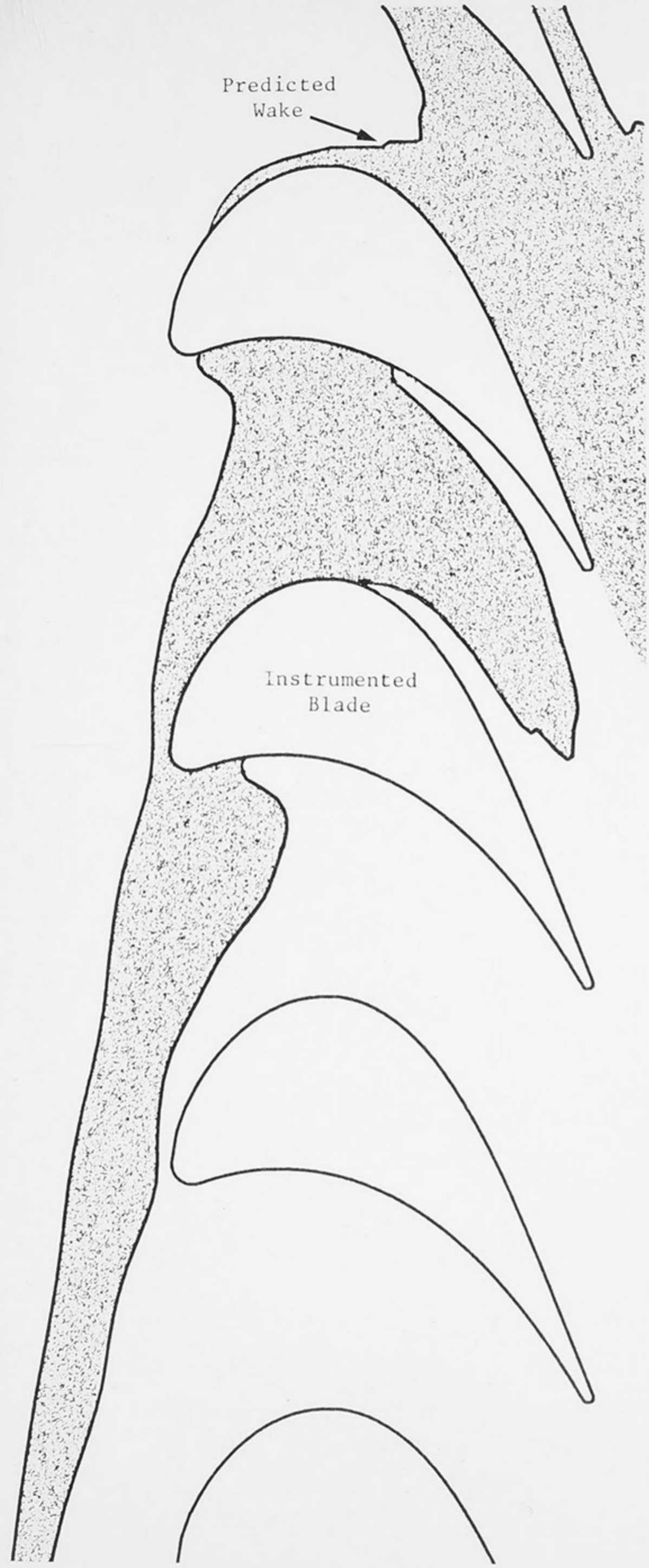

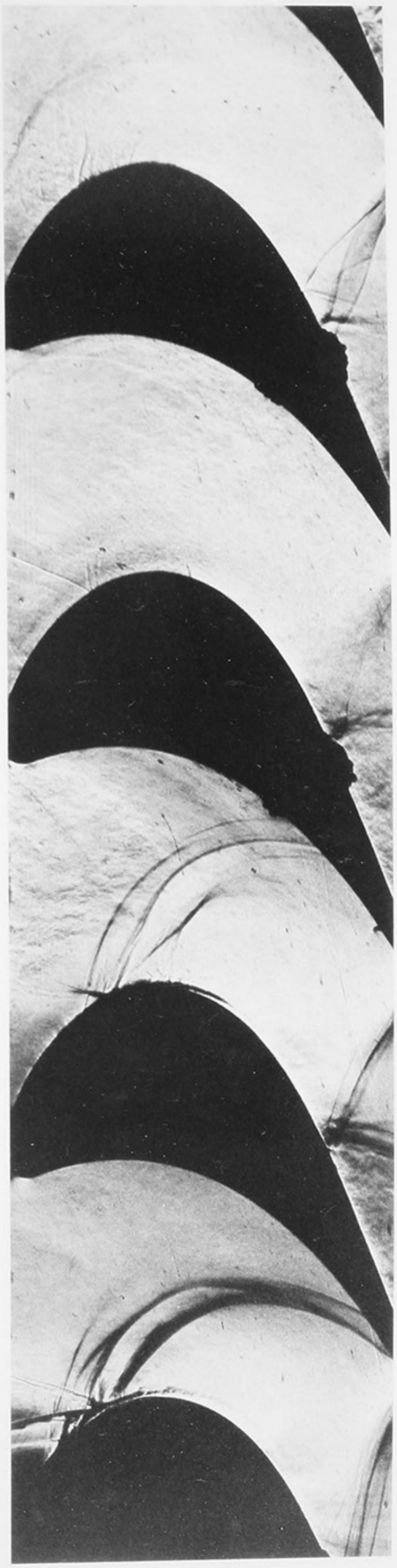

Plate 13 Schlieren Photograph for Run 5436 and Prediction for the Wake and Shock Positions:

Δt_c = 255 μs (11.88% cycle)

M_b = 1.216 (N = 13982 rpm)

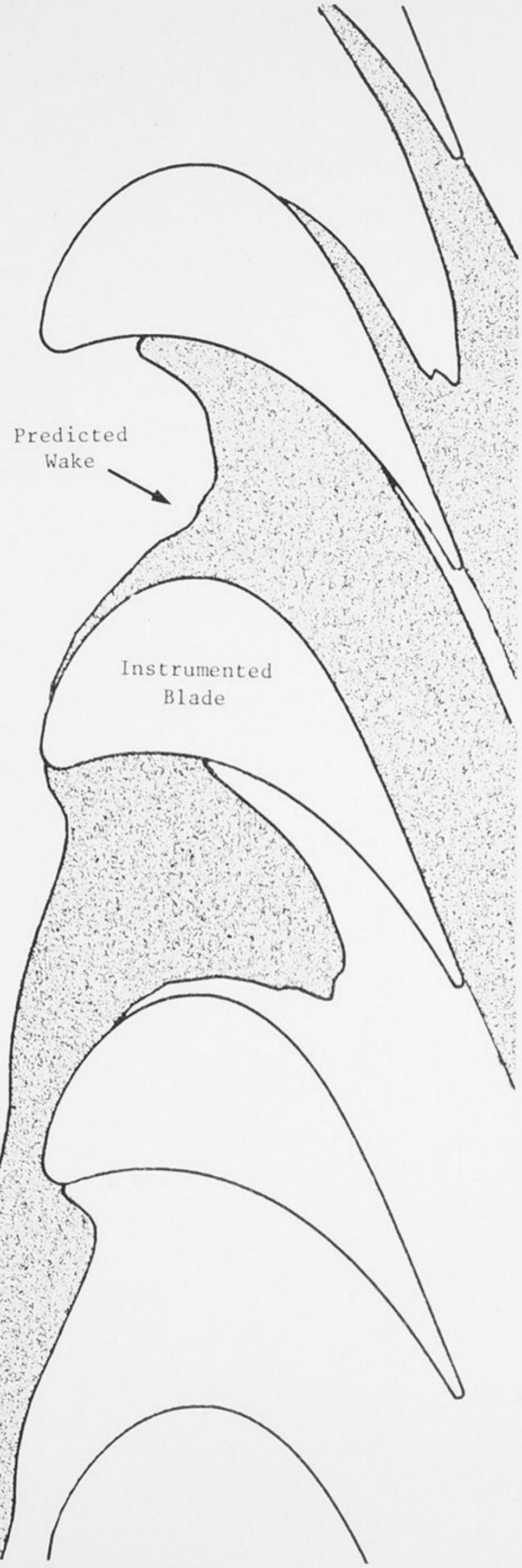

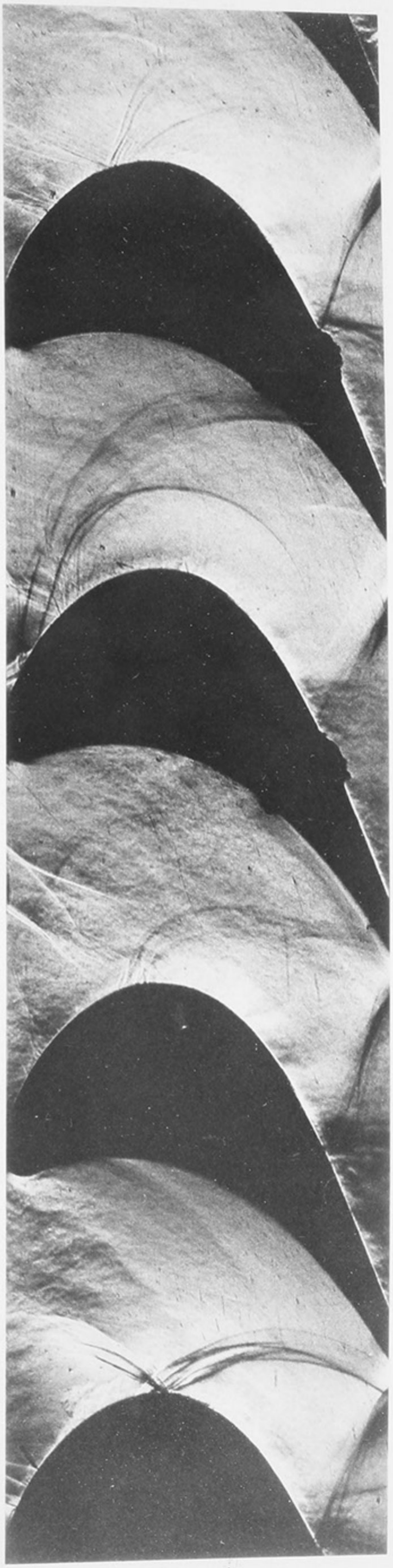

Plate 14 Schlieren Photograph for Run 5443 and Prediction for the Wake and Shock Positions:

Δt_c = 370 μs (17.29% cycle)

M_b = 1.219 (N = 14023 rpm)

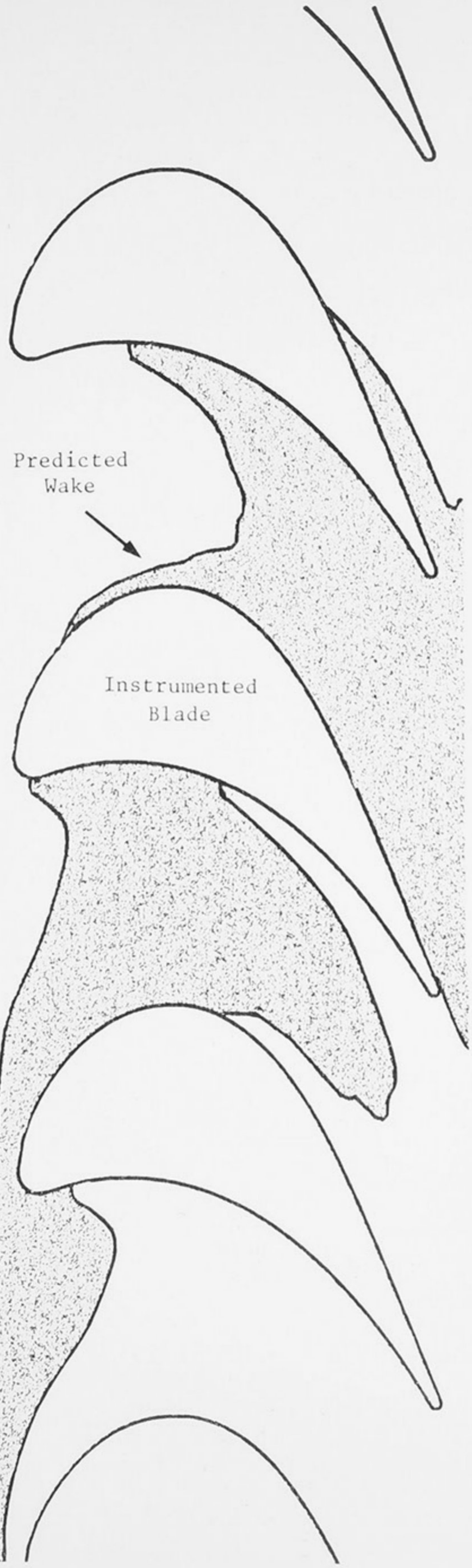

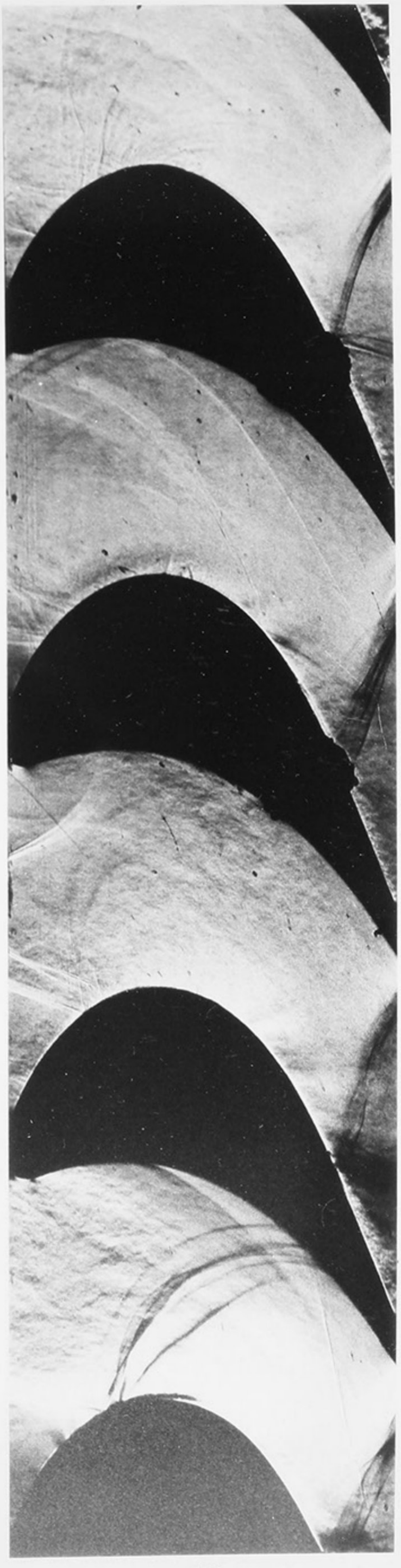

Plate 15 Schlieren Photograph for Run 5434 and Prediction for the Wake and Shock Positions:

Δt_c = 414 μs (19.35% cycle)

M_b = 1.213 (N = 14019 rpm)

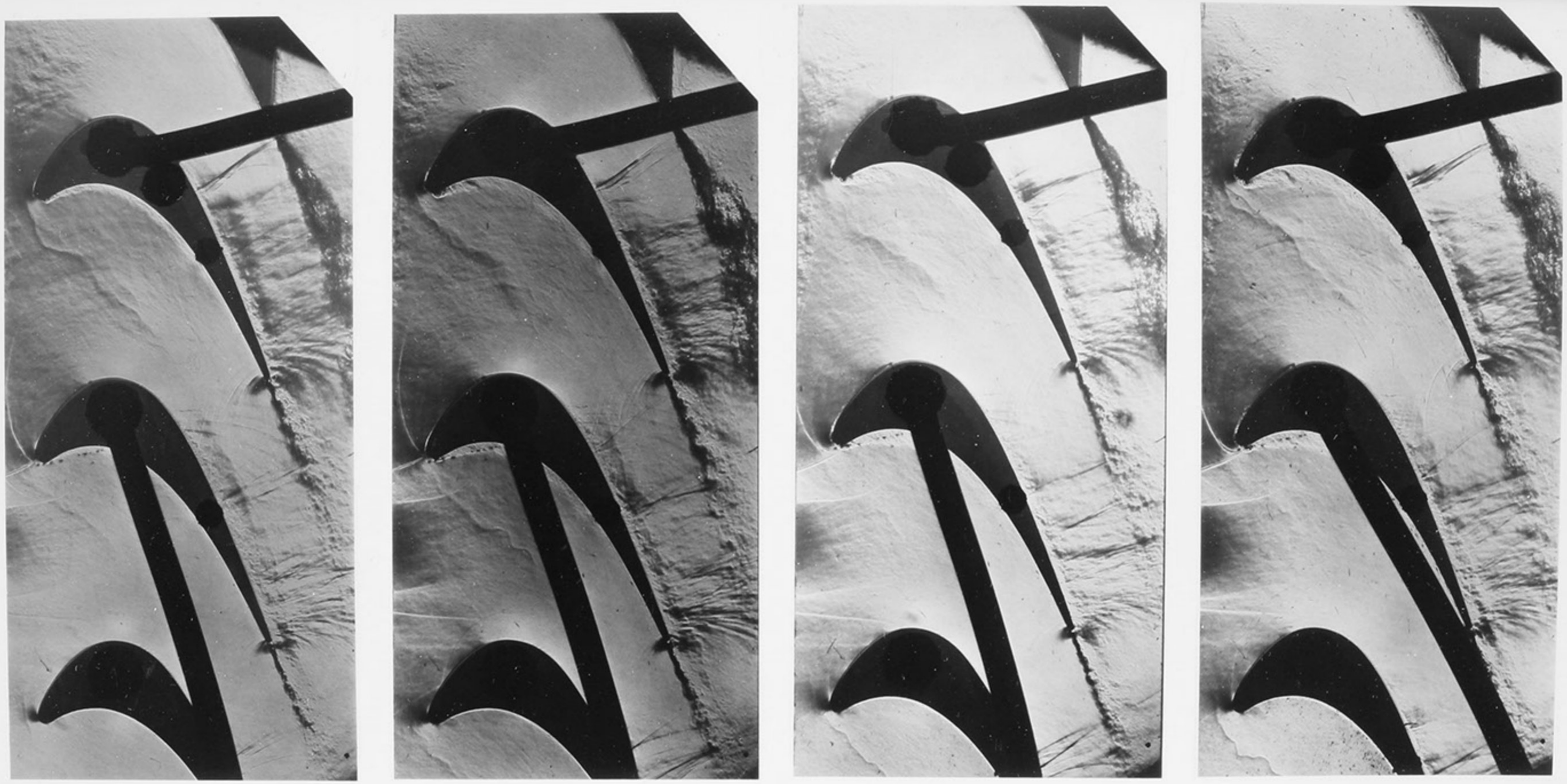

(a) Run 5189 (b) Run 5190 (c) Run 5191 (d) Run 5185

Plate 16 Schlieren Photographs of the B22 Cascade. Configuration 'A' at Similar Cycle Percentage, M_b = 0.92, M_2 = 0.96, Re_2 = 2.02E6 with Variation in Blowing Rate:

(a) B = 0.5 (4.68% cycle)

(b) B = 1.0 (4.57% cycle)

(c) B = 1.5 (5.11% cycle)

(d) B = 1.8 (4.91% cycle).

Schlieren Taken with a Horizontal Knife-Edge for the 2 Bar Case.

(a)
Run 5212

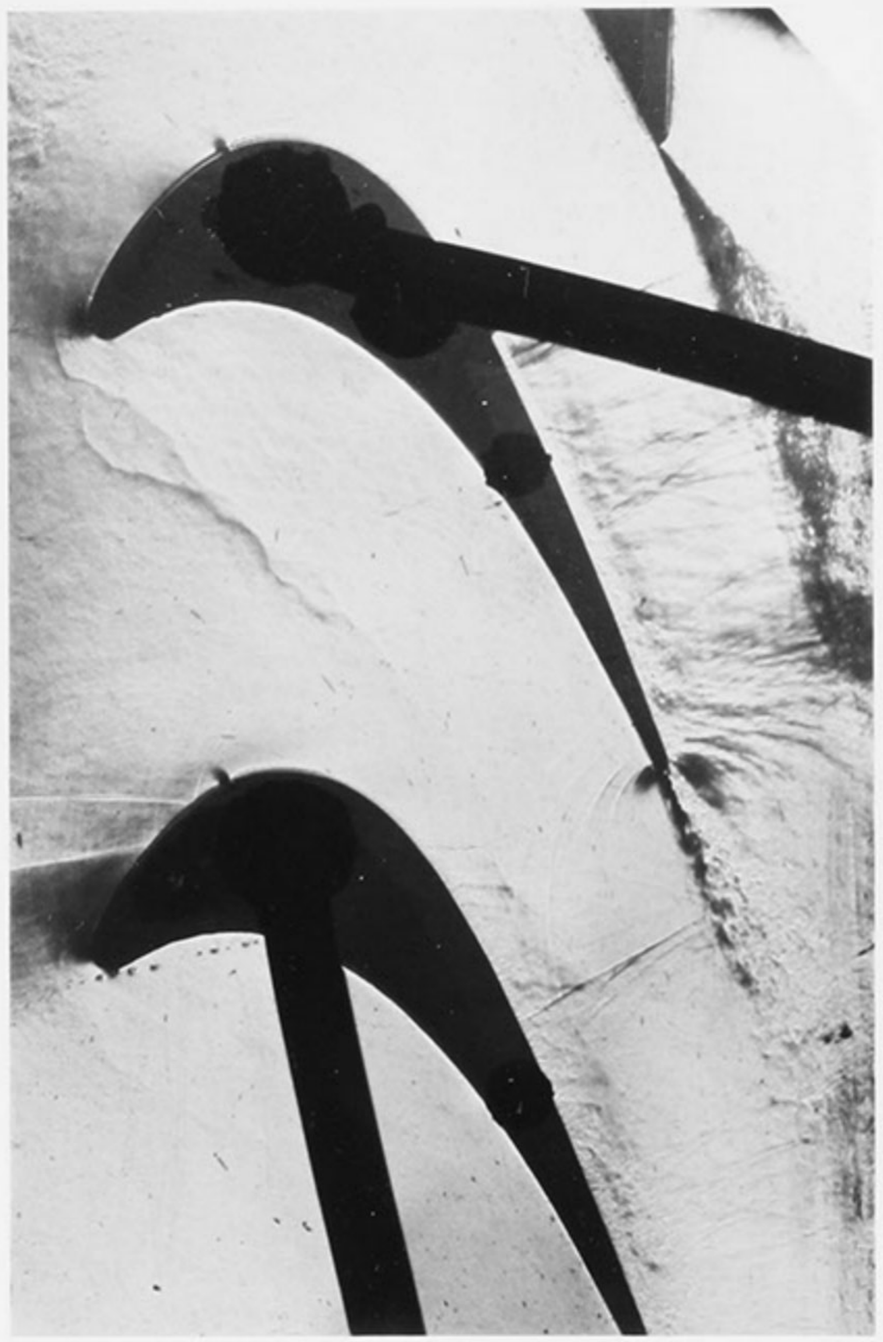

(b)
Run 5207

(c)
Run 5211

Plate 17 Schlieren Photographs of the B22 Cascade. Configuration 'B' at Similar Cycle Percentage, $M_b = 0.92$, $M_2 = 0.96$, $Re_2 = 2.02E6$ with Variation in Blowing Rate:

(a) B = 0.5 (1.17% cycle) (b) B = 1.0 (0.96% cycle) (c) B = 1.5 (0.94% cycle).

Schlieren Taken with a Horizontal Knife-Edge for the 2 Bar Case.

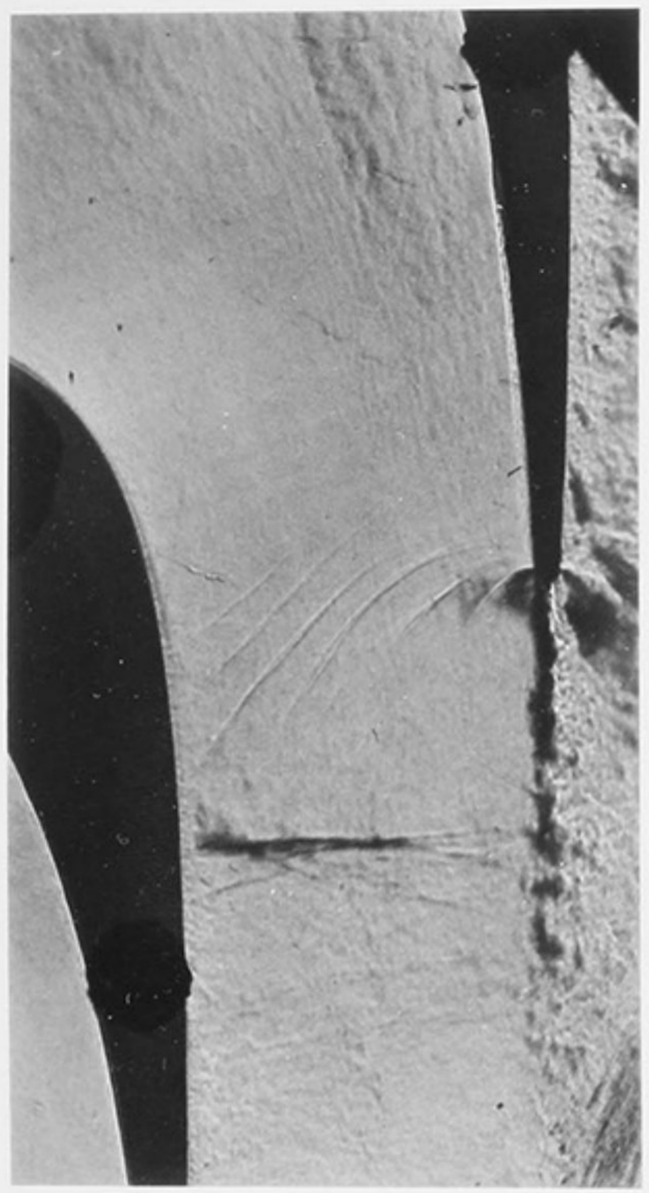

(a)
Run 5197

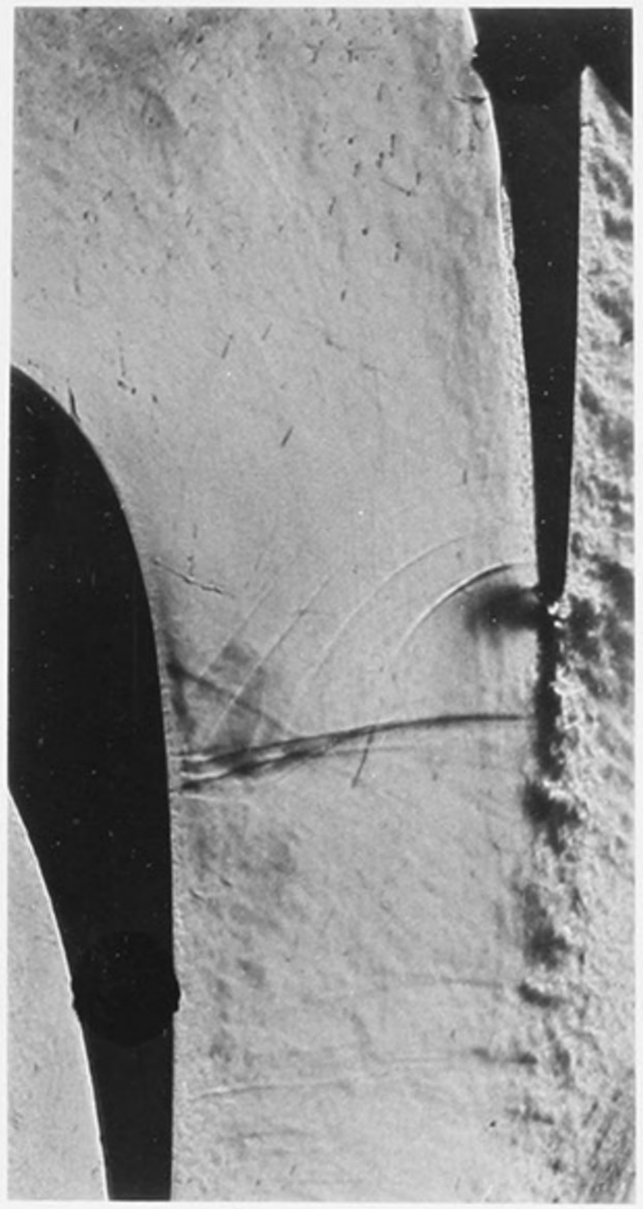

(b)
Run 5200

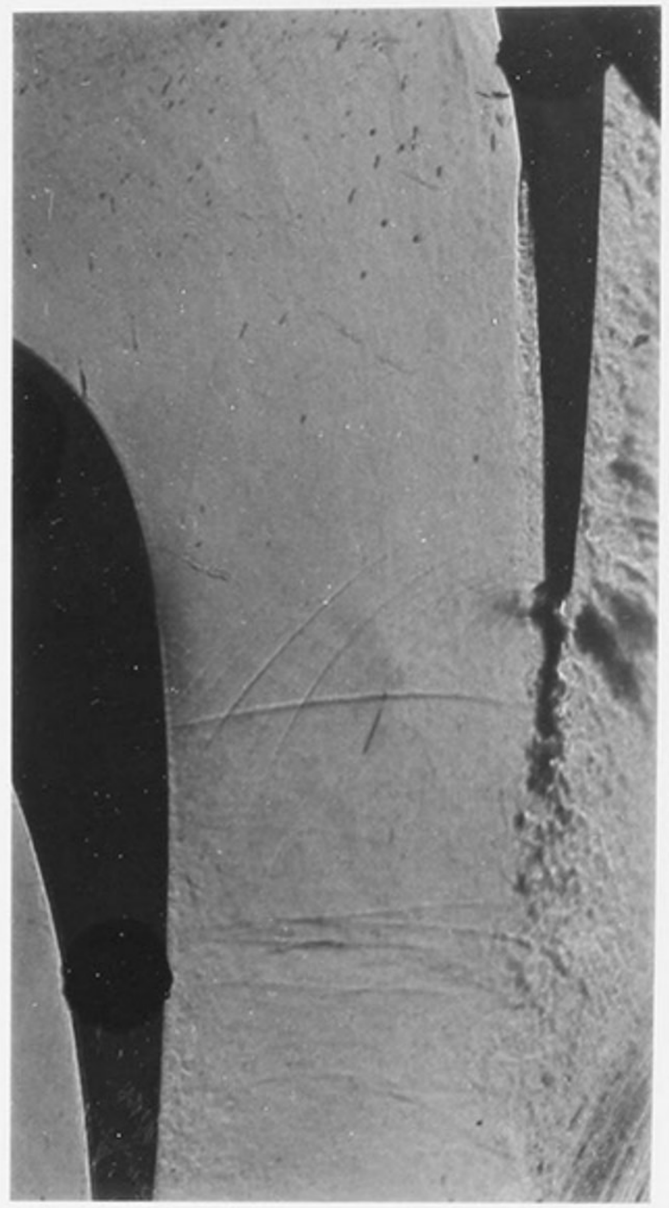

(c)
Run 5199

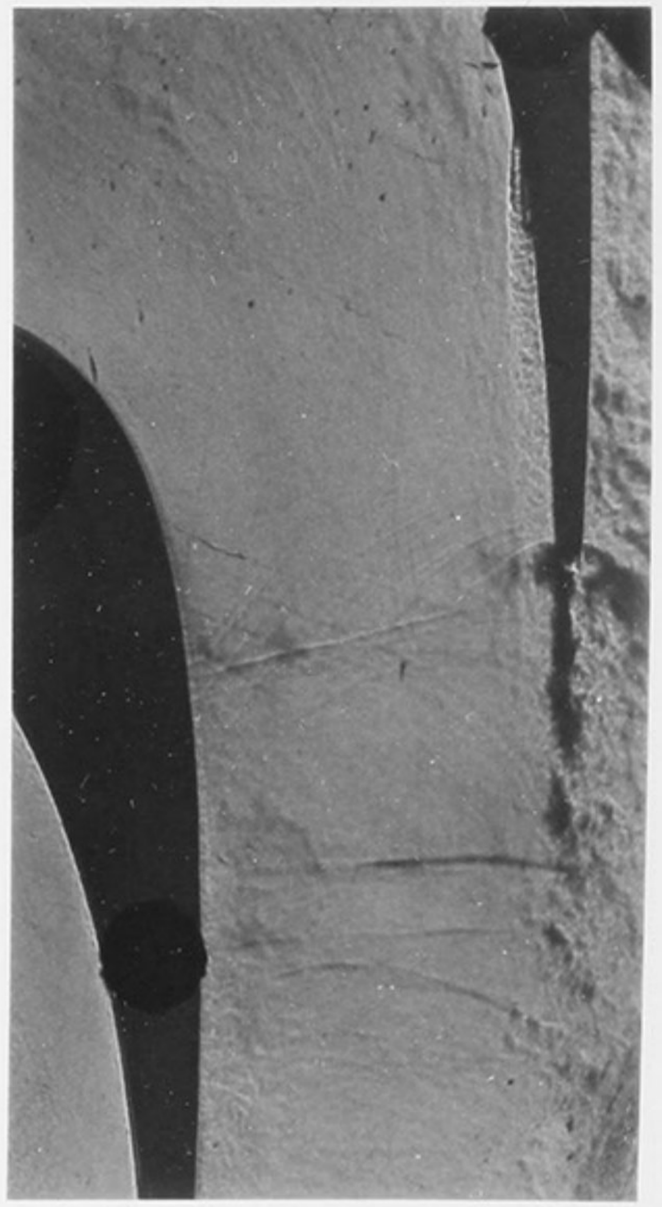

(d)
Run 5198

Plate 18 Schlieren Photographs of the B22 Cascade. Configuration 'C' (holes at 75% x/cax) for the 2 Bar Case with Variation in Blowing Rate:

(a) B = 1.0 (38.69% cycle)

(b) B = 1.3 (50.11% cycle)

(c) B = 2.0 (44.80% cycle)

(d) B = 2.8 (44.58% cycle).

Schlieren Taken with a Horizontal Knife-Edge for the 2 Bar Case.

Build 'B'
B = 0.5

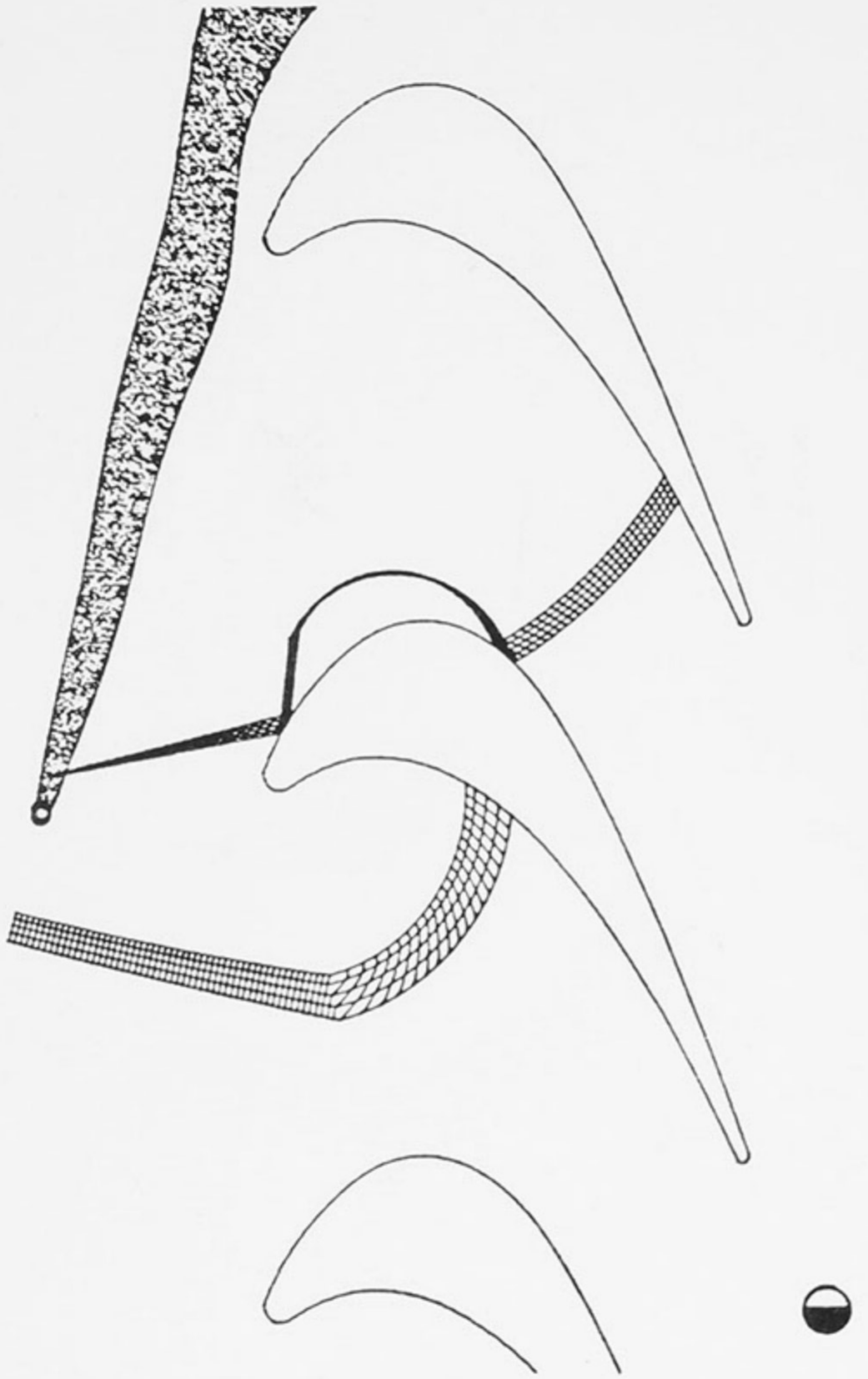

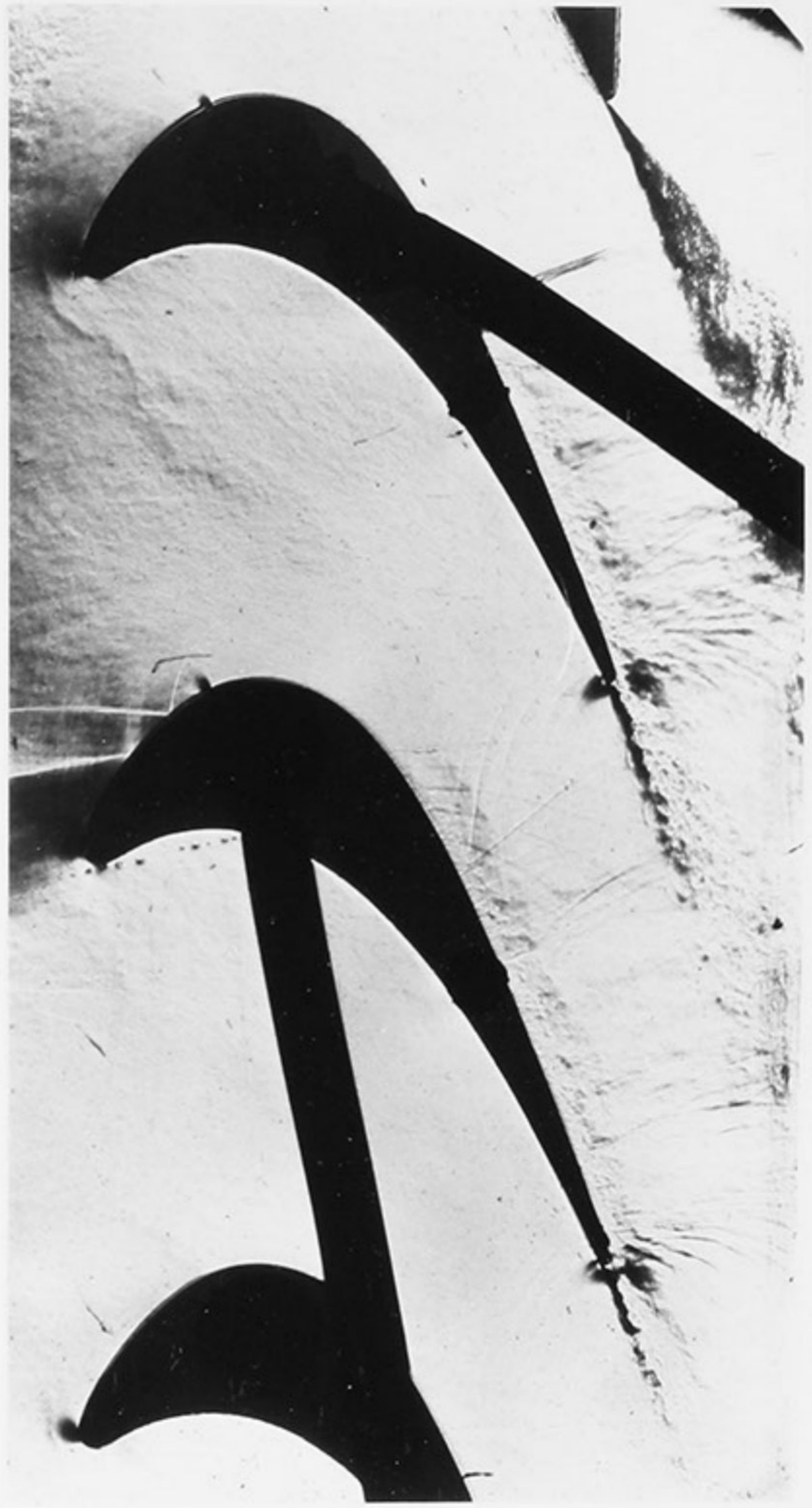

Plate 19 Schlieren Photograph for Run 5212 and Prediction for the Wake and Shock Positions:

Δt_c = -11 μs (-0.6% cycle);

M_b = 0.92, Estimated Bar Position at +3 mm.

Build 'A'
B = 1.8

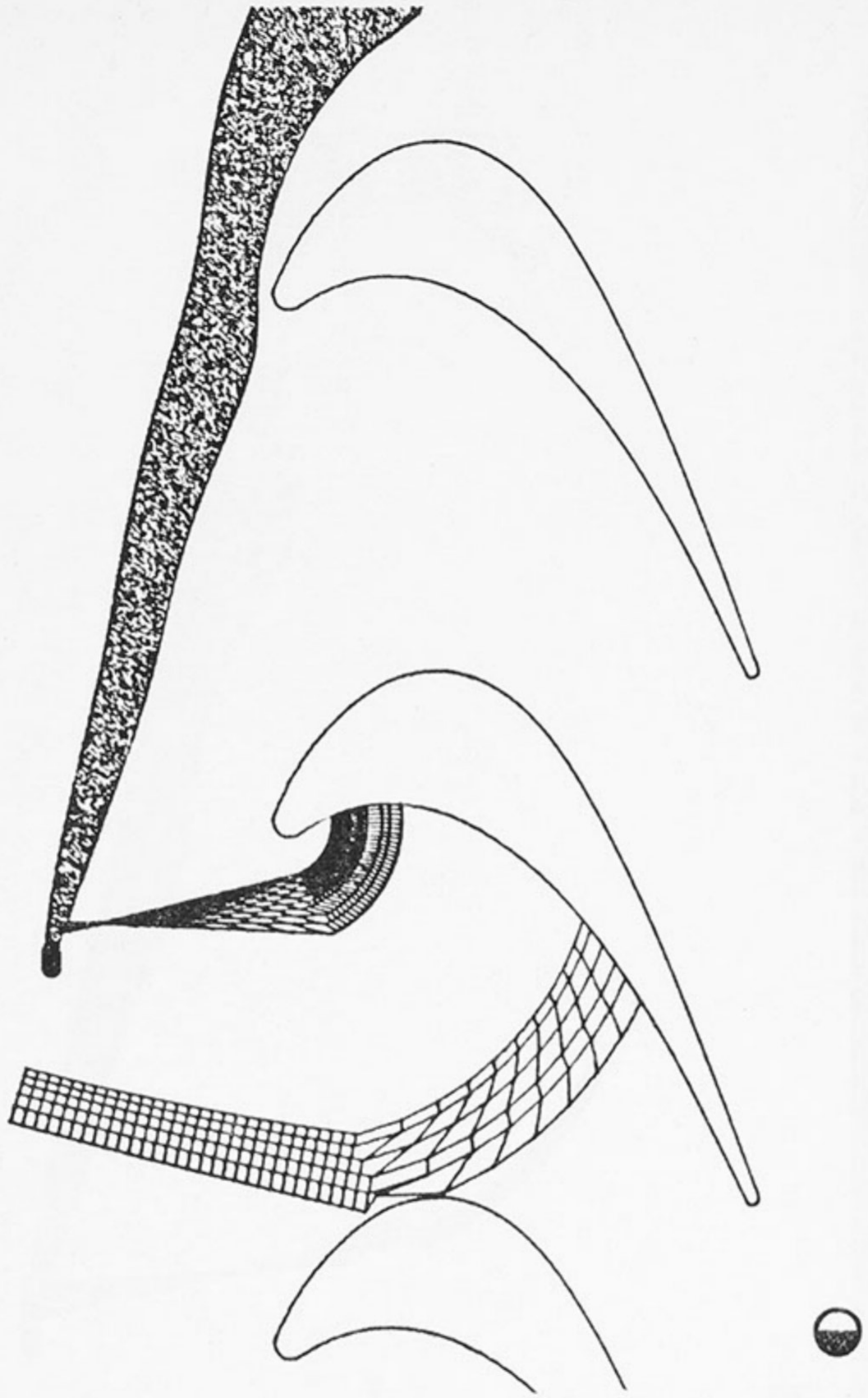

Plate 20 Schlieren Photograph for Run 5177 and Prediction for the Wake and Shock Positions:

Δt_c = 33 μs (1.7% cycle);

M_b = 0.92, Estimated Bar Position at -8 mm.

Build 'A'
B = 1.8

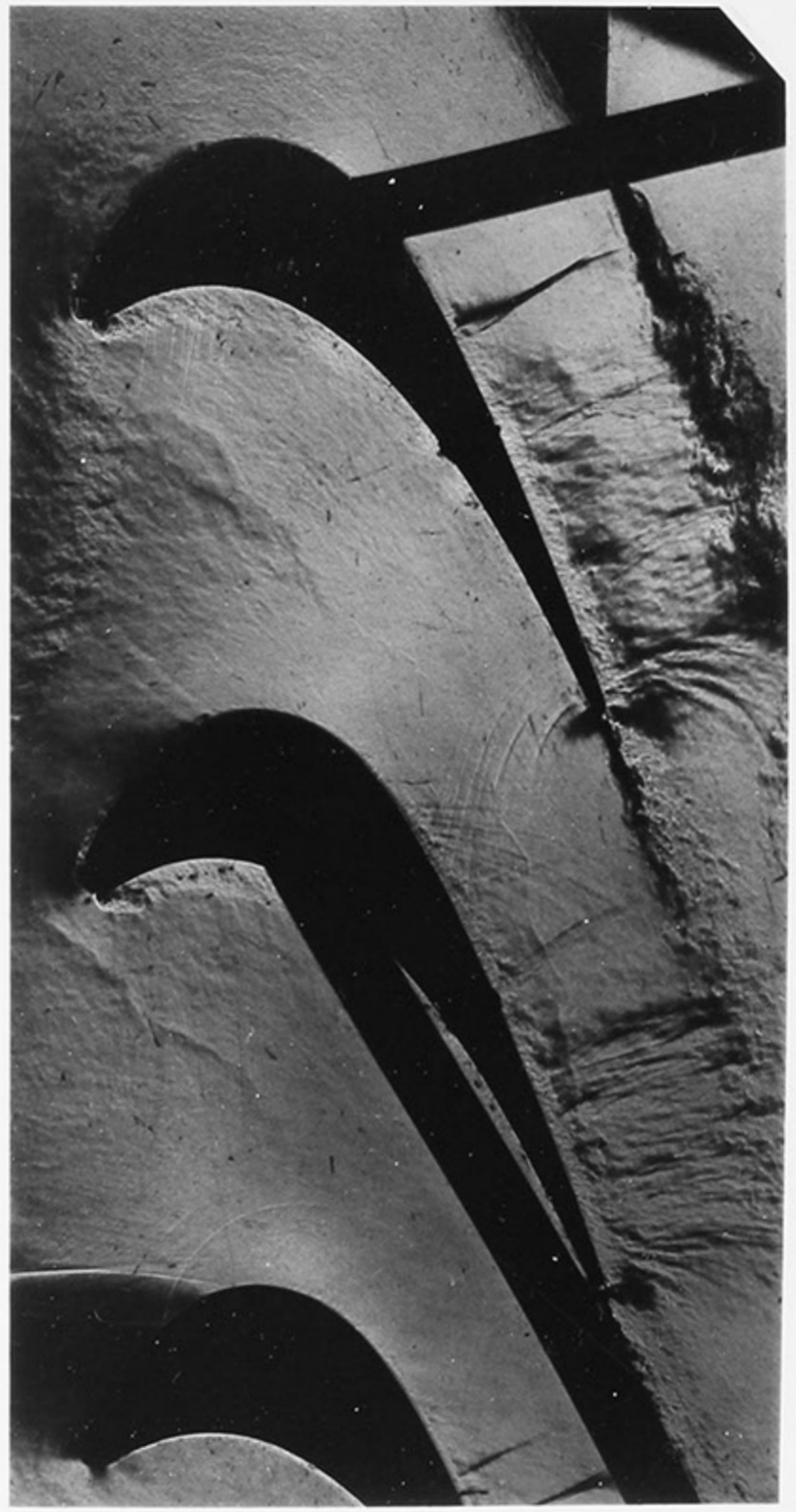

Plate 21 Schlieren Photograph for Run 5181 and Prediction for the Wake and Shock Positions:

Δt_c = 165 μs (8.3% cycle);

M_b = 0.92, Estimated Bar Position at -40 mm.

Build 'A'
B = 1.0

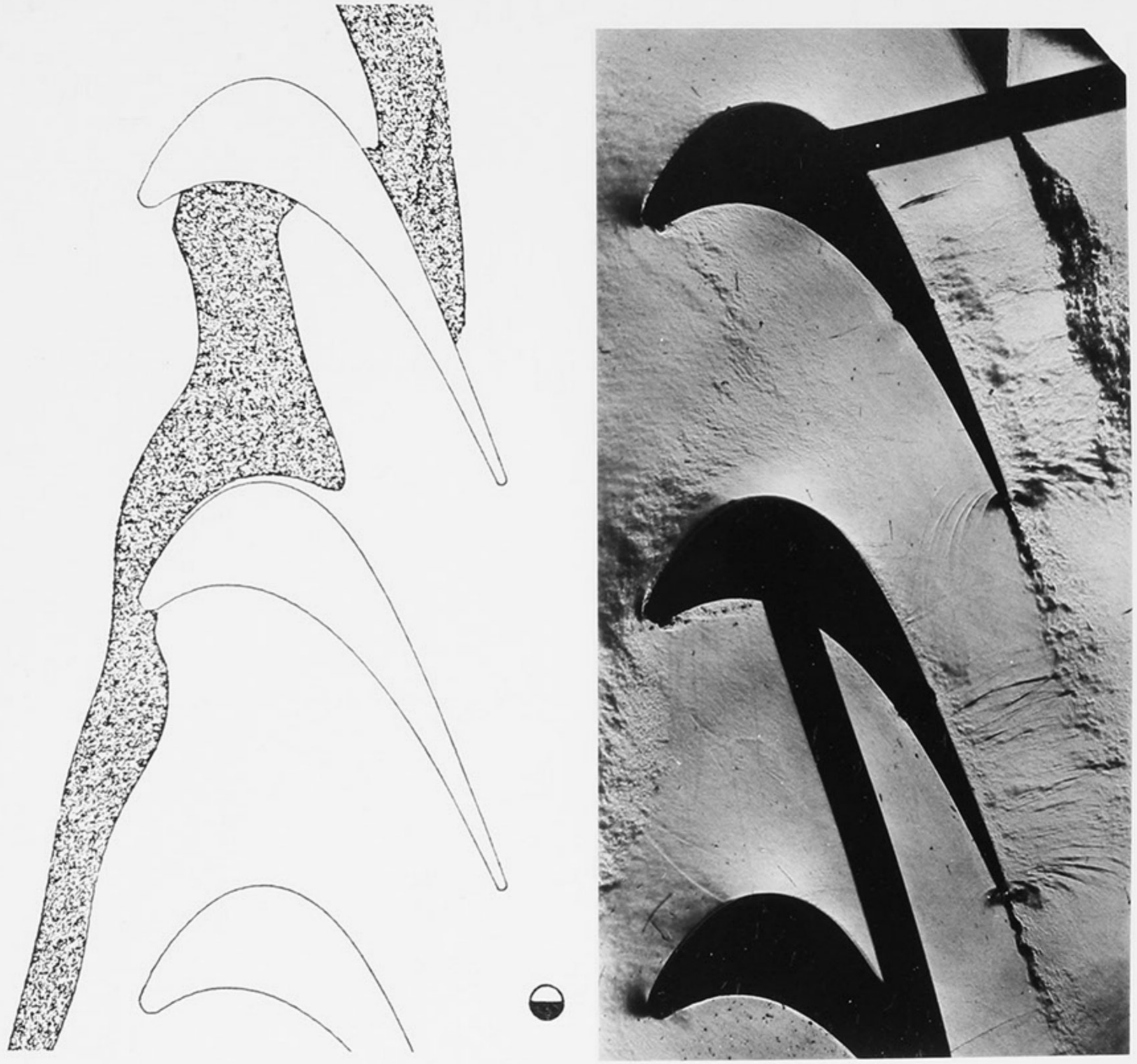

Plate 22 Schlieren Photograph for Run 5193 and Prediction for the Wake and Shock Positions:

Δt_c = 414 μs (20.7% cycle);

M_b = 0.92, Estimated Bar Position at -91 mm.

APPENDIX A

THE TRANSIENT HEAT CONDUCTION MODEL

The internal temperature distribution within the test model was predicted for the ACE blade using the 'MANIFOLD' modeller and 'fesdec' finite element package run in 'transient thermal analysis' mode. The use of such a modelling package enables accurate geometry and boundary conditions to be specified, and provides a solution to the two-dimensional heat diffusion equation:

$$\frac{\partial^2 T}{\partial x^2} + \frac{\partial^2 T}{\partial x^2} = \frac{1}{\alpha}\frac{\partial T}{\partial t}, \quad \alpha = k_s/\rho_s c_s, \quad T = T(x,y,t)$$

subject to the conditions that

$T(x,y,0) = T_{init}$ (initial temperature constant)

$T(x_s,y_s,t_i) = T_w(x_s,y_s,t_i)$ (prescribed temperatures at the surface at all times, i.)

where T_w is the surface temperature obtained from an ILPT test, approximating to a parabolic temperature rise with time. Before performing the analysis, two non-dimensional groups can be calculated which determine the nature of the heat conduction model:

(i) Fourier number, Fo:

$$Fo = \frac{\alpha\Delta t}{(\Delta x)^2} \simeq \frac{6.75E\text{-}7 \times 2.5E\text{-}3}{(0.1E\text{-}3)^2} = 0.17$$

This determines the stability of a transient heat conduction solution, a value of $Fo < 0.25$ typically required for explicit methods. For the given experimental sampling rate of 400Hz (or 2.5E-3 s) and fixed thermal diffusivity the smallest value of Δx allowing for a stable solution can therefore be determined. The mesh shown inset into Figure A.2 has a minimum Δx of 0.1 mm, with the

smallest elements near to the surface, where the maximum thermal gradients are to be found.

(ii) Biot number, Bi:

$$Bi = \frac{hC_{TN}}{k_s} \simeq \frac{1000 \times 0.05}{1.3} = 38.5 = \frac{\text{external convection}}{\text{internal conduction}}$$

where C_{TN} is the characteristic length, h the external heat transfer coefficient and k_s the substrate thermal conductivity. A value of Bi > 1 implies that thermal gradients exist within the substrate and a lumped capacity model is invalid.

The calculation procedure is given in Figure A.1. The profile co-ordinates, thin film gauge locations and temperature-time histories are transferred to the Hewlett-Packard Series 200 micro-computer on which the analysis is performed, and input boundary condition files for 'fesdec' automatically generated from this data using the program 'Set_temp' specifically written for this purpose. A transient solution is pursued up to a specified time, typically the measure point time $t_m \simeq 0.25$ seconds. The results at this time are presented in terms of isotherms within the blade in Figure A.2. These confirm the validity of the semi-infinite approximation, which requires that the isotherms run parallel to the surface. The most significant deviations occur near to the trailing-edge, as shown inset in Figure A.2, where some lateral heat conduction would take place. The 'fesdec' suite also predicts the surface heat flux into the body, whose mean value is consistent with that calculated by means of the analogue technique. Detailed distributions of heat transfer could not be obtained due to the limited grid resolution possible, which cause significant numerical difficulties in determining the temperature gradients normal to the external surface.

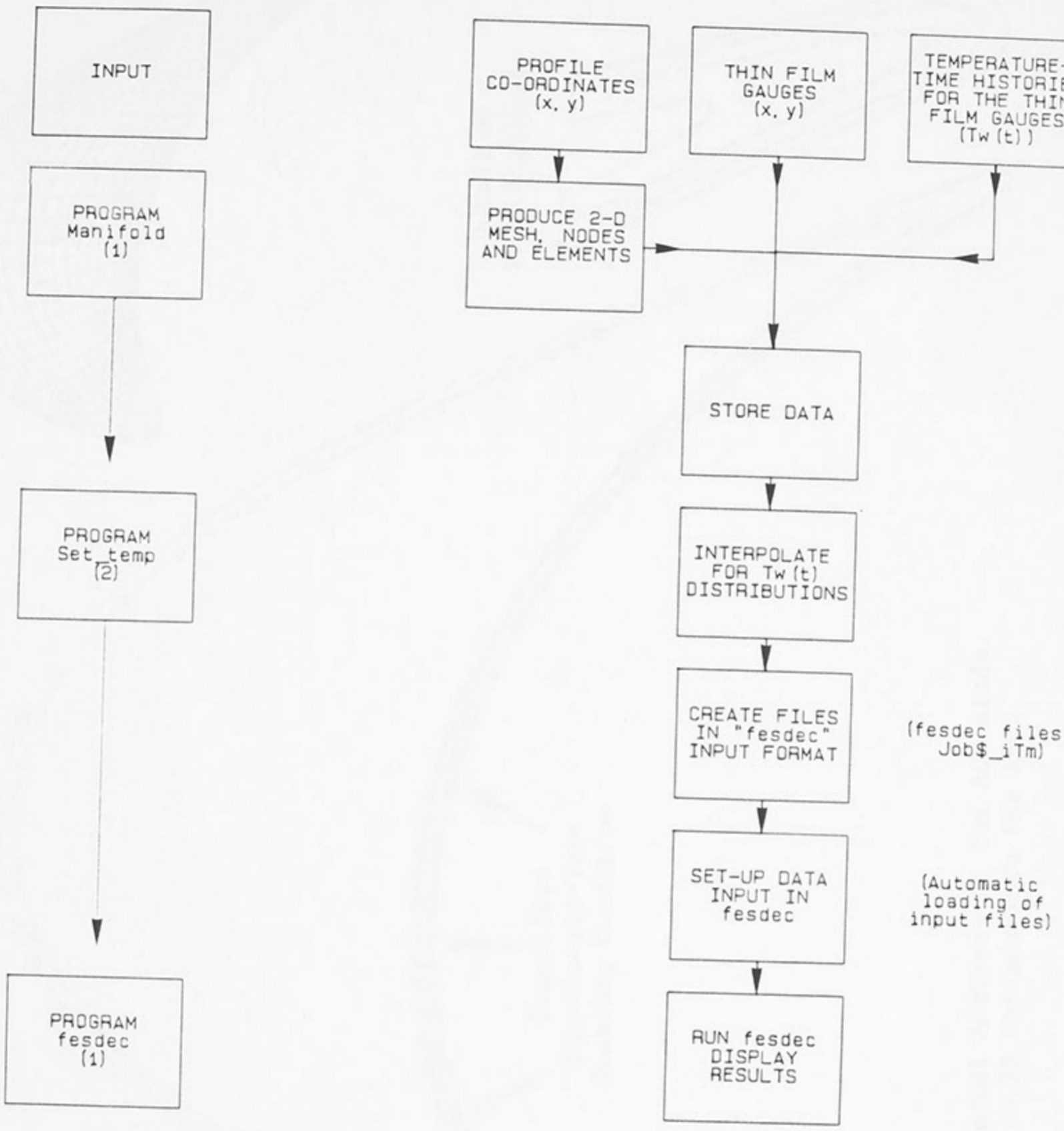

Fig. A.1 Flowchart of the Method used in Establishing a Transient Thermal Solution for the Internal Temperature Distribution of a Blade Subject to Pre-determined Surface Temperature-Time Histories.

(1) Supplied by ETA Systems.

(2) Written by the Author.

ACE BLADE
JOBNAME - B29
ISOTHERM CONTOURS
RESULT SET 5

VALUES K
A= 320
B= 340
C= 360
D= 380

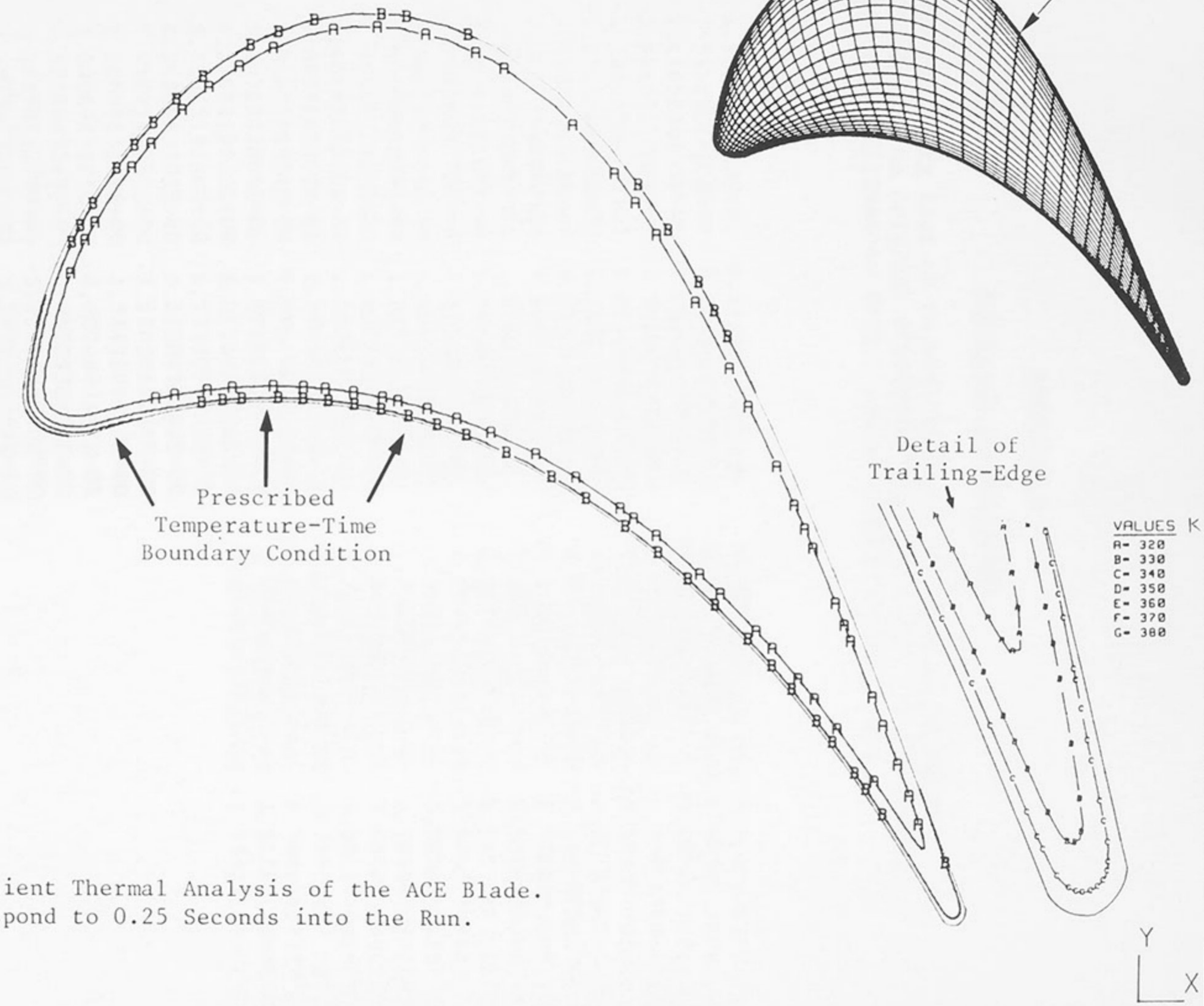

Fig. A.2 Results of a Transient Thermal Analysis of the ACE Blade. Isotherms Correspond to 0.25 Seconds into the Run.

APPENDIX B

ACE BLADE CO-ORDINATES

The following list of co-ordinates are the results of spline-fitting to an original PROCONSEL file record for the ACE profile, given in millimetres from a nominal blade centre datum.

-1.5777370003E+01	-6.3789715747E-01
-1.5316760408E+01	1.0869440037E+00
-1.4165236421E+01	3.6804122353E+00
-1.3013712434E+01	5.5570027619E+00
-1.1862188448E+01	7.0326629235E+00
-1.0710664461E+01	8.2592728063E+00
-9.5591404742E+00	9.2560630919E+00
-8.4076164874E+00	1.0063291980E+01
-7.2560925007E+00	1.0690091559E+01
-6.1045685139E+00	1.1142381836E+01
-4.9530445272E+00	1.1432964512E+01
-3.8015205404E+00	1.1566283530E+01
-2.6499965536E+00	1.1551915320E+01
-1.4984725669E+00	1.1387982327E+01
-3.4694858013E-01	1.1065114199E+01
8.0457540662E-01	1.0585435292E+01
1.9560993934E+00	9.9335964031E+00
3.1076233801E+00	9.0782016577E+00
4.2591473669E+00	8.0371696796E+00
5.4106713536E+00	6.7754070363E+00
6.5621953404E+00	5.2668474356E+00
7.7137193272E+00	3.5505669241E+00
8.8652433139E+00	1.5843807439E+00
1.0016767301E+01	-6.0074049981E-01
1.1168291287E+01	-2.9855933871E+00
1.2319815274E+01	-5.5642587009E+00
1.3471339261E+01	-8.2974466191E+00
1.4622863248E+01	-1.1114313941E+01
1.5774387234E+01	-1.4016129682E+01
1.6925911221E+01	-1.6912427458E+01
1.8077435208E+01	-1.9798529416E+01
1.8801467100E+01	-2.1714482400E+01
1.8607719280E+01	-2.2098221052E+01
1.8183904410E+01	-2.2170155240E+01
1.7650883040E+01	-2.1503907451E+01
1.6348954743E+01	-1.9372479815E+01
1.5047026445E+01	-1.7392060843E+01
1.3745098148E+01	-1.5549383852E+01
1.2443169850E+01	-1.3851112530E+01
1.1141241553E+01	-1.2299104450E+01
9.8393132554E+00	-1.0874599475E+01
8.5373849579E+00	-9.5845161412E+00
7.2354566603E+00	-8.4134249082E+00
5.9335283628E+00	-7.3642451549E+00
4.6316000653E+00	-6.4311473460E+00
3.3296717678E+00	-5.6071226354E+00
2.0277434702E+00	-4.8958978404E+00
7.2581517273E-01	-4.2870170946E+00
-5.7611312479E-01	-3.7843706938E+00
-1.8780414223E+00	-3.3790470663E+00
-3.1799697198E+00	-3.0750725034E+00
-4.4818980174E+00	-2.8658068807E+00
-5.7838263149E+00	-2.7504800695E+00
-7.0857546124E+00	-2.7268552904E+00
-8.3876829099E+00	-2.7947686292E+00
-9.6896112074E+00	-2.9507793594E+00
-1.0991539505E+01	-3.1996632733E+00
-1.2293467802E+01	-3.5410459020E+00
-1.3595396100E+01	-3.9846976000E+00
-1.4445937879E+01	-4.0884979076E+00
-1.5247256336E+01	-3.7855440317E+00
-1.5815734233E+01	-3.1446655715E+00
-1.5890921800E+01	-2.3129262000E+00
-1.5777370003E+01	-6.3789715747E-01